

Exploring the Photophysics of Novel Poly-Carbene/Pyridine Iron(II) Complexes

Modelling, Synthesis and Characterization

Dissertation zur Erlangung des Grades

Doctor rerum naturalium (Dr. rer. nat.)

Im Promotionsfach Chemie

am Fachbereich 09

Chemie, Pharmazie, Geographie und Geowissenschaften

Der Johannes Gutenberg-Universität Mainz

vorgelegt von

Thomas Reuter

Geboren am 13. Januar 1991 in Worms

Mainz, 2024



JOHANNES GUTENBERG
UNIVERSITÄT MAINZ

This thesis was written in the period from October 2017 to March 2024 at the Department of Chemistry of the Johannes Gutenberg University Mainz under the supervision of [REDACTED].

"I, Thomas Reuter, hereby declare that I wrote the dissertation submitted without any unauthorized external assistance and used only sources acknowledged in the work. All textual passages which are appropriated verbatim or paraphrased from published and unpublished texts as well as all information obtained from oral sources are duly indicated and listed in accordance with bibliographical rules. In carrying out this research, I complied with the rules of standard scientific practice as formulated in the statutes of Johannes Gutenberg University Mainz to insure standard scientific practice."

(Place, Date)

(Signature)

Dean: Prof. Dr. Eva Rentschler

First reviewer: [REDACTED]

Second reviewer: [REDACTED]

Date of the oral exam: January 20th, 2025

Abstract

The utilization of light energy plays an essential role in today's society, e.g. in the generation of electricity employing photovoltaics, optical sensing and imaging as well as photochemistry. To power such applications suitable materials are necessary.

A promising group of compounds for such light driven applications are transition metal complexes due to their electronic structure and the possibility to precisely control their atomic composition, allowing the fine-tuning of their properties for specific uses. In the past, however, many of the employed compounds relied on precious or rare metals. The high cost and lower availability of these metals impedes the usage of such complexes in large scale applications. In recent years research has focused on finding alternative systems that instead rely on earth-abundant metals as cheaper and more easily available options.

The research presented in this work pursues the development of novel (pseudo-)octahedral transition metal complexes based on the earth-abundant metal iron by investigating the fundamental photophysical properties of these compounds. Since poly-pyridine complexes of iron(II) only exhibit very short lifetimes of the excited $^3\text{MLCT}$ state (< 1 ps), suitable ligand systems to prolong the lifetime of the $^3\text{MLCT}$ state have to be investigated. The ligands employed in this work combine the concept of high local symmetry with a push-pull design, simultaneously stabilizing the metal-to-ligand charge transfer (MLCT) and destabilizing dark non-emissive metal centred (MC) excited states.

In the first part, the linear tridentate ligand 2,6-bis((3-methyl-2,3-dihydro-1*H*-imidazol-1-ylidene)methyl)pyridine (pbmi) combining a π -accepting pyridine bridged *via* methylene bridges in the 2- and 6-position to a σ -donating methyl-imidazolide moiety, respectively, was synthesized and utilized to attempt the synthesis of the homoleptic complex $[\text{Fe}(\text{pbmi})_2]^{2+}$. The detailed investigation of the photophysical properties of the homoleptic complex $[\text{Fe}(\text{pbmi})_2]^{2+}$ could not be carried since the compound could not be isolated. The synthesis and characterization of $[\text{Fe}(\text{pbmi})_2]^{2+}$ was later published by Gros et. al. so further research attempts were stopped.

In the second part the ligand design was modified to a tripodal structure incorporating two pyridine moieties as π -acceptors linked to a methyl-imidazolide as a σ -donor *via* a methine-bridge, in the ligand 2,2'-((3-methyl-2,3-dihydro-1*H*-imidazol-1-ylidene)methylene)dipyridine (dpmi). The homoleptic iron(II) complex $[\text{Fe}(\text{dpmi})_2]^{2+}$ was investigated regarding the lifetime of the $^3\text{MLCT}$

excited state utilizing ultra-fast transient absorption spectroscopy performed by Ayla Kruse (Group of Professor Lochbrunner) which revealed an extended lifetime of said excited state of about 9 ps.

The third part focused on the idea of increasing the number of σ -donating methyl-imidazolylidene moieties inside the ligand, which should further increase the destabilizing effect on the excited MC states and prolong the lifetime of the excited $^3\text{MLCT}$ state. Therefore the tridentate tripodal ligand 2-(bis(3-methyl-2,3-dihydro-1*H*-imidazol-1-ylidene)methyl)pyridine (pdmi) incorporating two methyl-imidazole moieties and one pyridine ring and its homoleptic iron(II) complexes *cis*- $[\text{Fe}(\text{pdmi})_2]^{2+}$ and *trans*- $[\text{Fe}(\text{pdmi})_2]^{2+}$ were synthesized and investigated towards their photophysical properties. The lifetime of the excited $^3\text{MLCT}$ state was only increased slightly compared to $[\text{Fe}(\text{dpmi})_2]^{2+}$ at 293 K. Variable-temperature ultra-fast transient absorption spectroscopy, however, revealed a temperature dependence of the lifetime of the $^3\text{MLCT}$ state of *cis*- $[\text{Fe}(\text{pdmi})_2]^{2+}$ and no such dependence in the *trans*-isomer. This temperature dependence of the lifetime was then utilized to investigate the electronic coupling between the excited $^3\text{MLCT}$ and ^3MC states using semi-classical Marcus-Hush theory, revealing an electronic coupling constant $H_{\text{AB}} = 81 \pm 6 \text{ cm}^{-1}$ for the inter conversion barrier between the excited $^3\text{MLCT}$ and ^3MC states.

Kurzzusammenfassung

Die Nutzung von Lichtenergie spielt eine wichtige Rolle in der heutigen Gesellschaft, z.B. in der Erzeugung von Strom durch Einsatz von Photovoltaik-Anlagen, in optischer Sensorik und Bildgebung als auch in der Photochemie. Um solche Anwendungen zu ermöglichen, bedarf es geeigneter Materialien.

Eine vielversprechende Gruppe von Verbindungen für solche lichtgetriebenen Anwendungen stellen Übergangsmetallkomplexe dar, aufgrund ihrer elektronischen Struktur als auch der Möglichkeit der präzisen Kontrolle ihrer atomaren Zusammensetzung, was die genaue Feinabstimmung dieser Systeme auf spezielle Anwendungen ermöglicht. In der Vergangenheit spielten Übergangsmetallkomplexe bestehend aus edlen oder seltenen Metallen eine große Rolle, die aufgrund der hohen Kosten und geringeren Verfügbarkeit solcher Metalle die Anwendung solcher Komplexe in großtechnischen Prozessen verhindert. Der Fokus der Forschung wandelte sich in den letzten Jahren darum hin zur Entwicklung alternativer Verbindungen welche statt der seltenen Metalle, billigere und leichter verfügbare Alternativen verwenden.

Diese Arbeit beschreibt die Entwicklung von (pseudo-)oktaedrischen Übergangsmetallkomplexen basierend auf dem häufig vorkommenden Metall Eisen und der Untersuchung der fundamentalen photophysikalischen Eigenschaften dieser Verbindungen. Aufgrund der kurzen Lebenszeit des angeregten $^3\text{MLCT}$ Zustands (< 1 ps) in Poly-Pyridin Eisen(II) Komplexen, müssen geeignete Ligandensysteme zur Verlängerung der Lebenszeit des $^3\text{MLCT}$ Zustandes untersucht werden. Die in dieser Arbeit verwendeten Liganden kombinieren hierbei das Konzept hoher lokaler Symmetrie mit dem Konzept von Push-Pull-Liganden, bei welchen gleichzeitig die Metall-zu-Ligand-Charge-Transfer (MLCT) angeregten Zustände stabilisiert und die dunklen, nicht emissiven, angeregten metallzentrierten (MC) Zustände destabilisiert werden.

Im ersten Teil der Arbeit wird der tridentate lineare Ligand 2,6-Bis((3-methyl-2,3-dihydro-1H-imidazol-1-yliden)methyl)pyridin (pbmi), welcher aus einem Pyridin als π -Akzeptor verbunden in 2- und 6-Position über Methylenbrücken mit je einem Methyl-Imidazol als σ -Donoren fungiert, und die Syntheseveruche des homoleptischen Eisen(II)-Komplexes beschrieben. Die Untersuchung der photophysikalischen Eigenschaften des Komplexes $[\text{Fe}(\text{pbmi})_2]^{2+}$ konnten aufgrund von Aufreinigungsproblemen nicht durchgeführt werden. Die Synthese und Charakterisierung von $[\text{Fe}(\text{pbmi})_2]^{2+}$ wurde später von Groß et. al. publiziert, sodass weitere Untersuchungen beendet wurden.

Im zweiten Teil der Arbeit wurde das Ligandendesign modifiziert und statt einen tridentate linearen Liganden ein tripodaler Ligand 2,2'-((3-Methyl-2,3-dihydro-1*H*-imidazol-1-yliden)methylen)-dipyridin (dpmi) bestehend aus zwei Pyridinen als π -Akzeptoren verknüpft mit einer Methyl-Imidazol-Einheit als σ -Donor über eine Methyl-Gruppe. Der homoleptische Komplex $[\text{Fe}(\text{dpmi})_2]^{2+}$ wurde bezüglich der Lebenszeit des angeregten $^3\text{MLCT}$ -Zustandes mittels ultra-schneller transients Absorptions-spektroskopie von Ayla Kruse untersucht. Diese Untersuchung ergab eine erhöhte Lebenszeit des angeregten $^3\text{MLCT}$ -Zustandes von 9 ps.

Im dritten Teil der Arbeit lag der Fokus auf der Frage welchen Einfluss eine Erhöhung der Anzahl der Methyl-Imidazol σ -Donor-Einheiten und der somit vergrößerte destabilisierende Einfluss auf die metallzentrierten Zustände auf die Lebenszeit des angeregten $^3\text{MLCT}$ -Zustand hat. Hierfür wurde der tripodale Ligand 2-(bis(3-methyl-2,3-dihydro-1*H*-imidazol-1-yliden)methyl)pyridin (pdmi) bestehend aus zwei Methyl-Imidazol-Einheiten und einem Pyridin und dessen homoleptische Eisen(II)-Komplexe *cis*- $[\text{Fe}(\text{pdmi})_2]^{2+}$ und *trans*- $[\text{Fe}(\text{pdmi})_2]^{2+}$ synthetisiert und bezüglich ihrer photophysikalischen Eigenschaften untersucht. Die Lebenszeit des angeregten $^3\text{MLCT}$ -Zustandes war im Vergleich zu $[\text{Fe}(\text{dpmi})_2]^{2+}$ nur wenig erhöht. Allerdings konnte durch variable Temperatur transiente Absorptionsspektroskopie eine Temperatur Abhängigkeit der Lebenszeit des angeregten $^3\text{MLCT}$ -Zustands von *cis*- $[\text{Fe}(\text{pdmi})_2]^{2+}$ festgestellt werden, welche im *trans*-Isomer nicht zu beobachten ist. Diese Temperaturabhängigkeit ermöglicht hier die Untersuchung der elektronischen Kopplung der angeregten $^3\text{MLCT}$ und ^3MC Zustände im Rahmen der Marcus-Hush Theorie. Diese Analyse gibt einen elektronischen Kopplungsparameter $H_{\text{AB}} = 81 \pm 6 \text{ cm}^{-1}$ für die Energiebarriere der internen Konversion zwischen den angeregten $^3\text{MLCT}$ und ^3MC Zuständen.

Table of Contents

Table of Contents	V
Abbreviations and Physical Quantities	VII
1 Introduction.....	1
1.1 Photophysics of TMCs	3
1.1.1 Luminescence	3
1.1.2 Non-radiative decay for CT-Emitters.....	6
1.2 Charge-Transfer Emitters	9
1.2.1 Emitters based on precious metals	9
1.2.2 Earth-abundant alternatives	10
1.3 Photophysical challenges of Iron(II) complexes	16
1.4 Marcus-Hush Theory/Electron Transfer.....	24
1.4.1 Non-adiabatic approach: Marcus Theory.....	24
1.4.2 Adiabatic approach: Marcus-Hush theory.....	27
1.5 Studying TMCs with transient absorption spectroscopy.....	29
2 Aim of work	33
3 Results and Discussion	35
3.1 Synthesis of $[H_2pbmi]^{2+}$ and synthesis attempts of its homoleptic iron(II) complex	37
3.2 Higher MLCT lifetime of carbene iron(II) complexes by chelate ring expansion	43
3.3 A Tetracarbene Iron(II) Complex with a Long-lived Triplet Metal-to-Ligand Charge Transfer State due to a Triplet-Triplet Barrier	49
3.4 Ground- and Excited-State Properties of Iron(II) Complexes Linked to Organic Chromophores.....	59
4 Summary and Outlook.....	77
5 References	81
6 Appendix.....	89

Table of Contents

6.1	Supporting Information for Section 3.1 "Synthesis of $[\text{H}_2\text{pbmi}]^{2+}$ and synthesis attempts of its homoleptic iron(II) complex"	89
6.2	Supporting Information for Section 3.2 "Higher MLCT lifetime of carbene iron(II) complexes by chelate ring expansion"	107
6.3	Supporting Information for Section 3.2 "A Tetracarbene Iron(II) Complex with a Long-lived Triplet Metal-to-Ligand Charge Transfer State due to a Triplet-Triplet Barrier"	137
6.4	Supporting Information for Section 3.2 "Ground- and Excited-State Properties of Iron(II) Complexes Linked to Organic Chromophores"	195
7	Acknowledgements	227
8	Curriculum vitae	228

Abbreviations and Physical Quantities

Abbreviations

a.u.	arbitrary units
A_{GS}	absorbance of the ground state species
A_{ox}	absorbance of the oxidized species
A_{red}	absorbance of the reduced species
<i>Abs.</i>	absorption
Ar	<i>para</i> -tolyl
bpy	2,2'-bipyridine
btz	3,3'-dimethyl-1,1'-bis(<i>p</i> -tolyl)-4,4'-bis(1,2,3-triazol-5-ylidene
B3LYP	Becke, 3-parameter, Lee-Yang-Parr
bimca ⁻	1,8-bis(imidazolin-2-yliden-1-yl)carbazolide
bmip	2,6-bis(imidazol-2-ylidene)pyridine
^t Bu	<i>tert</i> -butyl
CAAC	cyclic (alkyl)(amino)carbene
CPCM	conductor-like polarizable continuum model
CT	charge transfer
Cz	carbazole
D3BJ	Becke-Johnson damping
DCM	dichloromethane
dcpp	<i>N,N'</i> -dimethyl- <i>N,N'</i> -dipyridine-2-yl-pyridine-2,6-diamine
dFppy ⁻	anion of 2-(2,4-difluorophenyl)pyridine
DFT	density functional theory
dgpy	2,6-bis(2,3,4,6,7,8-hexahydropyrimido[1,2- <i>a</i>]pyrimidin-1-yl)pyridine
dgpz	2,6-bis(2,3,4,6,7,8-hexahydropyrimido[1,2- <i>a</i>]pyrimidin-1-yl)pyrazine
dipp	2,5-diisopropylphenyl
DMF	dimethylformamide
DMSO	dimethylsulfoxide
ϵ	molar extinction coefficient
ϵ_0	permittivity of the vacuum

Abbreviations and Physical Quantities

η	refractive index
ΔE	energy gap/difference
e.g.	exempli gratia
E	potential energy
E_a	activation energy
E_m	Half Stokes shift
ES	excited state
ESI	electrospray ionization
EXAFS	extended X-ray absorption fine structure
f	frequency
FcH	ferrocene
GS	ground state
\hat{H}	Hamiltonian
H_{AB}^2	electronic coupling matrix element
HPLC	high-performance liquid chromatography
IC	internal conversion
i.e.	id est
ILCT	intraligand charge transfer
IR	infra-red
ISC	intersystem crossing
k_B	Boltzmann constant
k_{ISC}	rate constant for non-radiative relaxation from emissive state into GS
$k_{nr,tot}$	rate constant for all processes of non-radiative relaxation
k_p	phosphorescence rate constant
k_r	rate constant for radiative relaxation
λ	reorganization energy
λ_s	solvent reorganization energy
L	ligand
LC	ligand centred
LL'CT	ligand-to-ligand charge transfer
LMCT	ligand-to-metal charge transfer

$ M(Q_0) $	transition dipole moment
M	metal
mbmi	1,1'-methylenebis-(3-methylimidazol-2-ylidene)
MC	metal centred
Me	methyl
MECP	minimum energy crossing point
Mes	mesityl
MLCT	metal-to-ligand charge transfer
$\tilde{\nu}$	wavenumber
NHC	<i>N</i> -heterocyclic carbene
NMR	nuclear magnetic resonance
Ph	phenyl
phen	1,10-phenanthroline
photoCORM	photoactive CO-releasing molecule
phtmeimb ⁻	phenyl(tris(3- methylimidazol-1-ylidene))borate
pphen ⁻	anion of 2-(3-(tert-butyl)phenyl)-1,10-phenanthroline
ppy ⁻	anion of 2-phenylpyridine
ⁱ Pr	<i>iso</i> -propyl
<i>r</i>	distance
RIJCOSX	resolution of the identity chain-of-spheres exchange
S_M	Huang-Rhys factor
SOC	spin-orbit coupling
<i>T</i>	temperature
TA	transient absorption
TD-DFT	time dependent density functional theory
THF	tetrahydrofuran
TMC	transition metal complex
tpe	1,1,1-tris(pyrid-2-yl)ethane
tpy	2,2';6',2''-terpyridine
TS	transition state
TZVP	valence triple-zeta polarisation

Abbreviations and Physical Quantities

UV/Vis	ultraviolet/visible
vs.	versus
XANES	X-Ray absorption near edge structure
ZORA	zeroth order regular approximation
δ	chemical shift (NMR spectroscopy)
Δ	ligand field splitting
ΔG	Gibbs free energy change
Δ_o	ligand field splitting in octahedral coordination
ϕ	emission quantum yield
Γ_{abs}	number of absorbed photons
Γ_{em}	number of emitted photons
τ	lifetime

Units

K	Kelvin
eV	electron Volt
V	Volt
J	Joule
cm^{-1}	reciprocal centimetre
nm	nanometre
Å	Ångström
s	second
μs	microsecond
ns	nanosecond
ps	picosecond
fs	femtosecond
°	degree
°C	degree Celsius
%	percent (1/100)
ppm	parts per million

1 Introduction

Today sustainability is regarded more important than ever, since energy and resource consumption is higher than ever.^{[1],[2]} Due to the increasing demand for energy, goods and fossil fuels, a shortage of these finite resources in the long run is inevitable.^[3] The increased usage of fossil fuels does furthermore contribute to earth's climate change and has detrimental influence on the environment.^[4] Therefore the United Nations recognized the need for changes and called into actions an agenda to "ensure sustainable consumption and production patterns" in 2015, trying to meet their goals by the year 2030.^[5]

This prompted researchers all over the world to find next-generation materials to tackle these pressing issues.

A way to replace fossil fuels is by using sunlight as a plentiful energy source, which can be used to either generate electricity, to meet today's energy needs, or to drive chemical reactions.^{[6]–[8]} These photochemical reactions, apart from possibly being more sustainable, give access to substrates otherwise not available via thermal reactions.^[9]

Research does not only focus on purely organic systems but also on a variety of transition metal complexes (TMCs) to harvest light as they are a very versatile class of compounds which can be used in a variety of applications such as light emitting diodes, solar energy conversion or light-driven chemistry.^{[9]–[11]} A TMC consists of a transition metal centre and an organic ligand scaffold. Transition metal complexes show properties, which can't be observed by only looking at the individual parts. Compared to solid state materials, TMCs have a distinct and tuneable structure, which can be used to tailor the properties of a TMC for specific uses.

In the last decades, the focus of research has been on photoactive TMCs based on rare-earth and precious metals, such as ruthenium, iridium and platinum. One of the most prominent examples of such a photoactive TMC is the complex $[\text{Ru}(\text{bpy})_3]^{2+}$ (bpy = 2,2'-bipyridine) whose photophysical properties have been extensively studied^{[12]–[15]} and which has been used, as well as its derivatives, in a variety of applications such as photocatalysis,^{[9],[16]} dye-sensitized solar cells,^{[17]–[19]} water splitting catalysis^[20] and photodynamic therapy^[21]. These studies gave a good understanding of the underlying photophysics and photochemical properties of not only poly-pyridine ruthenium complexes but also other photoactive precious metal complexes.^{[22]–[27]} However the low abundance of precious metals hinder large scale applications of such systems associated with the

Introduction

high cost of the required metals and also sometimes insufficient photostability of the compounds.^[28]

Therefore, in the last years there have been efforts to replace these rare *4d* and *5d* transition metals in photoactive TMCs by more earth-abundant alternatives, such as *3d* metals like Cr, Mn, Fe, Co and Cu, as well as the *4d*-metal Mo.^{[29]–[34]} These systems do not only pose a more sustainable alternative to the precious metals presented earlier but are also of scientific interest due to their differing photophysics compared to *4d* and *5d* metals. Unfortunately, most of these *3d/4d* metal complexes are not yet suitable for large-scale applications, due to either a lack of photostability, the complicated synthesis of ligands or more complex photophysical pathways, leading to low excited state lifetimes, hindering the application as photoactive compounds.^[35]

1.1 Photophysics of TMCs

To understand the photophysical properties of TMCs it is of great importance to investigate the excited states of the system, since the energies of the excited states is substantial for the photoactivity of the complexes. Hence, it is necessary to understand the underlying processes after photoexcitation of a TMC to be able to tune their properties to fit specific needs, e.g. excited state potentials for photoredox catalysis. In the following the photophysical processes that are relevant for the context of this work are going to be discussed using $[\text{Ru}(\text{bpy})_3]^{2+}$ as a prominent example.

1.1.1 Luminescence

Excitation of $[\text{Ru}(\text{bpy})_3]^{2+}$ using green or blue light initially leads to the population of a singlet metal-to-ligand charge-transfer ($^1\text{MLCT}$) state. In this excited state the metal centre is formally oxidized while one bipyridine ligand is formally reduced with a singly occupied π^* -orbital.^{[14],[36]} From this $^1\text{MLCT}$ state there are in principle three possible relaxation pathways accessible. First is the relaxation back into the singlet ground state (^1GS) *via* fluorescence, second a non-radiative decay back into the ground state and third is an intersystem crossing (ISC) into a $^3\text{MLCT}$ state. The ISC in $[\text{Ru}(\text{bpy})_3]^{2+}$ is ultrafast (< 110 fs) because of the strong spin-orbit coupling (SOC) due to the heavy ruthenium(II) centre which lifts the formal spin-selection rule.^{[37],[38]} Due to this fast ISC the aforementioned fluorescence only play a minor role.^{[39]–[41]}

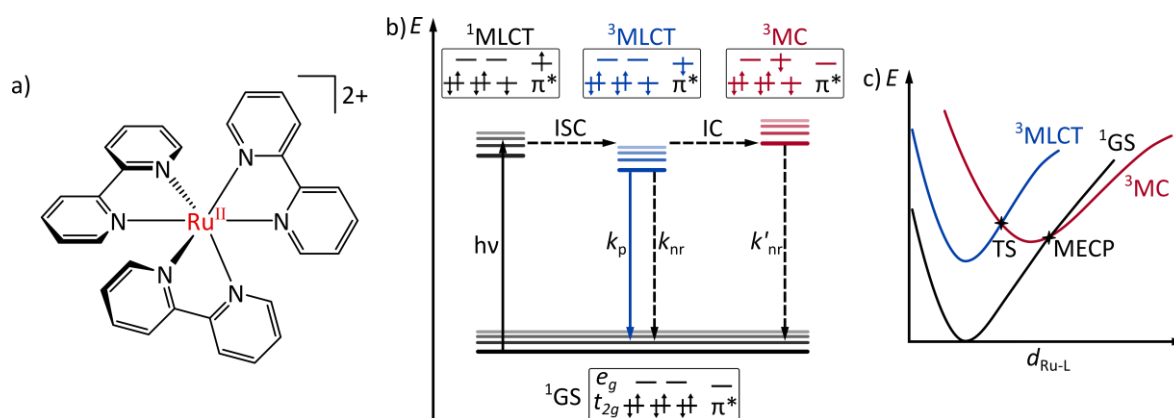


Figure 1: a) Chemical structure of $[\text{Ru}(\text{bpy})_3]^{2+}$, b) energy diagram with selected relaxation pathways and exemplary electron configurations for relevant electronic states, c) schematic potential energy surface diagram for (pseudo-)octahedral ruthenium(II) complexes (TS = transition state, MECP = minimum energy crossing point).

From this $^3\text{MLCT}$ state a relaxation *via* phosphorescence back into the electronic ground state can occur. Since the $^3\text{MLCT} \rightarrow ^1\text{GS}$ transition is formally spin-forbidden in nature, the deactivation of the photoexcited $[\text{Ru}(\text{bpy})_3]^{2+}$ is slow and a relatively long excited state lifetime of a few hundred

Introduction

nanoseconds in water (620 ns) and acetonitrile (855 ns) are observed.^{[42],[43]} The phosphorescence quantum yield of $[\text{Ru}(\text{bpy})_3]^{2+}$ equals to 6.3 % in water at room temperature and 6.2 % in acetonitrile.^{[43],[44]}

As seen above, the two main characteristics of luminescent excited states are their lifetime τ as well as their luminescence quantum yield ϕ . The excited state lifetime is thereby defined as the reciprocal of the sum of all radiative (k_r) and all non-radiative ($k_{nr,tot}$) rate constants (*tot.* = total) in the absence of a quencher as depicted in Eq. (1). For phosphorescent excited states this lifetime is in the regime of $\tau_p = 10^{-6} - 10^2$ s and surpasses the lifetimes normally obtained for fluorescence ($\tau_f = 10^{-10} - 10^{-7}$ s) due to the spin-forbidden nature of the relaxation via phosphorescence.^{[45]–[47]}

$$\tau = \frac{1}{k_r + k_{nr,tot}} = \frac{1}{k_r + k_{ISC} + k_{nr}} \quad (1)$$

Herein, k_{ISC} is the intersystem crossing (ISC) rate from the emissive state back into the ground state, while k_{nr} is the thermally activated non-radiative rate.^[47]

The luminescence quantum yield ϕ gives the efficiency of the luminescence which is defined by the ratio between the radiative decay constant k_r and the sum over all decay constants.^[42]

$$\phi = \frac{k_r}{k_r + k_{nr,tot}} \quad (2)$$

The luminescence quantum yield ϕ can also be expressed as the ratio of numbers of emitted photons Γ_{em} and absorbed photons Γ_{abs} , Eq. (2) can be modified by eliminating the rate constant for fluorescence k_f from the total quantum yield to obtain:^[42]

$$\phi_p = \frac{\Gamma_{em}}{\Gamma_{abs}} \quad (3)$$

The rate constants for phosphorescence (k_p) themselves are given by the Einstein coefficients for spontaneous emission:^{[48],[49]}

$$k_P = \frac{8\pi^2\eta^3\tilde{\nu}^3}{3\varepsilon_0\hbar} |M(Q_0)|^2 \quad (4)$$

In this equation η is the solvent refractive index, $\tilde{\nu}$ is the emission energy given in cm^{-1} and $|M(Q_0)|$ is the transition dipole moment of the transition between excited state and ground state. As seen in Eq. (4) both fluorescence and phosphorescence quantum yield depend on the transition dipole moment to the power of three as well as the emission energy to the power of two. This dependency of the fluorescence and phosphorescence rate constants on the emission energy only applies to atomic transitions or to molecules with fixed nuclei.^[48] Due to the motion of nuclei a broadening of emission bands is observed, composed of a number of vibrational transitions. To account for this spectral broadening the expression in Eq. (4) can be extended by Franck-Condon factors given the following equation:^[49]

$$k_{F,P} = \frac{8\pi^2\eta^3\tilde{\nu}^3}{3\varepsilon_0\hbar} |M_{ES\rightarrow GS}(Q_0)|^2 \sum_{\tilde{\nu}} \tilde{\nu}^3 \int |\psi_{GS_m}^* \psi_{ES_0} dQ|^2 \quad (5)$$

The transition dipole moment $|M(Q_0)|$ for this transition can be obtained via first-order perturbation interactions between the two involved states *via* spin-orbit coupling:^[49]

$$M_{ES\rightarrow GS}(Q_0) = \sum_{j \in x,y,z} \left| \sum_m \frac{\langle T_1 | H_{SOC} | S_m \rangle}{E(S_m) - E(T_1)} M_{S_m,j}(Q_0) \right|^2 \quad (6)$$

Herein the total transition dipole moment over all spatial directions j depends on the magnitude of SOC given by $\langle T_1 | H_{SOC} | S_m \rangle$ and the transition dipole moment $M_{S_m,j}(Q_0)$ between the two involved states of differing vibrational level m .

Another expression for the phosphorescence rate constants can be derived as the rate constants rely on intensity borrowing from excited states S_m with similar energy to the T_1 state, i.e. with small energy difference $E(S_m) - E(T_1)$:^{[50]–[52]}

$$k_p(\tilde{T}_1^\alpha) = \frac{4}{3\hbar^4 c^3} (\Delta E_{TS})^3 \sum_y \left| \sum_{m=1}^{\infty} \frac{\langle T_m^\alpha | H_{SOC} | S_0 \rangle}{E(S_0) - E(T_m)} \langle T_1^\alpha | M_\gamma | T_m^\alpha \rangle + \sum_{n=0}^{\infty} \frac{\langle S_n | H_{SOC} | T_1^\alpha \rangle}{E(T_1) - E(S_n)} \langle S_n | M_\gamma | S_0 \rangle \right|^2 \quad (7)$$

For efficient transition the excited S_m states should possess high transition dipole moments and different orbital compositions in contrast to the T_1 state to induce spin-orbit coupling and therefore efficient depopulation of the T_1 state.

1.1.2 Non-radiative decay for CT-Emitters

The luminescence of d^6 low-spin complexes often stems from excited ${}^3\text{MLCT}$ states, in which the complex geometry is more or less unchanged to the ground state.^[53] Excited states whose geometry only slightly differs from the GS geometry are called nested states. For these nested states there is only limited vibronic coupling to the ground state, slowing down non-radiative decay. In contrast, the strong coupling limit is only possible when the excited state is strongly distorted in comparison to the ground state, leading to a large displacement and crossing of the potential energy surfaces.^{[49],[52],[54]}

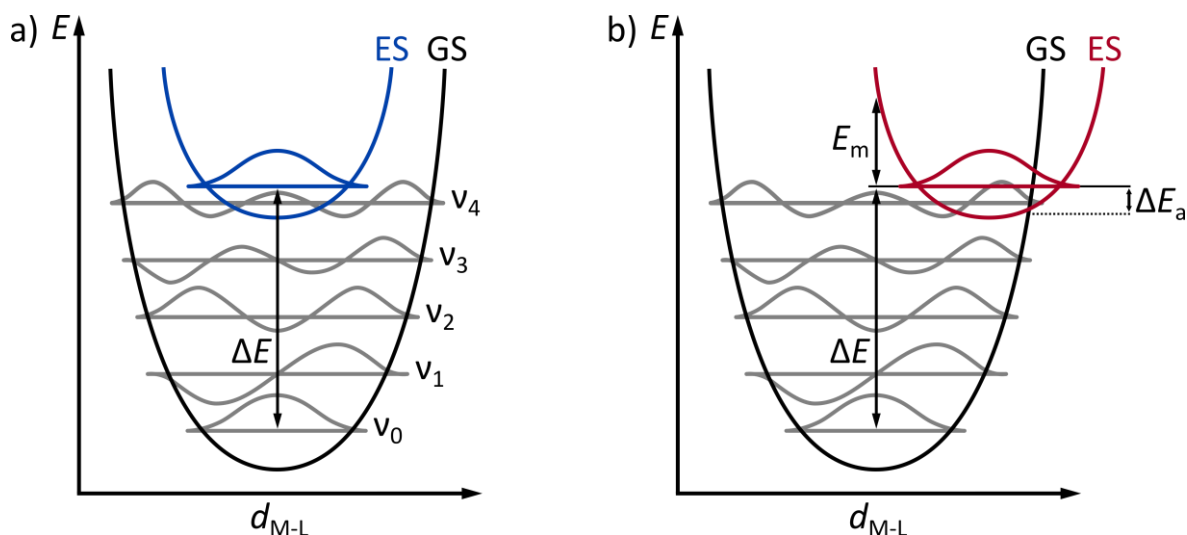


Figure 2: Potential energy well diagrams of ground state (GS) and excited state (ES) for a) weak and b) strong coupling limit in the harmonic approximation (ΔE = gap between GS (v_0) and ES (v_0), ΔE_a = activation energy, E_m = Half Stokes shift).

In detail, this means that a transition in the weak coupling limit starts with an isoenergetic (i.e. horizontal tunnelling from the excited state into a vibronically hot ground state level, followed by vibrational relaxation within the ground state manifold.^[54] The rate constant for the weak coupling limit is given by Eq. (8):^{[49],[55]}

$$k_{nr} = \frac{2\pi}{\hbar} \frac{H_{AB}^2}{\sqrt{4\pi\lambda_s k_B T}} \sum \left[\frac{S_M^{n_M}}{n_M!} e^{(-S_M)} e^{\left(-\frac{(\Delta E - n_M \hbar \omega_M - \lambda_s)^2}{4\lambda_s k_B T}\right)} \right] \quad (8)$$

In Eq. (8) H_{AB} is the coupling matrix element and λ_s is the reorganization energy of the solvent. The measure of the displacement of the ES minimum in contrast to the GS minimum along the coordinate Q is represented by the Huang-Rhys factor S_M . n_m gives the quantum number of the effective intraligand vibrational mode $\hbar\omega_M$, and the energy difference between ground and excited state in the vibrational ground state is given by ΔE .

Since the dependence of k_{nr} from ΔE is exponential this expression is often referred to as the 'energy gap law',^[54] meaning that a smaller energy gap will result in a larger k_{nr} in case of the weak coupling limit.

For the strong coupling limit the rate constant k_{nr} is defined by Eq. (9):^[54]

$$k_{nr} = \frac{k_B T}{\hbar} \frac{H_{AB}^2}{\sqrt{E_m} (k_B T)^3} e^{\left(-\frac{\Delta E_a}{k_B T}\right)} \quad (9)$$

In this equation E_m represents half the Stokes shift between excitation and emission energy.^[54] ΔE_a is the energy between the excited state minimum and the potential energy surface crossing point. In contrast to the weak coupling limit, the strong coupling limit does not show a dependence on ΔE . Instead an Arrhenius-like behaviour is observed, since a thermal energy barrier in form of ΔE_a is present and must be overcome for the transition to happen. In case of $\Delta E_a = 0$ the crossing point of the potential energy surfaces is directly through the energy minimum of the excited state, leading to barrier-less, very fast non-radiative deactivation.

Apart from the relaxation *via* phosphorescence in d^6 luminophores there exists another relaxation pathway back into the electronic ground state, namely *via* internal conversion (IC) into a metal-centred excited state (3MC) with an electron configuration of $(t_{2g})^5 (e_g^*)^1$. The population of an e_g^* orbital leads to a strong distortion of the complex due to the anti-bonding nature of the orbital in

respect to the metal-ligand σ -bond.^{[56]–[58]} This distortion leads to vibronic coupling with the electronic ground state (strong coupling limit) and leads to non-radiative relaxation. In d^6 complexes, the excited 3MC states are effectively non-emissive because of this large geometric distortion, leading to low excited state energies at the Franck-Condon point, giving rise to fast non-radiative decay. Furthermore, the relaxation of the 3MC state back to the GS is Laporte- and spin forbidden leading to low radiative rates as well.^{[41],[59],[60]}

For $[\text{Ru}(\text{bpy})_3]^{2+}$ the deactivation pathway $^3MLCT \rightarrow ^3MC$ is associated with an energy barrier ΔE of around 3600 cm^{-1} between the energetically lowest lying 3MLCT and 3MC states, so that the IC requires a thermal activation to take place.^{[61],[62]} However, only investigating the energy barrier between the 3MLCT and the energetically lowest 3MC state to determine the temperature dependence of $[\text{Ru}(\text{bpy})_3]^{2+}$ is a simplification that hinders correct predictions of the temperature dependence of the emission lifetimes of such systems. Therefore, not only the relaxation pathway via the lowest excited 3MC needs to be considered, but the pathways along the other excited 3MC states as well as their minimum energy crossing points (MECP) to the ground state need to be investigated as well.^[47] Nevertheless, the phosphorescence lifetime of $[\text{Ru}(\text{bpy})_3]^{2+}$ is strongly temperature dependant.^{[61],[62]}

With sufficient thermal energy the excited 3MC states can then be populated upon excitation and due to the anti-bonding nature of the e_g^* orbitals and the elongation of the metal ligand bonds dissociation becomes possible. Therefore, complexes like $[\text{Ru}(\text{bpy})_3]^{2+}$ or other complexes using bidentate poly-pyridine ligands can undergo photo-substitution reactions upon excitation, leading to lowered photostability.^{[63]–[65]} In general, the energy of the excited 3MC states relevant for the deactivation of the 3MLCT states is dependent on the ligand field splitting Δ_o , which describes the energy gap between the t_{2g} and e_g^* -orbitals in octahedral complexes.^[61]

Another detrimental property of $[\text{Ru}(\text{bpy})_3]^{2+}$ and similar complexes employing bidentate ligands is the Δ/Λ chirality which leads to the formation of diastereomers while using substituted bidentate ligands. This formation of diastereomers complicates the synthesis of pure diastereomers as well as associated characterization.^{[66]–[73]} Therefore tridentate ligands have become a focal point of research since.

Because of the high ligand field splitting in $[\text{Ru}(\text{bpy})_3]^{2+}$, the excited ^5MC high spin state, featuring an electron configuration of $(t_{2g})^4 (e_g^*)^2$ is pushed to high energies and is not relevant for the photophysical processes after excitation. For other lighter TMCs with a d^6 low spin configuration the quintet high spin state can however contribute strongly to non-radiative decay.^[74]

1.2 Charge-Transfer Emitters

So far, the photophysical processes of $[\text{Ru}(\text{bpy})_3]^{2+}$ have been discussed, in which the excited $^3\text{MLCT}$ states played an important role. Apart from excited MLCT states, other charge transfer excited states can play a vital role in the photophysics of TMCs.

Charge-transfer transitions (CT) can be described as a photoinduced intramolecular electron transfer and their nature is dependent on the type of orbitals involved in the underlying transition. Most common charge transfer transition include MLCT, ligand-to-metal charge transfer (LMCT), ligand-to-ligand charge transfer (LL'CT) and intraligand charge transfer (ILCT). Apart from such charge transfer states and the aforementioned excited MC states, $\pi\text{-}\pi^*$ also take place when using aromatic ligand systems (i.e. 2,2'-bipyridine) and are referred to as "ligand-centred" (LC).

The energy of the MC states is, as mentioned before, dependent on the ligand field splitting Δ_o in octahedral complexes. For the charge transfer states the energy depends on the energy gap between the electron donating and accepting parts involved, in case of MLCT transition those are the t_{2g} -orbitals of the metal centre and the π^* -orbitals of the ligands. Due to this dependence, it is possible to tune the colour of such CT-complexes over a broad spectral range.^{[13],[27],[75],[76]}

1.2.1 Emitters based on precious metals

Apart from poly-pyridine Ru^{II} as a CT emitter, varieties of other rare transition metals have garnered scientific interest over the last couple of decades such as Ir^{III} , Os^{II} , Pt^{II} and Rh^{I} . These metals are the basis for a plethora of photoactive compounds, which have been extensively studied regarding their photophysical properties.^{[13],[23],[26],[75],[77]} The implementation of such heavy metals induces a high SOC,^[37] which accelerates spin-forbidden processes such as ISC and phosphorescence. The use of such heavy metals furthermore pushes the deactivating ^3MC states to higher energies, which mitigates non-radiative decay and strengthens the metal-ligand bonds (see Chapter 1.2.2).

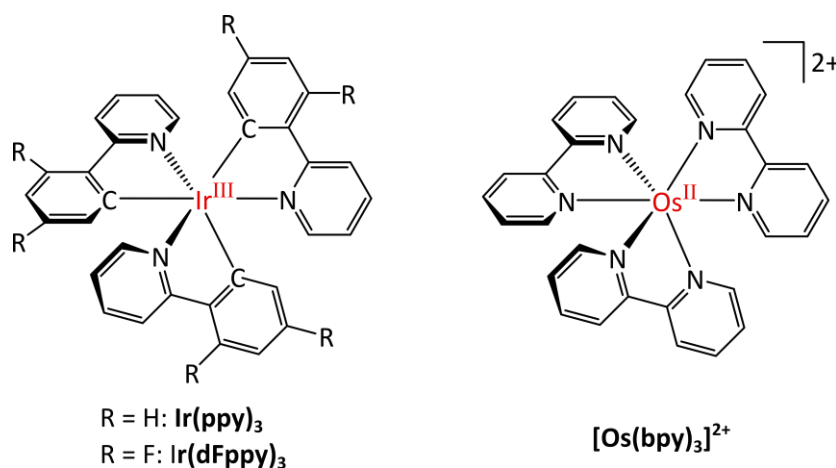


Figure 3: Chemical structures for Ir(ppy)₃ (left; ppy⁻ = deprotonated form of 2-phenylpyridine) and [Os(bpy)₃]²⁺ (bpy = 2,2'-bipyridine).

Ir(ppy)₃ (ppy⁻ = deprotonated form of 2-phenylpyridine), for example, is isoelectronic to [Ru(bpy)₃]²⁺ and shows green emission at 510 nm from a ³MLCT state with a lifetime of 2.38 μs and a quantum yield of 40 % in tetrahydrofuran under inert atmosphere.^[75] Ligand modification of ppy gives rise to a wide variety of Ir^{III} complexes with different excited state redox potentials.^{[75],[78]} For instance Ir(dFppy)₃ (dFppy⁻ = anion of 2-(2,4-difluorophenyl)pyridine) is used in energy transfer and photoredox catalysis due to its high triplet state energy of 2.75 eV and excited state oxidation potential of -1.66 V vs. FcH⁺/FcH.^{[78],[79]}

In contrast to the blue-shifted emission in Ir(ppy)₃ compared to [Ru(bpy)₃]²⁺ a red-shift can be achieved by using osmium as a metal centre. Osmium in [Os(bpy)₃]²⁺ is more easily oxidized than ruthenium leading to a smaller energy gap between the donating metal and accepting ligand orbitals, facilitating a lower energy MLCT transition. The MLCT emission in [Os(bpy)₃]²⁺ is shifted to 740 nm. Furthermore, due to the high SOC induced by osmium(II) the ³MLCT can be directly populated upon excitation which makes such a compound viable in photoredox catalysis activated by low-energy red light.^{[44],[80]}

1.2.2 Earth-abundant alternatives

Due to their low abundance, however, usage of such heavy metals leads to high costs, which prevents large scale applications. Therefore, scientific interest has shifted to more abundant alternatives like 3d/4d metals (Cr/Mn/Fe/Co/Ni/Cu/Zn/Mo) as more sustainable solutions.^{[29],[33],[81]} Apart from their higher abundance the shift in studies has been motivated by scientific curiosity concerning the exploration of novel compounds and the understanding of their photophysical properties as well as their potential novel reactivities.^[33]

Table 1: Abundance of selected metals in earth's crust in mg/kg.^[82]

Fe	Mn	Co	Cr	Cu	Mo	Ru	Ir
56300	950	250	102	60	1.2	0.001	0.001

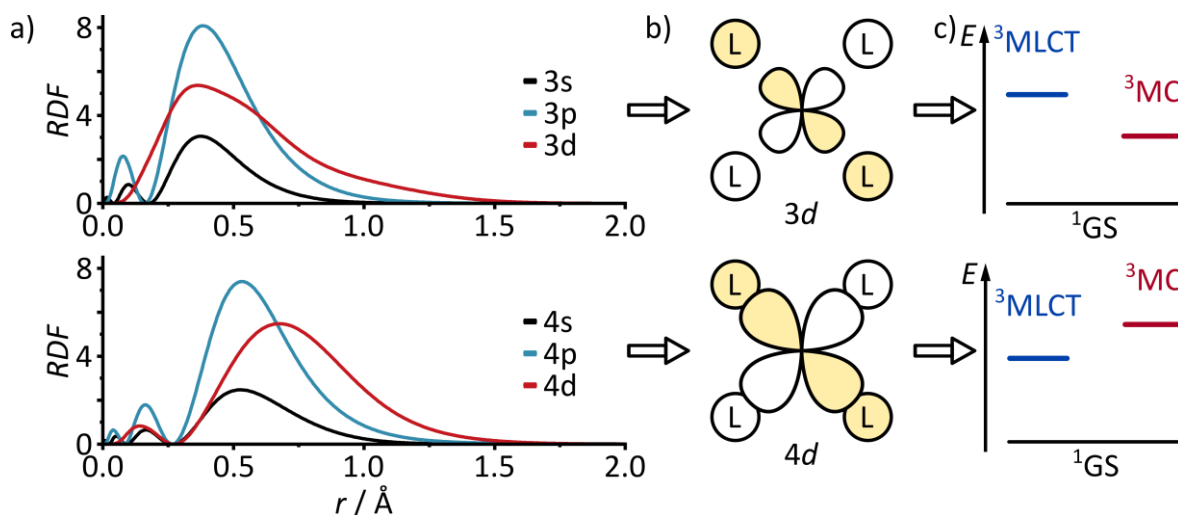


Figure 4: a) Radial distribution functions (RDFs) for the $n = 3$ shell of iron(II) (top) and the $n = 4$ shell of ruthenium(II) (bottom), b) the resulting overlap between 3d and 4d orbitals with ligand orbitals and c) schematic representation of the resulting ordering of excited states due to the primogenic effect in (pseudo-)octahedral iron(II) and ruthenium(II) complexes.^{[83],[84]}

A general problem for the usage of 3d metals in contrast to the heavier 4d and 5d metals is the smaller expansion of the 3d orbitals due to the primogenic effect, leading to a poorer metal-ligand orbital overlap (see **Figure 4**), therefore poorer metal-ligand interaction.^{[85],[86]} This effect stems from the absence of nodes in the radial distribution function of the first p, d and f shells (i.e. 2p, 3d, 4f) resulting in a higher effective nuclear charge and therefore a contraction of the respective orbitals. The lower metal-ligand interaction in 3d metals leads to a lower ligand field splitting and low energy excited MC-states, which offer an efficient pathway for non-radiative relaxation. To avoid the population of such short-lived excited states a wide variety of strategies have been researched.^[83]

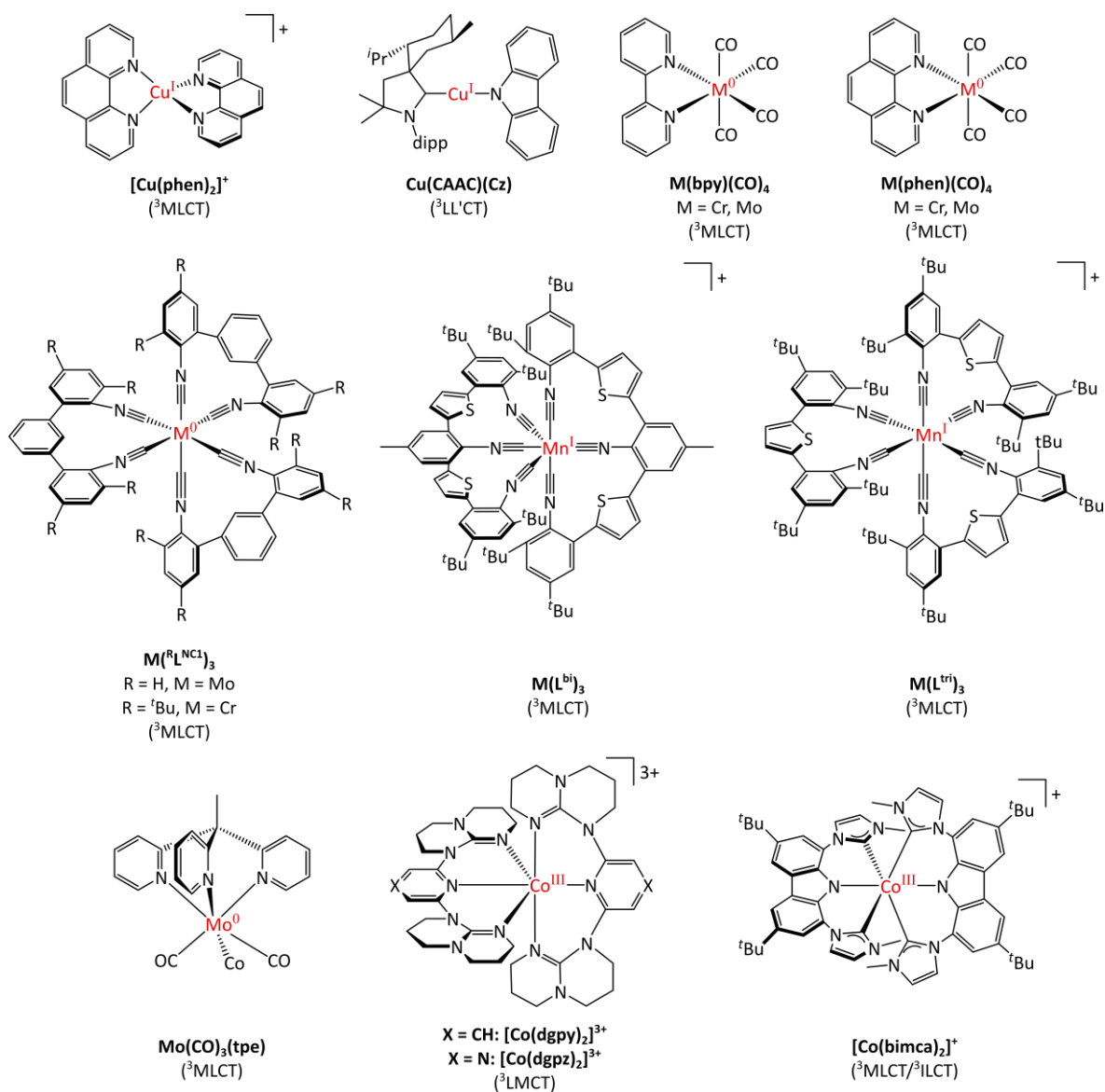


Figure 5: Photoactive TMCs incorporating earth-abundant transition metals relevant for the discussion in this chapter. The character of the photoactive state is given in parentheses. (ⁱPr = iso-propyl, dipp = 2,5-diisopropylphenyl, Me = methyl, Mes = mesityl, Cz = carbazolate, Ph = phenyl, ^tBu = tert-butyl).

One solution to avoid the population of energetically low-lying excited MC states is the usage of metal ions with a completely occupied d-shell such as Cu^I, where an excited MC state does not exist. Over the past decades, this concept of using Cu^I with a *d*¹⁰ electron configuration has gained a lot of attention,^[87] whereby a common design relies on tetrahedral copper complexes with ³MLCT states as the photoactive excited states.

One prominent example of such a Cu^I complexes [Cu(phen)₂]⁺ (phen = 1,10-phenanthroline). This tetrahedral complex, as are other Cu^I complexes, is formally oxidized to Cu^{II} upon MLCT excitation. Cu^{II} in contrast to Cu^I prefers a square-planar coordination geometry. These type of complexes

undergo a so-called "flattening distortion" upon excitation which opens an easy pathway for non-radiative relaxation *via* mixing of the states.^[88] To mitigate this excited state distortion derivatives of phen with sterically demanding groups in 2- and 9-positions have been synthesized but still show poor emission properties in solution.^[89] One break-through could be achieved by substituting not only the 2- and 9-positions of phen but also substituting in 3,4,7- and 8-positions to further rigidify the complex leading to lifetimes in solution of several μs ($\tau = 2.5\text{-}4.3 \mu\text{s}$) and quantum yields in the range of 5.3-12 % in dichloromethane.^[90] A further break-through was achieved with a different approach, by synthesizing linear Cu^{I} complexes, such as $\text{Cu}(\text{CAAC})(\text{Cz})$ (CAAC = cyclic (alkyl)(amino)carbene, Cz = carbazole). In this complex the emissive state changes from a $^3\text{MLCT}$ state as in $[\text{Cu}(\text{phen})_2]^+$ to a $^3\text{LL}'\text{CT}$ state which does not undergo non-radiative decay and shows quantitative luminescence with a phosphorescence quantum yield of $\phi > 99 \%$ in 2-methyl-THF solution.^[91]

Another approach to hinder such specific distortions in the possibly emissive excited state charge-transfer is by using pseudo-octahedral complexes with a d^6 electron configuration, as is the case for the already discussed $[\text{Ru}(\text{bpy})_3]^{2+}$. Alternative to the aforementioned heavier metals that have garnered scientific interest are $\text{Cr}^0/\text{Mn}^{\text{I}}/\text{Co}^{\text{III}}$ and Fe^{II} for 3d and Mo^0 for 4d metals.

Of these metals, the zero-valent metals Cr^0 and Mo^0 as well as Mn^{I} are promising candidates for earth abundant d^6 emitters. Compared to ruthenium, these metal centres have a high electron density and as such require a different ligand design utilizing π -accepting ligands such as CO or isonitriles to stabilize the low oxidation state.^[92] A first attempt at understanding luminescence in zero-valent molybdenum(0) or chromium(0) complexes was already reported 40 years ago wherein tetracarbonyl complexes of molybdenum and chromium of the type $\text{M}(\text{CO})_4(\text{bpy})$ or $\text{M}(\text{CO})_4(\text{phen})$ ($\text{M} = \text{Cr}^0, \text{Mo}^0$) were investigated towards their luminescence properties. However in such compounds the phosphorescence quantum yield of the $^3\text{MLCT}$ state ($\phi < 0.01 \%$) as well as their photostability were very low due to efficient CO loss upon irradiation. These detrimental properties hinder the usage of such complexes as photosensitizers.^{[93],[94]}

To mitigate the photostability reaction the usage of bidentate isonitrile ligands was probed, whereby the complex $\text{Mo}(\text{L}^{\text{NC1}})_3$ ($\text{L}^{\text{NC1}} = ,2''\text{-diisocyano-3,5,3'',5''-tetramethyl-1,1':3',1''\text{-terphenyl}$) shows emission originating from a $^3\text{MLCT}$ state at 560 nm with a lifetime of 74 ns in THF in deaerated solution at room temperature and a quantum yield of 0.6 %. The long lived $^3\text{MLCT}$ state shows an excited state redox potential of approx. $-2.6 \text{ V vs. FcH}^+/\text{FcH}$ and was used in the photocyclization of acyl cyclopropane.^[95]

More recently the molybdenum(0) complex $\text{Mo}(\text{CO})_3(\text{tpe})$ ($\text{tpe} = 1,1,1\text{-tris(pyrid-2-yl)ethane}$) bearing three carbonyl groups and a tripodal tris-pyridine ligand was synthesized. In comparison with $\text{Mo}(\text{L}^{\text{NC1}})_3$ and its intricate ligand synthesis, $\text{Mo}(\text{CO})_3(\text{tpe})$ is much more easily accessible. The complex shows a low energy absorption band with a maximum at 450 nm with MLCT character in acetonitrile. Excitation into this absorption band gives rise to red emission at 720 nm with a lifetime of 127 ns and a phosphorescence quantum yield of 0.13 % at room temperature in acetonitrile. Due to its high photostability ($\phi_{\text{degr}} = 0.00015 \%$) complex $\text{Mo}(\text{CO})_3(\text{tpe})$ was furthermore employed in photon upconversion reactions as well as photoredox catalysis in the dehalogenation reaction of chloropyriazine due to its excited state reduction potential of $-2.06 \text{ V vs. FcH}^+/\text{FcH}$.^[28]

As the lighter homologue of molybdenum(0), chromium(0) has also been a focal point of research. Using the analogue isonitrile ligands yielded chromium(0) complex $\text{Cr}(\text{tBuL}^{\text{NC1}})_3$ exhibiting emission at 630 nm with a lifetime of 2.2 ns in deaerated THF at room temperature. The quantum yield for the chromium complex with $\phi \approx 10^{-5}$ is however magnitudes lower than for the molybdenum complex, probably due to the much lower ligand field splitting of Cr^0 compared to Mo^0 .^[96]

Apart from Mo^0 and Cr^0 there have been reports about photoactive Mn^{I} complexes. Manganese(I) complexes utilizing carbonyls as ligands hereby undergo the same photosubstitution reactions as the molybdenum(0) and chromium(0) carbonyl congeners. For Mn^{I} carbonyl complexes this property was employed in biological and therapeutic applications as so called photoCORMS.^{[97],[98]} To mitigate this ligand loss upon photoexcitation the same strategy of using bi- or tridentate isonitrile ligands^[32] like in the case of Mo^0 and Cr^0 was employed and the complexes $[\text{Mn}(\text{L}^{\text{bi}})_3]^+$ and $[\text{Mn}(\text{L}^{\text{tri}})_2]^+$ were synthesized. Both complexes exhibit a MLCT absorption at around 400 nm and emission with a maximum at 525 nm in deaerated acetonitrile. The luminescence lifetimes were determined as 0.74 ns ($\phi = 0.05 \%$) and 1.73 ns ($\phi = 0.05 \%$) for $[\text{Mn}(\text{L}^{\text{bi}})_3]^+$ and $[\text{Mn}(\text{L}^{\text{tri}})_2]^+$ respectively.^[99]

Another example of possible d^6 low spin emitters are Co^{III} complexes. Due to their electron-deficiency Co^{III} complexes normally show low energy LMCT transitions, instead of MLCT transitions. The complexes $[\text{Co}(\text{dgp})_2]^{3+}$ ($\text{dgp} = 2,6\text{-bis}(2,3,4,6,7,8\text{-hexahydropyrimido}[1,2\text{-a}]\text{pyrimidin-1-yl})\text{pyridine}$) and $[\text{Co}(\text{dgpz})_2]^{3+}$ ($\text{dgpz} = 2,6\text{-bis}(2,3,4,6,7,8\text{-hexahydropyrimido}[1,2\text{-a}]\text{pyrimidin-1-yl})\text{pyrazine}$) using two bis-guanidine ligands as strong σ -donors show strong LMCT/ILCT absorptions at 311 nm and 340 nm, respectively. Excitation into these charge transfer bands gives rise to emission at 440 ($\tau = 5.07 \text{ ns}$) and 412 nm ($\tau_1 = 3.21 \text{ ns}$, $\tau_2 = 8.69 \text{ ns}$) with quantum yields of 0.70 % and 0.40 % for $[\text{Co}(\text{dgp})_2]^{3+}$ and $[\text{Co}(\text{dgpz})_2]^{3+}$ respectively. The emission for both these cobalt complexes stems from a spin-forbidden transition from the lowest $^3\text{LMCT}$ state to the ^1GS .^[100] Apart

from LMCT transitions there have also been reports of long-lived low energy MLCT transitions for Co^{III} complexes, as in the complex $[\text{Co}(\text{bimca})_2]^+$ ($\text{bimca}^- = 1,8\text{-bis}(\text{imidazolin-2-yliden-1-yl})\text{carbazolide}$). For this complex no luminescence was detectable, however the dark excited mixed $^3\text{MLCT}/^3\text{ILCT}$ state shows a lifetime of 1.2 ns, which was used for photoinduced electron transfer reactions with methylviologen.^[101]

1.3 Photophysical challenges of Iron(II) complexes

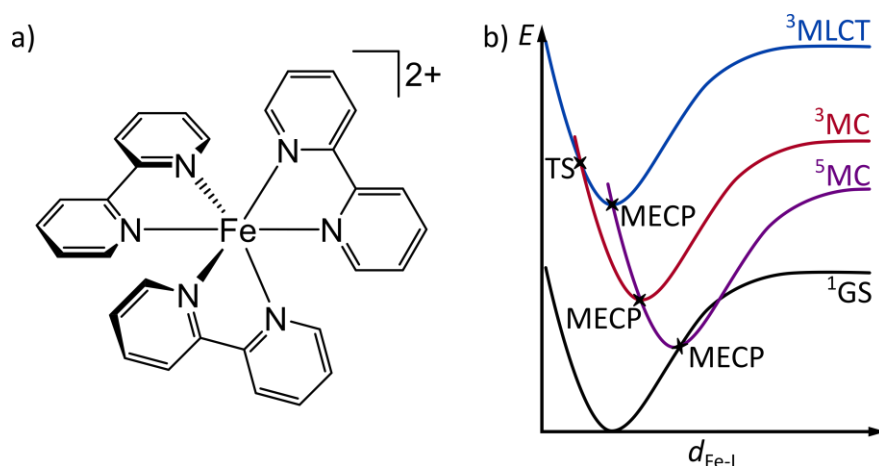


Figure 6: a) Chemical structure of $[\text{Fe}(\text{bpy})_3]^{2+}$ and b) schematic potential energy surface diagram for (pseudo-)octahedral polypyridine iron(II) complexes (TS = transition state; MECP = minimum energy crossing point).

Taking a look at the overall abundance of transition metals in the earth's crust, a cheap and readily available alternative to Ru^{II} , Ir^{III} , etc. would be iron, the lighter homologue of ruthenium (see **Table 1**).^{[82],[102]} Iron being the most abundant transition metal is usually present in the two prevalent oxidation states of +II and +III. Compared to ruthenium, these two common oxidation states of iron exhibit a much lower intrinsic ligand field splitting Δ_o due to the primogenic effect. This pushes the MC excited states to very low energies (see **Figure 6**).^{[74],[83]} $[\text{Fe}(\text{bpy})_3]^{2+}$ for instance does not show luminescence because of ultra-fast IC/ISC from the ³MLCT state into the dark ^{3/5}MC states within 50 fs after excitation. The so formed ⁵MC high-spin state then relaxes back into the ground state within 650 ps.^{[103]–[106]} The population of the excited metal centred state is hereby not only dependant on the relative energies of the involved excited states (e.g. ³MLCT and ³MC states) but furthermore also depends on the respective energy barrier between these states. This refers to the transition state (TS) between for instance ³MLCT and ³MC states, or the minimum energy crossing points (MECP) between the ³MC and ⁵MC states, as well as the ⁵MC state and ¹GS (see **Figure 6**).^[107]

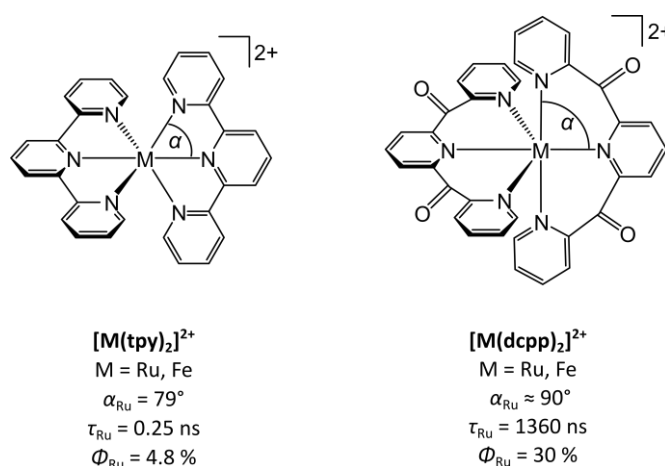


Figure 7: Increasing the lifetime of the photoluminescent properties in ruthenium(II) complexes by changing the bite angle of the ligand, schematically shown for $[\text{Ru}(\text{tpy})_2]^{2+}$ ($\text{tpy} = 2,2';6',2''\text{-terpyridine}$) and $[\text{Ru}(\text{dcpp})_2]^{2+}$ ($\text{dcpp} = N,N'\text{-dimethyl-}N,N'\text{-dipyridine-2-yl-pyridine-2,6-diamine}$). Data recorded in acetonitrile at room temperature.^[108]

To counteract the primogenic effect and therefore increase the ligand field splitting in pseudo-octahedral complexes of 3d TMs, switching from 5-membered ring chelating ligands, such as bpy or tpy, to ligands forming 6-membered ring chelates could be a viable strategy. This strategy, of increasing the bite angles of the ligands (see **Figure 7**) has already proven helpful in ruthenium(II) complexes. The phosphorescence quantum yield of $[\text{Ru}(\text{dcpp})_2]^{2+}$ ($\text{dcpp} = N,N'\text{-dimethyl-}N,N'\text{-dipyridine-2-yl-pyridine-2,6-diamine}$) could be increased to 30 % in acetonitrile at room temperature compared to 4.8 % for $[\text{Ru}(\text{tpy})_2]^{2+}$ ($\text{tpy} = 2,2';6',2''\text{-terpyridine}$) under the same conditions.^[109] The lifetime of $[\text{Ru}(\text{dcpp})_2]^{2+}$ could also be increased to 1.36 μs compared to 0.25 ns for $[\text{Ru}(\text{tpy})_2]^{2+}$.^[109] In case of the iron(II) homologue $[\text{Fe}(\text{dcpp})_2]^{2+}$ the effect is not as pronounced as in the case of the ruthenium complexes.^[110] The iron complex shows a lifetime of the energetically lowest excited state of 280 ps ($[\text{Fe}(\text{tpy})_2]^{2+}$: 960 ps) which was assigned to the excited ^5MC state by ultra-fast time resolved X-ray spectroscopy, giving the same relaxation pathway for the dcpp complex as for the tpy one ($^1\text{MLCT} \rightarrow ^3\text{MLCT} \rightarrow ^3\text{MC} \rightarrow ^5\text{MC} \rightarrow ^1\text{GS}$).^{[110]–[112]}

Since the main reason for Fe^{II} - and Fe^{III} -complexes not showing luminescence is the relaxation via excited dark metal-centred states, a major strategy consists of increasing the energy of these MC states in favour of the MLCT states in Fe^{II} and LMCT states in Fe^{III} complexes. This can be achieved by utilising strong σ -donors which increase the energy of the e_g^* -orbitals of the metal centre.^{[68],[113]} The most common type of σ -donor for this type of application are N-heterocyclic carbenes (NHCs).^{[114],[115]} Apart from NHCs, meso-ionic carbenes can be used as well. These carbenes show stronger σ -donor and π -acceptor properties than the N-heterocyclic carbenes.^{[116],[117]} The stronger σ -donating character can be explained by the formal negative charge on the carbene C-atom being

delocalized over the complete ring in a meso-ionic carbene, while the stronger π -accepting properties are due to energetically lower π^* -orbitals due to additional N-atoms in the ring.^{[116]–[118]}

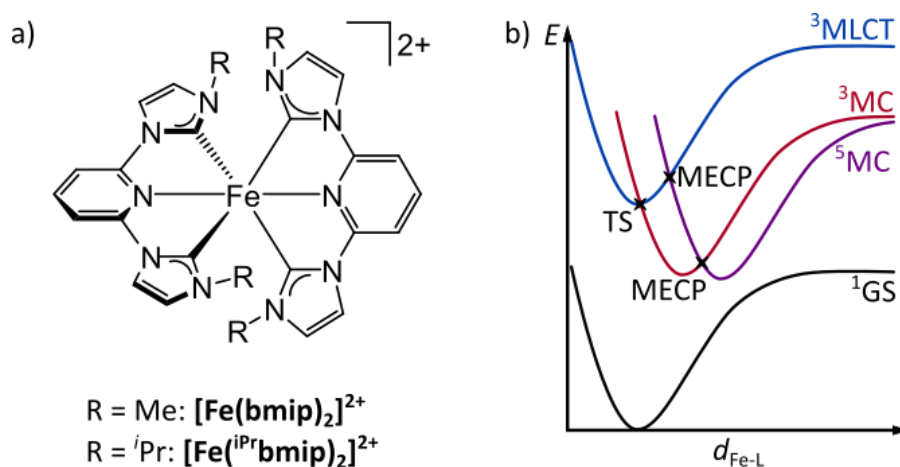


Figure 8: a) Chemical structure of $[\text{Fe}(\text{bmip})_2]^{2+}$ and $[\text{Fe}(\text{iPrbmip})_2]^{2+}$ and b) schematic potential energy surface diagram for (pseudo-)octahedral iron(II) complexes bearing strong σ -donating ligands (TS = transition state; MECP = minimum energy crossing point; Me = methyl, *i*Pr = *iso*-propyl).

The research in this field of iron(II) complexes started with the complex $[\text{Fe}(\text{bmip})_2]^{2+}$ (bmip = 2,6-bis(imidazol-2-ylidene)pyridine) reported in 2013.^[114] Using transient absorption (TA) spectroscopy a long-lived species with a lifetime of approx. 9 ps in acetonitrile was observed.^{[114],[119]} This long-lived state was assigned as the $^3\text{MLCT}$ state, starting of the field of iron-carbene complexes as promising compounds to increase the lifetime of the possibly luminescent $^3\text{MLCT}$ state.^{[114],[119]} The relaxation pathway after excitation was thought as $^1\text{MLCT} \rightarrow ^3\text{MLCT} \rightarrow ^3\text{MC} \rightarrow ^1\text{GS}$, bypassing the excited ^5MC high-spin state (see **Figure 8**).^{[114],[119]} However more recent studies utilizing more modern TA spectrometers suggest that the lifetime of 9 ps belongs to an excited ^3MC state, and that the $^3\text{MLCT}$ state of $[\text{Fe}(\text{bmip})_2]^{2+}$ is depopulated within a few hundred femtoseconds (< 300 fs). Compared to the earlier studies only the assignment of the long-lived excited state changed for $[\text{Fe}(\text{bmip})_2]^{2+}$. The overall relaxation pathway stayed the same, showing, that the destabilizing nature of carbene donors on the MC excited states in principle works but has a stronger influence on the ^5MC than on the ^3MC states.^[120]

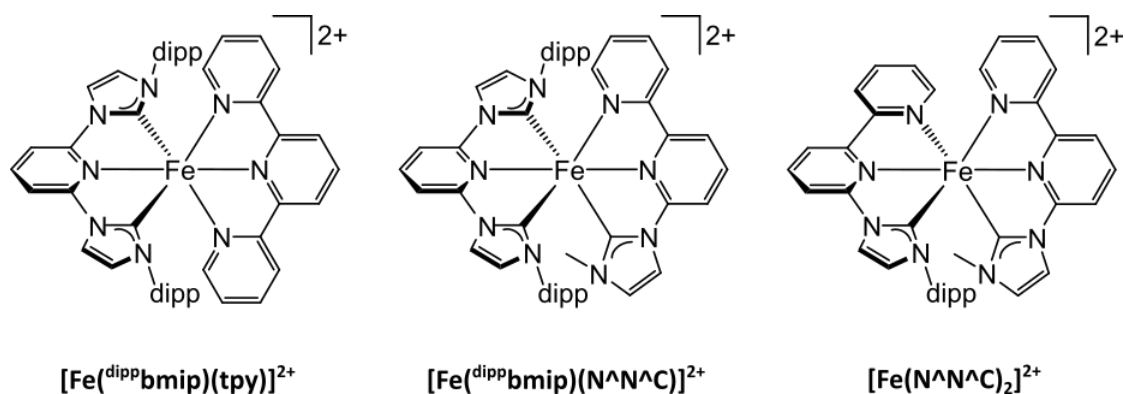


Figure 9: Chemical structures of $[\text{Fe}(\text{dippbmip})(\text{tpy})]^{2+}$, $[\text{Fe}(\text{dippbmip})(\text{N}^{\wedge}\text{N}^{\wedge}\text{C})]^{2+}$ and $[\text{Fe}(\text{N}^{\wedge}\text{N}^{\wedge}\text{C})_2]^{2+}$ (dipp = 2,5-diisopropylphenyl).

Other research focused on derivatives of $[\text{Fe}(\text{bmip})_2]^{2+}$ tried to show the dependence of the $^3\text{MLCT}$ lifetime in comparison to the number of carbene moieties in the complex. In this study the complexes $[\text{Fe}(\text{N}^{\wedge}\text{N}^{\wedge}\text{C})_2]^{2+}$, $[\text{Fe}(\text{dippbmip})(\text{tpy})]^{2+}$, $[\text{Fe}(\text{dippbmip})(\text{N}^{\wedge}\text{N}^{\wedge}\text{C})]^{2+}$ as well as $[\text{Fe}(\text{ipr}^{\wedge}\text{bmip})_2]^{2+}$ were synthesized and investigated towards their photophysical properties.^[121] The lifetime of the $^3\text{MLCT}$ state could be raised with the increasing amount of carbene donors in the complexes from < 100 fs (for $[\text{Fe}(\text{N}^{\wedge}\text{N}^{\wedge}\text{C})_2]^{2+}$ and $[\text{Fe}(\text{dippbmip})(\text{tpy})]^{2+}$), 3.6 ps (for $[\text{Fe}(\text{dippbmip})(\text{N}^{\wedge}\text{N}^{\wedge}\text{C})]^{2+}$) up to 8.1 ps (for $[\text{Fe}(\text{ipr}^{\wedge}\text{bmip})_2]^{2+}$), while the ^3MC lifetime decreased.^[121] For all four complexes as before with $[\text{Fe}(\text{bmip})_2]^{2+}$ the ^5MC excited state does not seem to play a role in the photophysics of these iron carbene compounds. Considering the aforementioned re-assignment of the long-lived excited state in $[\text{Fe}(\text{bmip})_2]^{2+}$ to the ^3MC state, the assignment of the excited states in these four complexes might also be switched.^{[120],[121]}

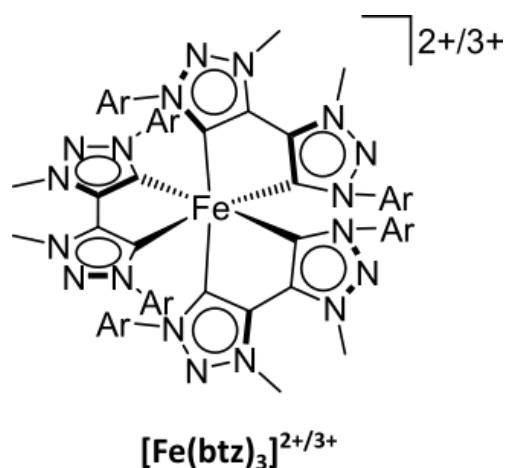


Figure 10: Chemical structure of $[\text{Fe}(\text{btz})_3]^{2+/3+}$ (Ar = para-tolyl).

The stronger destabilizing effect of increased amount of σ -donor moieties on the metal centred states could be proven by implementing the bidentate bis-carbene ligand btz (btz = 3,3'-dimethyl-1,1'-bis(*p*-tolyl)-4,4'-bis(1,2,3-triazol-5-ylidene)) to form the complex $[\text{Fe}(\text{btz})_3]^{2+}$.^{[116],[117]} This complex shows an increased lifetime of the $^3\text{MLCT}$ state of approximately 530 ps at room temperature in acetonitrile. The complex exhibits panchromatic absorption with a strong MLCT absorption band from approximately 600 nm tailing over 900 nm. Thus the emission should be somewhere in the near-IR region, which was outside the detection limit of the setup used and could not be investigated.^{[116],[117]}

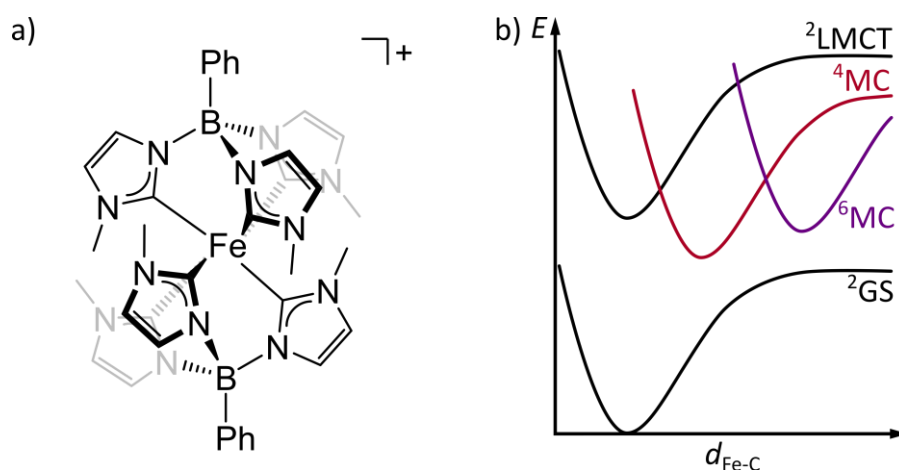


Figure 11: a) Chemical structure of $[\text{Fe}(\text{phtmeimb})_2]^+$ and b) schematic potential energy surface diagram for (pseudo-)octahedral iron(III) complexes bearing strong σ -donating ligands.

Apart from increasing the lifetime of the $^3\text{MLCT}$ state, the implementation of strong σ -donors also pushes the $\text{Fe}^{\text{II}}/\text{Fe}^{\text{III}}$ oxidation potential to lower energies, which gives rise to very easily oxidizable iron(II) complexes. For instance, the introduction of four carbenes in the complex $[\text{Fe}(\text{bmip})_2]^{2+}$ pushes the oxidation potential to +0.31 V vs. FcH^+/FcH compared to +0.72 V vs. FcH^+/FcH observed for $[\text{Fe}(\text{tpy})_2]^{2+}$.^[114] Introducing even more carbene moieties into the ligands pushes this potential down even further, as observed in the $[\text{Fe}(\text{btz})_3]^{2+}$ complex, whose $\text{Fe}^{\text{II}} \rightarrow \text{Fe}^{\text{III}}$ oxidation occurs at -0.58 V vs FcH^+/FcH .^[116] One compound with even lower oxidation potential is the complex $\text{Fe}(\text{phtmeimb})_2$, with an $\text{Fe}^{\text{II}} \rightarrow \text{Fe}^{\text{III}}$ oxidation at -1.16 V vs. FcH^+/FcH . These very low oxidation potentials impede the direct synthesis of the iron(II) complexes, and upon synthesis $[\text{Fe}(\text{btz})_3]^{3+}$ and $[\text{Fe}(\text{phtmeimb})_2]^+$ are obtained.^{[117],[122],[123]} For the latter reduction is quite challenging, due to the low oxidation potential and up until now no attempts for the synthesis of $\text{Fe}(\text{phtmeimb})_2$ have been reported. The reduction of $[\text{Fe}(\text{btz})_3]^{3+}$ can be carried out by the addition of sodium dithionite in deaerated acetonitrile solution.^[117] The d^5 low-spin complexes $[\text{Fe}(\text{btz})_3]^{3+}$ and $[\text{Fe}(\text{phtmeimb})_2]^+$

themselves show interesting photophysical properties since they show luminescence originating from a $^2\text{LMCT}$ excited state with a lifetime of 100 ps and 2 ns in acetonitrile at room temperature, respectively.^{[122],[123]} Contrary to the spin-forbidden phosphorescence observed in Ru^{II} and Ir^{III} complexes the here observed luminescence originates from a spin-allowed transition from the $^2\text{LMCT}$ state into the ^2GS . These Fe^{III} complexes show, that the destabilizing nature of carbenes not only works for Fe^{II} , but also pushes the dark excited $^4/6\text{MC}$ states in d^5 low-spin iron(III) complexes to higher energies, enabling fluorescence in such systems.^{[122],[123]}

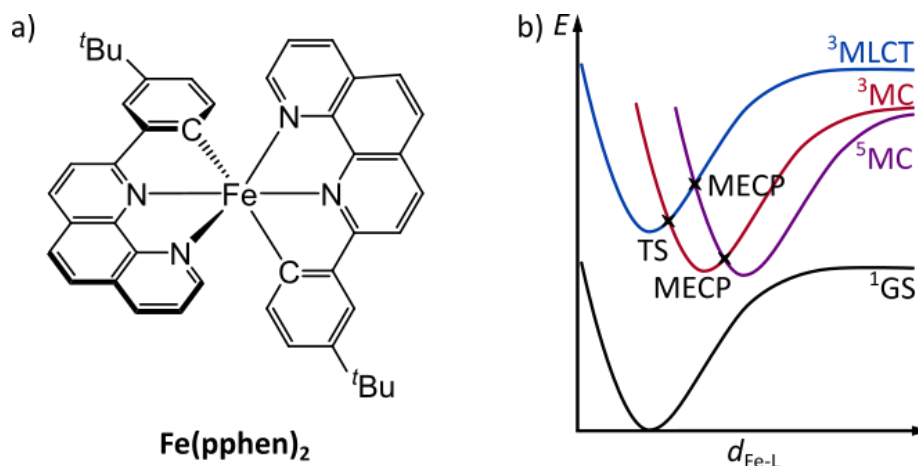


Figure 12: a) Chemical Structure of $\text{Fe}(\text{pphen})_2$ and b) schematic potential energy surface diagram for (pseudo-)octahedral iron(II) complexes bearing strong σ -donating and π -accepting ligands (TS = transition state; MECP = minimum energy crossing point; ^tBu = *tert*-butyl).

In the preceding paragraphs the strategy of destabilizing the MC states by implementing strong σ -donors was described. Instead of destabilizing the metal centred states, another strategy would be to stabilize the MLCT states by implementing stronger π -acceptors as ligands, thereby reducing the energy of the π^* -orbital of the ligands. In combination with σ -donor ligands so called push-pull complexes can be synthesized, in which the energy of the e_g^* -orbitals is increased while the energy of the π^* -orbitals is decreased simultaneously (see **Figure 6**). The beneficial effect of using such π -accepting ligands could be demonstrated by derivatizing the aforementioned $[\text{Fe}(\text{bmip})_2]^{2+}$, whereby the central pyridine-rings were substituted in the *para*-position by carboxylic acids. Compared to the unsubstituted complex, the lifetime of the complex was increased to approx. 20 ps in acetonitrile at room temperature.^{[120],[124]}

Another recent example where this strategy of simultaneously destabilizing MC states and stabilizing the MLCT states was implemented was the $\text{Fe}(\text{pphen})_2$ (pphen^- = deprotonated form of 2-(3-(*tert*-butyl)phenyl)-1,10-phenanthroline) complex.^[125] This complex incorporates two π -

accepting 1,10-phenanthroline (phen) and two σ -donating cyclometalated phenyl moieties. The complex exhibits panchromatic absorption with an intense band from approximately 650 nm tailing above 1050 nm, assigned to MLCT transitions. Excitation into this strong absorption feature gives rise to emission with a maximum at approximately 1220 nm in a d_8 -toluene/THF (9/1) solution at room temperature under argon. The lifetime of the lowest excited MLCT state was determined by TA and emission spectroscopy to be 1 ns.^[125] Furthermore, the complex shows strong solvent dependence on the photostability, since using acetonitrile or dichloromethane as co-solvents leads to a loss of the NIR emission feature. Further investigation via mass spectrometry and UV/Vis/NIR absorption spectroscopy point towards the formation of the oxidized complex $[\text{Fe}(\text{pphen})_2]^+$, implying oxidative quenching of the excited state. This oxidative quenching pathway could also be proven by photoreaction of 4-chlorobromobenzene with benzene using the iron(II) complex as photosensitizer.^[125]

In addition to the destabilizing effect of the cyclometalated phenyl group on the MC states, as well as the strong π -accepting strength of the 1,10-phenanthroline moiety another key feature of the compound is the strong rigidity of the phenanthroline group. The rigidification of the system hinders the strong distortion in the ^3MC excited state pushing the crossing point between the $^3\text{MLCT}$ and ^3MC hypersurface to higher energies, with an energy barrier for the $^3\text{MLCT}$ -to- ^3MC transition of around 0.02 eV in case of $\text{Fe}(\text{pphen})_2$.^[125]

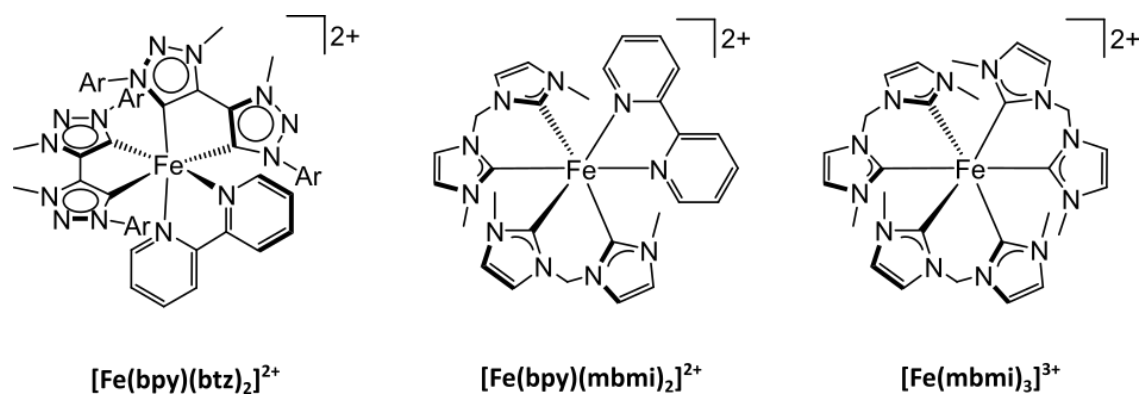


Figure 13: Chemical structures of $[\text{Fe}(\text{bpy})(\text{btz})_2]^{2+}$, $[\text{Fe}(\text{bpy})(\text{mbmi})_2]^{2+}$ and $[\text{Fe}(\text{mbmi})_3]^{3+}$ (Ar = *para*-tolyl).

The effect of rigidification of the ligand backbone on the excited state lifetimes could also be shown by comparison of the complexes $[\text{Fe}(\text{btz})_3]^{3+}$ and $[\text{Fe}(\text{mbmi})_3]^{3+}$ (mbmi = 1,1'-methylenebis-(3-methylimidazol-2-ylidene)).^[126] In $[\text{Fe}(\text{btz})_3]^{3+}$ the ligands form 5 membered ring-chelates since the two carbene moieties are directly linked together while in the mbmi-ligand the two carbene units are connected *via* a flexible methylene bridge. These differing connection motives have a direct

influence on the excited state lifetime of the complexes. As already mentioned earlier $[\text{Fe}(\text{btz})_3]^{3+}$ possesses a lifetime for the lowest excited state of 100 ps whereas the lifetime of the $^2\text{LMCT}$ state of $[\text{Fe}(\text{mbmi})_3]^{3+}$ decreased to 54 ps. These differences are due to the more distorted coordination sphere in the excited state of $[\text{Fe}(\text{mbmi})_3]^{3+}$ compared to $[\text{Fe}(\text{btz})_3]^{3+}$ leading to faster non-radiative decay. This can also be observed in the heteroleptic complexes $[\text{Fe}(\text{bpy})(\text{btz})_2]^{2+}$ and $[\text{Fe}(\text{bpy})(\text{mbmi})_2]^{2+}$ where the lifetimes of the excited $^3\text{MLCT}$ state were determined as 13 and 7.6 ps respectively.^[126] This shows that the rigidity of the ligands and therefore the resulting complexes has a direct influence on the lifetime of the excited CT states. This increase in the lifetime of the CT states in more rigid ligand environments is due to the transition state between the $^3\text{MLCT}$ and ^3MC states being pushed to higher energies, thereby increasing the energy barrier for the IC.

1.4 Marcus-Hush Theory/Electron Transfer

One of the most fundamental type of reactions in chemistry are redox reactions. These reactions involve the oxidation of one atom or molecule while another atom or molecule is reduced simultaneously. In short: one electron is transferred from one reactant to another. Since these type of electron transfer (ET) reactions play such a vital role in chemistry, their understanding is of high value and has garnered scientific interest. Understanding of the mechanism and kinetics of electron transfer reaction started in the 1940s with research of Marcus.^[127]

Examining the photoexcitation of TMCs with a d^6 low-spin electron configuration, for example $[\text{Ru}(\text{bpy})_3]^{2+}$, the transition from the ^1GS to the $^1\text{MLCT}$ state can be seen as an oxidation of the metal centre and the concomitant reduction of one of the bpy ligands (see **Figure 14**).^{[42],[128]} This transition is therefore also an electron transfer reaction within the same molecule. The same applies for the IC from the $^3\text{MLCT}$ to the ^3MC excited state, whereby the ET reaction takes place from the reduced ligand to the formally oxidized metal centre.^{[42],[128]}

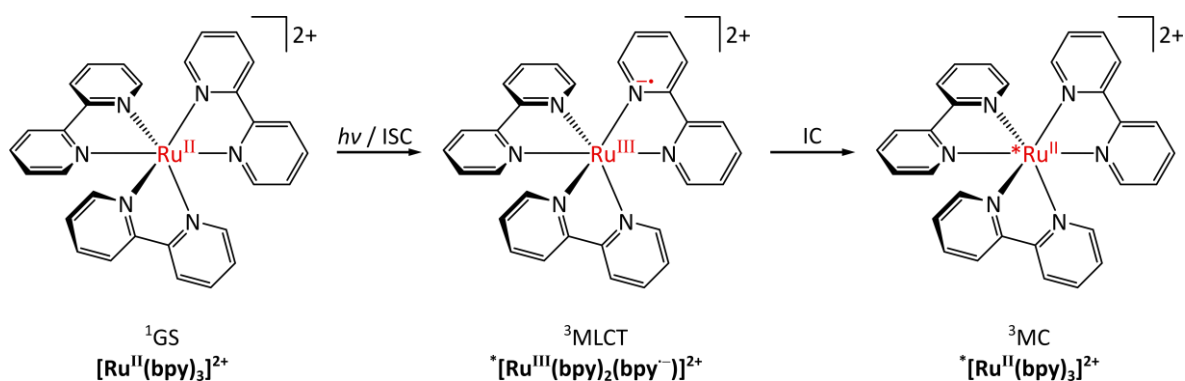
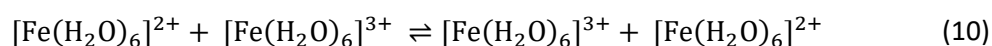


Figure 14: Schematic reaction of $[\text{Ru}(\text{bpy})_3]^{2+}$ upon photoexcitation from the ^1GS into the $^1\text{MLCT}$, ISC into the $^3\text{MLCT}$ and IC into the ^3MC state.

The description of the mechanisms and kinetics in thermal ET reactions was first described by R. A. Marcus and is covered below.

1.4.1 Non-adiabatic approach: Marcus Theory

The first approach for a quantitative description of electron transfer reactions was done theoretically for outer sphere self-exchange reactions, while it was later found that this theory was also applicable to ET reactions in general.^{[127],[129]}



The first assumption for the theory was that the ET reaction can be described as a motion of atoms on a potential energy surface. The atoms involved in this reaction include not only the reactants but also the solvent molecules surrounding them. These atoms and molecules can thereby be described by their nuclear coordinates.^{[127],[129]} A transition from the reactants to the products is only possible at the saddle point on the energy surface and can only occur if the system contains enough energy for the transition. This applies to all electron transfer reactions with weak electronic interaction between the two reactants.^{[127],[129]}

The theory for ET by Marcus states that during a thermal electron transfer the coordinates of the nuclei do not change, as is the case with optical electron transfer (Franck Condon principle). Because of energy conservation the ET reaction can only occur at the saddle point of the energy surface. To achieve this, fluctuations of all coordinates have to occur.^{[127],[129]}

To simplify this complex situation, which depends on nuclear motion, two approximations can be used. First is the assumption that the energy change for the motion of the reactants can be approximated by a harmonic potential. Second, any change of charge of the reactants during the ET process is proportional to the change of polarization of the solvent ("linear response approximation"). These approximations lead to free energy curves for the reactants G_r and products G_p , which are simple quadratic functions of a general reaction coordinate.^[127]

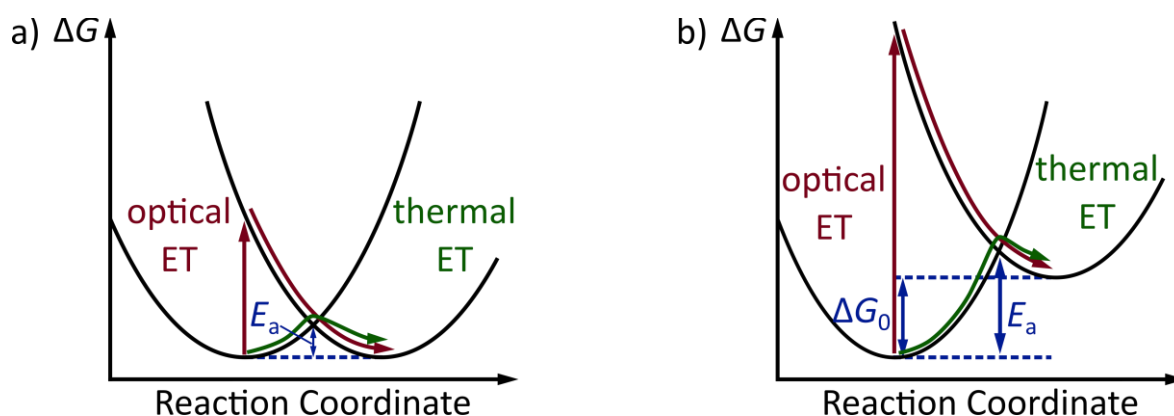


Figure 15: Schematic free energy surface for the non-adiabatic electron transfer for a) degenerate states (e.g. self-exchange) and b) non-degenerate states with both possible pathways for energy transfer (optical and thermal).

Keeping these simple energy diagrams in mind, the formulas for the description of the ET reaction derived by R. A. Marcus are easily understood.

The rate constant for the thermal electron transfer is given by an Arrhenius-like equation (Eq. (11)), where E_a is the activation barrier and A , the pre-exponential factor or frequency factor, is determined by the frequency of collisions and their orientation. E_a is given by Eq. (12) in which ΔG_0 is the standard free energy of the reaction. For the electron transfer two different cases can be observed dependant on the value of ΔG^0 . In the first case $\Delta G_0 = 0$ leading to degenerate states, in the other case $\Delta G_0 \neq 0$ resulting in non-degenerate states. In Eq. (12) λ describes the reorganization energy of the system involved in the ET process.

$$k = A e^{\left(-\frac{E_a}{k_B T}\right)} \quad (11)$$

$$E_a = \frac{(\lambda + \Delta G_0)^2}{4\lambda} \quad (12)$$

For the electron transfer there are three pathways possible. These pathways are the thermal one, which was explained above, an optical electron transfer (see **Figure 15**) and lastly tunnelling between the two energy surfaces is possible. In case of degenerate states, the optical excitation energy is equal to the reorganization energy λ . Therefore, the reorganization energy λ is equal to the liberated energy by rearranging the system after optical ET, yielding the new relaxed geometry. The reorganization energy can consists of two basic terms. One describes the inner reorganization energy λ_i which is the energy arising from the displacement of the nuclei in the product, the other contribution is the outer reorganization energy λ_o which is the energy needed to reorient the surrounding solvent molecules.^[127]

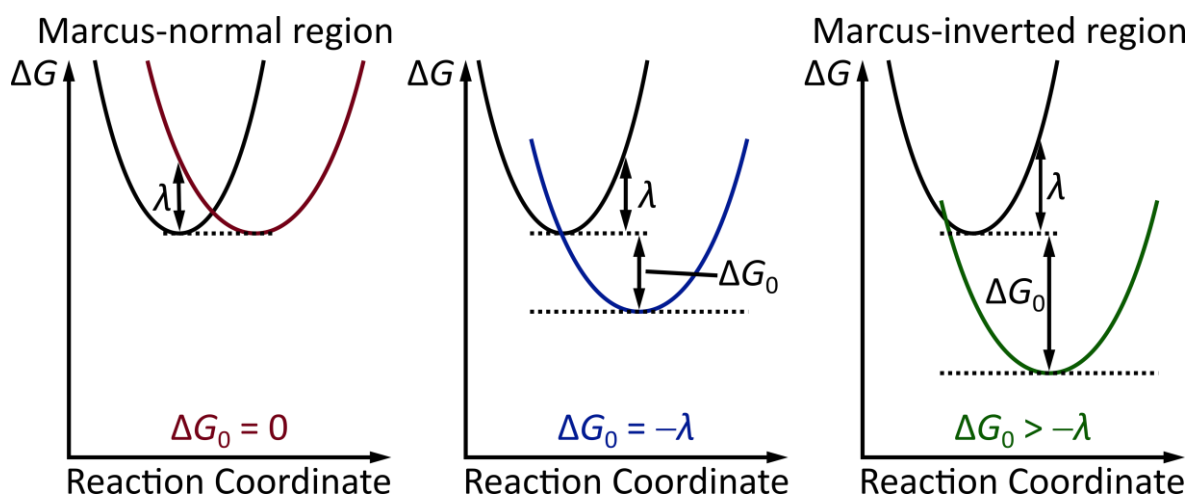


Figure 16: Schematic free energy surfaces for different values of ΔG_0 .

In case of non-degenerate states the optical excitation energy is equal to the sum of the reorganization energy λ and the standard free energy ΔG^0 .

Since the relation of λ and ΔG_0 has a direct influence on the activation energy E_a , three different limiting cases can be considered. If $\Delta G_0 = 0$ the activation energy is at a maximum, which is called Marcus-normal region. When ΔG_0 decreases, the activation energy decreases as well until $\Delta G_0 = -\lambda$, at which point the activation barrier $E_a = 0$, so no activation barrier is observed. If the standard enthalpy ΔG_0 keeps decreasing ($\Delta G_0 > -\lambda$) the activation energy rises again. This region is also called Marcus-inverted region. With this information, Eq. (11) means that the rate for electron transfer increases with increasing ΔG_0 until a maximum rate is reached. If the reaction then continues getting more exothermic the electron transfer rate constant decreases again, and electron transfer get slower.^[127]

The herein described Marcus theory leads to good quantitative results in general but exhibits one major drawback. Strictly speaking, the theory is only applicable for systems with very weak electronic interactions. For systems with a significant electronic coupling, as is observed in intramolecular ET reactions (e.g. the transition from the MLCT to MC excited states in d^6 low spin complexes as mentioned before), a more refined approach was made by Hush, to include strongly interacting systems.^[127]

1.4.2 Adiabatic approach: Marcus-Hush theory

As written above, the Marcus-Hush theory applies to systems where the electronic communication between two redox sites is not negligible anymore, meaning that the electronic coupling is greater than the thermal energy $k_B T$. The electronic communication is hereby quantified by the electron coupling parameter H_{AB} . The electronic coupling *via* H_{AB} of the two non-adiabatic free energy surfaces for reactants and products from the Marcus theory leads to the energy surfaces depicted in **Figure 17**. In case of electronic coupling between the two states a double minimum curve is obtained in the adiabatic ground state and a single minimum in the excited state. The electronic coupling parameter H_{AB} is given by the energetic separation between the GS and ES and is exactly equal to $2 H_{AB}$ in both degenerate and non-degenerate states.^[130]

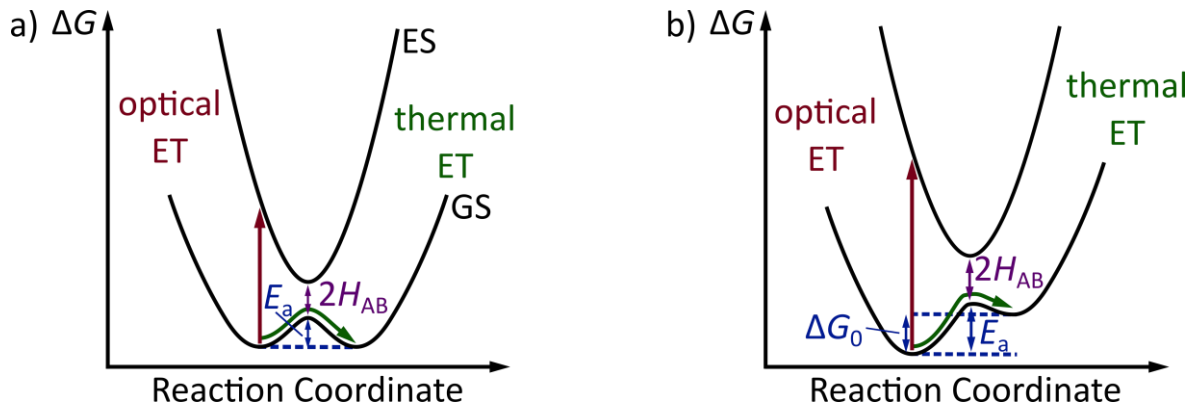


Figure 17: Schematic free energy surface for the adiabatic electron transfer for a) degenerate states and b) non-degenerate states with both possible pathways for energy transfer (optical and thermal).

Obtaining the values for the activation energy E_a in the adiabatic case is not as easy as in the non-adiabatic one, since the electronic coupling leads to a stabilization of the curve minima. To obtain expression for E_a a term for the free energy of the transition state as well as the reactant minimum depending on H_{AB} and ΔG_0 is formulated. This can be done since the terms for the reaction coordinate are also depending on H_{AB} and ΔG_0 . The difference of these two energies gives then the free energy of the activation E_a . For the degenerate and non-degenerate states two differing equations for E_a are obtained depicted in Eq. (13) and Eq. (14) respectively.^[130]

$$E_a = \frac{(\lambda - 2H_{AB})^2}{4\lambda} \quad (13)$$

$$E_a = \frac{\lambda}{4} + \frac{\Delta G_0^2}{2} + \frac{\Delta G_0^2}{4(\lambda - 2H_{AB})} - H_{AB} + \frac{H_{AB}^2}{\lambda + \Delta G_0} - \frac{H_{AB}^4 \Delta G_0}{(\lambda + \Delta G_0)^4} \quad (14)$$

1.5 Studying TMCs with transient absorption spectroscopy

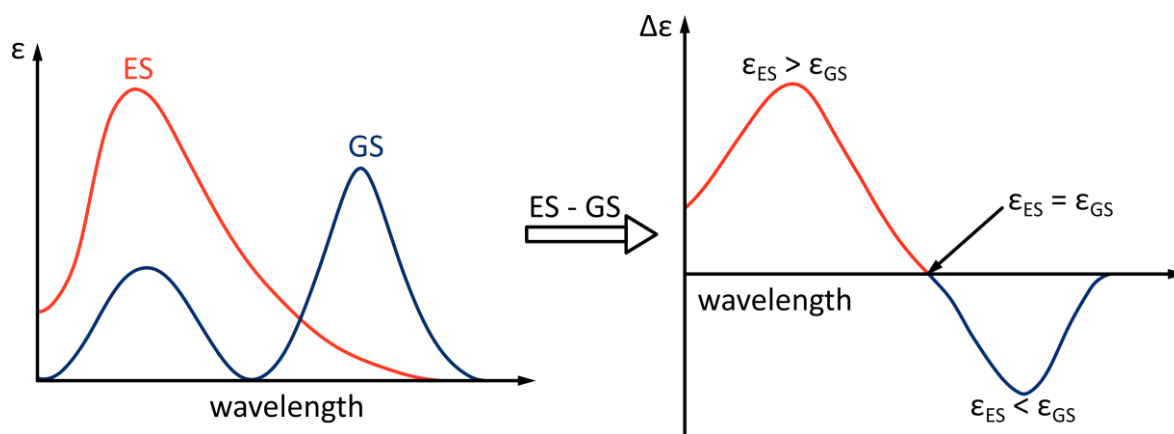


Figure 18: Schematic representation of how a difference spectrum is obtained. Left: Schematic absorption spectra of the ground state (GS, blue) and the excited state (ES, orange). Right: Schematic representation of the obtained transient absorption plot, after subtraction of the ground state absorption spectrum from the excited state absorption spectrum. The positive feature in orange represents excited state absorption (ESA), the negative blue feature represents ground state bleaching (GSB).^[42]

To gain insight into the photophysical properties of non-luminescent complexes and obtain information about the lifetime of dark excited states, (ultra-fast) time-resolved pump-probe spectroscopy is useful.^[42] After excitation with a (fs-)laser pulse (pump), time-resolved absorption spectra of the excited states (probe) are measured. Typically these absorption spectra of the excited state are subtracted by the ground state spectrum of the compound to yield difference spectra (see **Figure 18**). Characteristic excited state absorption bands as well as their time traces give a possibility to estimate the lifetime of these excited states. In the case of d^6 transition metal complexes exhibiting MLCT absorption (e.g. $[\text{Ru}(\text{bpy})_3]^{2+}$), these characteristic excited state absorption bands are related to LMCT absorptions shifted to lower energy and to the ligand radical anion at higher energy (see **Figure 14**). In other words, upon excitation of the initially populated MLCT state a charge transfer from the ligand to the metal centre occurs. Apart from excited state absorption another diagnostic feature in transient absorption (TA) spectra is the ground state bleach which stems from the loss of starting material (e.g. Ru^{II} for $[\text{Ru}(\text{bpy})_3]^{2+}$) in the excited state relative to the ground state (or presence of Ru^{III} after formal oxidation of $[\text{Ru}(\text{bpy})_3]^{2+}$).^[42]

To help the assignment of the excited state absorption bands measured in TA spectroscopy, the MLCT excited state absorption spectra can be simulated using spectroelectrochemical measurements.^[128] As mentioned before, the MLCT state can be viewed as a formal oxidation of the metal centre while simultaneously reducing the ligand. To simulate this excited state both electron transfer processes can be investigated separately by either electrochemical oxidation or

reduction using absorption spectroscopy. From the obtained sub-spectra a difference spectrum for the excited state can be determined using the following equation:^[128]

$$\Delta A_{\text{ex}} = (A_{\text{ox}} + A_{\text{red}})\eta - 2A_{\text{GS}}(1 - \eta) \quad (15)$$

Here ΔA_{ex} is the excited state difference absorbance obtained *via* the simulation and A_{ox} , A_{red} and A_{GS} the measured absorbances of the oxidized, reduced and ground state species. η is a scaling factor.

Apart from gaining insight into the excited state lifetimes of dark excited states, fs-TA spectroscopy has also been utilized to probe the activation barrier between excited states. This can be done by variable temperature TA measurements as was carried out for the high-spin to low-spin transition involved in the ground state recovery dynamics of $[\text{Fe}(\text{bpy})_3]^{2+}$. If a temperature dependence on the decay kinetics in a compound can be observed *via* (fs-)TA spectroscopic measurements, the obtained Arrhenius data allows interpretation of the underlying processes between two excited states in a semi-classical Marcus-type framework. This interpretation can be made by deriving simple relations between the Arrhenius equation (Eq. (11)) and a semi-classical formulation of Marcus theory given by the following equation:^[131]

$$k_{\text{nr}} = \frac{2\pi}{\hbar} |H_{\text{AB}}|^2 \frac{1}{\sqrt{4\pi\lambda k_B T}} e^{-\frac{(\lambda + \Delta G_0)^2}{4\lambda k_B T}} \quad (16)$$

In this equation ΔG_0 is the energy difference between the two involved excited states (i.e. the driving force; in case of $[\text{Fe}(\text{bpy})_3]^{2+}$ the two states involved are the 1A_1 ground and 5T_2 excited state). Comparing the Arrhenius equation (11) and equation (16) immediately gives a connection between the two pre-exponential terms:^[131]

$$A = \frac{2\pi}{\hbar} |H_{\text{AB}}|^2 \frac{1}{\sqrt{4\pi\lambda k_B T}} \quad (17)$$

An expression for the activation energy between the two excited states involved can be derived as follows:^[131]

$$E_a = \frac{(\lambda + \Delta G_0)^2}{4\lambda} \quad (18)$$

These two equations (Eq. (17) and Eq. (18)) allow the use of ultrafast variable-temperature TA data to obtain experimentally grounded estimates for the electronic coupling parameter H_{AB} between two excited states. This was done for instance for $[\text{Fe}(\text{bpy})_3]^{2+}$ and $[\text{Fe}(\text{tpy})_3]^{2+}$ for which electronic coupling parameters were determined as $4.4 \pm 0.2 \text{ cm}^{-1}$ and $6.2 \pm 1.2 \text{ cm}^{-1}$, respectively, for the coupling between the excited ^5MC and singlet ground state.^[131]

2 Aim of work

The photophysics of TMCs with noble metals, such as ruthenium(II), are well investigated and understood due to many years of intensive research. The major drawback of such compounds is, however, the low abundance of the metal centre and therefore the high cost. Due to its high earth abundance iron(II) represents a potential alternative candidate to replace ruthenium(II) as a photosensitizer. Therefore, the aim of this work is the design of novel photoactive iron(II) complexes. The focus herein lies on using tridentate six-membered-ring chelating ligands, increasing the ligand field splitting due to the larger bite-angle of the ligand and the better orbital overlap between the ligand and metal orbitals. This could potentially lead to an extension of the lifetime of the excited $^3\text{MLCT}$ state. This concept of high local (octahedral) symmetry in the first coordination sphere will be combined with the design of push-pull ligands using strong σ -donors in form of *N*-heterocyclic carbenes (NHCs) as well as pyridine moieties as π -acceptors. The usage of strong σ -donors should furthermore destabilize the dark non-emissive excited MC states, while using pyridine as a π -acceptor should lead to low-lying MLCT states.

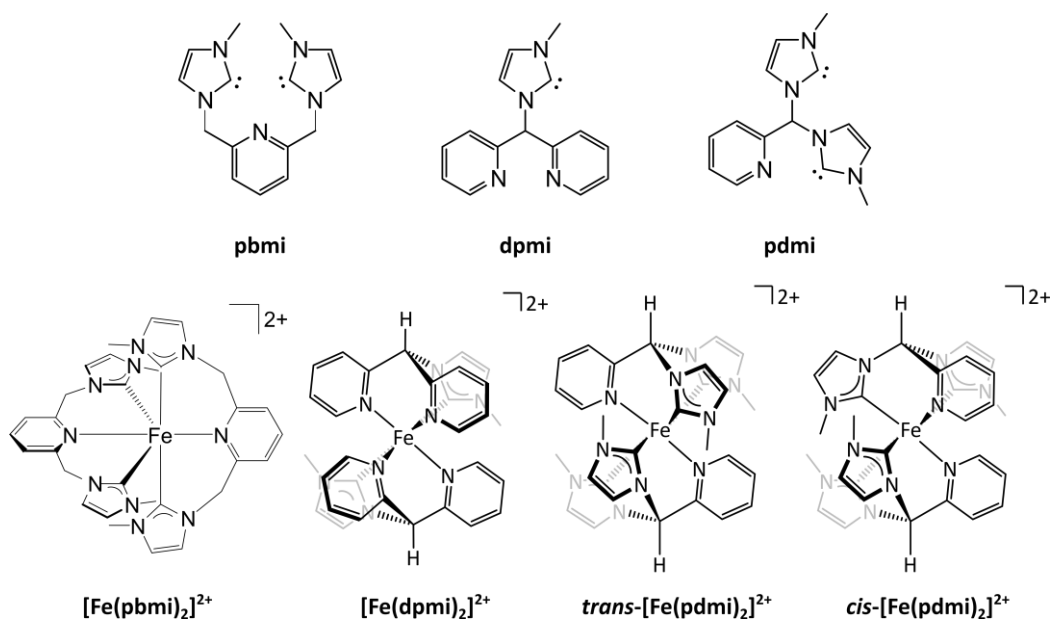


Figure 19: Ligands and complexes to be synthesized as part of this work.

For this, three novel ligands bearing NHCs were designed. Firstly, the linear ligand 2,6-bis((3-methyl-2,3-dihydro-1*H*-imidazol-1-ylidene)methyl)pyridine (pbmi) bearing a π -accepting pyridine as well as two σ -donating methyl-imidazole moieties linked by methylene bridges in the pyridine 2- and 6-

position will be synthesized. This ligand will then be used to attempt the synthesis of the homoleptic complex $[\text{Fe}(\text{pbmi})_2]^{2+}$.

Secondly, the tripodal ligands 2,2'-((3-methyl-2,3-dihydro-1*H*-imidazol-1-ylidene)methylene)dipyridine (dpmi), incorporating two pyridines and one methyl-imidazolylidene bridged *via* a methyl group, and 2-(bis(3-methyl-2,3-dihydro-1*H*-imidazol-1-ylidene)methyl)pyridine (pdmi), bearing one pyridine and two methyl-imidazolylidene bridged *via* a methyl group, will be synthesized. For these ligands the homoleptic complexes $[\text{Fe}(\text{dpmi})_2]^{2+}$ and *trans*- $[\text{Fe}(\text{pdmi})_2]^{2+}$ and *cis*- $[\text{Fe}(\text{pdmi})_2]^{2+}$ will be synthesized and characterized. The complexes will be investigated towards their structure using single crystal X-ray diffraction or X-ray absorption near-edge structure spectroscopy (XANES)/extended X-ray absorption fine structure (EXAFS), ^1H , ^{13}C , ^{19}F and ^{31}P NMR spectra, IR spectroscopy and mass spectrometry to verify the proposed composition and structure of the complexes. The photophysical properties of the complexes will be studied employing steady state and ultra-fast time-resolved absorption as well as emission spectroscopy supported by theoretical methods (DFT and TD-DFT), to obtain an understanding of the excited state landscape and the underlying excited state dynamics in the respective complexes. Furthermore electrochemical investigations will be carried out using cyclic voltammetry, square-wave voltammetry and UV-Vis spectroelectrochemistry for simulation and interpretation of the results obtained *via* ultra-fast transient absorption spectroscopy.

3 Results and Discussion

Most results of the research in this work have been published in peer-reviewed journals. In the following sections, the discussed publications are reprinted, as well as non-published results described.

The synthesis of the ligand pbmi and the attempts at synthesis for the complex $[\text{Fe}(\text{pbmi})_2]^{2+}$ are described in section 3.1, with results obtained by DFT and TD-DFT calculations.

Synthesis, characterization and quantum-chemical calculation of the novel iron(II) complex $[\text{Fe}(\text{dpmi})_2]^{2+}$ are presented in section 3.2 "*Higher MLCT lifetime of carbene iron(ii) complexes by chelate ring expansion*". The title complex was investigated towards the effect of lifetime extension of the excited $^3\text{MLCT}$ state by utilizing six-membered-ring chelates incorporating strong σ -donors in the form of *N*-heterocyclic carbenes. To evaluate the effect of using such a tripodal tridentate carbene ligand, the ligand and complex were synthesized and characterized by T. Reuter. To gain further insight into the structure, XANES and EXAFS was performed by R. Schoch from the group of Prof. M. Bauer (Universität Paderborn). Since no luminescence was observable for the complex, transient absorption measurements were carried out to gain an understanding of the excited state lifetimes. The TA experiments were carried out by A. Kruse from the group of Prof. S. Lochbrunner (Universität Rostock). These measurements show that the complex $[\text{Fe}(\text{dpmi})_2]^{2+}$ exhibits an extended lifetime of the $^3\text{MLCT}$ state of approx. 9 ps due to the six-membered-ring chelating nature of the ligand dpmi combined with its strong σ -donating methyl-imidazole moieties.

In Section 3.3 "*A Tetracarbene Iron(II) Complex with a Long-lived Triplet Metal-to-Ligand Charge Transfer State due to a Triplet-Triplet Barrier*" the preparation and characterization of the two isomers of $[\text{Fe}(\text{pdmi})_2]^{2+}$ is described. The synthesis and characterization of the ligand and complexes in the ground state were performed by T. Reuter, while the purification necessary to obtain pure *cis*- and *trans*-isomers was carried out *via* HPLC by D. Zorn. The single crystal X-Ray diffraction analyses reported were done by C. Förster. Since no luminescence of the complexes is observed either at room temperature or at 77 K in frozen solution, transient absorption spectroscopy was performed by R. Naumann. These TA spectroscopic measurements were performed at variable temperatures and reveal temperature dependency of the lifetime of the $^3\text{MLCT}$ state for *cis*- $[\text{Fe}(\text{pdmi})_2]^{2+}$. The so obtained Arrhenius data was then analysed using semi-classical Marcus theory to gain insight into the electronic coupling between the excited triplet state.

To help the interpretation of the measurements DFT and TD-DFT calculations were carried out by T. Reuter.

Section 3.4: "*Ground- and Excited-State Properties of Iron(II) Complexes Linked to Organic Chromophores*" describes the synthesis and characterization of two iron(II) complexes using modified bmip-ligands. The synthesis and most of the characterization in the ground state of the complexes was performed by P. Dierks from the group of Prof. M. Bauer (Universität Paderborn). The spectroelectrochemical measurements were performed by T. Reuter, while TA measurements were performed by Ayla Kruse (geb. Pöpcke) from the group of S. Lochbrunner (Universität Rostock).

3.1 Synthesis of $[\text{H}_2\text{pbmi}]^{2+}$ and synthesis attempts of its homoleptic iron(II) complex

DFT calculations (B3LYP, Def2-tzvp/J, D3BJ, RIJCOSX, ZORA, CPCM(acetonitrile), KDIIS) were performed for the homoleptic iron(II) complex $[\text{Fe}(\text{pbmi})_2]^{2+}$ to gain insight into the energetic position of the excited states in comparison to the ground state. The calculated single point energies at the optimized geometries relative to the energy of the ^1GS are shown in **Table 2**.

Table 2: Calculated energies of the electronic excited states of $[\text{Fe}(\text{pbmi})_2]^{2+}$ in acetonitrile relative to the energy of the ground state in eV.

	^1GS	$^3\text{MLCT}$	^3MC	^5MC
E / eV	0	---	0.32	0.95

The value for the energy of the $^3\text{MLCT}$ state is missing in the table, as no optimized geometry for this excited state could be obtained. The $^3\text{MLCT}$ state could only be optimized with geometric constraints, so the calculated energies cannot be compared to the energies of the relaxed geometries of the other states. By removing the constraints the calculation optimizes to the ^3MC state, hinting at a barrierless pathway from the $^3\text{MLCT}$ state to the ^3MC state during the calculation. The Jahn-Teller axis in the ^3MC excited state is here along the z-axis along the py-Fe-py-bonds.

Comparing the energies of the ^3MC and ^5MC excited states shows using four strong σ -donating carbene moieties in the complex seems to push the energy of the highly distorted ^5MC state to much higher energy than the excited ^3MC state. In the ^5MC state all Fe-C/N distances are elongated due to the population of both the d_{z^2} and $d_{x^2-y^2}$ orbitals, thereby imposing a large reorganisation barrier between the ^3MC and ^5MC states. Combined with the higher energy of the quintet excited state compared to the ^3MC state, and the very low energy of 0.32 eV of the ^3MC state, the lowest energetically excited state in $[\text{Fe}(\text{pbmi})_2]^{2+}$ should be the ^3MC state, according to DFT calculations.

In summary the DFT calculations show, by using four strong σ -donating carbene moieties the energy of the ^5MC state is pushed above the energy of the ^3MC state, but that the excited triplet metal centred state seems to still be the lowest excited state for $[\text{Fe}(\text{pbmi})_2]^{2+}$. Furthermore there doesn't seem to be a barrier between the $^3\text{MLCT}$ and ^3MC state indicated by the calculations of the $^3\text{MLCT}$ without constraints yielding the ^3MC state. This suggests that the lifetimes of the excited $^3\text{MLCT}$ state for $[\text{Fe}(\text{pbmi})_2]^{2+}$ could be relatively short.

Results and Discussion

To obtain the complex $[\text{Fe}(\text{pbmi})_2]^{2+}$ first the ligand has to be synthesized in the form of its proligand $[\text{H}_2\text{pbmi}]\text{X}_2$ ($\text{X}^- = \text{anion}$). The synthesis of this proligand is possible in three steps starting from 2,6-bis(hydroxymethyl)-pyridine (see **Figure 20**).

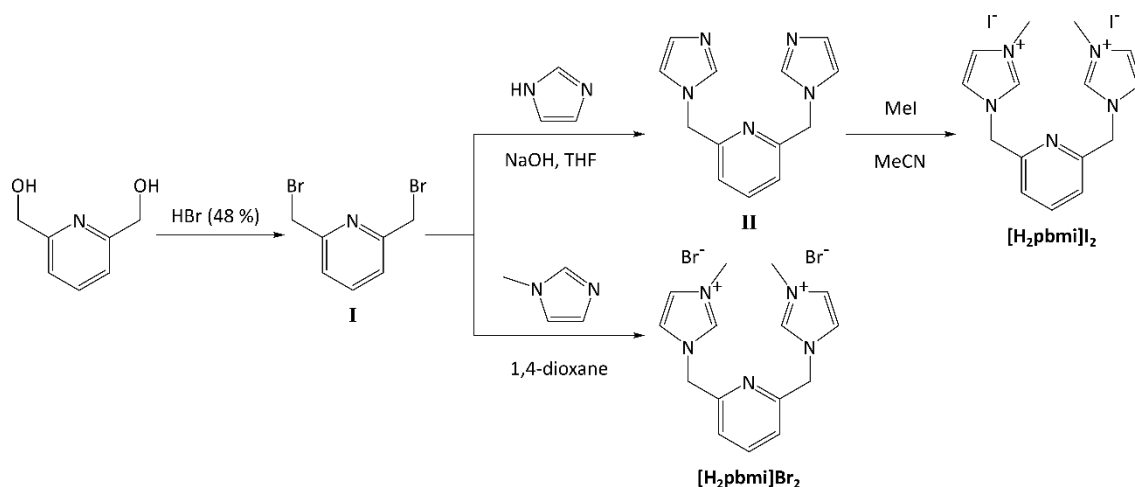


Figure 20: Synthesis scheme for $[\text{H}_2\text{pbmi}]^{2+}$.

In the first step 2,6-bis(hydroxymethyl)-pyridine is brominated *via* aqueous HBr (48 %) to 2,6-bis(bromomethyl)pyridine (**I**). This can either be reacted with 1*H*-imidazole and NaOH in THF to obtain 2,6-bis(*N*-methyleneimidazolium)pyridine (**II**), which can be methylated *via* methyl iodide, or the pro-ligand can be obtained by directly reacting the 2,6-bis(bromomethyl)pyridine (**I**) with 1-methylimidazole. In case of the first synthesis route the proligand is obtained as an iodide salt, in case of the second route as a bromide salt.

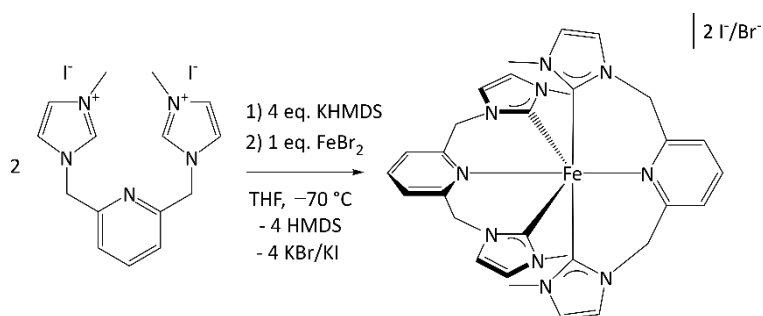


Figure 21: Synthesis scheme for $[\text{Fe}(\text{pbmi})_2]^{2+}$.

The synthesis of the homoleptic iron(II) complex was then first carried out analogous to known syntheses of iron(II) complexes bearing five-membered-ring chelating ligand bmip, namely suspending the proligand in THF at -70°C , addition of a solution of $\text{KN}(\text{SiMe}_3)_2$ (KHMDS) in THF to deprotonate the proligand, followed by addition of a solution of iron(II)bromide in THF (see **Figure**

21). Upon addition of the base, and deprotonation of the proligand, the formed ligand dissolved in THF and a yellow solution was obtained which turned purple-red upon addition of the iron(II)bromide. After removal of the solvent under reduced pressure, however no formation of the desired complex $[\text{Fe}(\text{pbmi})_2]^{2+}$ could be observed *via* ^1H NMR spectroscopy or ESI^+ -mass spectrometry.

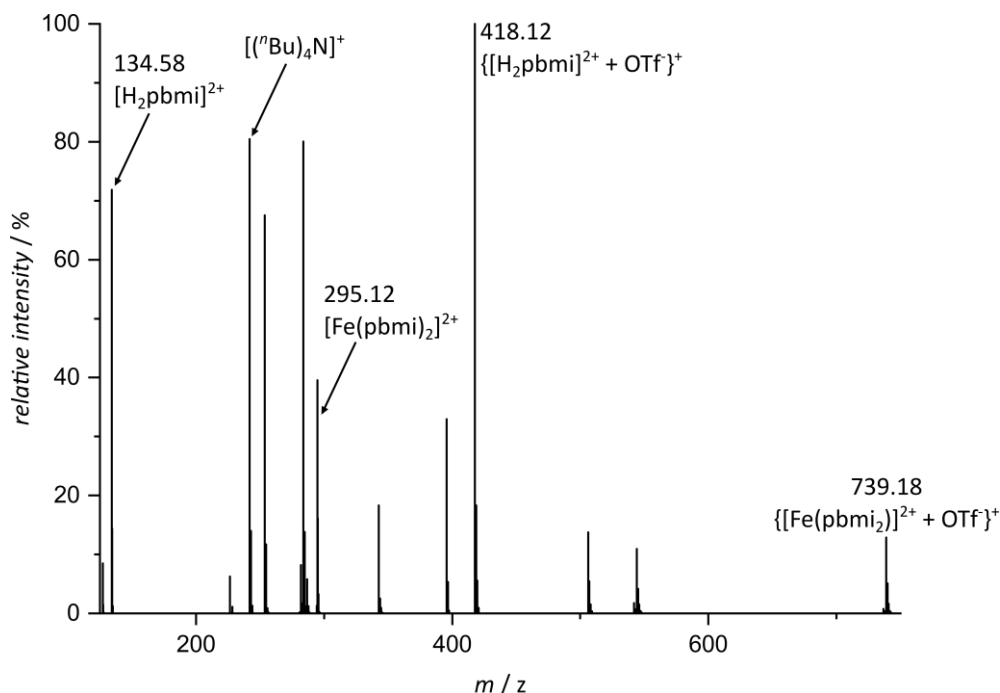


Figure 22: ESI^+ mass spectrum of the raw product obtained upon reaction of $\text{Fe}(\text{OTf})_2$ with KHMDS and $[\text{H}_2\text{pbmi}]_2$.

Changing the iron(II) source from iron(II)bromide to iron(II)triflate gave the same observations during the reaction and the formation of the desired complex $[\text{Fe}(\text{pbmi})_2]^{2+}$ could be observed via ESI^+ mass spectrometry (see **Figure 22**). The purification of the complex was not possible and no pure product was obtained. A probable reason was, that the conversion of the reaction to the complex was not large enough. Only little amounts of the complex were formed, as seen by the presence of proligand in the mass spectrum (see **Figure 22**).

To try and increase the yield of the complex several synthesis attempts were done by changing the base from KHMDS to potassium *tert*-butoxide (KO^tBu), sodium methoxide or ethoxide, 1,8-diazabicyclo(5.4.0)undec-7-ene (DBU), potassium or caesium carbonate, lithium diisopropylamide or to sodium hydride. For all the bases, apart from potassium and caesium carbonate, the same observations were made during the reaction as before with KHMDS but still no product could be isolated.

Results and Discussion

Apart from changing the base in the reaction, the counterions of the proligand were varied as well, from iodide to bromide, tetraphenylborate, triflate, or hexafluorophosphate. This did not seem to have a big influence on the formation of the complex, as the same observations were made as before. Still the purification of the complex obtained *via* these routes could not be achieved.

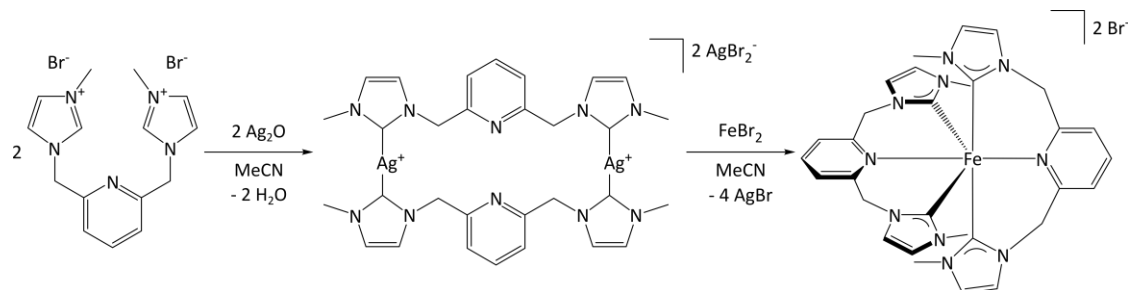


Figure 23: Synthetic scheme for the transmetalation reaction of [H₂pbmi]Br₂ with Ag₂O and subsequent reaction with FeBr₂.

Another way to try and increase the yield of the reaction was by utilizing silver(I)oxide as a transmetalation agent and reacting it with the bromide salt of the proligand (see **Figure 23**). The resulting silver complex was then reacted with iron(II)bromide. This reaction, however, did not work, and upon purification only the proligand was obtained again.

Due to the publication of the synthesis and characterization of [Fe(pbmi)₂]²⁺ by the group of Prof. Gros (University of Lorraine) the project was not continued.^[132]

Prof. Gros and his co-workers were able to synthesize the complex by reacting FeBr₂ with KO^tBu in anhydrous DMF under N₂ atmosphere at 0 °C. This yielded the complex in a yield of 19 % after column chromatography on silica with an acetone/H₂O/KNO₃(sat) = 10:3:3 mixture.^[132]

Fs-TA spectroscopy revealed three global lifetimes obtained as $\tau_1 = 0.3$ ps, $\tau_2 = 1.3$ ps and $\tau_3 = 7.3$ ps. The first lifetime was hereby assigned to the IC from the vibrationally excited ³MLCT states to the excited ³MC states, which are then de-populated after 1.3 ps leading to vibrationally excited "hot" ground state.^[132]

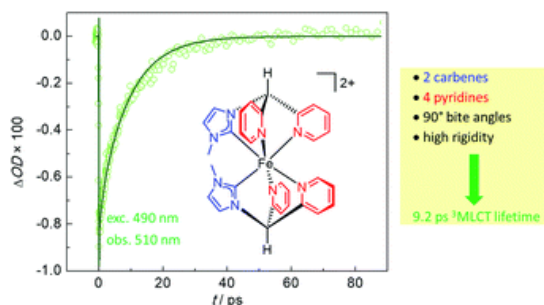
The very short lifetime of the excited ³MLCT state of [Fe(pbmi)₂]²⁺ stems from the high flexibility of the pbmi ligand, due to its methylene bridges, leading to strong distortion of the complex along the z-axis (py-Fe-py) in the excited ³MC state. This flexibility leads to energetically low lying ³MC states, with only small energy barriers for the ³MLCT → ³MC transition. This is in agreement to the results obtained *via* DFT calculations presented at the beginning of Chapter 3.1.

In summary $[\text{Fe}(\text{pbmi})_2]^{2+}$ exhibits only a very short lifetime of the excited $^3\text{MLCT}$ state due to the flexibility of the ligands, which prompted further research to use more rigid ligand structures while still incorporating the 6-membered chelate motive. This led to the employment of tripodal ligands for the synthesis of novel iron(II) complexes as described in chapters 0 and 3.3.

3.2 Higher MLCT lifetime of carbene iron(II) complexes by chelate ring expansion

Thomas Reuter, Ayla Kruse, Roland Schoch, Stefan Lochbrunner, Matthias Bauer, Katja Heinze

Chem. Comm. **2021**, 57, 7541-7544



This Article reports on the synthesis and characterization of the homoleptic iron(II) complex $[\text{Fe}(\text{dpml})_2]^{2+}$ (dpml = 2,2'-((3-methyl-2,3-dihydro-1*H*-imidazol-1-yl) methylene)dipyridine). It displays an extended lifetime of the excited $^3\text{MLCT}$ state of around 9 ps revealed by ultra-fast transient absorption spectroscopy.

Author Contributions

Synthesis and characterization of the compounds and DFT calculations were carried out by Thomas Reuter. Ultra-fast transient absorption measurements were performed by Ayla Kruse (group of Prof. Dr. S. Lochbrunner). Roland Schoch (group of Prof. Dr. Matthias Bauer) performed the Xanes and EXAFS measurements, as well as the simulation of the obtained data. The manuscript was written by Prof. Dr. Katja Heinze (90 %) and Thomas Reuter (10 %).

Supporting Info

Can be found at pp. 107.

The full supporting information can be obtained [here](#).

"Reprinted with permission from Thomas Reuter, Ayla Kruse, Roland Schoch, Stefan Lochbrunner, Matthias Bauer and Katja Heinze. Copyright 2021 Royal Society of Chemistry"

Cite this: *Chem. Commun.*, 2021,
57, 7541Received 24th April 2021,
Accepted 16th June 2021

DOI: 10.1039/d1cc02173g

rsc.li/chemcomm

Higher MLCT lifetime of carbene iron(II) complexes by chelate ring expansion†

Thomas Reuter,^a Ayla Kruse,^b Roland Schoch,^c Stefan Lochbrunner,^b
Matthias Bauer^c and Katja Heinze^{id}*^a

Combining strong σ -donating N-heterocyclic carbene ligands and π -accepting pyridine ligands with a high octahedricity in rigid iron(II) complexes increases the ³MLCT lifetime from 0.15 ps in the prototypical [Fe(tpy)]²⁺ complex to 9.2 ps in [Fe(dpml)]²⁺ 1²⁺. The tripodal CNN ligand dpml (di(pyridine-2-yl)(3-methylimidazol-2-yl)methane) forms six-membered chelate rings with the iron(II) centre leading to close to 90° bite angles and enhanced iron-ligand orbital overlap.

Replacing expensive ruthenium(II) and iridium(III) complexes possessing long-lived metal-to-ligand charge transfer (MLCT) states in photochemical or photophysical applications with cheaper and more abundant alternatives is a highly important yet very challenging objective for future large-scale implementation.^{1–4} Iron(II) complexes, isoelectronic to Ru^{II} and Ir^{III} have found tremendous interest for these purposes.^{5–8} However, due to a much smaller ligand field splitting,⁹ Fe^{II} complexes possess low-energy metal-centred states (³MC and ⁵MC) which provide efficient non-radiative relaxation pathways. Consequently, the MLCT photochemistry of iron(II) complexes is much less developed than for the classical ruthenium(II) or iridium(III) complexes.^{10,11} Concepts to prolong the lifetime of the potentially emissive ³MLCT state aim to increase the energy of the MC states and to decrease the energy of ³MLCT states.^{5–7}

The latter has been targeted by using electron-poor π -accepting ligands^{12–15} while the energy of the MC states has been increased using a better metal–ligand orbital overlap in highly octahedral polypyridyl complexes with N–M–N angles close to 180°^{12–14} or strong σ -donating carbene ligands.^{6,7,15–20} The concept of large bite angles to separate ³MLCT from MC states had been very

successful in the photophysical optimisation of ruthenium(II) sensitizers and phosphorescent emitters.^{21–25} In structurally related carbene pyridine iron(II) complexes with tridentate ligands forming five-membered chelate rings, the number of carbene donors dictates the ³MLCT lifetime.¹⁷ The highest lifetime (528 ps) of carbene iron(II) complexes has been achieved with six carbene donors in [Fe(btz)₃]²⁺ (btz = 3,3'-dimethyl-1,1'-bis(*p*-tolyl))-4,4'-bis(1,2,3-triazol-5-ylidene).²⁰ The effect of six-membered chelate rings to increase the metal ligand orbital overlap and consequently the energy of MC states of 3d metal complexes has been demonstrated with polypyridyl vanadium(III) and chromium(III) complexes^{26–28} as well as hexacarbene manganese(IV) and iron(III) complexes,^{29,30} while polypyridyl iron(II) complexes with high octahedricity still feature low MLCT lifetimes. The combination of four carbenes with six-membered chelate rings in iron(II) complexes with tridentate meridionally coordinating CNC ligands only provided low MLCT lifetimes of around 1 ps of the majority of the excited state population which has been ascribed to a higher flexibility of this CNC ligand.³¹

Here, we combine high octahedricity with π -accepting pyridine and σ -donating carbene ligands in a more rigid coordination environment to increase the ³MLCT lifetime of iron(II) complexes. We compare the [C₂N₄] donor set in the novel more octahedral carbene iron(II) complex [Fe(dpml)]²⁺ 1²⁺ (Scheme 1) featuring facially coordinating dpml ligands (di(pyridine-2-yl)(3-methylimidazol-2-yl)methane) that form six-membered chelate rings with distorted [Fe(CNC)₂]²⁺ and [Fe(CNN)₂]²⁺ complexes possessing five-membered chelate rings in terms of the resulting ³MLCT lifetime. The distorted [Fe(CNC)₂]²⁺ and [Fe(CNN)₂]²⁺ complexes with five-membered rings exhibit ³MLCT lifetimes below 0.1 ps.¹⁷ We demonstrate that the more octahedral and rigid complex geometry increases the lifetime even beyond that of a [C₄N₂] donor set in distorted carbene pyridine iron(II) complexes (τ = 9, 8.1, <0.3 ps for [Fe(CNC)₂]²⁺ with Me, ⁱPr, ^tBu N-substituents).^{16,17} Consequently, the higher octahedricity and rigidity of 1²⁺ has a similar boosting effect as two strong carbene σ -donors in distorted [Fe(CNC)₂]²⁺ complexes.

^a Department of Chemistry, Johannes Gutenberg University of Mainz, Duesbergweg 10-14, Mainz 55128, Germany. E-mail: katja.heinze@uni-mainz.de

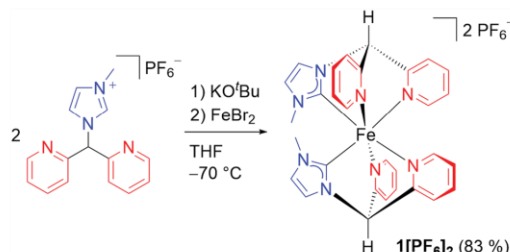
^b Institute for Physics and Department of Life, Light and Matter, University of Rostock, Rostock 18051, Germany

^c Faculty of Science, Chemistry Department and Centre for Sustainable Systems Design, Paderborn University, Paderborn 33098, Germany

† Electronic supplementary information (ESI) available: General procedures, synthesis, spectral data, computational data. See DOI: 10.1039/d1cc02173g



Communication



Scheme 1 Synthesis of **1[PF₆]₂** starting from the pro-ligand [Py₂MelmH][PF₆].³²

The tridentate facially coordinating CNN ligand derived from [Py₂MelmH][PF₆]³² after deprotonation forms six-membered chelate rings with iron(II) in the homoleptic complex cation **1²⁺** (Scheme 1). Complex **1²⁺** with a [C₂N₄] donor set was characterised by IR, NMR spectroscopy, ESI⁺ mass spectrometry and elemental analysis (ESI). The 12 and 15 ¹H and ¹³C NMR resonances observed (ESI) are consistent with a *cis* configuration of the carbene donors and the expected destabilising *trans* influence in a conceivable *trans* configuration. Six Fe–C/N atom distances of 1.99(8) Å were determined by iron K-edge EXAFS of **1[PF₆]₂** (ESI). Four Fe–N distances of 2.79(4) Å fit to the four NHC nitrogen atoms. The averaged Fe–C/N distances obtained by the EXAFS experiment agree with a structural model derived from quantum chemical calculations of low-spin **1²⁺** (DFT CPCM(acetonitrile)-RIJCOSX-B3LYP-D3BJ-ZORA/def2-TZVP; averaged Fe–C/N distance of 1.999 Å and averaged Fe–N_{carbene} distances of 2.943 Å; ESI). The pre-edge peak at 7113.3 eV in the iron K-edge X-ray absorption spectrum³³ and the NMR data of **1[PF₆]₂** confirm the low-spin state of the iron(II) centre. The energies of the pre-peak and the near-edge shoulders around 7120 and 7123 eV of **1²⁺** (ESI) are essentially identical to that of a [Fe(CNN)₂]²⁺ complex with *cis*-positioned carbene donors in a more distorted geometry (7113.3, 7120, 7123 eV).¹⁷

The electronic absorption spectrum of **1²⁺** in acetonitrile shows two absorption bands at 415 nm ($\epsilon = 17310 \text{ L mol}^{-1} \text{ cm}^{-1}$) and 500 nm ($\epsilon = 19390 \text{ L mol}^{-1} \text{ cm}^{-1}$) (Fig. 1a). Their intensities agree with allowed charge transfer transitions and exceed those of other carbene and pyridine iron(II) complexes, e.g. 700 nm (2000 $\text{L mol}^{-1} \text{ cm}^{-1}$), 508/557 nm (4700/7000 $\text{L mol}^{-1} \text{ cm}^{-1}$), 503/538 nm (9800/8600 $\text{L mol}^{-1} \text{ cm}^{-1}$) and 551 nm (7000 $\text{L mol}^{-1} \text{ cm}^{-1}$) for [Fe(bt₂)₃]²⁺,²⁰ [Fe(CNN)₂]²⁺, [Fe(CNC)(tpy)]²⁺ and [Fe(tpy)₂]²⁺, respectively.¹⁷ According to time-dependent DFT (TDDFT) calculation and charge transfer number analysis,³⁴ these two intense bands consist of $d_{\text{Fe}} \rightarrow \pi_{\text{pyridine}}$ MLCT transitions, while $d_{\text{Fe}} \rightarrow \pi_{\text{carbene}}$ MLCT transitions appear at higher energy (ESI). Less allowed transitions are calculated at lower energy. The charge transfer number analysis assigns mainly ¹MC character to these bands, suggesting that ¹MC states are lower in energy than ¹MLCT states.

The iron(II) complex **1²⁺** is reversibly oxidised to **1³⁺** at $E_{1/2} = 0.26 \text{ V vs. ferrocene}$ in the cyclic voltammogram (MeCN, [ⁿBu₄N][PF₆], ESI). Spectro-electrochemical oxidation of **1²⁺** to **1³⁺**

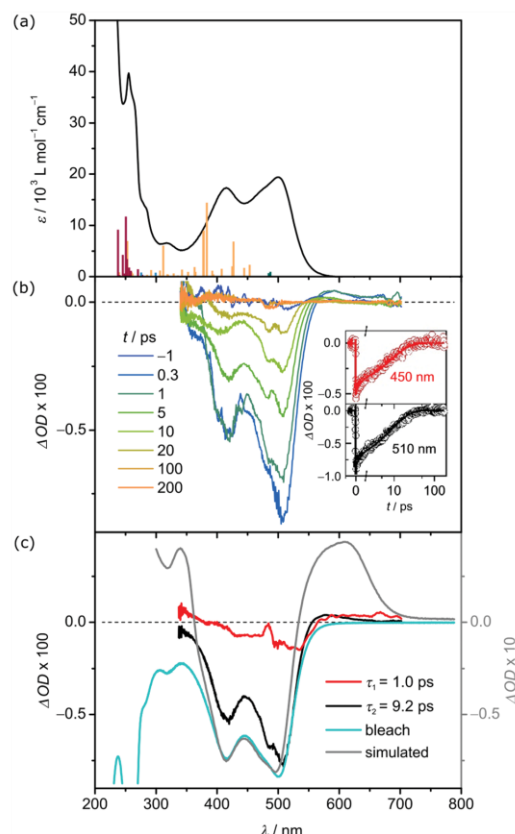


Fig. 1 (a) UV/Vis absorption spectrum of **1[PF₆]₂** (black) in deaerated acetonitrile and TDDFT calculated transitions of **1²⁺** with the colour code indicating the character of the transition according to charge transfer analysis (dark green: MC, orange: MLCT, dark red: LLCT). (b) Transient absorption spectra of **1[PF₆]₂** in deaerated acetonitrile at selected time points from 0.3 to 200 ps after excitation at 490 nm. The insets show time traces probed at 450 nm (red) and 510 nm (black) and corresponding fits. (c) Decay associated amplitude spectra (DAS) of the 1.0 ps (red) and 9.2 ps (black) decay component compared to the scaled bleach (blue) and the difference spectrum³⁵ between **1³⁺** and **1²⁺** (grey).

bleaches the MLCT absorption bands while two new bands appear at 522 and 610 nm (ESI). These are ascribed to carbene/pyridine-to-iron charge transfer transitions (LMCT). Isosbestic points form at 253, 267, 356 and 544 nm confirming the reversible nature of the oxidation process. Chemical oxidation of orange **1²⁺** to blue **1³⁺** using [NO][PF₆] as oxidant is successful as well as supported by an identical UV/Vis spectral pattern (ESI).

Transient absorption (TA) spectroscopy on **1[PF₆]₂** in deaerated MeCN discloses the excited state dynamics after excitation at 490 nm (MLCT). Fig. 1b shows the TA spectra recorded at selected time delays following excitation at 490 nm. The TA spectra display two negative bands at 420 and 505 nm, which correspond to the ground state bleach (GSB), and a weaker



excited state absorption (ESA) at approximately 560 nm. All signals decay on the 10 ps time scale (Fig. 1b, insets).

The dynamics is analysed by applying a global, triple-exponential fit, yielding a dominant decay component with a time constant of $\tau_2 = 9.2$ ps and a weaker one of $\tau_1 = 1.0$ ps. The third contribution exhibits a lifetime of only a few femtoseconds, which is much shorter than the actual time resolution, and resembles an artefact at time zero due to cross phase modulation. Fig. 1c compares the decay associated amplitude spectra (DAS) of the two relevant components τ_1 and τ_2 to the scaled bleach and the difference spectrum between 1^{3+} and 1^{2+} . The DAS of the dominant $\tau_2 = 9.2$ ps component is quite similar to the bleach but exhibits additional ESA contributions in the wavelength range 550–650 nm. The difference spectrum indicates that oxidation of iron(II) to iron(III) causes such an additional absorption. Below 400 nm the TA signal approaches zero with decreasing wavelength in contrast to the bleach pointing also there to an additional ESA contribution. This too, would be in line with an oxidation of the iron center. Accordingly, the 9.2 ps component describes the decay of a state involving iron(III) suggesting that it is the MLCT state.³⁰ The absorption band of 1^{3+} at 610 nm and consequently the ESA of 1^{2+} are of ligand \rightarrow iron(III) LMCT character. The DAS of the 1.0 ps component is weak and exhibits a shape, which has some similarities with the dominant contribution but is slightly red shifted (see Fig. 1c). Therefore, it is assigned to energy redistribution processes, e.g. charge localisation in the ligand, which cause a blue shift of the TA spectra.

With this interpretation and literature precedent,^{15–17,35} the DAS within the first few picoseconds are assigned to the $^3\text{MLCT}$ state of 1^{2+} . Intersystem crossing from $^1\text{MLCT}$ to $^3\text{MLCT}$ is faster than the time resolution of our instrument (< 100 fs). Based on the observed decay of the TA spectra, relaxation of the $^3\text{MLCT}$ state back to the ground state occurs either directly or via an intermediate state that is only transiently populated and thus not observed. Typically, ^3MC and ^5MC states serve as deactivating pathways for iron(II) complexes.^{5–8} Iron(II) complexes with the ^5MC state as lowest excited state possess high ^5MC lifetimes up to several nanoseconds, for example the $^5\text{T}_2\text{-}^1\text{A}_1$ ground state recovery time of $[\text{Fe}(\text{tpy})_2]^{2+}$ is 4 ns.^{36,37} On the other hand, complexes with the ^3MC state lower than the ^5MC state possess ^3MC lifetimes of only a few ps and sometimes even less. For example, $[\text{Fe}(\text{CNC})_2]^{2+}$ complexes with methyl and isopropyl N-substituents show ^3MC lifetimes < 2 ps and < 8 ps, significantly shorter than the $^3\text{MLCT}$ lifetime.^{16,17} A similar situation might be operative in 1^{2+} with only two carbene ligands: the ^5MC state is higher in energy than the ^3MC state which decays rapidly to the ground state and is consequently not observed, similar to $[\text{Fe}(\text{CNC})_2]^{2+}$.¹⁹

To substantiate this interpretation, the lowest triplet and quintet MC states of 1^{2+} were calculated by DFT (Fig. 2). The ^3MC state is slightly lower in energy than the ^5MC state. In the triplet state, the two Fe–N distances of the *trans* positioned pyridines are strongly elongated from 2.013/2.015 Å to 2.348/2.358 Å, while the other Fe–C/N distances are hardly affected. This is consistent with the population of the d_{z^2} orbital with the

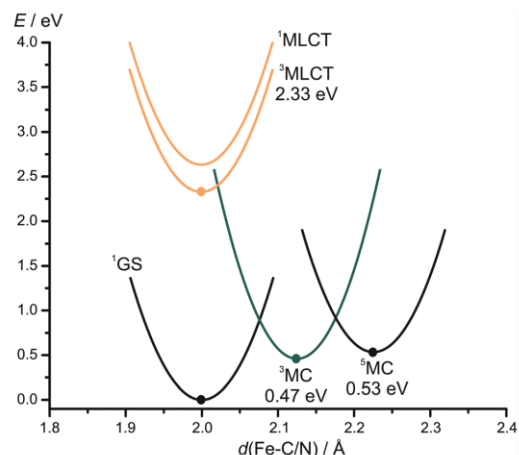


Fig. 2 Summary of the quantum chemically calculated energetics of 1^{2+} as obtained from DFT calculations () or experimental data ($^1\text{MLCT}$), with parabolic energy surfaces sketched qualitatively as visual guides for discussion purposes.

z -axis experiencing the weakest ligand field strength. In the ^5MC high spin-state, all Fe–C/N distances are elongated due to the population of the d_{z^2} and $d_{x^2-y^2}$ orbitals. The large distortions impose a reorganisation barrier between the nearly degenerate ^3MC and ^5MC states. This substantiates the interpretation that the ^5MC state is by-passed and that the ^3MC state undergoes ISC to the ground state. Attempts to optimise the $^3\text{MLCT}$ state by DFT without constraints were unsuccessful as all optimisation attempts converged to the ^3MC state. By constraining all Fe–C/N bond distances to 1.9 Å, convergence to a $^3\text{MLCT}$ state with spin density at the iron and a pyridine ring and an energy of 2.33 eV (532 nm) was achieved. This estimated $^3\text{MLCT}$ energy is consistent with the experimental $^1\text{MLCT}$ state energy of 2.48 eV (500 nm). Assuming that all MLCT states are rather nested with the ground state,¹⁹ population transfer from the $^1\text{MLCT}$ states to the ^3MC state is burdened with a reorganisation energy. In combination with the comparably high ^3MC energy, this barrier accounts for the high $^3\text{MLCT}$ lifetime of 1^{2+} of 9.2 ps. Such a high lifetime of a $^3\text{MLCT}$ state in iron(II) complexes has been only realised so far using four carbene donors instead of only two in 1^{2+} .^{16,17}

Emission from the $^3\text{MLCT}$ state after excitation of 1^{2+} at 413 or 500 nm at room temperature in MeCN or at 77 K in a frozen $^n\text{PrCN}$ glass was not observed indicating that the $^3\text{MLCT}$ – ^3MC barrier can efficiently be overcome even at 77 K.

Carbenes also stabilise low-spin iron(III) and $^2\text{LMCT}$ states of iron(III) complexes can be photoactive.^{30,38} Consequently, emission of the iron(III) complex 1^{3+} , prepared *in situ* by oxidation of 1^{2+} with $[\text{NO}][\text{PF}_6]$, was probed by exciting at 524 and 609 nm at room temperature and at 77 K. However, no $^2\text{LMCT}$ fluorescence of 1^{3+} was detected with our instrument.

The iron(II) complex $[\text{Fe}(\text{dpmi})_2]^{2+}$ 1^{2+} with a two carbene/four pyridine $[\text{C}_2\text{N}_4]$ donor set and a high octahedral symmetry enabled by six-membered chelate rings in a rigid environment



Communication

exhibits a high ³MLCT lifetime of 9.2 ps. This value compares to lifetimes of iron(II) complexes with a four carbene/two pyridine [C₄N₂] donor set in a more distorted environment with five-membered chelate rings. This observation validates the high symmetry concept to increase the energy of MC states by a better metal–ligand orbital overlap. Deactivation of the ³MLCT state of **1**²⁺ likely occurs *via* the tetragonally distorted ³MC state by-passing the ⁵MC state resembling the photodynamics of classical polypyridine ruthenium(II) complexes.¹⁹ The combination of six-membered chelates and strong σ-donating carbenes paves the way to photoactive, luminescent and solar energy-converting iron(II) complexes with long ³MLCT lifetimes. A future challenge will be the increasingly facile Fe^{II}/Fe^{III} oxidation with a high number of carbene donors and the smaller MLCT extinction coefficient in all-carbene complexes lacking π-accepting ligands.^{20,30,37}

TR performed the synthesis, ground state characterisation and the DFT calculations. AK and SL measured and interpreted the TA data. RS and MB measured and interpreted the XAS data. KH designed and supervised the project, analysed the data and wrote the manuscript.

Financial support from the Deutsche Forschungsgemeinschaft [Priority Program SPP 2102 “Light-controlled reactivity of metal complexes” (HE 2778/14-1, BA 4467/7-1, LO 714/11-1)] is gratefully acknowledged. Parts of this research were conducted using the supercomputers MOGON and Elwetritsch and advisory services offered by Johannes Gutenberg university Mainz (<http://www.hpc.uni-mainz.de>) and TU Kaiserslautern (<https://elwe.rhrk.uni-kl.de>), which are members of the AHRP. PETRA III is kindly acknowledged for provision of beamtime at beamline P65.

Conflicts of interest

There are no conflicts to declare.

Notes and references

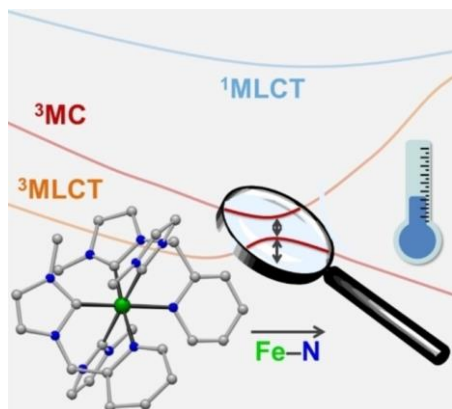
- C. Förster and K. Heinze, *Chem. Soc. Rev.*, 2020, **49**, 1057.
- O. S. Wenger, *J. Am. Chem. Soc.*, 2018, **140**(42), 13522.
- C. Bizzarri, E. Spuling, D. M. Knoll, D. Volz and S. Bräse, *Coord. Chem. Rev.*, 2018, **373**, 49.
- B. M. Hockin, C. Li, N. Robertson and E. Zysman-Colman, *Catal. Sci. Technol.*, 2019, **9**, 889.
- O. S. Wenger, *Chem. – Eur. J.*, 2019, **25**, 6043.
- Y. Liu, P. Persson, V. Sundström and K. Wärnmark, *Acc. Chem. Res.*, 2016, **49**, 1477.
- S. Kauffhold and K. Wärnmark, *Catalysts*, 2020, **10**, 132.
- B. C. Paulus, S. L. Adelman, L. L. Jamula and J. K. McCusker, *Nature*, 2020, **582**, 214.
- J. K. McCusker, *Science*, 2019, **363**, 484.
- S. Campagna, F. Puntoriero, F. Nastasi, G. Bergamini and V. Balzani, *Photochemistry and Photophysics of Coordination Compounds: ruthenium*, *Topics in Current Chemistry*, Springer, Berlin, Heidelberg, 2007, vol. 280, p. 117.
- L. Flamigni, A. Barbieri, C. Sabatini, B. Ventura and F. Barigelli, *Photochemistry and Photophysics of Coordination Compounds: iridium*, *Topics in Current Chemistry*, Springer, Berlin, Heidelberg, 2007, vol. 281, p. 143.
- L. L. Jamula, A. M. Brown, D. Guo and J. K. McCusker, *Inorg. Chem.*, 2014, **53**, 15.
- A. K. C. Mengel, C. Förster, A. Breivogel, K. Mack, J. R. Ochsmann, F. Laquai, V. Ksenofontov and K. Heinze, *Chem. – Eur. J.*, 2015, **21**, 704.
- A. K. C. Mengel, C. Bissinger, M. Dorn, O. Back, C. Förster and K. Heinze, *Chem. – Eur. J.*, 2017, **23**, 7920.
- M. Darari, E. Domenichini, A. Francés-Monerris, C. Cebrián, K. Magra, M. Beley, M. Pastore, A. Monari, X. Assfeld, S. Haacke and P. C. Gros, *Dalton Trans.*, 2019, **48**, 10915.
- Y. Liu, T. C. B. Harlang, S. E. Canton, P. Chábera, K. Suárez-Alcántara, A. Fleckhaus, D. A. Vithanage, E. Göransson, A. Corani, R. Lomoth, V. Sundström and K. Wärnmark, *Chem. Commun.*, 2013, **49**, 6412.
- P. Zimmer, L. Burkhardt, A. Friedrich, J. Steube, A. Neuba, R. Schepper, P. Müller, U. Flörke, M. Huber, S. Lochbrunner and M. Bauer, *Inorg. Chem.*, 2018, **57**, 360.
- T. Harlang, Y. Liu, O. Gordivska, L. Fredin, C. Fonseca Jr., P. Huang, P. Chábera, K. Kjær, H. Mateos, J. Uhlig, R. Lomoth, R. Wallenberg, S. Styring, P. Persson, V. Sundström and K. Wärnmark, *Nat. Chem.*, 2015, **7**, 883.
- L. A. Fredin, M. Pápai, E. Rozsályi, G. Vanko, K. Wärnmark, V. Sundström and P. Persson, *J. Phys. Chem. Lett.*, 2014, **5**, 2066.
- P. Chábera, K. Kjær, O. Prakash, A. Honarfar, Y. Liu, L. Fredin, T. Harlang, S. Lidin, J. Uhlig, V. Sundström, R. Lomoth, P. Persson and K. Wärnmark, *J. Phys. Chem. Lett.*, 2018, **9**, 459.
- M. Abrahamsson, M. Jäger, T. Österman, L. Eriksson, P. Persson, H.-C. Becker, O. Johansson and L. Hammarström, *J. Am. Chem. Soc.*, 2006, **128**, 12616.
- M. Abrahamsson, H.-C. Becker, L. Hammarström, C. Bonnefous, C. Chamchouis and R. P. Thummel, *Inorg. Chem.*, 2007, **46**, 10354.
- M. Abrahamsson, M. Jäger, R. J. Kumar, T. Österman, P. Persson, H.-C. Becker, O. Johansson and L. Hammarström, *J. Am. Chem. Soc.*, 2008, **130**, 15533.
- A. Breivogel, C. Förster and K. Heinze, *Inorg. Chem.*, 2010, **49**, 7052.
- A. Breivogel, M. Meister, C. Förster, F. Laquai and K. Heinze, *Chem. – Eur. J.*, 2013, **19**, 13745.
- M. Dorn, J. Kalmbach, P. Boden, A. Pápcke, S. Gómez, C. Förster, F. Kuczelinis, L. M. Carrella, L. Büldt, N. Bings, E. Rentschler, S. Lochbrunner, L. González, M. Gerhards, M. Seitz and K. Heinze, *J. Am. Chem. Soc.*, 2020, **142**, 7947.
- S. Treiling, C. Wang, C. Förster, F. Reichenauer, J. Kalmbach, P. Boden, J. P. Harris, L. Carrella, E. Rentschler, U. Resch-Genger, C. Reber, M. Seitz, M. Gerhards and K. Heinze, *Angew. Chem., Int. Ed.*, 2019, **58**, 18075.
- S. Otto, M. Grabolle, C. Förster, C. Kreitner, U. Resch-Genger and K. Heinze, *Angew. Chem., Int. Ed.*, 2015, **54**, 11572.
- J. P. Harris, C. Reber, H. E. Colmer, T. A. Jackson, A. P. Forshaw, J. M. Smith, R. A. Kinney and J. Telser, *Can. J. Chem.*, 2020, **98**, 250.
- K. S. Kjær, N. Kaul, O. Prakash, P. Chábera, N. W. Rosemann, A. Honarfar, O. Gordivska, L. A. Fredin, K.-E. Bergquist, L. Häggström, T. Ericsson, L. Lindh, A. Yartsev, S. Styring, P. Huang, J. Uhlig, J. Bendix, D. Strand, V. Sundström, P. Persson, R. Lomoth and K. Wärnmark, *Science*, 2019, **363**, 249.
- M. Darari, A. Francés-Monerris, B. Marekha, A. Doudouh, E. Wenger, A. Monari, S. Haacke and P. C. Gros, *Molecules*, 2020, **25**, 5991.
- V. Tran, K. E. Allen, M. Garcia Chavez, C. Aaron, J. J. Dumais, J. T. York and E. C. Brown, *Polyhedron*, 2018, **147**, 131.
- G. Vankó, T. Neisius, G. Molnár, F. Renz, S. Kárpáti, A. Shukla and F. M. F. de Groot, *J. Phys. Chem. B*, 2006, **110**, 11647.
- F. Plasser, *J. Chem. Phys.*, 2020, **152**, 084108.
- A. M. Brown, C. E. McCusker and J. K. McCusker, *Dalton Trans.*, 2014, **43**, 17635.
- J. K. McCusker, A. L. Rheingold and D. N. Hendrickson, *Inorg. Chem.*, 1996, **35**, 2100.
- A. Hauser, C. Enachescu, M. L. Daku, A. Vargas and N. Amstutz, *Coord. Chem. Rev.*, 2006, **250**, 1642.
- P. Chábera, Y. Liu, O. Prakash, E. Thyraug, A. El Nahhas, A. Honarfar, S. Essén, L. A. Fredin, T. C. B. Harlang, K. S. Kjær, K. Handrup, F. Ericson, H. Tatsuno, K. Morgan, J. Schnadt, L. Häggström, T. Ericsson, A. Sobkowiak, S. Lidin, P. Huang, S. Styring, J. Uhlig, J. Bendix, R. Lomoth, V. Sundström, P. Persson and K. Wärnmark, *Nature*, 2017, **543**, 695.



3.3 A Tetracarbene Iron(II) Complex with a Long-lived Triplet Metal-to-Ligand Charge Transfer State due to a Triplet-Triplet Barrier

Thomas Reuter, Dimitri Zorn, Robert Nauman, Jan Klett, Christoph Förster, Katja Heinze

Angew. Chem. Int. Ed. **2024**, 63, e202406438



This article reports on the synthesis and characterization of the homoleptic complexes *trans*- and *cis*- [Fe(pdmi)₂]²⁺ (pdmi = 2-(bis-(3-methyl-2,3-dihydro-1H-imidazol-1-yl)-methyl)pyridine). The complexes show an extended lifetime of the excited ³MLCT state of approx. 15 ps in acetonitrile. Variable temperature TA measurements reveal an energy barrier between the excited ³MLCT and ³MC states for the *cis*-isomer which is analysed using semi-classical Marcus theory.

Author contribution

Synthesis and characterization of the title compounds as well as DFT calculations were carried out by Thomas Reuter. The purification of the title compounds *via* HPLC was performed by Dimitri Zorn. TA and variable temperature TA measurements, as well as emission spectroscopy was carried out by Dr. Robert Naumann. Raman spectra were measured by Dr. Jan Klett. Dr. Christoph Förster solved the crystal structure of the title compounds. The manuscript was written by Prof. Dr. Katja Heinze (90 %) and Thomas Reuter (10 %).

Supporting Information

Can be found at pp. 137.

The full supporting information can be obtained [here](#).

“Reprinted with permission from Thomas Reuter, Dimitri Zorn, Robert Naumann, Christoph Förster and Katja Heinze. Copyright 2024 Wiley”

Photosensitizers

A Tetracarbene Iron(II) Complex with a Long-lived Triplet Metal-to-Ligand Charge Transfer State due to a Triplet-Triplet Barrier

Thomas Reuter, Dimitri Zorn, Robert Naumann, Jan Klett, Christoph Förster, and Katja Heinze*

Abstract: Mixed N-heterocyclic carbene (NHC) / pyridyl iron(II) complexes have attracted a great deal of attention recently because of their potential as photocatalysts and light sensitizers made from Earth-abundant elements. The most decisive challenge for their successful implementation is the lifetime of the lowest triplet metal-to-ligand charge transfer state ($^3\text{MLCT}$), which typically decays via a triplet metal-centered (^3MC) state back to the ground state. We reveal by variable-temperature ultrafast transient absorption spectroscopy that the tripodal iron(II) bis(pyridine) complex isomers *trans*- and *cis*-[Fe(pdmi) $_2$] $^{2+}$ with four NHC donors show $^3\text{MLCT} \rightarrow ^3\text{MC}$ population transfers with very different barriers and rationalize this by computational means. While *trans*-[Fe(pdmi) $_2$] $^{2+}$ possesses an unobservable activation barrier, the *cis* isomer exhibits a barrier of 492 cm^{-1} , which leads to a nanosecond $^3\text{MLCT}$ lifetime at 77 K. The kinetic and quantum chemical data were analyzed in the context of semi-classical Marcus theory revealing a high reorganization energy and small electronic coupling between the two triplet states. This highlights the importance of detailed structural control and kinetic knowledge for the rational design of photosensitizers from first row transition metals such as iron.

(MLCT) states are often well characterized by (ultrafast) optical transient absorption (TA) spectroscopy thanks to their characteristic absorption bands pertaining to a ligand radical anion^[5] and an oxidized metal center, the largely photoinactive MC states are challenging to identify by TA spectroscopy. In selected cases, ultrafast X-ray spectroscopies at XFELs (X-Ray Free-Electron Lasers) can fill this knowledge gap provided that suitable model complexes for intermediate states are available.^[6] Femto-second transient mid-IR spectroscopy has been recently used to disentangle triplet and quintet metal centered states (^3MC and ^5MC) of iron(II) complexes.^[7] The dynamics of the classical polypyridine complex [Fe(bpy) $_3$] $^{2+}$ follows a sequential model $^3\text{MLCT} \rightarrow ^3\text{MC} \rightarrow ^5\text{MC}$ on a sub-picosecond time scale before decaying to the singlet ground state ^1GS on longer times scales (bpy = 2,2'-bipyridine, Figure 1).^[6] The $^5\text{MC} \rightarrow ^1\text{GS}$ spin-crossover of [Fe(bpy) $_3$] $^{2+}$ has been probed by variable-temperature (VT) TA spectroscopy by McCusker giving an activation barrier $E_a = 310 \text{ cm}^{-1}$ and a very small electronic coupling constant $H_{ab} = 4.3 \text{ cm}^{-1}$ due to the spin change of $\Delta S = 2$.^[8] In polycarbene iron(II) complexes the ^5MC state is often too high in energy to be populated and hence the dynamics can be described by a

1. Introduction

Controlling the interplay between charge transfer (CT) and metal-centered (MC) excited states constitutes an essential ingredient to the development of 3d metal complex luminophores and photoredox catalysts, in particular with iron as the most abundant transition metal.^[1–4] While the photoactive metal-to-ligand charge transfer

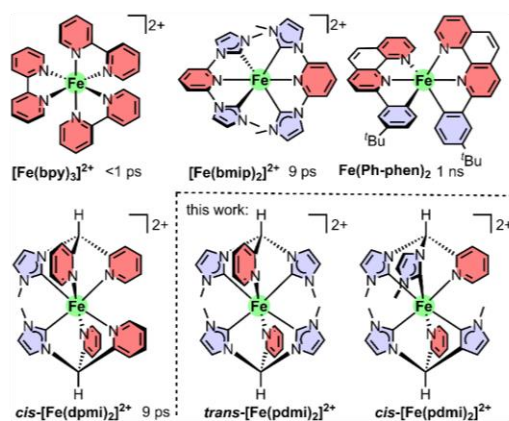


Figure 1. Molecular structures of selected pyridine iron(II) complexes with their $^3\text{MLCT}$ lifetimes at room temperature and the isomeric tetracarbene iron(II) complexes *trans*- and *cis*-[Fe(pdmi) $_2$] $^{2+}$ designed and examined in this work.

* T. Reuter, D. Zorn, Dr. R. Naumann, Dr. J. Klett, Dr. C. Förster, Prof. Dr. K. Heinze
Department of Chemistry
Johannes Gutenberg University Mainz
Duesbergweg 10–14, 55128 Mainz, Germany
E-mail: katja.heinze@uni-mainz.de

© 2024 The Authors. Angewandte Chemie International Edition published by Wiley-VCH GmbH. This is an open access article under the terms of the Creative Commons Attribution License, which permits use, distribution and reproduction in any medium, provided the original work is properly cited.

three-state model as $^3\text{MLCT} \rightarrow ^3\text{MC} \rightarrow ^1\text{GS}$ after an ultrafast intersystem crossing (ISC) from the $^1\text{MLCT}$ state. Yet, branching can occur from hot $^3\text{MLCT}$ or $^1\text{MLCT}$ states to the cold $^3\text{MLCT}$ and ^3MC states.^[9,10] In *Wärnmark's* seminal tetracarbene photosensitizer $[\text{Fe}(\text{bmip})_2]^{2+}$ the $^3\text{MLCT} \rightarrow ^3\text{MC}$ population transfer occurs with a time constant of 9 ps^[11] according to ultrafast X-ray spectroscopies (bmip = 2,6-bis(3-methylimidazole-1-ylidene)pyridine, Figure 1).^[12] VT-TA spectroscopic experiments, which do not rely on XFELs, were not yet performed for iron(II) complexes with extended lifetimes, such as polycarbene iron(II) complexes, to access the decisive $^3\text{MLCT} \rightarrow ^3\text{MC}$ barrier for the $^3\text{MLCT}$ lifetime, although this “would be of highest interest”.^[13]

The number of NHCs in polypyridine iron(II) complexes with meridional coordinating tridentate ligands contributes to the $^3\text{MLCT}$ lifetime enhancement,^[14] implying that an additive ligand field,^[15,16] which determines the ^3MC state energy, can be assumed in this series. Electron withdrawing substituents at the pyridine or replacement of the pyridine by electron-deficient pyrazine or pyrimidine boost the lifetime of derivatives of $[\text{Fe}(\text{bmip})_2]^{2+}$ to 26 ps and even 32 ps by lowering the MLCT state energies.^[17,18] A tripodal coordination motif in $\text{cis-}[\text{Fe}(\text{dpmi})_2]^{2+}$ instead of the meridional motif achieves a 9 ps $^3\text{MLCT}$ lifetime already with two NHCs instead of four in $[\text{Fe}(\text{bmip})_2]^{2+}$ (dpmi = di(pyridine-2-yl)(3-methylimidazol-2-yl)methane, Figure 1).^[19] Tris(bidentate) carbene/pyridine complexes $[\text{Fe}(\text{C}^{\wedge}\text{N})_3]^{2+}$ possess $^3\text{MLCT}$ lifetimes of 3–20 ps with *facial* isomers featuring the longer lifetimes. This difference between *fac* and *mer* isomers shows that a simple additive ligand field is not a sufficient descriptor for the excited state dynamics.^[20] Rather *trans* effects^[21] might influence the excited state dynamics. The hexacarbene complex $[\text{Fe}(\text{btz})_3]^{2+}$ displays the highest $^3\text{MLCT}$ lifetime (528 ps) of a carbene iron(II) complex so far (btz = 3,3'-dimethyl-1,1'-bis(*p*-tolyl)-4,4'-bis(1,2,3-triazol-5-ylidene)).^[22] Dixon and co-workers had computationally investigated the relative $^3\text{MLCT}/^3\text{MC}$ energy levels in iron(II) complexes with tridentate phenylbipyridine ligands. The ^3MC state is destabilized when *trans*-N–Fe–C arrangements dominate, i.e. not only the number, but also the coordination site of the phenyl σ -donor determines the ^3MC state energies.^[23,24] This prediction was experimentally confirmed with the luminescent bis(cyclometalated) complex $\text{Fe}(\text{Ph-phen})_2$ with a $^3\text{MLCT}$ lifetime of 1 ns (H–Ph-phen = 9-phenylphenanthroline, Figure 1).^[25]

Clearly, the number and position of NHCs/pyridines, the octahedrity (X-Fe-Y angles)^[26–30] and the rigidity/flexibility^[31,32] in the excited states play key roles for the (thermally activated) $^3\text{MLCT}$ to ^3MC internal conversion. However, the barrier and the electronic coupling between these triplet states decisive for the excited state dynamics are challenging to identify. *trans*-N–Fe–N coordination^[23,24] with a rather weak average ligand field strength along this axis (z) will become the preferred Jahn–Teller axis in the lowest energy ^3MC state in NHC/pyridine iron(II) complexes. We hypothesize that the ^3MC

state energy will be higher in the absence of an active N–Fe–N Jahn–Teller axis.

In this study, we probe the electronic and dynamic effects of the presence or absence of a weak ligand field axis by means of two designed iron(II) complex isomers with the same average $[\text{FeN}_2\text{C}_4]$ ligand field spanned by two pyridines and four NHCs in a strictly octahedral geometry, but with different arrangements of the nitrogen donors, namely *trans*- and *cis*- $[\text{Fe}(\text{pdmi})_2]^{2+}$ (H_2pdmi = (2-pyridyl)di(3-methylimidazolium-1-yl)methane-bis(hexafluorophosphate); Figure 1).

2. Results and Discussion

2.1. Quantum Chemical Calculations

Geometries and energies of the singlet ground state (^1GS) and the lowest energy triplet and quintet states for both isomers *trans*- and *cis*- $[\text{Fe}(\text{pdmi})_2]^{2+}$ were calculated by quantum chemical methods on the density functional theory level (DFT, B3LYP functional, TZVP basis set, with dispersion and relativistic correction and continuum solvent model; Figures S1–S4; Tables S1–S4).

The key metrics of the iron(II) coordination in the optimized ^1GS and ^3MC states is depicted in Figure 2. The main changes involve the Fe–N bonds, which increase from ca. 2 Å in the ^1GS to 2.445 Å and to 2.518/2.175 Å in the ^3MC states of the *trans* and *cis* isomers, respectively. Energies of the lowest singlet, triplet and quintet states were calculated along the respective Fe–N elongation pathways (Figure 2). The first excited singlet and triplet states were estimated by time-dependent DFT (TDDFT) methods at the respective geometries and plotted in the potential energy diagrams (Figure 2). The $^3\text{MLCT}$ or ^3MC character of the triplet states was identified by inspection of the calculated spin densities.

For both isomers the high-spin state (^5MC) is higher in energy than the ^3MC state, which is typical for carbene iron(II) complexes,^[14,17–19,33] but not for polypyridine iron(II) complexes.^[26–30] At the Franck–Condon geometry, the ^3MC state of the *cis* isomer is higher than the MLCT states, while the ^5MC state of the *trans* isomer is closer to the MLCT states, although the $^{1,3}\text{MLCT}$ states are likely calculated too high in energy. In contrast to the $^1\text{MLCT}$ states at the Franck–Condon geometry, which are delocalized over the iron center and all pyridines (Tables S3 and S4), the spin densities of the $^3\text{MLCT}$ states are confined to the iron center and a single pyridine (Figure 2). Hence, the energies of the relaxed $^3\text{MLCT}$ states of the pyridine iron(II) complexes are rather similar. At short Fe–N distances, the lowest triplet state possesses $^3\text{MLCT}$ character, while at larger distances the ^3MC state rapidly decreases in energy and the ^3MC character dominates the lowest triplet state. Consequently, the ^3MC state crosses the $^3\text{MLCT}$ state. Importantly, the optimized ^3MC state of *cis*- $[\text{Fe}(\text{pdmi})_2]^{2+}$ is at higher energy by 0.36 eV than the optimized ^3MC state of the *trans* isomer (Figure 2). The higher energy ^3MC state arises from the

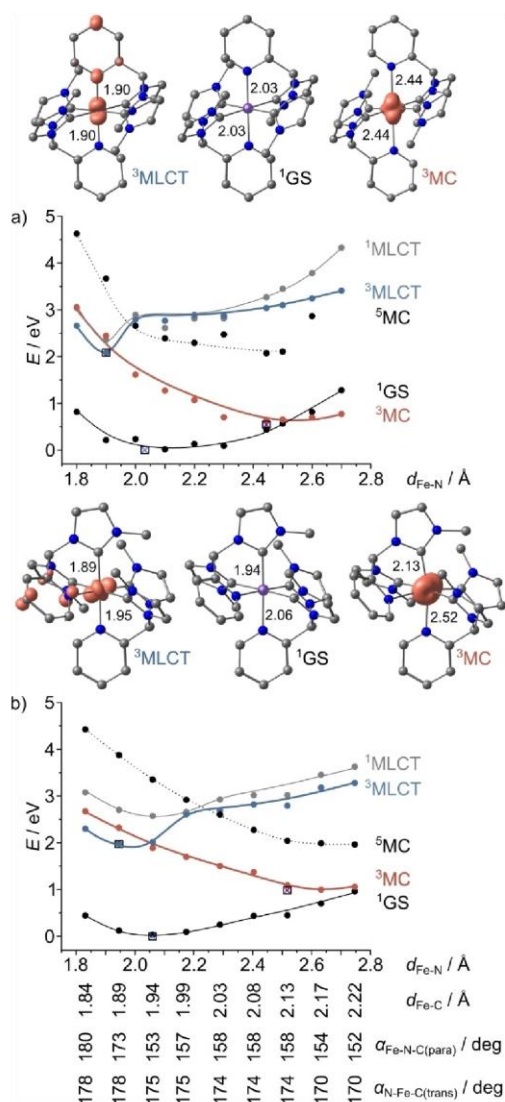


Figure 2. Schematic representation of the potential energy curves estimated by DFT/TDDFT methods of a) *trans*-[Fe(pdmi)₂]²⁺ along the symmetric Fe–N stretching mode and b) *cis*-[Fe(pdmi)₂]²⁺ along a single Fe–N stretching mode. The “diabatic” lines merely serve as a guide to the eye. Geometries with spin densities (orange, isosurface value 0.01 a.u.; H atoms omitted) of the ³MC and ³MLCT states are depicted at the indicated points \square with distances in Å.

presence of only *trans*-N–Fe–C and *trans*-C–Fe–C coordination and the absence of an “easy Jahn–Teller axis” with *trans*-N–Fe–N coordination similar to the computational predictions for cyclometalated complexes.^[23,24] The ³MC energy of the *trans* isomer rapidly decreases along the Jahn–Teller axis, while the ³MC energy gradient is less steep for the *cis* isomer with a *trans*-N–Fe–C easy axis

(Figure 2). This different gradient of the ³MC energies along the Jahn–Teller axes shifts the ³MLCT/³MC crossing point to larger geometric distortions and suggests a higher barrier of the thermally activated ³MLCT→³MC internal conversion for *cis*-[Fe(pdmi)₂]²⁺. These computational predictions will be elaborated experimentally in the following.

2.2. Syntheses, Structures and Redox Chemistry

The pro-ligand [H₂pdmi][PF₆]₂ was prepared from pyridine-2-carbaldehyde and 1,1-carbonyldiimidazole in 41% overall yield (Figures S5–S6). Coordination of the tripodal ligand pdmi to iron(II) at –70 °C, chromatographic workup and recrystallization yielded [Fe(pdmi)₂][PF₆]₂ as orange crystalline material as confirmed by ESI mass spectrometry and elemental analysis (Figure S7). HPLC analysis suggested the presence of *trans* and *cis* isomers in a 4:1 ratio (Figure S8). Preparative HPLC yielded pure *trans*-[Fe(pdmi)₂][PF₆]₂ (Figures S9–S16). Due to low amount of *cis* isomer formed at –70 °C, a high temperature synthesis was developed to increase the proportion of the desired *cis* isomer. This isomer is slightly thermodynamically stabilized according to the DFT calculations with $\Delta G_{298\text{K}} = -5 \text{ kJ mol}^{-1}$. Yet, higher temperature also favors NHC ligand decomposition. Gratifyingly, at 20 °C the *trans*:*cis* ratio increased to 1:2 (Figure S17). HPLC separation yielded pure *cis*-[Fe(pdmi)₂][PF₆]₂ (Figures S18–S22). NMR and IR/Raman spectroscopic data of *trans*-[Fe(pdmi)₂]²⁺ and *cis*-[Fe(pdmi)₂]²⁺ are compatible with the proposed symmetries and the diamagnetic nature (low-spin) of the iron(II) complexes (Figures S10–S11, S14–S16, Figures S19–S24). The structures of the cations were confirmed by SC-XRD (Figures S25–S26).^[34] The DFT calculations reproduce the high octahedricity, the Fe–N/C distances (Tables S1–S2) and the vibrational frequencies and intensities (Figures S23–S24).

Thanks to the strongly σ -donating carbene ligands, the iron(II) complexes are easily oxidized to the respective purple iron(III) complexes by spectroelectrochemistry or by using [NO][PF₆] (Figure S27–S30). The iron(III) complexes show characteristic CT absorption bands at 517/572 nm and 490/529/582/620(sh) nm for *trans*- and *cis*-[Fe(pdmi)₂]³⁺, respectively (Figures S29–S30), similar to the 522/610 nm absorption bands of the bis(carbene) complex *cis*-[Fe(dpmi)₂]³⁺.^[19] The absorption bands of the iron(III) complexes will assist the interpretation of the TA data below.

2.3. Non-Radiative Decay: Steady-State and Time-Resolved Spectroscopy

Both iron(II) isomers display intense ¹MLCT absorption bands in the visible spectral region (Figure 3a, Figures S3–S4). The maxima appear at 521 and 471 nm (7430 and 8680 M⁻¹ cm⁻¹) for *trans*- and *cis*-[Fe(pdmi)₂]²⁺, respec-

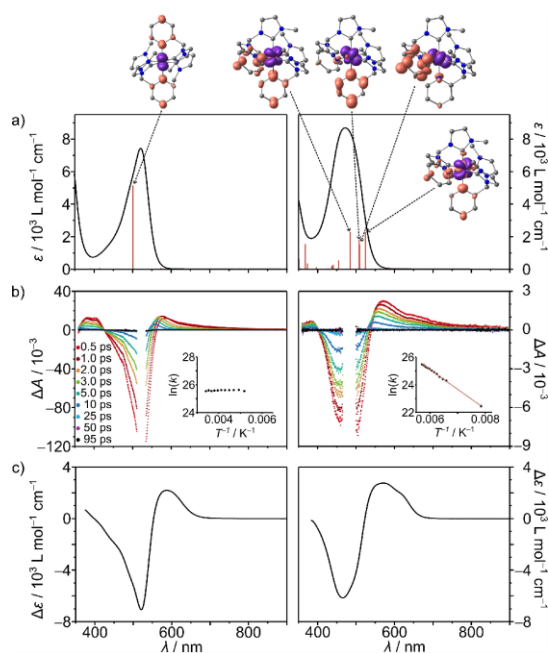


Figure 3. a) Absorption spectra of *trans*-[Fe(pdmi)₂]²⁺ (left) and *cis*-[Fe(pdmi)₂]²⁺ (right) in MeCN at 293 K. DFT calculated singlet transitions shown as sticks (bathochromically shifted by 3600 cm⁻¹). Selected difference densities at 0.006 a.u. (purple = electron density loss, orange = electron density gain; hydrogen atoms omitted). b) fs-TA spectra of *trans*-[Fe(pdmi)₂]²⁺ (left, λ_{exc} = 520 nm) and *cis*-[Fe(pdmi)₂]²⁺ (right, λ_{exc} = 470 nm) in MeOH/EtOH (2:3 v/v) at 293 K. ln(*k*) vs. 1/*T* plot in the insets, with *k* = 1/*τ* of the long-lived component. Arrhenius fit *k* = e^(-E_a/RT) for *cis*-[Fe(pdmi)₂]²⁺ shown in red. c) Difference spectrum between *trans*-[Fe(pdmi)₂]²⁺ and *trans*-[Fe(pdmi)₂]³⁺ (left) and between *cis*-[Fe(pdmi)₂]³⁺ and *cis*-[Fe(pdmi)₂]²⁺ (right) at 293 K in MeCN.

tively, and are characterized by charge shifts from the iron center to the two pyridines (Figure 3a, top). According to TDDFT calculations and charge transfer number analyses (Tables S3–S4, Figures S3–S4), the sharper band of the *trans* complex is assigned to a single transition (Fe→py₂; calcd at 424 nm, with oscillator strength *f* = 0.162), while the broader band of the *cis* isomer is composed of four Fe→py₂ transitions at 413, 429, 430 and 441 nm with similar oscillator strengths (*f* = 0.047, 0.037, 0.031, 0.047). Hence, the TDDFT calculations nicely reproduce the experimental ¹MLCT band shape. According to the calculations, the *trans* and *cis* isomers exhibit additional weak low-energy transitions at 475/470/462/455 (*f* = 0.00152/8.0×10⁻⁹/1.1×10⁻⁸/1.5×10⁻⁸) and 483/468 nm (*f* = 0.00185/0.00058), respectively (Tables S3–S4). The presence of only weakly allowed low-energy ¹MLCT bands will be relevant for the discussion of the radiative decay below.

To probe the excited state dynamics, we employed VT ultrafast TA spectroscopy (Figures S31–S63). fs-TA spec-

tra of both iron(II) complexes were recorded at 293 K in MeOH/EtOH (2:3 v/v) (Figure 3b, Figures S31–S32). In both cases, the ground state bleach (GSB) fits to the respective (negative) ¹MLCT absorption band suggesting only weak excited state absorptions (ESAs) in this spectral region (Figure 3). Low-energy ESA at 570/585 nm (hot, i.e. <0.5 ps) and 555/545 nm (thermally relaxed) is apparent for the *trans/cis* isomers. These ESAs fit to the absorption bands of the respective iron(III) complexes (Figure 3c, Figures S29–S30). This match suggests an iron(III) character of the excited states supporting the MLCT nature as typically observed for NHC iron(II) complexes.^[11,13,14,17–20,32,33] The ESAs around 400 nm can be assigned to the signature of pyridine radical anions with electron withdrawing substituents.^[5] This fits to the MLCT assignment of this state.^[35] The TDDFT calculated absorption bands of the ³MLCT state matching with the TA spectra (Figures S62–S63) and the solvent dependence of the dynamics (Figures S31–S32, S60–S61) further confirm the ³MLCT assignment. Consequently, the ³MC→¹GS ISC occurs directly without a measurable barrier in both cases. The parallel ESA decay and GS recovery without accumulation of intermediate states confirm that only a single reaction dominates the dynamics in the ³MLCT→³MC→¹GS sequence. This is also suggested by the DFT calculations (Figure 2).

The ³MLCT lifetimes of the *trans* and *cis* isomers at 293 K amount to τ_{293K}(*trans*) = 8.0/14.5 ps and τ_{293K}(*cis*) = 8.6/15.2 ps MeOH/EtOH (2:3 v/v) and MeCN, respectively (Figures S31–S32/S60–S61). Conversely, ³MLCT lifetimes of a bis(cyanido) macrocyclic iron(II) complex are longer in MeOH than in MeCN, which might be explained by distinct Lewis acid/Lewis base interactions of the solvent with the coordinated cyanide.^[31] The values for [Fe(pdmi)₂]²⁺ are similar to the 9 ps ³MLCT lifetime of the bis(carbene) complex *cis*-[Fe(dpml)₂]²⁺ in spite of the larger average ligand field imposed by four carbenes.^[19] The different excited state dynamics of *cis*-[Fe(pdmi)₂]²⁺ as compared to the *trans* isomer reveals itself at lower temperature.

VT-TA spectroscopy for *trans*-[Fe(pdmi)₂]²⁺ between 293 and 193 K in fluid MeOH/EtOH solution shows no change in the lifetime, hence no activation barrier is observable (Figure 3b, left inset; Figures S33–S44). On the other hand, the VT-TA data of *cis*-[Fe(pdmi)₂]²⁺ reveal an Arrhenius-like behavior with an activation barrier *E*_a = 492 cm⁻¹ and a pre-exponential factor *A* = 1.35×10¹² s⁻¹ (Figure 3b, right inset; Figures S45–S56). The larger barrier for the *cis* than for the *trans* isomer agrees with the DFT model (Figure 2). Expectedly, the barrier of *cis*-[Fe(pdmi)₂]²⁺ is much smaller than the barrier of 3800 cm⁻¹ in the 4d metal complex [Ru(bpy)₃]²⁺ obtained by VT-luminescence lifetime measurements.^[36–38] At 130 K in the viscous MeOH/EtOH mixture, the ³MLCT lifetime of the *cis* isomer even increases to τ_{130K}(*cis*) = 177 ps (Figure S57).

In the following, the Arrhenius data of *cis*-[Fe(pdmi)₂]²⁺ are discussed in the picture of semi-classical Marcus theory using harmonic potentials, although this

might be an oversimplification in light of the anharmonic potentials calculated by DFT (Figure 2).^[8] E_a is connected to the reorganization energy λ and the driving force ΔG_0 by eq. 1.^[8]

$$E_a = \frac{(\Delta G_0 + \lambda)^2}{4\lambda} \quad (1)$$

$$A = \frac{2\pi}{\hbar} \frac{|H_{ab}^2|}{\sqrt{4\pi\lambda k_B T}} \quad (2)$$

As the driving force ΔG_0 is unknown experimentally, we estimate $\Delta G_0 = -(1.929 - 0.985) \text{ eV} = -7620 \pm 1000 \text{ cm}^{-1}$ from DFT derived energies of the $^3\text{MLCT}$ and ^3MC states (Figure 2). Solving the quadratic relationship for the reorganization energy gives $\lambda_1 = 12720 \pm 1250 \text{ cm}^{-1}$ and $\lambda_2 = 4570 \pm 750 \text{ cm}^{-1}$, respectively. The lower value for the reorganization energy (λ_2) is discarded on the basis of the DFT calculations predicting a large energy difference (17290 cm^{-1}) between the ^3MC and $^3\text{MLCT}$ electronic structures at the ^3MC geometry. The substantial reorganization energy of $\lambda_1 = 12720 \text{ cm}^{-1}$ arises from the large displacement of the ^3MC potential curve along the Fe–N distortional axis (from ca. 2.0 to ca. 2.5 Å, Figure 2b). From the connection of the Arrhenius factor A with the electronic coupling H_{ab} by eq. 2, we estimate $H_{ab} = 81 \pm 6 \text{ cm}^{-1}$ for the $^3\text{MLCT} \rightarrow ^3\text{MC}$ internal conversion.

We discuss this unprecedented value of H_{ab} for a $^3\text{MLCT}$ to ^3MC reaction path of an iron(II) complex in comparison to the spin-crossover ($^3\text{MC} \rightarrow ^1\text{GS}$) process of $[\text{Fe}(\text{bpy})_3]^{2+}$ and $\text{M}^{3+}/\text{M}^{2+}$ electron self-exchange reactions of iron and ruthenium complexes. Due to the second-order nature of the spin-crossover process, the electronic coupling between ^3MC and ^1GS is with $H_{ab} = 4.3 \text{ cm}^{-1}$ very small.^[8] In the present case of $^3\text{MLCT}/^3\text{MC}$ coupling, no spin change is involved, so that a larger H_{ab} is plausible. The observed electronic coupling is somewhat larger than that for the $[\text{Fe}(\text{H}_2\text{O})_6]^{3+/2+}$ self-exchange reaction ($H_{ab} = 30 \text{ cm}^{-1}$ at an Fe–Fe distance of 6.36 Å),^[39,40] but smaller than for $\text{Ru}^{3+/2+}$ self-exchange reactions at even larger distances ($H_{ab} = 100/145 \text{ cm}^{-1}$, 10.5/13.3 Å).^[39,41,42] Considering the short electron transfer distance for the $^3\text{MLCT} \rightarrow ^3\text{MC}$ transition, which can formally be described by a charge shift from the π^* orbital of the pyridine to the $3d_{z^2}$ orbital of iron^[43] with a ring center to iron distance of ca. 3.3 Å, the value $H_{ab} = 81 \pm 6 \text{ cm}^{-1}$ appears rather small.

A closer look at the symmetries of the involved wave functions of the $^3\text{MLCT} \rightarrow ^3\text{MC}$ internal conversion and the spin densities (Figure 2b) of the $^3\text{MLCT}$ and ^3MC states is instructive (Figure 4). The pyridine π^* and the iron $3d_{z^2}$ orbital are close to orthogonal. This orthogonality should lead to a vanishing electronic coupling $H_{ab} \rightarrow 0$. However, in the ^3MC state, the pyridine is tilted with a Fe–N–C_{para} angle of 158° in addition to the Fe–N elongation and a small N–Fe–C(trans) angle compression from 178° to 174° (Figures 3 and 4).

The tilting of the ligand and the decrease of the N–Fe–C(trans) angle, which is already apparent at the $^3\text{MLCT}/^3\text{MC}$ crossing point (Figure 2b), leads to overlap of

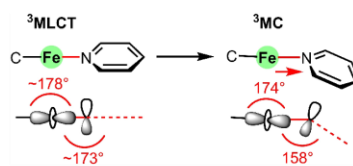


Figure 4. Schematic description of the modes determining the $^3\text{MLCT} \rightarrow ^3\text{MC}$ transition including the relevant orbitals, which affect the electronic coupling H_{ab} .

the pyridine π^* and the iron $3d_{z^2}$ orbitals as schematically illustrated in Figure 4. This overlap enables vibronic coupling^[44–46] along this mode. In rigid matrices, tilting and hence the coupling might be reduced. Consequently, we measured the $^3\text{MLCT}$ lifetime of the *cis* isomer in a frozen MeOH/EtOH mixture at 77 K. Indeed, the $^3\text{MLCT}$ lifetime increases to the nanosecond range with $\tau_{77\text{K}}(\text{cis}) = 1.67 \text{ ns}$ (Figures S58–S59).

With the above interpretation of the $^3\text{MLCT}$ to ^3MC population transfer in the framework of Marcus theory, the parameters to raise the activation barrier for this detrimental process are the driving force ΔG_0 , the reorganization energy λ and the electronic coupling H_{ab} . So far, the main efforts in the design of iron(II) photoactive complexes were devoted to lowering ΔG_0 by increasing the energy of the ^3MC and/or decreasing the energy of the $^3\text{MLCT}$ states. Here, we suggest λ and H_{ab} as additional decisive parameters. The reorganization energy λ is composed of inner-sphere and outer-sphere components λ_i and λ_o . The inner-sphere reorganization energy λ_i increases by a large nuclear displacement along a specific mode. However, large displacements also lower the energy of the relaxed ^3MC state, which raises ΔG_0 . The outer-sphere reorganization energy λ_o should increase in polar solvents as the $^3\text{MLCT}$ and ^3MC states have large and small dipole moments, respectively. The DFT calculated change in dipole moment amounts to $\Delta\mu = 11 \text{ D}$ for *cis*- $[\text{Fe}(\text{pdmi})_2]^{2+}$. Huge dipole moments have also been measured for the $^1^3\text{MLCT}$ states of $[\text{Fe}(\text{bpy})_3]^{2+}$.^[43] Hence solvent polarity might be a useful parameter. However, polar solvents also stabilize the MLCT states, which counteracts the increase in λ_o . Furthermore solvent effects can even play subtle roles in transitions between MC states, e.g. in the $^5\text{MC} \rightarrow ^1\text{GS}$ spin-crossover.^[47] These considerations on λ make straightforward predictions challenging.

2.4. Radiative Decay

The long $^3\text{MLCT}$ lifetime of *cis*- $[\text{Fe}(\text{pdmi})_2]^{2+}$ at 77 K prompted us to attempt luminescence measurements with MLCT excitation (450 nm cw laser; 450 and 470 nm Xe arc lamp; observation range 475–1600 nm) in frozen MeOH/EtOH solution and in the solid state at 77 K. However, no $^3\text{MLCT}$ luminescence band could be observed with our equipment.

$$\begin{aligned}
 & k_p(\tilde{T}_1^\alpha) \\
 &= \frac{4}{3\hbar^4 c^3} (\Delta E_{TS})^3 \sum_{\gamma} \sum_{m=1}^{\infty} \frac{\langle T_m^\alpha | H_{SO} | S_0 \rangle}{E(S_0) - E(T_m)} \langle T_1^\alpha | M_\gamma | T_m^\alpha \rangle \\
 &+ \sum_{n=0}^{\infty} \frac{\langle S_n | H_{SO} | T_1^\alpha \rangle^*}{E(T_1) - E(S_n)} \langle S_n | M_\gamma | S_0 \rangle \Big|^2
 \end{aligned} \quad (3)$$

This raises the question why the phosphorescence rate $k_p(T_1 \rightarrow S_0)$ of **cis-[Fe(pdmi)]₂²⁺** is so small that no luminescence is observed in spite of the nanosecond lifetime (with $T_1 = {}^3\text{MLCT}$ and $S_0 = {}^1\text{GS}$). Phosphorescence rate constants k_p (eq. 3) rely on intensity borrowing of the T_1 state (${}^3\text{MLCT}$) from S_m states (${}^1\text{MLCT}$'s), which are close in energy, i.e. with small $E(S_m) - E(T_1)$ energy differences. These singlet states should possess high transition dipole moments $\langle S_0 | \sum_j e \vec{r}_j | S_m \rangle$ and a different orbital composition than the T_1 state to induce spin-orbit coupling $\langle S_m | \hat{H}_{SO} | T_1 \rangle$.^[44–46] Inspection of the lowest energy ${}^1\text{MLCT}$ transitions of **cis-[Fe(pdmi)]₂²⁺** calculated by TDDFT (Table S4) reveals that the lowest energy ${}^1\text{MLCT}$ states, which are close in energy to the ${}^3\text{MLCT}$ state, possess only very small oscillator strengths $f < 0.0016$ and hence small transition dipole moments. Furthermore, their orbital composition is similar to that of the lowest energy ${}^3\text{MLCT}$ state, which prevents large spin-orbit coupling. Overall, the presence of these low-energy, low-intensity ${}^1\text{MLCT}$ states might explain the absence of luminescence of **cis-[Fe(pdmi)]₂²⁺** in spite of the long ${}^3\text{MLCT}$ lifetime. Long lived but dark ${}^3\text{MLCT}$ states of iron(II) complexes had been reported before in a few cases, yet this discrepancy was not discussed before.^[22,31]

3. Conclusion

For the tetracarbenic pyridine iron(II) complex **cis-[Fe(pdmi)]₂²⁺** variable temperature transient absorption (VT-TA) spectroscopic measurements revealed an activation barrier of 492 cm⁻¹ for the ${}^3\text{MLCT} \rightarrow {}^3\text{MC}$ internal conversion leading to a nanosecond ${}^3\text{MLCT}$ lifetime at 77 K. The so far essentially neglected parameter of the excited state decay of iron(II) sensitizers, the electronic coupling of the ${}^3\text{MLCT}$ and ${}^3\text{MC}$ states H_{ab} , has been estimated for the first time and an iron-pyridine bending mode is suggested to vibronically couple these triplet states. Our study demonstrates that VT-TA measurements in conjunction with DFT calculations can reveal important information of the excited state dynamics, which would have been missed with room temperature spectroscopic data only. Reducing H_{ab} might be a viable strategy to retard non-radiative decay of iron(II) sensitizers. This might be achieved by increasing the electron transfer distance in the ${}^3\text{MLCT} \rightarrow {}^3\text{MC}$ conversion and by rigidification of the chromophore. With the new information at hand, we actively strive to achieve high ${}^3\text{MLCT}$ lifetimes of iron(II) sensitizers at higher temperature.

Supporting Information

The Supporting Information contains synthesis and separation procedures, experimental spectroscopic data and quantum chemical data (pdf) including Cartesian coordinates (xyz). The authors have cited additional references within the Supporting Information.^[48–71]

Acknowledgements

The authors acknowledge Dr. Dieter Schollmeyer and Dr. Luca M. Carrella for collection of XRD data and Philipp Sikora for initial experiments concerning ligand synthesis. This work was supported by the Deutsche Forschungsgemeinschaft (Priority Program SPP 2102 “Light-controlled reactivity of metal complexes”, HE 2778/14-2) and through grants INST 247/1018-1 FUGG and INST 247/1082-1 FUGG to KH. Parts of this research were conducted using the supercomputer Elwetritsch and advisory services offered by the RPTU Kaiserslautern-Landau (<https://hpc.rz.rptu.de>) which is a member of the AHRP. Open Access funding enabled and organized by Projekt DEAL.

Conflict of Interest

The authors declare no conflict of interest.

Data Availability Statement

The data that support the findings of this study are available in the supplementary material of this article.

Keywords: iron · carbene ligands · Marcus theory · pyridine ligands · transient absorption spectroscopy

- [1] L. H. M. de Groot, A. Ilic, J. Schwarz, K. Wärnmark, *J. Am. Chem. Soc.* **2023**, *145*, 9369–9388.
- [2] N. Sinha, O. S. Wenger, *J. Am. Chem. Soc.* **2023**, *145*, 4903–4920.
- [3] C. Förster, K. Heinze, *Chem. Soc. Rev.* **2020**, *49*, 1057–1070.
- [4] O. S. Wenger, *Chem. Eur. J.* **2019**, *25*, 6043–6052.
- [5] V. Kalyanaraman, C. N. R. Rao, M. V. George, *J. Chem. Soc. B* **1971**, 2406–2409.
- [6] K. S. Kjær, T. B. Van Driel, T. C. B. Harlang, K. Kunnus, E. Biasin, K. Ledbetter, R. W. Hartsoc, M. E. Reinhard, S. Koroidov, L. Li, M. G. Laursen, F. B. Hansen, P. Vester, M. Christensen, K. Haldrup, M. M. Nielsen, A. O. Dohn, M. I. Pápai, K. B. Møller, P. Chabera, Y. Liu, H. Tatsuno, C. Timm, M. Jarenmark, J. Uhlig, V. Sundström, K. Wärnmark, P. Persson, Z. Németh, D. Sárosiné Szemes, E. Bajnóczy, G. Vankó, R. Alonso-Mori, J. M. Glowina, S. Nelson, M. Sikorski, D. Sokaras, S. E. Canton, H. T. Lemke, K. J. Gaffney, *Chem. Sci.* **2019**, *10*, 5749–5760.
- [7] C. Zahn, M. Pastore, J. L. P. Lustres, P. C. Gros, S. Haacke, K. Heyne, *J. Am. Chem. Soc.* **2024**, *146*, 9347–9355.
- [8] M. C. Carey, S. L. Adelman, J. K. McCusker, *Chem. Sci.* **2019**, *10*, 134–144.

- [9] H. Tatsuno, K. S. Kjær, K. Kunnus, T. C. B. Harlang, C. Timm, M. Guo, P. Chábera, L. A. Fredin, R. W. Hartsock, M. E. Reinhard, S. Koroidov, L. Li, A. A. Cordones, O. Gordivska, O. Prakash, Y. Liu, M. G. Laursen, E. Biasin, F. B. Hansen, P. Vester, M. Christensen, K. Haldrup, Z. Németh, D. Sárosiné Szemes, P. Bajnóczy, G. Vankó, T. B. Van Driel, R. Alonso-Mori, J. M. Glowina, S. Nelson, M. Sikorski, H. T. Lemke, D. Sokaras, S. E. Canton, A. O. Dohn, K. B. Møller, M. M. Nielsen, K. J. Gaffney, K. Wärnmark, V. Sundström, P. Persson, J. Uhlig, *Angew. Chem. Int. Ed.* **2020**, *59*, 364–372.
- [10] F. Hainer, N. Alagna, A. Reddy Marri, T. J. Penfold, P. C. Gros, S. Haacke, T. Backup, *J. Phys. Chem. Lett.* **2021**, *12*, 8560–8565.
- [11] Y. Liu, T. Harlang, S. E. Canton, P. Chábera, K. Suárez-Alcántara, A. Fleckhaus, D. A. Vithanage, E. Göransson, A. Corani, R. Lomoth, V. Sundström, K. Wärnmark, *Chem. Commun.* **2013**, *49*, 6412–6414.
- [12] K. Kunnus, M. Vacher, T. C. B. Harlang, K. S. Kjær, K. Haldrup, E. Biasin, T. B. van Driel, M. Pápai, P. Chábera, Y. Liu, H. Tatsuno, C. Timm, E. Källman, M. Delcey, R. W. Hartsock, M. E. Reinhard, S. Koroidov, M. G. Laursen, F. B. Hansen, P. Vester, M. Christensen, L. Sandberg, Z. Németh, D. S. Szemes, É. Bajnóczy, R. Alonso-Mori, J. M. Glowina, S. Nelson, M. Sikorski, D. Sokaras, H. T. Lemke, S. E. Canton, K. B. Møller, M. M. Nielsen, G. Vankó, K. Wärnmark, V. Sundström, P. Persson, M. Lundberg, J. Uhlig, K. J. Gaffney, *Nat. Commun.* **2020**, *11*, 634.
- [13] C. Cebrián, M. Pastore, A. Monari, X. Assfeld, P. C. Gros, S. Haacke, *ChemPhysChem* **2022**, *23*, e202100659.
- [14] P. Zimmer, L. Burkhardt, A. Friedrich, J. Steube, A. Neuba, R. Schepper, P. Müller, U. Flörke, M. Huber, S. Lochbrunner, M. Bauer, *Inorg. Chem.* **2018**, *57*, 360–373.
- [15] R. J. Deeth, D. L. Foulis, B. J. Williams-Hubbard, *Dalton Trans.* **2003**, 3949–3955.
- [16] J. Glerup, O. Mønsted, C. E. Schäfer, *Inorg. Chem.* **1976**, *15*, 1399–1407.
- [17] L. Liu, T. Duchanois, T. Etienne, A. Monari, M. Beley, X. Assfeld, S. Haacke, P. C. Gros, *Phys. Chem. Chem. Phys.* **2016**, *18*, 12550–12556.
- [18] M. Darari, E. Domenichini, A. Francés-Monerris, C. Cebrián, K. Magra, M. Beley, M. Pastore, A. Monari, X. Assfeld, S. Haacke, P. C. Gros, *Dalton Trans.* **2019**, *48*, 10915–10926.
- [19] T. Reuter, A. Kruse, R. Schoch, S. Lochbrunner, M. Bauer, K. Heinze, *Chem. Commun.* **2021**, *57*, 7541–7544.
- [20] K. Magra, E. Domenichini, A. Francés-Monerris, C. Cebrián, M. Beley, M. Darari, M. Pastore, A. Monari, X. Assfeld, S. Haacke, P. C. Gros, *Inorg. Chem.* **2019**, *58*, 5069–5081.
- [21] B. J. Coe, S. J. Glenwright, *Coord. Chem. Rev.* **2000**, *203*, 5–80.
- [22] P. Chábera, K. S. Kjær, O. Prakash, A. Honarfar, Y. Liu, L. A. Fredin, T. C. B. Harlang, S. Lidin, J. Uhlig, V. Sundström, R. Lomoth, P. Persson, K. Wärnmark, *J. Phys. Chem. Lett.* **2018**, *9*, 459–463.
- [23] I. M. Dixon, S. Khan, F. Alary, M. Boggio-Pasqua, J.-L. Heully, *Dalton Trans.* **2015**, *44*, 13498–13503.
- [24] I. M. Dixon, F. Alary, M. Boggio-Pasqua, J.-L. Heully, *Dalton Trans.* **2014**, *43*, 15898–15905.
- [25] W. Leis, M. A. Argüello Cordero, S. Lochbrunner, H. Schubert, A. Berkefeld, *J. Am. Chem. Soc.* **2022**, *144*, 1169–1173.
- [26] L. L. Jamula, A. M. Brown, D. Guo, J. K. McCusker, *Inorg. Chem.* **2014**, *53*, 15–17.
- [27] A. K. C. Mengel, C. Förster, A. Breivogel, K. Mack, J. R. Ochsmann, F. Laquai, V. Ksenofontov, K. Heinze, *Chem. Eur. J.* **2015**, *21*, 704–714.
- [28] A. K. C. Mengel, C. Bissinger, M. Dorn, O. Back, C. Förster, K. Heinze, *Chem. Eur. J.* **2017**, *23*, 7920–7931.
- [29] A. Britz, W. Gawelda, T. A. Assefa, L. L. Jamula, J. T. Yarranton, A. Galler, D. Khakhulin, M. Diez, M. Harder, G. Doumy, A. M. March, É. Bajnóczy, Z. Németh, M. Pápai, E. Rozsályi, D. Sárosiné Szemes, H. Cho, S. Mukherjee, C. Liu, T. K. Kim, R. W. Schoenlein, S. H. Southworth, L. Young, E. Jakubikova, N. Huse, G. Vankó, C. Bressler, J. K. McCusker, *Inorg. Chem.* **2019**, *58*, 9341–9350.
- [30] J. Moll, R. Naumann, L. Sorge, C. Förster, N. Gessner, L. Burkhardt, N. Ugur, P. Nuernberger, W. Seidel, C. Ramanan, M. Bauer, K. Heinze, *Chem. Eur. J.* **2022**, *28*, e202201858.
- [31] J. T. Malme, R. A. Clendenning, R. Ash, T. Curry, T. Ren, J. Vura-Weis, *J. Am. Chem. Soc.* **2023**, *145*, 6029–6034.
- [32] M. Darari, A. Francés-Monerris, B. Marekha, A. Doudouh, E. Wenger, A. Monari, S. Haacke, P. C. Gros, *Molecules* **2020**, *25*, 5991.
- [33] L. Lindh, P. Chábera, N. W. Rosemann, J. Uhlig, K. Wärnmark, A. Yartsev, V. Sundström, P. Persson, *Catalysts* **2020**, *10*, 315.
- [34] Deposition numbers 2339759 (for *trans*-[Fe(pdmi)₂][PF₆]₂) and 2339759 (for *cis*-[Fe(pdmi)₂][PF₆]₂) contain the supplementary crystallographic data for this paper. These data are provided free of charge by the joint Cambridge Crystallographic Data Centre and Fachinformationszentrum Karlsruhe Access Structures service.
- [35] A. M. Brown, C. E. McCusker, J. K. McCusker, *Dalton Trans.* **2014**, *43*, 17635–17646.
- [36] D. Hernández-Castillo, R. E. P. Nau, M.-A. Schmid, S. Tschierlei, S. Rau, L. González, *Angew. Chem. Int. Ed.* **2023**, *62*, e202308803.
- [37] J. Van Houten, R. J. Watts, *J. Am. Chem. Soc.* **1976**, *98*, 4853–4858.
- [38] J. V. Caspar, T. J. Meyer, *J. Am. Chem. Soc.* **1983**, *105*, 5583–5590.
- [39] E. J. Piechota, G. J. Meyer, *J. Chem. Educ.* **2019**, *96*, 2450–2466.
- [40] M. D. Newton, *Int. J. Quantum Chem.* **1980**, *18*, 363–391.
- [41] J. E. Sutton, H. Taube, *Inorg. Chem.* **1981**, *20*, 3125–3134.
- [42] C. Patoux, J.-P. Launay, M. Beley, S. Chodorowski-Kimmes, J.-P. Collin, S. James, J.-P. Sauvage, *J. Am. Chem. Soc.* **1998**, *120*, 3717–3725.
- [43] A. B. Maurer, G. J. Meyer, *J. Am. Chem. Soc.* **2020**, *142*, 6847–6851.
- [44] a) T. J. Penfold, E. Gindensperger, C. Daniel, C. M. Marian, *Chem. Rev.* **2018**, *118*, 6975–7025; b) A. Steffen, B. Hupp, in *Comprehensive Coordination Chemistry III* (Eds. E. C. Constable, G. Parkin, L. Que Jr), Elsevier **2021**, pp. 466–502.
- [45] G. Baryshnikov, B. Minaev, H. Ågren, *Chem. Rev.* **2017**, *117*, 6500–6537.
- [46] B. Minaev, G. Baryshnikov, H. Ågren, *Phys. Chem. Chem. Phys.* **2014**, *16*, 1719–1758.
- [47] J. N. Miller, J. K. McCusker, *Chem. Sci.* **2020**, *11*, 5191–5204.
- [48] C. Müller, T. Pascher, A. Eriksson, P. Chábera, J. Uhlig, *J. Phys. Chem. A* **2022**, *126*, 4087–4099.
- [49] F. Neese, *WIREs Comput. Mol. Sci.* **2018**, *8*, e1327.
- [50] A. D. Becke, *J. Chem. Phys.* **1993**, *98*, 5648–5652.
- [51] C. Lee, W. Yang, R. G. Parr, *Phys. Rev. B* **1988**, *37*, 785–789.
- [52] B. Miehlich, A. Savin, H. Stoll, H. Preuss, *Chem. Phys. Lett.* **1989**, *157*, 200–206.
- [53] D. A. Pantazis, X.-Y. Chen, C. R. Landis, F. Neese, *J. Chem. Theory Comput.* **2008**, *4*, 908–919.
- [54] F. Weigend, R. Ahlrichs, *Phys. Chem. Chem. Phys.* **2005**, *7*, 3297–3305.
- [55] F. Neese, F. Wennmohs, A. Hansen, U. Becker, *Chem. Phys.* **2009**, *356*, 98–109.
- [56] R. Izsák, F. Neese, *J. Chem. Phys.* **2011**, *135*, 144105.
- [57] S. Miertuš, E. Scrocco, J. Tomasi, *Chem. Phys.* **1981**, *55*, 117–129.
- [58] V. Barone, M. Cossi, *J. Phys. Chem. A* **1998**, *102*, 1995–2001.

- [59] S. Grimme, J. Antony, S. Ehrlich, H. Krieg, *J. Chem. Phys.* **2010**, *132*, 154104.
- [60] S. Grimme, S. Ehrlich, L. Goerigk, *J. Comput. Chem.* **2011**, *32*, 1456–1465.
- [61] S. Mai, F. Plasser, J. Dorn, M. Fumanal, C. Daniel, L. González, *Coord. Chem. Rev.* **2018**, *361*, 74–97.
- [62] F. Plasser, Theodore 2.0, <http://theodore-qc.sourceforge.net>.
- [63] STOE & Cie, X-Area, STOE & Cie GmbH, Darmstadt, Germany.
- [64] R. H. Blessing, *Acta Crystallogr. Sect. A* **1995**, *51*, 33–38.
- [65] A. L. Spek, *Acta Crystallogr. Sect. D* **2009**, *65*, 148–155.
- [66] J. Koziskova, F. Hahn, J. Richter, J. Kožíšek, *Acta Chim. Slov.* **2016**, *9*, 136–140.
- [67] STOE & Cie, X-Area LANA, STOE & Cie GmbH, Darmstadt, Germany.
- [68] G. M. Sheldrick, *Acta Crystallogr. Sect. A* **2015**, *71*, 3–8.
- [69] G. M. Sheldrick, *Acta Crystallogr. Sect. C* **2015**, *71*, 3–8.
- [70] G. M. Sheldrick, *Acta Crystallogr. Sect. A* **2008**, *64*, 112–122.
- [71] C. B. Hübschle, G. M. Sheldrick, B. Dittrich, *J. Appl. Crystallogr.* **2011**, *44*, 1281–1284.

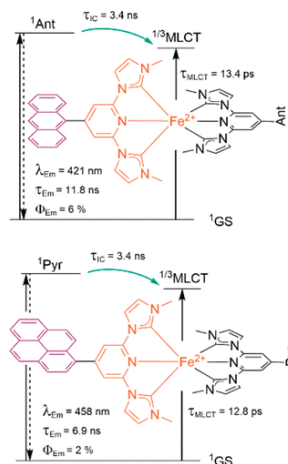
Manuscript received: April 5, 2024

Accepted manuscript online: July 1, 2024

Version of record online: August 23, 2024

3.4 Ground- and Excited-State Properties of Iron(II) Complexes Linked to Organic Chromophores

Philipp Dierks, Ayla Pöpcke, Olga S. Bokareva, Björn Altenburger, Thomas Reuter, Katja Heinze, Oliver Kühn, Stefan Lochbrunner, Matthias Bauer



The article reports on the synthesis and characterization of the homoleptic complexes $[\text{Fe}(\text{bim-ant})_2]^{2+}$ and $[\text{Fe}(\text{bim-pyr})_2]^{2+}$ (bim = 1,1'-(pyridine-2,6-diyl)bis(3-methyl-1*H*-imidazol-3-ylidene); ant = 9-anthracenyl; pyr = 1-pyrenyl). The compounds were investigated towards an antenna effect. Both complexes show luminescence from the singlet excited state of the anthracenyl- and pyrenyl-moiety with a red-shift compared to the non-coordinated anthracene and pyrene.

Author Contribution

Synthesis and characterization of the title compounds was carried out by Philipp Dierks (group of Prof. Dr. Matthias Bauer). Transient absorption spectroscopy was performed by Ayla Pöpcke and Björn Altenburger (group of Prof. Dr. Stefan Lochbrunner). Spectroelectrochemical measurements were carried out by Thomas Reuter and interpretation of the data was performed by Thomas Reuter and Prof. Dr. Katja Heinze. Theoretical calculations were performed by Olga S. Bokareva (group of Prof. Dr. Oliver Kühn).

Supporting Information

Can be found at pp. 195.

The full supporting information can be obtained [here](#).

“Reproduced from Ref.^[133] with permission from ACS Publications.”

Ground- and Excited-State Properties of Iron(II) Complexes Linked to Organic Chromophores

Philipp Dierks, Ayla Pöpcke, Olga S. Bokareva, Björn Altenburger, Thomas Reuter, Katja Heinze, Oliver Kühn, Stefan Lochbrunner, and Matthias Bauer*

Cite This: *Inorg. Chem.* 2020, 59, 14746–14761

Read Online

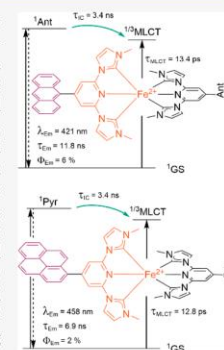
ACCESS |

Metrics & More

Article Recommendations

Supporting Information

ABSTRACT: Two new bichromophoric complexes, $[\text{Fe}(\text{bim-ant})_2]^{2+}$ and $[\text{Fe}(\text{bim-pyr})_2]^{2+}$ ($[\text{H}_2\text{-bim}]^{2+} = 1,1'-(\text{pyridine-2,6-diyl})\text{bis}(3\text{-methyl-1H-imidazol-3-ium})$; ant = 9-anthracenyl; pyr = 1-pyrenyl), are investigated to explore the possibility of tuning the excited-state behavior in photoactive iron(II) complexes to design substitutes for noble-metal compounds. The ground-state properties of both complexes are characterized thoroughly by electrochemical methods and optical absorption spectroscopy, complemented by time-dependent density functional theory calculations. The excited states are investigated by static and time-resolved luminescence and femtosecond transient absorption spectroscopy. Both complexes exhibit room temperature luminescence, which originates from singlet states dominated by the chromophore ($^1\text{Chrom}$). In the cationic pro-ligands and in the iron(II) complexes, the emission is shifted to red by up to 110 nm (5780 cm^{-1}). This offers the possibility of tuning the organic chromophore emission by metal-ion coordination. The fluorescence lifetimes of the complexes are in the nanosecond range, while triplet metal-to-ligand charge-transfer ($^3\text{MLCT}$) lifetimes are around 14 ps. An antenna effect as in ruthenium(II) polypyridine complexes connected to an organic chromophore is found in the form of an internal conversion within 3.4 ns from the $^1\text{Chrom}$ to the $^1\text{MLCT}$ states. Because no singlet oxygen forms from triplet oxygen in the presence of the iron(II) complexes and light, efficient intersystem crossing to the triplet state of the organic chromophore ($^3\text{Chrom}$) is not promoted in the iron(II) complexes.



INTRODUCTION

With the goal of utilizing solar energy in photocatalysis or obtaining new luminescent materials, molecular approaches based on transition-metal complexes are currently intensively investigated.^{1–3} Following efficient absorption of light and the population of active electronically excited states, the lifetimes of these states need to be sufficiently large. Long-lived and high-energy metal-to-ligand charge-transfer (MLCT) states fulfill this requirement and are usually found in complexes of ruthenium(II), iridium(III), osmium(II), and rhenium(I) featuring a $4d^6$ or $5d^6$ electron configuration coordinated by polypyridine ligands with low-energy π^* orbitals, e.g., $[\text{Ru}(\text{bpy})_3]^{2+}$ (bpy = 2,2'-bipyridine).⁴ The basic description of the photoexcitation processes in such complexes is based on the simplified octahedral ligand field, describing the metal-centered (MC) states and low-energy π^* orbitals of the ligands. In an octahedral ligand field, the MC d orbitals split into three orbitals with t_{2g} symmetry and two orbitals with e_g symmetry. The six valence electrons occupy the t_{2g} orbitals because of the strong ligand-field splitting, resulting from the effective metal–ligand interactions in the cases of 4d and 5d metal complexes.⁵ The e_g orbitals remain unoccupied. This leads to a t_{2g}^6 low-spin ground-state configuration. Moreover, the t_{2g} orbitals typically represent the highest occupied molecular orbitals (HOMOs). The unoccupied π^* orbitals of

the polypyridine ligands are higher in energy than the t_{2g} orbitals, but typically lower than the e_g orbitals and represent the lowest unoccupied molecular orbitals (LUMOs) of the complex. Consequently, the lowest electronically excited state has MLCT character. From the singlet ground state (^1GS), the singlet MLCT ($^1\text{MLCT}$) state is initially populated, followed by a rapid intersystem crossing (ISC), which takes place on the femtosecond time scale.⁶ The finally populated triplet MLCT ($^3\text{MLCT}$) states are quite long-lived, often emissive, and able to drive photocatalytic processes.⁷

Recently, efforts to replace scarce elements with base metals or abundant elements^{2,8,9} outgrew their niche existence. In particular, iron,^{3,10,11} copper,^{12,13} zirconium,^{14,15} and molybdenum¹⁶ were identified as promising candidates. Despite many conceptual approaches, no iron(II) complexes with $^3\text{MLCT}$ luminescence have been reported so far. Yet, iron(III) complexes display doublet ligand-to-metal charge-transfer ($^2\text{LMCT}$) fluorescence.^{17–19} Additionally, a few successful

Special Issue: Light-Controlled Reactivity of Metal Complexes

Received: July 9, 2020

Published: September 16, 2020



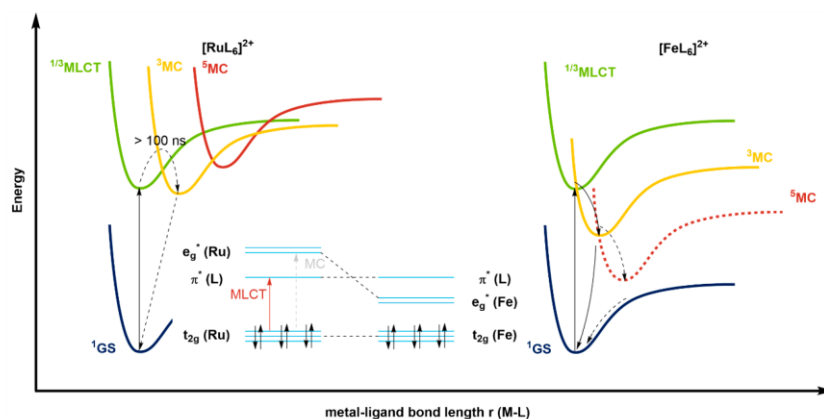


Figure 1. Schematic ground- and excited-state landscapes of ruthenium(II) (left) and iron(II) (right) polypyridine complexes. Middle: Simplified molecular orbital diagrams for the corresponding ruthenium(II) and iron(II) complexes.

applications of iron(II) complexes as active photosensitizers/initiators have been reported.^{20,21} Clearly, the quest for strategies to extend the lifetime of photoactive MLCT states in iron(II) complexes is still open.

In $\text{Fe}^{\text{II}}\text{L}_6$ complexes with the $3d^6$ configuration, the smaller ligand-field splitting compared to that of the $\text{Ru}^{\text{II}}\text{L}_6$ analogues hinders a useful photofunctionality.⁵ As shown in Figure 1, the e_g orbitals are less destabilized in iron(II) complexes and found at lower energies than the ligand π^* orbitals. Because $t_{2g}-e_g$ transitions are Laporte-forbidden, the most probable absorption processes lead to the population of $^1\text{MLCT}$ states, transforming to $^3\text{MLCT}$ states after rapid ISC. According to the energy diagram in Figure 1, the $^3\text{MLCT}$ state evolves into the lower triplet MC (^3MC) states essentially without a barrier. ISC and vibrational cooling follows, leading to a long-lived and nonemissive quintet MC (^5MC) state.²² These MC states are inactive in a photocatalytic sense.^{23,24} Accordingly, the general deactivation pathway in iron(II) complexes with low ligand-field splitting can be summarized as $^1\text{MLCT} \rightarrow ^3\text{MLCT} \rightarrow ^3\text{MC} \rightarrow ^5\text{MC} \rightarrow ^1\text{GS}$. To prevent ultrafast deactivation via MC states, two main strategies that target the inversion of $^3/5\text{MC}$ and MLCT state energies are currently followed, namely, the stabilization of $^3\text{MLCT}$ and the destabilization of MC states, ideally in a combined fashion.^{3,25} Ligand design concepts for this purpose focus on a stronger ligand field by optimization of the octahedral symmetry or by using strong σ -donating ligands to destabilize the MC states. On the other hand, an enlarged π -acceptor system of ligands or the introduction of electron-withdrawing groups is employed to stabilize the MLCT states.^{26–29}

High local symmetry is achieved by chelating ligands coordinating the iron center with bond angles as close as possible to the 180° N–Fe–N trans angle in FeN_6 ligand systems. In such an ideal octahedral geometry, the overlap between the metal and ligand orbitals is maximized, resulting in destabilization of the e_g levels. A N–Fe–N trans angle of 178.3° was achieved by McCusker and co-workers in a $[\text{Fe}(\text{dcpp})_2]^{2+}$ complex.²⁶ The 2,6-bis(2-carboxypyridinyl)pyridine (dcpp) ligand contains electron-withdrawing carbonyl groups, which further lead to stabilized π^* orbitals of the

ligands. An excited state of ^5MC character with a lifetime of 280 ps was identified at room temperature in this complex.²⁷ Heinze and co-workers combined the electron-withdrawing dcpp with an electron-rich N,N' -dimethyl- N,N' -dipyridin-2,6-diamine (ddpd) ligand and realized a N–Fe–N trans angle of 178.4° . Because of the electron-donating amines instead of the carbonyl groups, ddpd is more electron-rich. Such a push–pull ligand design yields a ground-state recovery within 528 ps but still a $^3\text{MLCT} > ^3/5\text{MC}$ energy order.^{28,29}

The introduction of strongly σ -donating N-heterocyclic carbenes (NHCs) induces a stronger ligand field and significant destabilization of the e_g orbitals. Ground-breaking studies on iron(II) photosensitizers with NHC ligands reported $[\text{Fe}(\text{bim})_2]^{2+}$ ($[\text{H}_2\text{-bim}]^{2+} = 1,1'$ -(pyridine-2,6-diyl)-bis(3-methyl-1H-imidazol-3-ium)) with a lifetime of 9 ps assigned to a $^3\text{MLCT}$ state. This was the highest $^3\text{MLCT}$ lifetime at that time, the record $^3\text{MLCT}$ lifetime was later extended to 528 ps in acetonitrile (MeCN).^{30,31} A computational study using density functional theory (DFT) and time-dependent DFT (TDDFT) methods investigated the excited-state landscape. The study confirmed the assignment of the $^3\text{MLCT}$ state and showed that the MC states are destabilized by the NHC ligands compared to $[\text{Fe}(\text{tpy})_2]^{2+}$. To populate a ^5MC state, large structural rearrangements and significant elongation of the metal–ligand bonds are necessary. Population of this state is therefore unlikely, and it is bypassed in the deactivation cascade.³² A systematic study of the NHC iron(II) polypyridyl complexes with a variable number of NHC donors showed a clear correlation between the number of NHC ligands and the resulting increase in the $^3\text{MLCT}$ lifetime.³³ A drawback of this approach are the high-lying π^* levels due to the poor π -accepting properties of NHCs, which causes an undesired concomitant increase of the $^3\text{MLCT}$ energy. Attaching electron-withdrawing carboxyl groups to the pyridine part of the ligands further increases the $^3\text{MLCT}$ lifetimes.³⁴ Related approaches use mesoionic carbenes³¹ or cyclometalated ligands.³⁵

Only a few publications address the extension of the π -acceptor system.^{36–38} A straightforward approach is to

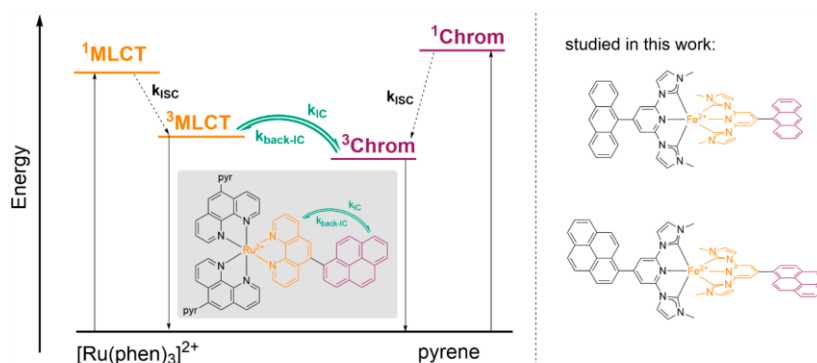


Figure 2. Effective prolongation of $^3\text{MLCT}$ lifetimes by chromophore states populated by MLCT states and repopulation (reservoir effect) in ruthenium(II) complexes according to Castellano et al.^{39,40} Complexes investigated in this work following the multichromophoric approach are shown on the right side.

exchange the imidazolylidene ligand in $[\text{Fe}(\text{bim})_2]^{2+}$ by benzimidazolylidene in $[\text{Fe}(\text{bbim})_2]^{2+}$ ($[\text{H}_2\text{-bbim}]^{2+} = 3,3'-(\text{pyridine-2,6-diyl})\text{bis}(1\text{-methyl-1H-benzo}[d]\text{imidazole-3-ium})$). In this way, the $^3\text{MLCT}$ lifetime could be extended to 16 ps by the reduced LUMO energy. However, the HOMO–LUMO gap unfortunately increases because the t_{3g} orbitals (HOMOs) are stabilized in this ligand design.³⁶ The combination of a strong σ -donating NHC ligand with a pyridine-substituted terpyridine ligand in $[\text{Fe}(\text{bih})(\text{pytpy})]^{2+}$ ($\text{pytpy} = 4'-(\text{pyridine-4-yl})-2,2':6',2''\text{-terpyridine}$; $[\text{H}_2\text{-bih}]^{2+} = 1,1'-(\text{pyridine-2,6-diyl})\text{bis}(3\text{-hexyl-1H-imidazol-3-ium})$) shifts the π^* orbitals in terpyridine, and consequently the MLCT state, to lower energy caused by the extended π system. Additionally, a larger absorption coefficient than that in the homoleptic carbene complex is achieved.^{33,37} If the pyridine backbone of a similar heteroleptic iron(II) complex is used to coordinate chlorido-bis(dimethylglyoximate)cobalt(III), a dyad is obtained, in which the $^3\text{MLCT}$ lifetime is slightly increased compared to the free photosensitizer.³⁸

Functionalization of the coordinating ligands by a second organic chromophore with a long triplet lifetime in order to increase the $^3\text{MLCT}$ lifetimes has been proposed for ruthenium photosensitizers. In such multichromophoric complexes, π -extension leads to energetically lowered $^3\text{MLCT}$ states as described above. Additionally, the long-lived excited triplet states of the organic chromophores can act as reservoirs for population of the $^3\text{MLCT}$ states.^{39,40}

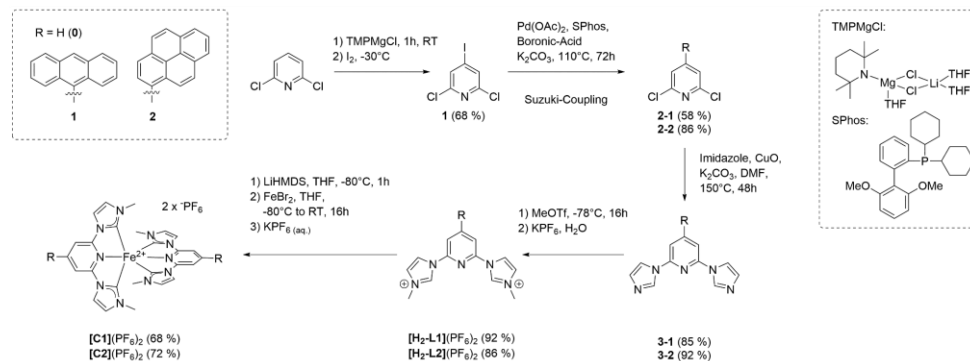
The fundamental processes of this reservoir effect are depicted in Figure 2 for the complex $[\text{Ru}(\text{phen-pyr})_3]^{2+}$ ($\text{phen-pyr} = 5-(\text{pyren-1-yl})-1,10\text{-phenanthroline}$) bearing a pyrene backbone.^{39,40} The initial excitation of the metal complex into a $^1\text{MLCT}$ state is followed by ISC into the $^3\text{MLCT}$ state. From the $^3\text{MLCT}$ state, the energy can be transferred in an internal conversion (IC) step to the nearly isoenergetic triplet chromophore ($^3\text{Chrom}$; k_{IC}) state. Back-IC ($k_{\text{back-IC}}$) yields the $^3\text{MLCT}$ state, resulting in thermal equilibrium of the $^3\text{MLCT}$ and $^3\text{Chrom}$ states. Because of this equilibrium caused by coupling with a long-lived organic chromophore, the $^3\text{MLCT}$ lifetime is significantly extended, and the organic chromophore can be described as a reservoir for the $^3\text{MLCT}$ state. Equilibration is most efficient with the isoenergetic

$^3\text{MLCT}$ and $^3\text{Chrom}$ states; however, the effect of energetic differences between both states has not been studied in a systematic way yet. Even for chromophores with lower triplet energies than the $^3\text{MLCT}$ states, successful results have been achieved in ruthenium complexes.^{41,42}

Despite numerous examples for the application of anthracene and pyrene derivatives with ruthenium(II), this approach is experimentally unexplored for iron(II) in combination with C^NC NHC-pyridine ligands.⁴³ A recent theoretical study evaluates the potential of anthracene-functionalized $[\text{Fe}(\text{bim})_2]^{2+}$ complexes. Results show that even for the direct connection of anthracene to the bim ligand the lowest-energy triplet state is localized on anthracene, which could act as a reservoir for an excited-state population. The authors suggested a mitigation of the fast excited-state decay of iron(II) excited states due to the attachment of anthracene.⁴⁴

In this study, we explore the concept of homoleptic bichromophoric iron(II) complexes displayed in Figure 2 to increase the MLCT lifetimes in addition to the strategy of using strong σ -donor ligands to destabilize MC states. Critical parameters like the possible influence of spin–orbit coupling via a heavy-atom effect imposed by iron on a potentially accessible $^1\text{Chrom}$ – $^3\text{Chrom}$ ISC and optimization of the energy match between the two triplet states will be discussed. The intrinsic properties of iron complexes like the generally reduced $^3\text{MLCT}$ lifetime and lower energy of this state in comparison to that of the ruthenium analogues make the realization of this concept more challenging here.

The well-known NHC pro-ligand $[\text{H}_2\text{-bim}]^{2+}$ ($[\text{H}_2\text{-L0}]^{2+}$) is functionalized in the 4 position of the central pyridine with anthracene and pyrene to yield the pro-ligands $[\text{H}_2\text{-L1}]^{2+}$ and $[\text{H}_2\text{-L2}]^{2+}$, respectively. The corresponding homoleptic complexes $[\text{Fe}(\text{bim-ant})_2]^{2+}$ ($[\text{C1}]^{2+}$) and $[\text{Fe}(\text{bim-pyr})_2]^{2+}$ ($[\text{C2}]^{2+}$) are accessible after deprotonation of the respective pro-ligands. The effects of the appended organic chromophores (i) on the luminescence properties and (ii) on the excited-state dynamics of the iron(II) complexes are probed via extensive ground- and excited-state characterization methods in combination with TDDFT calculations to judge their potential as emitters and photosensitizers, respectively.

Scheme 1. Synthesis of Anthracene- and Pyrene-Linked Complexes [C1](PF₆)₂ and [C2](PF₆)₂

EXPERIMENTAL SECTION

Synthesis. All syntheses were carried out under an argon atmosphere using Schlenk technique. Solvents were dried over molecular sieves in a MBraun Solvent Purification System and degassed prior to reactions. Chemicals were purchased from Sigma-Aldrich and abcr GmbH and used without further purification. [H₂-LO]²⁺ and [CO]²⁺ ([Fe(bim)₂]²⁺) were prepared for comparison purposes. NMR spectra were recorded using a Bruker Ascend 700 spectrometer. Electrospray ionization mass spectrometry (ESI-MS) spectra were measured using a Waters Synapt G2 quadrupole time-of-flight spectrometer, and MS spectra of the complexes were simulated by the Waters software *MassLynx V4.1*. Elemental analysis was performed by a Vario MICROCube.

The synthesis of 4-iodo-2,6-dichloropyridine (**1**) is described in the literature.⁴⁵ [CO]²⁺ was prepared following known protocols.^{30,46} To obtain 4-(anthracen-9-yl)-2,6-dichloropyridine (**2-1**) and 2,6-dichloro-4-(pyren-1-yl)pyridine (**2-2**), palladium acetate (0.05 equiv) and 2-dicyclohexylphosphino-2',6'-dimethoxybiphenyl (SPhos; 0.22 equiv) were stirred in degassed toluene for 30 min (Scheme 1). In parallel, **1** (1 equiv) and the corresponding boronic acid (1.2 equiv) were suspended in degassed toluene. The solution containing the palladium catalyst was transferred to the reactant suspension. K₂CO₃ (2.4 equiv) was dissolved in water, degassed by argon stream, and added to the reaction mixture. The mixture was stirred at 105 °C for 3 days. The reaction was cooled and the product extracted with dichloromethane (DCM). The combined organic layers were washed with water and dried over Na₂SO₄. The solvent was removed under reduced pressure, and the product was obtained after flash chromatography using *n*-hexane/DCM (9:1, v/v; stationary phase SiO₂).

2-1. The product was obtained as a bright-yellow solid (58%). ¹H NMR (700 MHz, CDCl₃): δ 8.57 (s, 1H, H_{anthracene}), 8.07 (d, 2H, J = 8.4 Hz, H_{anthracene}), 7.51–7.47 (m, 4H, H_{anthracene}), 7.47–7.45 (m, 2H, H_{anthracene}), 7.39 (s, 2H, H_{pyridine}). ¹³C NMR (176 MHz, CDCl₃): δ 153.5 (C_q, 1C, C_{anthracene}), 151.2 (C_q, 2C, C_{pyridine}), 131.3 (C_q, 2C, C_{anthracene}), 130.7 (C_q, 1C, C_{pyridine}), 129.4 (C_q, 2C, C_{anthracene}), 128.9 (s, 2C, C_{anthracene}), 128.8 (s, 1C, C_{anthracene}), 126.9 (s, 2C, C_{anthracene}), 125.8 (s, 2C, C_{pyridine}), 125.7 (s, 2C, C_{anthracene}), 125.4 (s, 2C, C_{anthracene}). ESI-MS(+) (MeCN). Calcd for C₁₉H₁₁Cl₂N ([M + H]⁺): *m/z* 323.0269. Found: *m/z* 324.0336.

2-2. The product was obtained as a bright-yellow solid (86%). ¹H NMR (700 MHz, CDCl₃): δ 8.27 (d, 1H, J = 7.6 Hz, H_{pyrene}), 8.24 (d, 2H, J = 7.8 Hz, H_{pyrene}), 8.18–8.04 (m, 5H, H_{pyrene}), 7.90 (d, 1H, J = 7.8 Hz, H_{pyrene}), 7.56 (s, 2H, H_{pyridine}). ¹³C NMR (176 MHz, CDCl₃): δ 155.2 (s, 1C, C_q, C_{pyrene}), 151.1 (s, 2C, C_q, C_{pyridine}), 132.4 (s, 1C, C_q, C_{pyrene}), 131.9 (s, 1C, C_q, C_{pyridine}), 131.7 (s, 1C, C_q, C_{pyrene}), 131.1 (s, 1C, C_q, C_{pyrene}), 129.4 (s, 1C, C_{pyrene}), 129.1 (s, 1C, C_{pyrene}),

128.5 (s, 1C, C_q, C_{pyrene}), 127.6 (s, 1C, C_{pyrene}), 127.1 (s, 1C, C_{pyrene}), 126.9 (s, 1C, C_{pyrene}), 126.4 (s, 1C, C_{pyrene}), 126.1 (s, 1C, C_{pyrene}), 125.3 (s, 1C, C_q, C_{pyrene}), 125.2 (s, 1C, C_{pyrene}), 124.9 (s, 1C, C_q, C_{pyrene}), 124.8 (s, 2C, C_{pyridine}), 123.8 (s, 1C, C_{pyrene}). ESI-MS(+) (MeCN). Calcd for C₁₉H₁₁Cl₂N ([M + H]⁺): *m/z* 347.0269. Found: *m/z* 348.0432.

The synthesis of 4-(anthracen-9-yl)-2,6-di(1*H*-imidazol-1-yl)pyridine (**3-1**) and 2,6-di(1*H*-imidazol-1-yl)-4-(pyren-1-yl)pyridine (**3-2**) was achieved by suspending **2-1** or **2-2** (1 equiv), imidazole (2.4 equiv), K₂CO₃ (2.4 equiv), and copper(II) oxide (0.2 equiv) in *N,N*-dimethylformamide (DMF; 10 mL mmol⁻¹), degassing by an argon stream, and stirring at 150 °C for 48 h. DMF was removed under reduced pressure. Flash chromatography with pure DCM showed incompletely coupled **2-1/2-2** and imidazole. The corresponding 2,6-di(1*H*-imidazol-1-yl)-4-(chromophore)pyridine was obtained by flash chromatography with DCM/methanol (MeOH; 9:1, v/v; stationary phase SiO₂). If the product contained free imidazole, the mixture was dissolved in DCM and extracted with water to transfer residual imidazole to the aqueous phase.

3-1. In contrast to the general procedure, the reaction mixture was stirred for 72 h at 150 °C to increase the yield. The product was obtained as a bright-yellow solid (85%). ¹H NMR [700 MHz, dimethyl sulfoxide (DMSO)-*d*₆]: δ 8.87 (t, 2H, J = 1.0 Hz, H_{imidazole}), 8.82 (s, 1H, H_{anthracene}), 8.24 (t, 2H, J = 1.3 Hz, H_{imidazole}), 8.22 (d, 2H, J = 8.5 Hz, H_{anthracene}), 7.96 (s, 2H, H_{pyridine}), 7.71 (d, 2H, J = 8.4 Hz, H_{anthracene}), 7.60–7.57 (m, 2H, H_{anthracene}), 7.53–7.48 (m, 2H, H_{anthracene}), 7.16 (t, 2H, J = 1.1 Hz, H_{imidazole}). ¹³C NMR (176 MHz, DMSO-*d*₆): δ 153.8 (s, C_q, 1C, C_{anthracene}), 148.1 (s, C_q, 2C, C_{pyridine}), 135.8 (s, 2C, C_{imidazole}), 132.5 (s, C_q, 1C, C_{pyridine}), 130.7 (s, C_q, 2C, C_{anthracene}), 130.4 (s, 2C, C_{imidazole}), 128.8 (s, C_q, 2C, C_{anthracene}), 128.5 (s, 2C, C_{anthracene}), 127.8 (s, 1C, C_{anthracene}), 126.7 (s, 2C, C_{anthracene}), 125.7 (s, 2C, C_{anthracene}), 125.6 (s, 2C, C_{anthracene}), 116.9 (s, 2C, C_{imidazole}), 112.0 (s, 2C, C_{pyridine}). ESI-MS(+) (MeCN). Calcd for C₂₅H₁₅N₅ ([M + H]⁺): *m/z* 387.1484. Found: *m/z* 388.1566.

3-2. The product was obtained as a bright-yellow solid (92%). ¹H NMR (700 MHz, CDCl₃): δ 8.48 (t, 2H, J = 1.1 Hz, H_{imidazole}), 8.32–8.25 (m, 3H, H_{pyrene}), 8.21–8.08 (m, 5H, H_{pyrene}), 8.01 (d, 1H, J = 7.8 Hz, H_{pyrene}), 7.75 (t, 2H, J = 1.4 Hz, H_{imidazole}), 7.55 (s, 2H, H_{pyridine}), 7.27 (m, 2H, H_{imidazole}). ¹³C NMR (176 MHz, CDCl₃): δ 156.4 (s, 1C, C_q, C_{pyrene}), 148.7 (s, 2C, C_q, C_{pyridine}), 135.4 (s, 2C, C_{imidazole}), 132.7 (s, 1C, C_q, C_{pyridine}), 132.4 (s, 1C, C_q, C_{pyrene}), 131.6 (s, 1C, C_q, C_{pyrene}), 131.4 (s, 2C, C_{imidazole}), 130.9 (s, 1C, C_q, C_{pyrene}), 129.4 (s, 1C, C_{pyrene}), 129.0 (s, 1C, C_{pyrene}), 128.4 (s, 1C, C_q, C_{pyrene}), 127.4 (s, 1C, C_{pyrene}), 126.9 (s, 1C, C_{pyrene}), 126.7 (s, 1C, C_{pyrene}), 126.4 (s, 1C, C_{pyrene}), 126.0 (s, 1C, C_{pyrene}), 125.2 (s, 1C, C_q, C_{pyrene}), 125.1 (s, 1C, C_{pyrene}), 124.8 (s, 1C, C_q, C_{pyrene}), 123.6 (s, 1C, C_{pyrene}), 116.5 (s, 2C, C_{imidazole}), 111.7 (s, 2C, C_{pyridine}). ESI-MS(+) (MeCN).

Calcd for $C_{27}H_{17}N_5$ ($[M + H]^+$): m/z 411.1484. Found: m/z 412.1675.

The synthesis of pro-ligands $[H_2-L1](PF_6)_2$ and $[H_2-L2](PF_6)_2$ was carried out by suspending the respective substituted 3-1 or 3-2 (1 equiv) in DCM and cooling to -78°C . Methyl trifluoromethanesulfonate (MeOTf; 2.05 equiv) was added dropwise. The suspension was stirred for 16 h while slowly warming to room temperature. It was again cooled in an ice bath, and *n*-pentane was added. The product was obtained as a solid precipitate, filtered, and, if necessary, washed again by cold *n*-pentane. The obtained triflate salt was dissolved in a small amount of acetone and added dropwise into an aqueous solution of KPF_6 (10 equiv). The precipitate was filtered and purified by recrystallization via solvent diffusion (acetone/diethyl ether).

$[H_2-L1](PF_6)_2$. The product was obtained as a bright-yellow solid (92%). ^1H NMR (700 MHz, DMSO- d_6): δ 10.32 (s, 2H, $H_{\text{imidazole}}$), 8.91 (s, 1H, $H_{\text{anthracene}}$), 8.81 (s, 2H, $H_{\text{imidazole}}$), 8.43 (s, 2H, H_{pyridine}), 8.27 (d, 2H, $J = 8.5$ Hz, $H_{\text{anthracene}}$), 8.06 (s, 2H, $H_{\text{imidazole}}$), 7.68 (d, 2H, $J = 8.8$ Hz, $H_{\text{anthracene}}$), 7.65–7.61 (m, 2H, $H_{\text{anthracene}}$), 7.56–7.52 (m, 2H, $H_{\text{anthracene}}$), 4.01 (s, 6H, H_{methyl}). ^{13}C NMR (176 MHz, DMSO- d_6): δ 155.1 (s, C_{q} 1C, $C_{\text{anthracene}}$), 145.8 (s, C_{q} 2C, C_{pyridine}), 136.5 (s, 2C, C_{carbene}), 130.7 (s, C_{q} 1C, C_{pyridine}), 130.6 (s, C_{q} 2C, $C_{\text{anthracene}}$), 128.7 (s, 1C, $C_{\text{anthracene}}$), 128.6 (s, 2C, $C_{\text{anthracene}}$), 127.0 (s, 2C, $C_{\text{anthracene}}$), 125.8 (s, 2C, $C_{\text{anthracene}}$), 125.3 (s, 2C, $C_{\text{anthracene}}$), 125.0 (s, 2C, $C_{\text{imidazole}}$), 119.8 (s, C_{q} 2C, $C_{\text{anthracene}}$), 119.2 (s, 2C, $C_{\text{imidazole}}$), 116.4 (s, 2C, C_{pyridine}), 36.6 (s, 2C, C_{methyl}). ESI-MS(+) (MeCN). Calcd for $C_{27}H_{17}N_5$ ($[M - 2PF_6]^{2+}$): m/z 208.5971. Found: m/z 208.5984. Elem. anal. Calcd for $C_{27}H_{17}F_{12}N_5P_2$: C, 45.84%; H, 3.28%; N, 9.90%. Found: C, 45.64%; H, 3.59%; N, 9.57%.

$[H_2-L2](PF_6)_2$. The product was obtained as a bright-yellow solid (86%). ^1H NMR (700 MHz, acetone- d_6): δ 10.18 (s, 2H, $H_{\text{imidazole}}$), 8.82 (t, 2H, $J = 1.8$ Hz, $H_{\text{imidazole}}$), 8.61 (s, 2H, H_{pyridine}), 8.50–8.18 (m, 9H, H_{pyrene}), 8.08 (t, 2H, $J = 1.7$ Hz, $H_{\text{imidazole}}$), 4.27 (s, 6H, H_{methyl}). ^{13}C NMR (176 MHz, acetone- d_6): δ 157.9 (s, C_{q} 1C, C_{pyrene}), 146.2 (s, C_{q} 2C, C_{pyridine}), 136.1 (s, 2C, $C_{\text{imidazole}}$), 132.6 (s, C_{q} 1C, C_{pyrene}), 131.6 (s, C_{q} 1C, C_{pyrene}), 131.4 (s, C_{q} 1C, C_{pyridine}), 130.8 (s, C_{q} 1C, C_{pyrene}), 129.3 (s, 1C, C_{pyrene}), 129.1 (s, 1C, C_{pyrene}), 128.2 (s, C_{q} 1C, C_{pyrene}), 127.4 (s, 1C, C_{pyrene}), 127.3 (s, 1C, C_{pyrene}), 126.9 (s, 1C, C_{pyrene}), 126.4 (s, 1C, C_{pyrene}), 125.9 (s, 2C, $C_{\text{imidazole}}$), 125.5 (s, 1C, C_{pyrene}), 125.1 (s, 1C, C_{pyrene}), 124.6 (s, C_{q} 1C, C_{pyrene}), 124.2 (s, C_{q} 1C, C_{pyrene}), 123.6 (s, 1C, C_{pyrene}), 119.9 (s, 2C, $C_{\text{imidazole}}$), 116.3 (s, 2C, C_{pyridine}), 36.7 (s, 2C, C_{methyl}). ESI-MS(+) (MeCN). Calcd for $C_{29}H_{23}N_5$ ($[M - 2PF_6]^{2+}$): m/z 220.5971. Found: m/z 220.5985. Elem. anal. Calcd for $C_{29}H_{23}F_{12}N_5P_2$: C, 47.62%; H, 3.17%; N, 9.57%. Found: C, 48.29%; H, 3.51%; N, 9.67%.

For the synthesis of complexes $[C1](PF_6)_2$ and $[C2](PF_6)_2$, the respective pro-ligand (2 equiv) was suspended in tetrahydrofuran (THF) and cooled to -78°C . Lithium bis(trimethylsilyl)amide (LiHMDS; 6 equiv, 1 M, in THF) was added dropwise. After complete deprotonation, found to result in a clear solution, FeBr_2 (1 equiv) was dissolved in THF and added dropwise to the carbene solution. The mixture instantly turned into a dark-red suspension, which was stirred for 16 h while slowly heating to room temperature. The solvent was removed, and the residue was dissolved in acetone. Residues were filtered off. Acetone was removed to a minimum amount and added dropwise to a solution of KPF_6 (10 equiv) in water cooled by an ice bath, and stirred for 15 min. The resulting precipitate was filtered off and rinsed with cold water. The crude complex was finally purified by recrystallization via solvent diffusion (acetone/diethyl ether).

$[C1](PF_6)_2$. The complex was obtained as a red powder (68%). ^1H NMR (700 MHz, acetone- d_6): δ 8.89 (s, 2H, $H_{\text{anthracene}}$), 8.52 (d, 4H, $J = 2.1$ Hz, $H_{\text{imidazole}}$), 8.31 (s, 4H, H_{pyridine}), 8.29 (d, 4H, $J = 8.6$ Hz, $H_{\text{anthracene}}$), 7.81 (d, 4H, $J = 8.8$ Hz, $H_{\text{anthracene}}$), 7.66–7.62 (m, 4H, $H_{\text{anthracene}}$), 7.57–7.53 (m, 4H, $H_{\text{anthracene}}$), 7.43 (d, 4H, $J = 2.0$ Hz, $H_{\text{imidazole}}$), 3.20 (s, 12H, H_{methyl}). ^{13}C NMR (176 MHz, acetone- d_6): δ 200.6 (s, C_{q} 4C, C_{carbene}), 154.7 (s, C_{q} 4C, C_{pyridine}), 149.9 (s, C_{q} 2C, C_{pyridine}), 132.1 (s, C_{q} 2C, $C_{\text{anthracene}}$), 131.4 (s, C_{q} 4C, $C_{\text{anthracene}}$), 129.4 (s, C_{q} 4C, $C_{\text{anthracene}}$), 128.9 (s, 2C, $C_{\text{anthracene}}$), 128.7 (s, 4C, $C_{\text{anthracene}}$), 127.0 (s, 4C, $C_{\text{imidazole}}$), 125.7 (s, 4C, $C_{\text{anthracene}}$), 125.3 (s, 4C, $C_{\text{anthracene}}$), 117.1 (s, 4C, $C_{\text{imidazole}}$), 108.6

(s, 4C, C_{pyridine}), 34.7 (s, 4C, C_{methyl}). ESI-MS(+) (MeCN). Calcd for $C_{54}H_{42}FeN_{10}$ ($[M - 2PF_6]^{2+}$): m/z 443.1466. Found: m/z 443.1478 ($[M - 2PF_6]^{2+}$). Elem. anal. Calcd for $C_{54}H_{42}F_{12}FeN_{10}P_2$: C, 55.12%; H, 3.60%; N, 11.90%. Found: C, 55.24%; H, 4.22%; N, 11.39%.

$[C2](PF_6)_2$. The complex was obtained as a red powder (72%). ^1H NMR (700 MHz, acetone- d_6): δ 8.62 (d, 4H, $J = 2.0$ Hz, $H_{\text{imidazole}}$), 8.54 (d, 2H, $J = 7.7$ Hz, H_{pyrene}), 8.52 (s, 4H, H_{pyridine}), 8.49 (d, 2H, $J = 9.2$ Hz, H_{pyrene}), 8.45 (d, 2H, $J = 7.6$ Hz, H_{pyrene}), 8.43–8.40 (m, 4H, H_{pyrene}), 8.38–8.32 (m, 4H, H_{pyrene}), 8.29 (d, 2H, $J = 9.3$ Hz, H_{pyrene}), 8.20 (t, 2H, $J = 7.5$ Hz, H_{pyrene}), 7.43 (d, 4H, $J = 2.0$ Hz, $H_{\text{imidazole}}$), 3.09 (s, 12H, H_{methyl}). ^{13}C NMR (176 MHz, acetone- d_6): δ 201.6 (s, C_{q} 4C, C_{carbene}), 155.3 (s, C_{q} 4C, C_{pyridine}), 152.8 (s, C_{q} 2C, C_{pyridine}), 134.4 (s, C_{q} 2C, C_{pyrene}), 133.2 (s, C_{q} 2C, C_{pyrene}), 132.5 (s, C_{q} 2C, C_{pyrene}), 131.8 (s, C_{q} 2C, C_{pyrene}), 129.9 (s, 2C, C_{pyrene}), 129.7 (s, 2C, C_{pyrene}), 129.2 (s, C_{q} 2C, C_{pyrene}), 128.9 (s, 2C, C_{pyrene}), 128.4 (s, 2C, C_{pyrene}), 127.84 (s, 4C, $C_{\text{imidazole}}$), 127.83 (s, 2C, C_{pyrene}), 127.3 (s, 2C, C_{pyrene}), 126.7 (s, 2C, C_{pyrene}), 126.1 (s, 2C, C_{pyrene}), 125.8 (s, C_{q} 2C, C_{pyrene}), 125.4 (s, C_{q} 2C, C_{pyrene}), 125.1 (s, 2C, C_{pyrene}), 117.9 (s, 4C, $C_{\text{imidazole}}$), 108.4 (s, 4C, C_{pyridine}), 35.7 (s, 4C, C_{methyl}). ESI-MS(+) (MeCN). Calcd for $C_{58}H_{42}FeN_{10}$ ($[M - 2PF_6]^{2+}$): m/z 467.1466. Found: m/z 467.1528. Elem. anal. Calcd for $C_{58}H_{42}F_{12}FeN_{10}P_2$: C, 56.88%; H, 3.46%; N, 11.44%. Found: C, 56.78%; H, 3.97%; N, 10.81%.

Cyclic Voltammetry. Potentiometric measurements were performed at room temperature using a PGSTAT 101 potentiostat from Metrohm-Autolab in deoxygenated MeCN with an analyte concentration of 10^{-3} M and with $[n\text{-Bu}_4\text{N}][PF_6]$ at a concentration of 0.1 M as the inert electrolyte. A platinum working electrode (1 mm diameter), a silver/0.01 M AgNO_3 and 0.1 M $[n\text{-Bu}_4\text{N}][PF_6]$ in MeCN reference electrode, and a platinum pin counter electrode were used in a three-electrode configuration. After measurements, ferrocene (FcH) was added as an internal standard to reference against the FcH/FcH^+ redox couple. The resulting voltammograms were analyzed using the software Nova 2.1.3. The reversibility of the redox couples was checked by using the criteria from Nicholson and Shain^{47,48} and the Randles–Sevcik equation.⁴⁹

UV/Vis Spectroscopy. Absorption spectra were recorded at concentrations of 10^{-5} M on a PerkinElmer Lambda 465 single-beam spectrophotometer and with a Specord 50 UV/vis spectrometer from Analytik Jena. Spectroscopic-grade solvents from VWR and quartz cuvettes by Hellma with a path length of 1 cm were used.

Luminescence Measurements. The emission spectra were recorded using a FluoroMax-4 fluorometer from Horiba Scientific. Excitation spectra were recorded on a Jasco FP-8300 fluorometer.

Spectroelectrochemistry. Spectroelectrochemical measurements were performed at room temperature in an optically transparent cell ($d = 4$ mm) in deoxygenated MeCN/0.1 M $[n\text{-Bu}_4\text{N}][PF_6]$ and a platinum wire mesh working electrode. Spectral changes during oxidations/reductions were recorded on a Varian Cary 50 spectrophotometer.

Time-Resolved Emission Measurements. Time-resolved luminescence measurements were carried out by means of a streak camera system (C10627, Hamamatsu Photonics) using ultrashort excitation pulses at 388 nm. The latter were generated by frequency doubling the output of a regenerative Ti:sapphire laser system (CPA 2001, Clark MXR, Inc.), which provided 160-fs-long laser pulses with a center wavelength of 775 nm at a repetition rate of 1 kHz. MeCN solutions of the compounds were prepared under argon and measured in a 1-cm-thick fused-silica cuvette.

Transient Absorption Spectroscopy. Transient absorption spectra were measured with a time resolution of about 100 fs by means of a pump-probe setup in which a noncollinear optical parametric amplifier (NOPA) tuned to a center wavelength of 480 nm was used for exciting the sample and a white-light continuum generated in a CaF_2 crystal for probing.⁵⁰ Both the NOPA and white-light stage were pumped by a regenerative Ti:sapphire laser system (CPA 2001, Clark MXR, Inc.) operating at a center wavelength of 775 nm and a repetition rate of 1 kHz. Dispersion of the NOPA pulses was minimized by a compressor based on fused-silica prisms, and the polarizations of the pump and probe pulses were set to magic angle

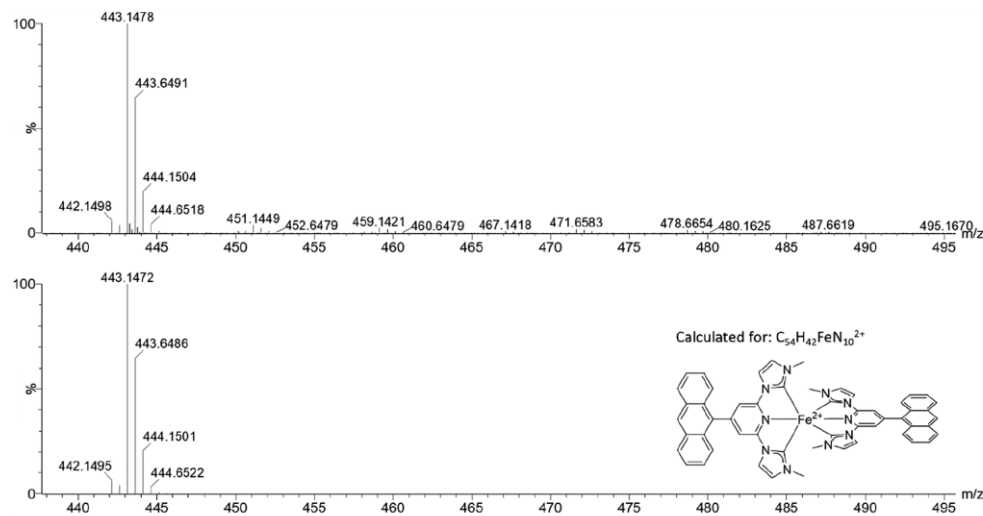


Figure 3. Observed isotope pattern for $[C1]^{2+}$ (top) and calculated isotope pattern for $C_{54}H_{42}FeN_{10}^{2+}$ (bottom). Intensities are given in relation to the most intense signal.

with respect to each other to avoid the effects caused by orientational relaxation. The pump and probe beam were focused on the sample to overlapping spots with diameters of approximately 200 and 100 μm , respectively. After the sample, the probe was dispersed by a prism and transient absorption changes were spectrally resolved and recorded by a photodiode array detector. Transient absorption spectra with an excitation wavelength of 400 nm were recorded with a similar setup using another Ti:sapphire laser system (Spitfire Ace PA, Spectra Physics). The compounds were dissolved in MeCN under argon, and the sample solution was filled into a fused-silica cuvette with a thickness of 1 mm.

Singlet-Oxygen (1O_2)-Generation Experiments. The reaction of 1,3-diphenylisobenzofuran (DPBF) with 1O_2 was used to indirectly detect the presence of nonluminescent triplet states. The measurements were carried out at room temperature in air-saturated MeOH. A total of 2.5 mL of DPBF (20 μM) was mixed with 0.5 mL of ligand (2×10^{-4} M) or complex (10^{-4} M) in a 1-cm-path-length Hellma fluorescence cuvette and illuminated with $\lambda = 480 \pm 5$ nm in a Jasco FP-8300 fluorescence spectrophotometer. The consumption of DPBF was detected by monitoring the decreasing luminescence intensity at 475 nm. $[\text{Ru}(\text{bpy})_3]^{2+}$ with a 1O_2 quantum yield of 0.86 in air-saturated MeOH was used as a reference.⁵¹

Quantum-Chemical Calculations of Absorption Spectra. Absorption spectra were computed with linear-response TDDFT using the optimally tuned LC-BLYP functional together with the polarizable continuum model⁵² to account for solvent effects (MeCN). The two-parameter optimal tuning of LC-BLYP was done via the ΔSCF method;^{53–55} the details of the present setup can be found in the literature.⁵⁶ The 6-31G(d) basis set was used for the tuning procedure, while def2-TZVP was employed for calculation of the absorption spectra. Calculations of the whole complexes will be referred to as the supermolecule approach. We assume that $[C1]^{2+}$ and $[C2]^{2+}$ can be modeled in the spirit of the Frenkel exciton approach.^{57,58} Here, the chromophores were separated from the $[\text{Fe}(\text{bim})_2]^{2+}$ core and saturated with hydrogen atoms, and all units were considered separately. The optimal parameters for LC-BLYP were chosen separately for every unit to ensure the appropriate description of excited states within the unit. Excited-state transitions of the total system were calculated by including the Coulomb

interaction between the electronic transition densities. In the present study, we restricted ourselves to approximating the transition densities by transition dipoles. Specifically, we have included 100 transitions for both the core and chromophores. Broadening of the resulting stick spectra was done with Gaussians of fwhm 0.15 eV. All calculations were performed with the *Gaussian16* suite of programs.⁵⁹ Excited-state analysis was done using the *TheoDORÉ* package,⁶⁰ which enables automatic quantitative wave-function analysis and localization of excitations at predefined molecular moieties. Pre- and postprocessing of data were done with homemade programs.

RESULTS

Synthesis. Synthesis of the pro-ligands and iron(II) complexes was performed according to *Scheme 1* in four steps using 2,6-dichloropyridine as the starting material, which was deprotonated in the 4 position by 2,2,6,6-tetramethylpiperidinylmagnesium chloride/lithium chloride (TMPPMgCl) and iodinated to obtain **1**. The iodo derivative was coupled with 9-anthracenylboronic acid in a Suzuki–Miyaura reaction using slightly modified standard procedures.⁶¹ Moderate yields and anthracene as the byproduct were obtained as a result of protodeboronation of boronic acid. The diimidazole **3-1** was obtained from **2-1** in an Ullmann-style coupling reaction with imidazole and finally methylated to give pro-ligand $[\text{H}_2\text{-L1}]^{2+}$. Pro-ligand $[\text{H}_2\text{-L2}]^{2+}$ was synthesized analogously using 1-pyrenylboronic acid. The iron(II) complexes $[C1]^{2+}$ and $[C2]^{2+}$ were obtained according to *Scheme 1* by deprotonation of the imidazolium ligands $[\text{H}_2\text{-L1}]^{2+}$ and $[\text{H}_2\text{-L2}]^{2+}$ with LiHMDS in THF, followed by the addition of FeBr_2 as the iron(II) source. $[C0]^{2+}$ is prepared for comparison purposes by neat coupling of 2,6-dichloropyridine with methylimidazole and subsequent coordination.⁴⁶

Ground-State Characterization. A combination of NMR spectroscopy, elemental analysis, and mass spectrometry was used to identify the complexes $[C1](\text{PF}_6)_2$ and $[C2](\text{PF}_6)_2$ and prove their purity because no crystals suited for single-

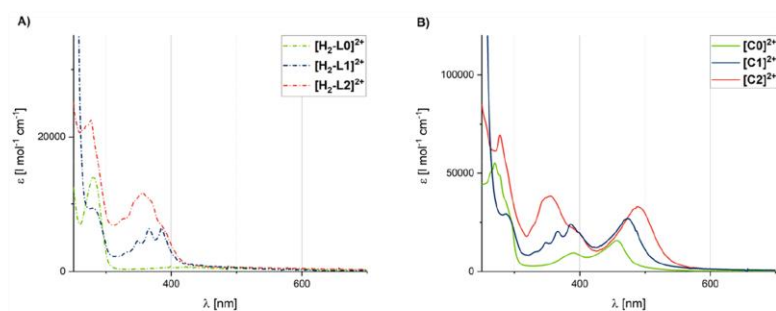


Figure 4. Absorption spectra of (A) $[\text{H}_2\text{-L0}]^{2+}$ – $[\text{H}_2\text{-L2}]^{2+}$ and (B) $[\text{C0}]^{2+}$ – $[\text{C2}]^{2+}$ ($c = 10^{-5}$ M in MeCN).

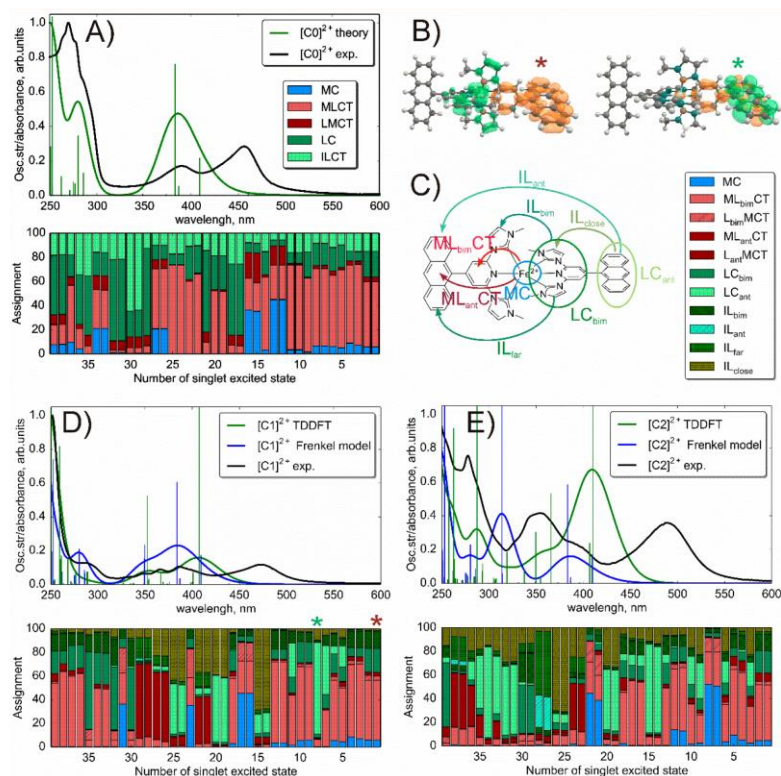


Figure 5. Absorption spectra of $[\text{C0}]^{2+}$ (A), $[\text{C1}]^{2+}$ (D), and $[\text{C2}]^{2+}$ (E) computed with different approaches compared to the experimental data. In part B, the transition density differences of the low-lying MLCT (left) and chromophore (right) transitions of $[\text{C1}]^{2+}$ are presented; the green color corresponds to the hole and orange to the particle (isovalue of the surface = 0.0009); the asterisks mark the respective transition in the lower part of panel B. The lower parts of panels A, D, and E present the density-matrix analysis of TDDFT transitions. The partitioning of a supermolecule into a fragment for TDDFT analysis is given in panel C on the example of $[\text{C1}]^{2+}$. The assignments in the upper and lower panels of A, D, and E are given not on the energy scale (as the spectra) but according to the number of states; e.g., the two intense transitions around 400 nm have numbers 5 and 7 in the lower part of panel D. The full assignment data can be found in Tables S1–S5.

crystal X-ray diffraction analysis could be obtained. Figure 3 shows the unique isotope pattern of $[C1]^{2+}$ in comparison to the simulation. All other analytical data are shown in the Supporting Information.

For all complexes $[C0]^{2+}$ – $[C2]^{2+}$, the absorption spectra given in Figure 4 are composed of three distinct spectral regions. The intense bands at wavelengths shorter than 320 nm correspond to π – π^* transitions within the bim moieties of the ligands (vide infra).^{20,30,37} In the range of 320–420 nm, π – π^* transitions of the organic chromophores in the backbones of $[H_2-L1]^{2+}$ and $[H_2-L2]^{2+}$ containing several intrachromophore transitions can be found.⁶² The anthracenyl derivatives $[H_2-L1]^{2+}$ and $[C1]^{2+}$ show the typical vibrational fine structure of anthracene.⁶³ According to the results of TDDFT calculations, the low-intensity band at 389 nm of $[C0]^{2+}$ has a dominant MLCT character (Figure 5, panel A).³⁴ At longer wavelengths, MLCT transitions appear for all complexes. These bands are clearly red-shifted for the bichromophoric complexes compared to $[C0]^{2+}$ and in line with the electrochemical data discussed below. The absorption bands and intensities shift from 473 nm ($26800 \text{ M}^{-1} \text{ cm}^{-1}$) to 489 nm ($32900 \text{ M}^{-1} \text{ cm}^{-1}$) upon going from $[C1]^{2+}$ to $[C2]^{2+}$, respectively, which correlates with the size of the organic chromophore in the ligand backbone. The absorption maxima at longer wavelengths and higher absorption coefficients render the bichromophoric complexes potentially more suited as photosensitizers than $[C0]^{2+}$.

The TDDFT supermolecule calculations of the complexes are shown in Figure 5. In principle, TDDFT correctly predicts the position of the lowest MLCT transitions (cf. Tables S4 and S5). At the same time, the intensities of these transitions are very low, which leads to a visual absence of the absorption band around 450–500 nm. It should be noted that the computed spectra include only singlet–singlet transitions. From 400 nm onward, there is a substantial density of formally forbidden singlet–triplet excitations. Thus, spin–orbit coupling could cause spectral redistribution. According to calculations with a smaller basis set [6-31G(d)], there are many singlet–triplet transitions for all studied complexes above 400 nm, whereas the spin–orbit couplings strongly vary for different transitions. Of course, because of the approximation nature of TDDFT, transitions could also be blue-shifted depending on their nature.

The assignment of excited states in the lower parts of panels A, D, and E of Figure 5 is done based on fragmentations of the complexes. For $[C1]^{2+}$ and $[C2]^{2+}$,⁶⁰ partitioning of the complex and names for different types of transitions are depicted in Figure 5C. Among the 40 lowest transitions, the MLCT type is a dominant one for $[C0]^{2+}$. However, the addition of side chromophore ligands introduces significant changes in the character of excited states. Apart from MLCT transitions to the bim ligand, MLCT transitions also end up at the chromophores. The same applies to ligand-centered (LC) transitions: derivation leads to the appearance of transitions localized purely on the chromophores. Additionally, there are transitions where intraligand charge-transfer between bim and ant ligands takes place.

Within the Frenkel model, the interactions between the moieties clearly depend on mutual orientation of the side chromophores. However, this interaction is quite weak for all possible mutual orientations of ligands pointing to effects beyond the current approximations. Candidates are higher multipole terms in the Coulomb interaction, contributions due

to exchange, or charge-transfer effects. Indeed, if the transition density differences of low-lying states of MLCT and chromophore transitions are analyzed (cf. Figure 5B) for $[C1]^{2+}$, a delocalization of the actual chromophore transition over the whole functionalized bim–ant ligand can be noticed, pointing to its CT character; the same holds true for the bim–pyr ligand of $[C2]^{2+}$.

Cyclic voltammograms of the iron(II) complexes in Figure 6 show no distinct trend in the shift of the fully reversible $Fe^{II}/$

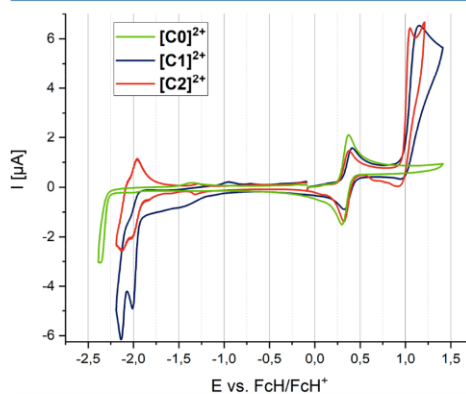


Figure 6. Cyclic voltammograms of complexes $[C0]^{2+}$ – $[C2]^{2+}$ versus FcH/FcH^+ in $MeCN/[n-Bu_4][PF_6]$ (scan rate: 100 mV s^{-1}).

Fe^{III} oxidation potentials in the row from $[C0]^{2+}$ (0.34 V) to $[C1]^{2+}$ (0.37 V) and $[C2]^{2+}$ (0.34 V), indicating similar energies of the HOMOs. Irreversible oxidations can be found at anodic potentials for complexes $[C1]^{2+}$ and $[C2]^{2+}$ but not for $[C0]^{2+}$. A comparison of the cyclic voltammograms of $[H_2-L0]^{2+}$ – $[H_2-L2]^{2+}$ with those of pure anthracene and pyrene (see Figures S31 and S32) and with those of the complexes $[C0]^{2+}$ – $[C2]^{2+}$ reveals that the irreversible oxidation can be assigned to oxidation of the organic chromophore.⁴⁸ At cathodic potentials, irreversible ligand-based reductions occur and are assigned to the bim moiety in each ligand. $[C0]^{2+}$ is reduced irreversibly at -2.37 V versus FcH/FcH^+ , while $[C1]^{2+}$ is reduced at -2.01 V versus FcH/FcH^+ and $[C2]^{2+}$ at -2.02 V versus FcH/FcH^+ . These values are in accordance with the electron-accepting properties of $[H_2-L1]^{2+}$ and $[H_2-L2]^{2+}$ and the lower energies of their π^* levels in comparison to $[H_2-L0]^{2+}$.²⁸ A similar behavior is found in iron(II) bis(polypyridine) complexes, where two consecutive one-electron reductions are observed for each polypyridine ligand.⁶⁴ The resulting electrochemical energy gap ΔE_p corresponds approximately to the optical energy gap ΔE_o (Table 1). The values confirm the assignment of the lowest-energy absorptions to MLCT states.

The redox processes of $[C1]^{2+}$ and $[C2]^{2+}$ were probed by UV/vis/near-IR (NIR) spectroelectrochemistry (Figures 7, 8, and S33 and S34). The oxidation processes of $[C1]^{2+}$ to $[C1]^{3+}$ and $[C2]^{2+}$ to $[C2]^{3+}$ are fully reversible, as confirmed by several isosbestic points (Figures 7a and 8a). The reversibility even persists on the long time scale of the electrochemical re-reduction (Figures S33 and S34). Upon oxidation, the MLCT bands of $[C1]^{2+}$ and $[C2]^{2+}$ at 473 and

Table 1. Physicochemical Properties of $[C0]^{2+}$ – $[C2]^{2+}$

compound	$E_{ox}(Fe^{II}/Fe^{III})$ [V]	$E_{red}(\text{ligand-based})$ [V]	$E_{ox}(\text{ligand-based})$ [V]	ΔE_p [eV]	λ_{MLCT} [nm]	ΔE_0 [eV]
$[C0]^{2+}$	0.34	–2.37		2.71	457	2.71
$[C1]^{2+}$	0.37	–2.01	1.15	2.38	473	2.62
$[C2]^{2+}$	0.34	–2.02	1.05	2.36	489	2.54

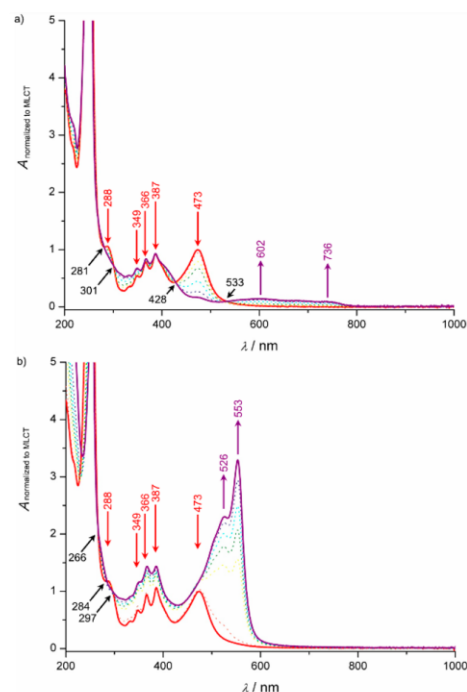


Figure 7. Changes in the UV/vis/NIR spectra of $[C1]^{2+}$ (a) during oxidation (red \rightarrow purple) and (b) during reduction (red \rightarrow purple) in MeCN/ $[n\text{-Bu}_4\text{N}][PF_6]$.

489 nm bleaching and weak LMCT bands of the iron(III) congeners $[C1]^{3+}$ and $[C2]^{3+}$ appear at 602/736 and 594/734 nm, respectively (Figures 7a and 8a). The first reduction processes are reversible during the forward reaction, as shown by the presence of isosbestic points (Figures 7b and 8b). However, at longer time scales, side reactions of the radical anions preclude a long-term stability (Figures S33 and S34). Reduction of $[C1]^{2+}$ and $[C2]^{2+}$ leads to a partial bleaching of the MLCT bands, consistent with the reduction of one coordinated ligand and the persistence of one unaffected ligand. The reduced ligands in $[C1]^+$ and $[C2]^+$ give rise to characteristic bands at 526/553 and 579/621 nm, respectively.

Luminescence Properties and Excited-State Dynamics. Both ligands $[H_2-L1]^{2+}$ and $[H_2-L2]^{2+}$ exhibit luminescence in solution at room temperature. Excitation at different wavelengths in the region of the $\pi-\pi^*$ transitions of the organic chromophores ($\lambda_{ex} = 320\text{--}390$ nm) leads to emission, as shown in Figure 9. The results of these measurements are given in Table 2. Both ligands show an emission spectrum that

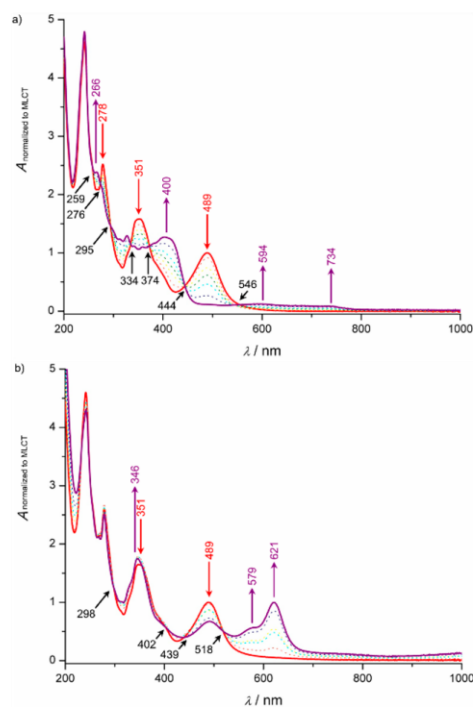


Figure 8. Changes in the UV/vis/NIR spectra of $[C2]^{2+}$ (a) during oxidation (red \rightarrow purple) and (b) during reduction (red \rightarrow purple) in MeCN/ $[n\text{-Bu}_4\text{N}][PF_6]$.

is independent of the excitation wavelength. This emission is assigned to the lowest electronically excited singlet states of the organic chromophores. Coupling of the organic chromophore to the (bim) ligand results in a red shift by around 100 nm (5140 cm^{-1}) and 110 nm (5780 cm^{-1}) for anthracene in $[H_2-L1]^{2+}$ and pyrene in $[H_2-L2]^{2+}$, respectively.⁶² This lower energy points to low-lying π^* orbitals, which further supports the conclusion of $[H_2-L1]^{2+}$ and $[H_2-L2]^{2+}$ being good π -acceptor ligands. Quantum yields are determined as 37% and 79% for $[H_2-L1]^{2+}$ ($\lambda_{ex} = 367$ nm) and $[H_2-L2]^{2+}$ ($\lambda_{ex} = 356$ nm). Streak camera measurements reveal a single-exponential decay of the luminescent state population with lifetimes of 10.2 and 5.9 ns in $[H_2-L1]^{2+}$ and $[H_2-L2]^{2+}$ (Figure 10).

The luminescence lifetime of the singlet excited state of pyrene in organic solvents is with 170–338 ns⁶⁵ remarkably higher than that of $[H_2-L2]^{2+}$, while for anthracene, it is 5.1 ns in MeOH and thus smaller than that in $[H_2-L1]^{2+}$.⁶⁶ The pronounced lifetime reduction in the case of $[H_2-L2]^{2+}$ is well-known for 1-substituted pyrenes.⁶⁷

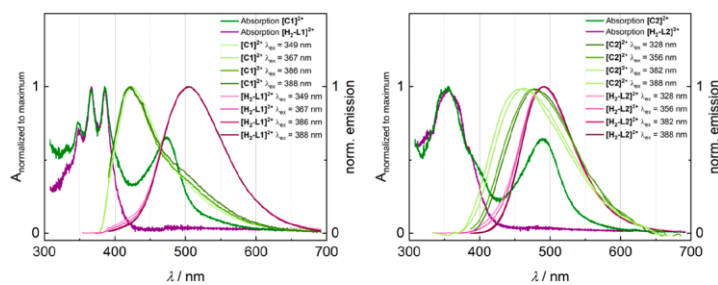


Figure 9. Luminescence spectra of $[\text{H}_2\text{-L1}]^{2+}$ (left, purple), $[\text{C1}]^{2+}$ (left, green), $[\text{H}_2\text{-L2}]^{2+}$ (right, purple), and $[\text{C2}]^{2+}$ (right, green) recorded in MeCN at room temperature.

Table 2. Photophysical Properties of $[\text{H}_2\text{-L1}]^{2+}$, $[\text{H}_2\text{-L2}]^{2+}$, $[\text{C1}]^{2+}$, and $[\text{C2}]^{2+}$ in Air-Saturated MeCN at Room Temperature^a

compound	λ_{em} [nm]	quantum yield Φ_{em} [%]	τ_{em} [ns]	τ_{MLCT} [ps]
$[\text{H}_2\text{-L1}]^{2+}$	502	37	10.2	
$[\text{C1}]^{2+}$	421	6	11.8 and 3.4	13.4
$[\text{H}_2\text{-L2}]^{2+}$	492	79	5.9	
$[\text{C2}]^{2+}$	468 ^b	2	6.9 and 3.4	12.8

^aThe quantum yields Φ_{em} were determined in degassed MeCN.

^bAveraged value of the emission maxima of $[\text{C2}]^{2+}$ shifting from $\lambda_{\text{em}} = 458$ to 477 nm.

Both complexes $[\text{C1}]^{2+}$ and $[\text{C2}]^{2+}$ also exhibit luminescence at room temperature in solution after excitation of the organic chromophores ($\lambda_{\text{ex}} = 320\text{--}390$ nm). The emission bands are shifted to higher energies, namely, $\lambda_{\text{em}} = 421$ nm for $[\text{C1}]^{2+}$ and $\lambda_{\text{em}} = 468$ nm for $[\text{C2}]^{2+}$, as shown in Figure 9, in comparison to ligands $[\text{H}_2\text{-L1}]^{2+}$ and $[\text{H}_2\text{-L2}]^{2+}$. The emission spectra of $[\text{C1}]^{2+}$ at different excitation energies match nearly perfectly; thus, in $[\text{C1}]^{2+}$, the emission originates always from the same radiative states irrespective of the excitation wavelength. In $[\text{C2}]^{2+}$, the emission maximum slightly shifts to shorter wavelengths (from $\lambda_{\text{em}} = 477$ to 458 nm), while changing to longer excitation wavelengths (from $\lambda_{\text{ex}} = 328$ to 388 nm). A potential origin of this effect might be the low emission intensity of $[\text{C2}]^{2+}$. The rather small shift of only 19

nm (870 cm^{-1}) does not contradict the conclusion that the emission in $[\text{C2}]^{2+}$ also originates from the same radiative state irrespective of the excitation energy.

The excitation spectra recorded at an emission wavelength of 430 nm for $[\text{C1}]^{2+}$ and $[\text{C2}]^{2+}$ are depicted in Figure 11. Excitation spectra recorded at an emission wavelength of 530 nm to track the MLCT absorption band for $[\text{C1}]^{2+}$ and $[\text{C2}]^{2+}$ and the corresponding excitation spectra of the pro-ligands $[\text{H}_2\text{-L1}]^{2+}$ and $[\text{H}_2\text{-L2}]^{2+}$ are shown in Figures S36–S39. The excitation spectra of both complexes reproduce merely the part of the absorption spectrum that is related to the organic chromophore but not the MLCT absorption band. Consequently, the observed emission is safely attributed to the singlet state of the appended organic chromophores anthracene and pyrene, respectively. However, through coordination to the iron(II) center, this chromophore-based luminescence is shifted by around 22 nm (1310 cm^{-1}) and at least 75 nm (4280 cm^{-1}) for anthracene in $[\text{C1}]^{2+}$ and pyrene in $[\text{C2}]^{2+}$. This is still in line with the interpretation of the low-lying π^* orbitals of the good π -acceptor ligands.

The quantum yields were determined to be 6% ($\lambda_{\text{ex}} = 367$ nm) for $[\text{C1}]^{2+}$ and 2% ($\lambda_{\text{ex}} = 356$ nm) for $[\text{C2}]^{2+}$; i.e., they are reduced by a factor of 6–40 compared to the free pro-ligands. In both complexes, two exponential time constants were required to fit the emission decay, with $\tau_1 = 11.8$ ns and $\tau_2 = 3.4$ ns in $[\text{C1}]^{2+}$ and $\tau_1 = 6.9$ ns and $\tau_2 = 3.4$ ns in $[\text{C2}]^{2+}$, respectively (Figure 10). Because of the similarity of the longer

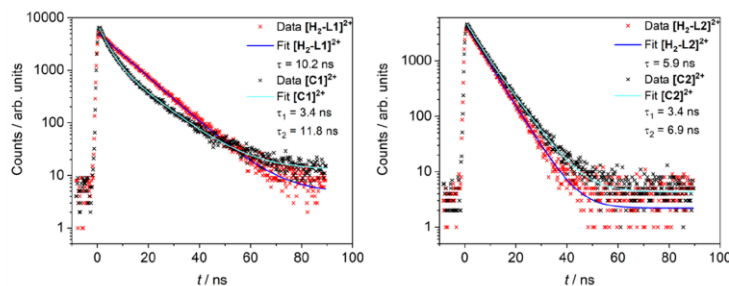


Figure 10. Emission decays of $[\text{H}_2\text{-L1}]^{2+}$ and $[\text{C1}]^{2+}$ (left) and of $[\text{H}_2\text{-L2}]^{2+}$ and $[\text{C2}]^{2+}$ (right) after excitation with $\lambda_{\text{ex}} = 388$ nm. Blue curves represent monoexponential fits to the luminescence kinetics of the pro-ligands and cyan curves double-exponential fits to the luminescence kinetics of the complexes. The obtained time constants are given in the legends.

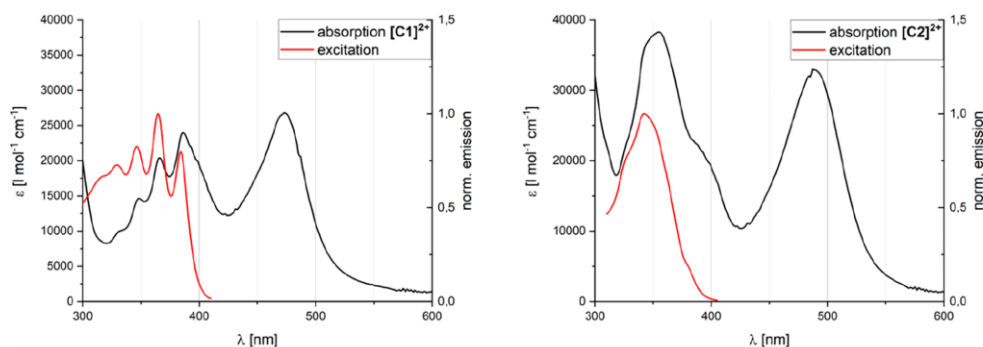


Figure 11. Absorption (black) and normalized excitation (red) spectra of $[C1]^{2+}$ (left) and $[C2]^{2+}$ (right). Excitation spectra showing the intensity of the emission at $\lambda_{em} = 430$ nm as a function of the excitation wavelength.

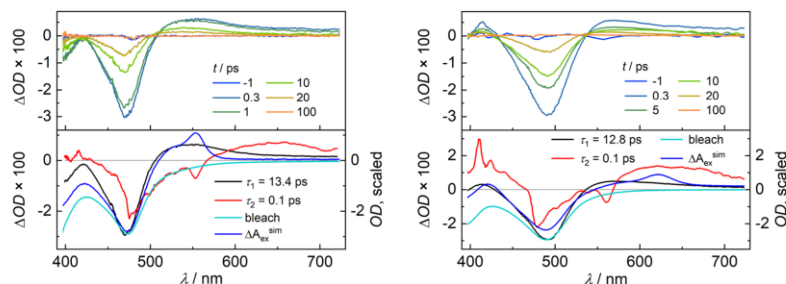


Figure 12. Transient absorption spectra (top) and DAS (bottom) of $[C1]^{2+}$ (left) and $[C2]^{2+}$ (right). Excited-state differential spectra of $[C]^{3+} - [C]^{2+}$ approximated according to McCusker et al.⁷² and scaled for comparison.

lifetimes τ_1 to those of the pro-ligands, 10.2 ns for $[H_2-L1]^{2+}$ and 5.9 ns for $[H_2-L2]^{2+}$, and because of the fact that excitation spectra of the complexes resemble the absorption spectra of the pro-ligands, the luminescence is assigned to fluorescence of the organic chromophore (Figures 11 and S35–S38). The shorter average lifetimes of the complexes compared to the ligands can only partially explain the strongly reduced quantum yields of the complexes. However, from Figure 9, it becomes clear that in the spectral region below 400 nm not only do the organic chromophores absorb but there is also a background absorption due to transitions involving other absorbing moieties of the complexes. The corresponding excited states probably have short lifetimes and do not contribute to the emission. In this case, a large fraction of the absorbed photons does not lead to population of the local chromophore states and does not lead to fluorescence, resulting in a low overall emission yield.

Complex formation by coordination of the chromophore-functionalized ligand to iron(II) results in a second, shorter lifetime of $\tau_2 = 3.4$ ns in the luminescence decay of $[C1]^{2+}$ and $[C2]^{2+}$. This suggests that an additional nonradiative pathway is opened by the iron(II) center. Figure 9 shows that a broad spectral overlap between the singlet emission band of the ligand and the 1MLCT absorption of the complexes exists. A key requirement for a Förster resonance energy transfer (FRET) or a Dexter energy transfer is thus fulfilled.⁶⁸ The

excited organic chromophore singlet state can therefore act as a donor in a FRET process, resulting in a population of the 1MLCT state. However, because of the behavior found in the absorption and emission spectra and the theoretical results (cf. the upper panel in Figure 5A), which indicates a CT character of low-lying bim-ant transitions, it has to be admitted here that an IC could be a more appropriate description of this effect. We will thus use this more general expression in the remaining discussion because separation of the complex into an organic chromophore and a Fe-bim complex is an oversimplification of the real situation. In fact, because of the delocalized character of the involved states, a double-hole process characterized by the interference of two CT states [organic chromophore to bim and iron(II) to bim] is also a plausible mechanism.

The 1MLCT state decays rapidly to the 3MLCT state and further to the non-luminescent $^3MC/{}^5MC$ states. Within this excited-state kinetic model, the time constant of the IC process amounts to 3.4 ns in both $[C1]^{2+}$ and $[C2]^{2+}$. This contributes to the reduced luminescence quantum yields of $[C1]^{2+}$ and $[C2]^{2+}$ with respect to their pro-ligands $[H_2-L1]^{2+}$ and $[H_2-L2]^{2+}$. The rate of the IC depends also on the orientation of the transition dipole of the emission relative to the dipole of the absorbing transition.⁶⁸ Because of the rotational flexibility of the appended chromophores, the molecules of an ensemble probably exhibit a distribution of angles between the transition

dipoles. This would result in the distribution of transfer rates and in nonexponential kinetics. The fitted double-exponential decay obtained by the fitting procedures then represents an approximation of this behavior. The short time constants reflect the dynamics in molecules with a favorable dipole orientation and strong coupling, while the longer constants of 11.8 and 6.9 ns are representative for molecules with small or negligible energy-transfer rates.

Following the discussion above, attachment of an organic chromophore to a photoactive iron(II) complex shows unprecedented and so far unreported luminescence results.⁶⁹ No MLCT emission is observed, but the emission wavelength of the organic chromophore can be tuned by coupling to the bim ligand motif and coordination to an iron(II) center over a range of up to 110 nm (5780 cm⁻¹). The result of forming a complex of the chromophore-connected ligand with the iron metal center indeed affects the luminescence originating from the local states of the organic chromophore in a characteristic way.

According to the preceding discussion, luminescence measurements cannot access the photochemically relevant MLCT states. Therefore, femtosecond (fs)-transient absorption measurements with excitation pulses at 480 nm were used to track the early excited-state dynamics of [C1]²⁺ and [C2]²⁺. The transient absorption spectra are shown in Figure 12 together with decay-associated spectra (DAS) resulting from a global multiexponential fit of the data. For both complexes, a pronounced excited-state absorption (ESA) is found at wavelengths larger than 500 nm besides the ground-state bleaching at 480 nm. The kinetics can be fitted with two time constants that are similar in [C1]²⁺ and [C2]²⁺. In both compounds, a very short lifetime of 0.1 ps and a longer one that differs slightly with 13.4 ps in [C1]²⁺ and 12.8 ps in [C2]²⁺ were found. The DAS of the long-lived component show two ESA signals, in the blue and red spectral regions, respectively. This feature is very similar to the reported transient absorption spectra for the ³MLCT state of [C0]²⁺ and different from the characteristic ESA of ³T₂ states, observed, for example, in [Fe(tpy)₂]²⁺.³⁰ Moreover, the difference spectra of [C1]³⁺–[C1]²⁺ and [C2]³⁺–[C2]²⁺ obtained by spectroelectrochemistry (see the Supporting Information for details) reproduce the ESA reasonably well, except for a sharp signal in each case, assigned to a reduced ligand. Consequently, the 13.4 ps time constant was assigned to the ³MLCT lifetime of [C1]²⁺ and 12.8 ps to the ³MLCT lifetime of [C2]²⁺. The fast decay component with a time constant of 0.1 ps shows in both complexes sharp features, which are typical for Raman artifacts at time zero, and red-shifted replicas of the main ESA and bleach bands pointing to contributions of vibrational redistribution.^{36,70} Therefore, this component is not further considered in the analysis. Because no feature in the transient absorption points to the population of MC states, the ³MC lifetimes in [C1]²⁺ and [C2]²⁺ are supposed to be much shorter than the ³MLCT lifetimes. In this case, the observed dynamics leads to negligible population of the MC states and repopulation of the electronic ground states from the ³MLCT states occurs essentially within the ³MLCT lifetime. This behavior is frequently reported for iron NHC complexes with ³MLCT lifetimes in the picosecond range.^{34,36,71}

In order to identify an excitation wavelength dependence of the ultrafast relaxation dynamics, transient absorption measurements with pump pulses at 400 nm were additionally carried

out. The corresponding transient spectra and DAS of a global analysis are shown in Figure S39. The spectra are basically identical with those obtained after excitation at 480 nm, and the dynamics are very similar. For the slowest and dominant exponential component, a decay time of 12.2 ps was found in the case of [C1]²⁺ and 14.2 ps for [C2]²⁺. This matches within our experimental accuracy the results after excitation at 480 nm, which indicates that depopulation of the ³MLCT state is at most weakly dependent on the excess energy. The fast component of the transient absorption seems to be slightly slower after excitation at 400 nm and is fitted by a time constant of 0.3 ps for [C1]²⁺ and of 0.2 ps for [C2]²⁺. This is probably caused by the larger excess energy, which results in more pronounced vibrational redistribution processes. In [C2]²⁺, an additional intermediate decay component with a time constant of 3.2 ps is observed if the complex is pumped at 400 nm. Its origin is unknown, but it might result from a relaxation process within the MLCT states. These states probably contribute to the shoulder of the second absorption band around 400 nm in the stationary spectrum of [C2]²⁺ (cf. Figure 11). A long-lived component that could be assigned to an emitting local state of the chromophores was observed for neither of the complexes. This is in line with the fluorescence excitation spectra, which indicate that the emitting states are only efficiently excited at wavelengths shorter than 400 nm.

Long-lived triplet states can undergo energy transfer to ³O₂ and generate highly reactive ¹O₂.⁷³ To finally complement the model for the excited-state dynamics, the existence of long-lived triplet states is chemically probed by the reaction of luminescent DPBF with reactive ¹O₂ to nonluminescent *o*-dibenzoylbenzene.⁷⁴ In none of the probed iron complexes [C0]²⁺–[C2]²⁺ was reactive ¹O₂ detected after irradiation with λ_{irr} = 480 nm (Figure S40). [Ru(bpy)₃]²⁺ as a reference for effective oxygen sensitization is selected for comparison. This result is expected for [C0]²⁺ because in this compound the only possible triplet states are the short-lived ³MLCT and ³MC states. In contrast, the excited-state landscapes in [C1]²⁺ and [C2]²⁺ could, in principle, include ³Chrom states in addition to the ³MLCT states. The lifetimes of the anthracene and pyrene triplet states are typically in the microsecond range and therefore are able to sensitize the formation of ¹O₂.⁶⁷ Accordingly, the lack of ¹O₂ formation after irradiation of [C1]²⁺ and [C2]²⁺ suggests that there is no appreciable population of ³Chrom states in these complexes. Consequently, no equilibrium between ³Chrom and ³MLCT states—which is found in ruthenium complexes that exhibit the “reservoir” effect^{40,41,75,76}—is present in [C1]²⁺ and [C2]²⁺. Rapid deactivation of the ³MLCT state occurs.

Additionally, the population of ³Chrom via ¹Chrom states in [H₂-L1]²⁺, [H₂-L2]²⁺, [C1]²⁺, and [C2]²⁺ has been probed with an excitation wavelength of λ_{irr} = 346 nm (Figure S41). For none of the compounds could a significant reactive oxygen generation be detected. This is in line with the assignment of the long-lived luminescence lifetime in [H₂-L1]²⁺ and [H₂-L2]²⁺ to singlet states.

In summary, these results indicate the absence of observable ISC from the ¹Chrom state to the ³Chrom state due to the spin–orbit coupling imposed by iron(II) in [C1]²⁺ and [C2]²⁺. Accordingly, the ³Chrom state cannot act as a reservoir for emission originating from the ³MLCT state. Instead, emission can only be observed from the states that are dominated by the ¹Chrom state, which is quenched by IC into the ¹MLCT states in [C1]²⁺ and [C2]²⁺. Although the

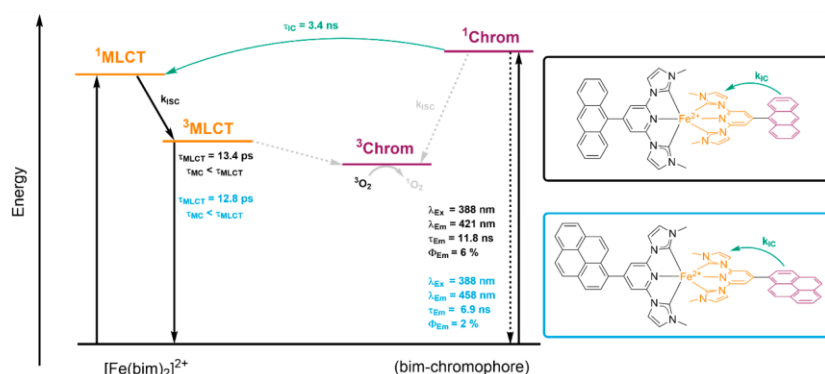


Figure 13. Schematic representation of the excited-state dynamics in $[C1]^{2+}$ (black values) and $[C2]^{2+}$ (blue values). $^3\text{MLCT}$ lifetime as seen by transient absorption spectroscopy (black arrow), $^1\text{Chrom}$ lifetime and IC time as deduced from streak camera measurements (black dotted/green arrow). $^3\text{Chrom}$ is not effectively populated by $^1\text{Chrom}$ or the $^3\text{MLCT}$ state according to $^1\text{O}_2$ experiments (gray dotted arrows). The nomenclature $^3\text{Chrom}$ indicates a chromophore-dominated electronic state within the bim-chromophore ligand assembly.

discussed iron(II) complexes are indeed luminescent, the emission properties result from a metal-modified emission from the organic chromophore. The excited-state details are summarized in Figure 13. It has to be emphasized that the separation between $[\text{Fe}(\text{bim})_2]^{2+}$ and the chromophore constituents is somewhat artificial and used for better clarity and comparison with ruthenium-based work. Actually, the involved chromophore transitions are likely to be delocalized onto the bim ligand (CT type) such that a strict separation does not conform to reality. This also explained the failure of a simple Frenkel exciton description of the absorption spectra. The energy of the states is estimated based on the literature values.^{23,67} High-energy irradiation causes an excitation of the appended anthracene or pyrene connected to the NHC pyridine ligand directly populating the singlet state of the chromophore. ISC into the low-lying chromophore-localized triplet state does not occur to a significant extent. Instead, either fluorescence or an IC from the chromophore-dominated ligand states to the $^1\text{MLCT}$ state occurs. The $^1\text{MLCT}$ state undergoes fast ISC into the $^3\text{MLCT}$ state, as deduced from the fs-transient absorption data. In contrast to chromophore-functionalized ruthenium(II) polypyridine complexes, no reservoir effect, allowing for a $^3\text{MLCT} \rightleftharpoons ^3\text{Chrom}$ equilibrium, resulting in long-lived MLCT states, is observed here. Two reasons might be speculated for this observation: on the one hand, the mismatch between the $^3\text{MLCT}$ and $^3\text{Chrom}$ state energies for both anthracenyl and pyrenyl substituents; on the other hand, the very short lifetime of the $^3\text{MLCT}$ state precluding back-IC to chromophore-dominated triplet states.

CONCLUSION

The transfer of the multichromophoric approach from ruthenium(II) polypyridine complexes to iron(II) NHC complexes with the aim of generating long-lived $^3\text{MLCT}$ states by the so-called reservoir effect has been investigated. Coordination of deprotonated $[\text{H}_2\text{-L1}]^{2+}$ and $[\text{H}_2\text{-L2}]^{2+}$ to iron(II) indeed yields luminescent complexes. The origin of the emission lies, however, in singlet states that are localized at the respective organic chromophores' anthracene and pyrene. The connection of these chromophores to the cationic

bis(NHC) pyridine pro-ligands and the charged iron(II) center shifts the emission from 399 nm in anthracene and 383 nm in pyrene to 502 nm in $[\text{H}_2\text{-L1}]^{2+}$ and 492 nm in $[\text{H}_2\text{-L2}]^{2+}$, i.e., by about 100 nm (5140 cm^{-1}) and 110 nm (5780 cm^{-1}), respectively. The combination of streak camera luminescence measurements, fs-transient absorption spectroscopy, and $^1\text{O}_2$ generation yields detailed insights into the excited-state dynamics in these new complexes. A $^3\text{MLCT}$ lifetime of around 14 ps was obtained in both complexes, which is slightly increased compared to that of the unfunctionalized complex.³⁰ This short lifetime of the $^3\text{MLCT}$ state, together with an IC on the singlet hypersurface taking place within 3.4 ns from the chromophore-dominated singlet to the $^1\text{MLCT}$ state, is most likely preventing a long-lived $^3\text{MLCT}$ state because no population of the $^3\text{Chrom}$ state of the chromophore can be achieved. Accordingly, no "reservoir" for the MLCT state exists.

With multichromophoric iron(II) NHC complexes, the absorption properties can be tuned and the MLCT absorption maximum can be shifted toward the red part of the visible spectrum. An antenna effect can be observed from the excited-state chromophore to the $^1\text{MLCT}$ state of the iron(II) chromophore. Yet, no full ruthenium(II)-like behavior results, most probably because of the very short $^3\text{MLCT}$ lifetime of the iron(II) complexes. Consequently, the $^3\text{MLCT}$ lifetime needs to be further increased in order to enable useful rate constants in the equilibrium $^3\text{MLCT} \rightleftharpoons ^3\text{Chrom}$. Additionally, the influence of the energy match between the two triplet states has to be further investigated. What remains open is the role of the spin-orbit coupling via the heavy-atom effect imposed by iron on the potentially useful $^1\text{Chrom} \rightarrow ^3\text{Chrom}$ ISC rate.

ASSOCIATED CONTENT

Supporting Information

The Supporting Information is available free of charge at <https://pubs.acs.org/doi/10.1021/acs.inorgchem.0c02039>.

NMR spectra, MS data, information on computational studies, electrochemistry, details concerning electrochemistry and spectroelectrochemistry, additional results

concerning luminescence properties, results of transient absorption measurements at 400 nm excitation wavelength, and results for $^1\text{O}_2$ experiments (PDF)

AUTHOR INFORMATION

Corresponding Author

Matthias Bauer – Faculty of Science, Chemistry Department and Center for Sustainable Systems Design, Paderborn University, 33098 Paderborn, Germany; orcid.org/0000-0002-9294-6076; Email: matthias.bauer@uni-paderborn.de

Authors

Philipp Dierks – Faculty of Science, Chemistry Department and Center for Sustainable Systems Design, Paderborn University, 33098 Paderborn, Germany

Ayla Pöpcke – Institute of Physics and Department of Life, Light and Matter, University of Rostock, 18059 Rostock, Germany

Olga S. Bokareva – Institute of Physics, University of Rostock, 18059 Rostock, Germany; Department of Physical Chemistry, Kazan Federal University, 420008 Kazan, Russia; orcid.org/0000-0002-2313-7996

Björn Altenburger – Institute of Physics, University of Rostock, 18059 Rostock, Germany; Department of Physics, Chalmers University of Technology, SE-412 96 Göteborg, Sweden

Thomas Reuter – Department of Chemistry, Johannes Gutenberg University of Mainz, 55128 Mainz, Germany

Katja Heinze – Department of Chemistry, Johannes Gutenberg University of Mainz, 55128 Mainz, Germany; orcid.org/0000-0003-1483-4156

Oliver Kühn – Institute of Physics and Department of Life, Light and Matter, University of Rostock, 18059 Rostock, Germany; orcid.org/0000-0002-5132-2961

Stefan Lochbrunner – Institute of Physics and Department of Life, Light and Matter, University of Rostock, 18059 Rostock, Germany; orcid.org/0000-0001-9729-8277

Complete contact information is available at:

<https://pubs.acs.org/10.1021/acs.inorgchem.0c02039>

Notes

The authors declare no competing financial interest.

ACKNOWLEDGMENTS

Financial support from the Deutsche Forschungsgemeinschaft [Priority Program SPP 2102 "Light-controlled reactivity of metal complexes" (Grants BA 4467/7-1, HE 2778/14-1, LO 714/11-1, and KU952/12-1)] is gratefully acknowledged. P.D. thanks the Fonds der Chemischen Industrie for a Kekulé grant. O.B. thanks Omar Baig (University of Vienna) for helpful discussions of the fragmentation scheme for the assignment of transitions and is grateful for Grant 14.Y26.31.0019 from the Ministry of Education and Science of Russian Federation providing financial support.

REFERENCES

- Bizzarri, C.; Spuling, E.; Knoll, D. M.; Volz, D.; Bräse, S. Sustainable metal complexes for organic light-emitting diodes (OLEDs). *Coord. Chem. Rev.* **2018**, *373*, 49–82.
- Förster, C.; Heinze, K. Photophysics and photochemistry with Earth-abundant metals - fundamentals and concepts. *Chem. Soc. Rev.* **2020**, *49*, 1057–1070.
- Wenger, O. S. Is Iron the New Ruthenium? *Chem. - Eur. J.* **2019**, *25*, 6043–6052.

- Balzani, V.; Bergamini, G.; Campagna, S.; Puntoriero, F. Photochemistry and Photophysics of Coordination Compounds: Overview and General Concepts. In *Photochemistry and Photophysics of Coordination Compounds I*; Balzani, V., Campagna, S., Eds.; Topics in Current Chemistry; Springer: Berlin, 2007; pp 1–36.

- McCusker, J. K. Electronic structure in the transition metal block and its implications for light harvesting. *Science (Washington, DC, U. S.)* **2019**, *363*, 484–488.

- Damrauer, N. H.; Cerullo, G.; Yeh, A.; Boussie, T. R.; Shank, C. V.; McCusker, J. K. Femtosecond Dynamics of Excited-State Evolution in $[\text{Ru}(\text{bpy})_3]^{2+}$. *Science (Washington, DC, U. S.)* **1997**, *275*, 54–57.

- Prier, C. K.; Rankic, D. A.; MacMillan, D. W. C. Visible light photoredox catalysis with transition metal complexes: applications in organic synthesis. *Chem. Rev.* **2013**, *113*, 5322–5363.

- Wenger, O. S. Photoactive Complexes with Earth-Abundant Metals. *J. Am. Chem. Soc.* **2018**, *140*, 13522–13533.

- Wenger, O. S. A bright future for photosensitizers. *Nat. Chem.* **2020**, *12*, 323–324.

- Liu, Y.; Persson, P.; Sundström, V.; Wärnmark, K. Fe N-Heterocyclic Carbene Complexes as Promising Photosensitizers. *Acc. Chem. Res.* **2016**, *49*, 1477–1485.

- Kaufhold, S.; Wärnmark, K. Design and Synthesis of Photoactive Iron N-Heterocyclic Carbene Complexes. *Catalysts* **2020**, *10*, 132.

- Heberle, M.; Tschierlei, S.; Rockstroh, N.; Ringenberg, M.; Frey, W.; Junge, H.; Beller, M.; Lochbrunner, S.; Karnahl, M. Heteroleptic Copper Photosensitizers: Why an Extended π -System Does Not Automatically Lead to Enhanced Hydrogen Production. *Chem. - Eur. J.* **2017**, *23*, 312–319.

- McCusker, C. E.; Castellano, F. N. Design of a long-lifetime, earth-abundant, aqueous compatible Cu(I) photosensitizer using cooperative steric effects. *Inorg. Chem.* **2013**, *52*, 8114–8120.

- Zhang, Y.; Petersen, J. L.; Milsman, C. A Luminescent Zirconium(IV) Complex as a Molecular Photosensitizer for Visible Light Photoredox Catalysis. *J. Am. Chem. Soc.* **2016**, *138*, 13115–13118.

- Zhang, Y.; Lee, T. S.; Favale, J. M.; Leary, D. C.; Petersen, J. L.; Scholes, G. D.; Castellano, F. N.; Milsman, C. Delayed fluorescence from a zirconium(IV) photosensitizer with ligand-to-metal charge-transfer excited states. *Nat. Chem.* **2020**, *12*, 345–352.

- Herr, P.; Glaser, F.; Büldt, L. A.; Larsen, C. B.; Wenger, O. S. Long-Lived, Strongly Emissive, and Highly Reducing Excited States in Mo(0) Complexes with Chelating Isocyanides. *J. Am. Chem. Soc.* **2019**, *141*, 14394–14402.

- Kjær, K. S.; Kaul, N.; Prakash, O.; Chábera, P.; Rosemann, N. W.; Honarfar, A.; Gordivska, O.; Fredin, L. A.; Bergquist, K.-E.; Häggström, L.; et al. Luminescence and reactivity of a charge-transfer excited iron complex with nanosecond lifetime. *Science (Washington, DC, U. S.)* **2019**, *363*, 249–253.

- Chábera, P.; Liu, Y.; Prakash, O.; Thyraug, E.; Nahhas, A. E.; Honarfar, A.; Essén, S.; Fredin, L. A.; Harlang, T. C. B.; Kjær, K. S.; et al. A low-spin Fe(III) complex with 100-ps ligand-to-metal charge transfer photoluminescence. *Nature* **2017**, *543*, 695–699.

- Braun, J. D.; Lozada, I. B.; Kolodziej, C.; Burda, C.; Newman, K. M. E.; van Lierop, J.; Davis, R. L.; Herbert, D. E. Iron(II) coordination complexes with panchromatic absorption and nanosecond charge-transfer excited state lifetimes. *Nat. Chem.* **2019**, *11*, 1144–1150.

- Zimmer, P.; Müller, P.; Burkhardt, L.; Schepper, R.; Neuba, A.; Steube, J.; Dietrich, F.; Flörke, U.; Mangold, S.; Gerhards, M.; et al. N-Heterocyclic Carbene Complexes of Iron as Photosensitizers for Light-Induced Water Reduction. *Eur. J. Inorg. Chem.* **2017**, *2017*, 1504–1509.

- Duchanois, T.; Liu, L.; Pastore, M.; Monari, A.; Cebrián, C.; Trolez, Y.; Darari, M.; Magra, K.; Francés-Monerris, A.; Domenichini, E.; et al. NHC-Based Iron Sensitizers for DSSCs. *Inorganics* **2018**, *6*, 63.

- (22) Penfold, T. J.; Gindensperger, E.; Daniel, C.; Marian, C. M. Spin-Vibronic Mechanism for Intersystem Crossing. *Chem. Rev.* **2018**, *118*, 6975–7025.
- (23) Pápai, M.; Vankó, G.; Rozgonyi, T.; Penfold, T. J. High-Efficiency Iron Photosensitizer Explained with Quantum Wavepacket Dynamics. *J. Phys. Chem. Lett.* **2016**, *7*, 2009–2014.
- (24) Baitalik, S.; Wang, X.-y.; Schmehl, R. H. A trimetallic mixed Ru(II)/Fe(II) terpyridyl complex with a long-lived excited state in solution at room temperature. *J. Am. Chem. Soc.* **2004**, *126*, 16304–16305.
- (25) Medlycott, E. A.; Hanan, G. S. Designing tridentate ligands for ruthenium(II) complexes with prolonged room temperature luminescence lifetimes. *Chem. Soc. Rev.* **2005**, *34*, 133–142.
- (26) Jamula, L. L.; Brown, A. M.; Guo, D.; McCusker, J. K. Synthesis and characterization of a high-symmetry ferrous polypyridyl complex: approaching the $5T_2/3T_1$ crossing point for Fe(II). *Inorg. Chem.* **2014**, *53*, 15–17.
- (27) Britz, A.; Gawelda, W.; Assefa, T. A.; Jamula, L. L.; Yarranton, J. T.; Galler, A.; Khakhulin, D.; Diez, M.; Harder, M.; Doumy, G.; et al. Using Ultrafast X-ray Spectroscopy To Address Questions in Ligand-Field Theory: The Excited State Spin and Structure of Fe(dcpp)22. *Inorg. Chem.* **2019**, *58*, 9341–9350.
- (28) Mengel, A. K. C.; Förster, C.; Breivogel, A.; Mack, K.; Ochsmann, J. R.; Laquai, F.; Ksenofontov, V.; Heinze, K. A heteroleptic push-pull substituted iron(II) bis(tridentate) complex with low-energy charge-transfer states. *Chem. - Eur. J.* **2015**, *21*, 704–714.
- (29) Förster, C.; Dorn, M.; Reuter, T.; Otto, S.; Davarci, G.; Reich, T.; Carrella, L.; Rentschler, E.; Heinze, K. Ddpd as Expanded Terpyridine: Dramatic Effects of Symmetry and Electronic Properties in First Row Transition Metal Complexes. *Inorganics* **2018**, *6*, 86.
- (30) Liu, Y.; Harlang, T.; Canton, S. E.; Chábera, P.; Suárez-Alcántara, K.; Fleckhaus, A.; Vithanage, D. A.; Göransson, E.; Corani, A.; Lomoth, R.; et al. Towards longer-lived metal-to-ligand charge transfer states of iron(II) complexes: an N-heterocyclic carbene approach. *Chem. Commun. (Cambridge, U. K.)* **2013**, *49*, 6412–6414.
- (31) Chábera, P.; Kjaer, K. S.; Prakash, O.; Honarfar, A.; Liu, Y.; Fredin, L. A.; Harlang, T. C. B.; Lidin, S.; Uhlig, J.; Sundström, V.; et al. FeII Hexa N-Heterocyclic Carbene Complex with a 528 ps Metal-to-Ligand Charge-Transfer Excited-State Lifetime. *J. Phys. Chem. Lett.* **2018**, *9*, 459–463.
- (32) Fredin, L. A.; Pápai, M.; Rozsályi, E.; Vankó, G.; Wärnmark, K.; Sundström, V.; Persson, P. Exceptional Excited-State Lifetime of an Iron(II)-N-Heterocyclic Carbene Complex Explained. *J. Phys. Chem. Lett.* **2014**, *5*, 2066–2071.
- (33) Zimmer, P.; Burkhardt, L.; Friedrich, A.; Steube, J.; Neuba, A.; Schepper, R.; Müller, P.; Flörke, U.; Huber, M.; Lochbrunner, S.; et al. The Connection between NHC Ligand Count and Photophysical Properties in Fe(II) Photosensitizers: An Experimental Study. *Inorg. Chem.* **2018**, *57*, 360–373.
- (34) Duchanois, T.; Etienne, T.; Cebrián, C.; Liu, L.; Monari, A.; Beley, M.; Assfeld, X.; Haacke, S.; Gros, P. C. An Iron-Based Photosensitizer with Extended Excited-State Lifetime: Photophysical and Photovoltaic Properties. *Eur. J. Inorg. Chem.* **2015**, *2015*, 2469–2477.
- (35) Steube, J.; Burkhardt, L.; Pápcke, A.; Moll, J.; Zimmer, P.; Schoch, R.; Wölper, C.; Heinze, K.; Lochbrunner, S.; Bauer, M. Excited-State Kinetics of an Air-Stable Cyclometalated Iron(II) Complex. *Chem. - Eur. J.* **2019**, *25*, 11826–11830.
- (36) Liu, L.; Duchanois, T.; Etienne, T.; Monari, A.; Beley, M.; Assfeld, X.; Haacke, S.; Gros, P. C. A new record excited state (3)MLCT lifetime for metalorganic iron(ii) complexes. *Phys. Chem. Chem. Phys.* **2016**, *18*, 12550–12556.
- (37) Duchanois, T.; Etienne, T.; Beley, M.; Assfeld, X.; Perpète, E. A.; Monari, A.; Gros, P. C. Heteroleptic Pyridyl-Carbene Iron Complexes with Tuneable Electronic Properties. *Eur. J. Inorg. Chem.* **2014**, *2014*, 3747–3753.
- (38) Zimmer, P.; Burkhardt, L.; Schepper, R.; Zheng, K.; Gosztola, D.; Neuba, A.; Flörke, U.; Wölper, C.; Schoch, R.; Gawelda, W.; et al. Towards Noble-Metal-Free Dyads: Ground and Excited State Tuning by a Cobalt Dimethylglyoxime Motif Connected to an Iron N-Heterocyclic Carbene Photosensitizer. *Eur. J. Inorg. Chem.* **2018**, *2018*, 5203–5214.
- (39) Tyson, D. S.; Bialecki, J.; Castellano, F. N. Ruthenium(II) complex with a notably long excited state lifetime. *Chem. Commun.* **2000**, 2355–2356.
- (40) Tyson, D. S.; Castellano, F. N. Intramolecular Singlet and Triplet Energy Transfer in a Ruthenium(II) Diimine Complex Containing Multiple Pyrenyl Chromophores. *J. Phys. Chem. A* **1999**, *103*, 10955–10960.
- (41) Morales, A. F.; Accorsi, G.; Armaroli, N.; Barigelletti, F.; Pope, S. J. A.; Ward, M. D. Interplay of Light Antenna and Excitation “Energy Reservoir” Effects in a Bichromophoric System Based on Ruthenium-Polypyridine and Pyrene Units Linked by a Long and Flexible Poly(ethylene glycol) Chain. *Inorg. Chem.* **2002**, *41*, 6711–6719.
- (42) Passalacqua, R.; Loiseau, F.; Campagna, S.; Fang, Y.-Q.; Hanan, G. S. In search of ruthenium(II) complexes based on tridentate polypyridine ligands that feature long-lived room-temperature luminescence: the multichromophore approach. *Angew. Chem., Int. Ed.* **2003**, *42*, 1608–1611.
- (43) Basu, U.; Khan, I.; Koley, D.; Saha, S.; Kondiah, P.; Chakravarty, A. R. Nuclear targeting terpyridine iron(II) complexes for cellular imaging and remarkable photocytotoxicity. *J. Inorg. Biochem.* **2012**, *116*, 77–87.
- (44) Francés-Monerris, A.; Gros, P. C.; Pastore, M.; Assfeld, X.; Monari, A. Photophysical properties of bichromophoric Fe(II) complexes bearing an aromatic electron acceptor. *Theor. Chem. Acc.* **2019**, *138*, 13522.
- (45) Krasovskiy, A.; Krasovskaya, V.; Knochel, P. Mixed Mg/Li amides of the type R2NMgCl. LiCl as highly efficient bases for the regioselective generation of functionalized aryl and heteroaryl magnesium compounds. *Angew. Chem., Int. Ed.* **2006**, *45*, 2958–2961.
- (46) Park, H.-J.; Chung, Y. K. Ru(II) complexes with N-heterocyclic carbene ligands or terpyridine analogues: synthesis, characterization, and electrochemical and proton-dependent spectrometric properties. *Dalton transactions (Cambridge, England: 2003)* **2012**, *41*, S678–S686.
- (47) Nicholson, R. S.; Shain, I. Theory of Stationary Electrode Polarography. Single Scan and Cyclic Methods Applied to Reversible, Irreversible, and Kinetic Systems. *Anal. Chem.* **1964**, *36*, 706–723.
- (48) Heinze, J. Cyclovoltammetrie — die “Spektroskopie” des Elektrochemikers. *Angew. Chem.* **1984**, *96*, 823–840.
- (49) Randles, J. E. B. A cathode ray polarograph. Part II.—The current-voltage curves. *Trans. Faraday Soc.* **1948**, *44*, 327–338.
- (50) Pápcke, A.; Friedrich, A.; Lochbrunner, S. Revealing the initial steps in homogeneous photocatalysis by time-resolved spectroscopy. *J. Phys.: Condens. Matter* **2020**, *32*, 153001.
- (51) Demas, J. N.; Harris, E. W.; McBride, R. P. Energy transfer from luminescent transition metal complexes to oxygen. *J. Am. Chem. Soc.* **1977**, *99*, 3547–3551.
- (52) Tomasi, J.; Mennucci, B.; Cammi, R. Quantum mechanical continuum solvation models. *Chem. Rev.* **2005**, *105*, 2999–3093.
- (53) Livshits, E.; Baer, R. A density functional theory for symmetric radical cations from bonding to dissociation. *J. Phys. Chem. A* **2008**, *112*, 12789–12791.
- (54) Stein, T.; Kronik, L.; Baer, R. Reliable prediction of charge transfer excitations in molecular complexes using time-dependent density functional theory. *J. Am. Chem. Soc.* **2009**, *131*, 2818–2820.
- (55) Stein, T.; Kronik, L.; Baer, R. Prediction of charge-transfer excitations in coumarin-based dyes using a range-separated functional tuned from first principles. *J. Chem. Phys.* **2009**, *131*, 244119.
- (56) Möhle, T.; Bokareva, O. S.; Grell, G.; Kühn, O.; Bokarev, S. I. Tuned Range-Separated Density Functional Theory and Dyson Orbital Formalism for Photoelectron Spectra. *J. Chem. Theory Comput.* **2018**, *14*, 5870–5880.
- (57) May, V.; Kühn, O. *Charge and energy transfer dynamics in molecular systems*, 3rd ed.; Wiley-VCH: Weinheim, Germany, 2011.

- (58) Preuße, M.; Bokarev, S. I.; Aziz, S. G.; Kühn, O. Towards an ab initio theory for metal L-edge soft X-ray spectroscopy of molecular aggregates. *Struct. Dyn.* **2016**, *3*, 62601.
- (59) Frisch, M. J.; Trucks, G. W.; Schlegel, H. B.; Scuseria, G. E.; Robb, M. A.; Cheeseman, J. R.; Scalmani, G.; Barone, V.; Petersson, G. A.; Nakatsuji, H.; et al. *Gaussian 16*, revision C.01; Gaussian Inc.: Wallingford, CT, 2016.
- (60) Plasser, F. TheoDORE: A toolbox for a detailed and automated analysis of electronic excited state computations. *J. Chem. Phys.* **2020**, *152*, 84108.
- (61) Walker, S. D.; Barder, T. E.; Martinelli, J. R.; Buchwald, S. L. A rationally designed universal catalyst for Suzuki-Miyaura coupling processes. *Angew. Chem., Int. Ed.* **2004**, *43*, 1871–1876.
- (62) Kumke, M. U.; Löhmansröben, H. G.; Roch, T. Fluorescence spectroscopy of polynuclear aromatic compounds in environmental monitoring. *J. Fluoresc.* **1995**, *5*, 139–152.
- (63) Lakowicz, J. R. *Principles of fluorescence spectroscopy*, 3rd ed.; Springer: New York, 2006.
- (64) Braterman, P. S.; Song, J. I.; Peacock, R. D. Electronic absorption spectra of the iron(II) complexes of 2,2'-bipyridine, 2,2'-bipyrimidine, 1,10-phenanthroline, and 2,2':6',2''-terpyridine and their reduction products. *Inorg. Chem.* **1992**, *31*, 555–559.
- (65) Nakajima, A. Fluorescence Lifetime of Pyrene in Different Solvents. *Bull. Chem. Soc. Jpn.* **1973**, *46*, 2602–2604.
- (66) Boens, N.; Qin, W.; Basarić, N.; Hofkens, J.; Ameloot, M.; Pouget, J.; Lefèvre, J.-P.; Valeur, B.; Gratton, E.; vandeVen, M.; et al. Fluorescence lifetime standards for time and frequency domain fluorescence spectroscopy. *Anal. Chem.* **2007**, *79*, 2137–2149.
- (67) Murov, S. L. *Handbook of photochemistry*; Dekker: New York, 1973.
- (68) Förster, T. Energy migration and fluorescence. 1946. *J. Biomed. Opt.* **2012**, *17*, 11002.
- (69) Lochenie, C.; Schötz, K.; Panzer, F.; Kurz, H.; Maier, B.; Puchler, F.; Agarwal, S.; Köhler, A.; Weber, B. Spin-Crossover Iron(II) Coordination Polymer with Fluorescent Properties: Correlation between Emission Properties and Spin State. *J. Am. Chem. Soc.* **2018**, *140*, 700–709.
- (70) Kovalenko, S. A.; Schanz, R.; Hennig, H.; Ernsting, N. P. Cooling dynamics of an optically excited molecular probe in solution from femtosecond broadband transient absorption spectroscopy. *J. Chem. Phys.* **2001**, *115*, 3256–3273.
- (71) Liu, Y.; Kjaer, K. S.; Fredin, L. A.; Chábera, P.; Harlang, T.; Canton, S. E.; Lidin, S.; Zhang, J.; Lomoth, R.; Bergquist, K.-E.; et al. A heteroleptic ferrous complex with mesoionic bis(1,2,3-triazol-5-ylidene) ligands: taming the MLCT excited state of iron(II). *Chem. - Eur. J.* **2015**, *21*, 3628–3639.
- (72) Brown, A. M.; McCusker, C. E.; McCusker, J. K. Spectroelectrochemical identification of charge-transfer excited states in transition metal-based polypyridyl complexes. *Dalton transactions (Cambridge, England: 2003)* **2014**, *43*, 17635–17646.
- (73) Schweitzer, C.; Schmidt, R. Physical mechanisms of generation and deactivation of singlet oxygen. *Chem. Rev.* **2003**, *103*, 1685–1757.
- (74) Howard, J. A.; Mendenhall, G. D. Autoxidation and Photooxidation of 1,3-Diphenylisobenzofuran: A Kinetic and Product Study. *Can. J. Chem.* **1975**, *53*, 2199–2201.
- (75) Ford, W. E.; Rodgers, M. A. J. Reversible triplet-triplet energy transfer within a covalently linked bichromophoric molecule. *J. Phys. Chem.* **1992**, *96*, 2917–2920.
- (76) Wilson, G. J.; Launikonis, A.; Sasse, W. H. F.; Mau, A. W.-H. Excited-State Processes in Ruthenium(II) Bipyridine Complexes Containing Covalently Bound Arenes. *J. Phys. Chem. A* **1997**, *101*, 4860–4866.

■ NOTE ADDED AFTER ASAP PUBLICATION

This paper was published on the Web on September 16, 2020, with data missing from the left panel of Figure 12. The corrected version was reposted on September 22, 2020.

4 Summary and Outlook

Finding cheaper alternatives for photosensitizers based on rare and noble metals such as ruthenium(II) and iridium(III) has been of great scientific interest in the last couple of years. One such alternative is the lighter homologue of ruthenium(II), namely iron(II). In contrast to ruthenium, iron(II) complexes show vastly different photophysical behaviour upon excitation due to the lower intrinsic ligand field splitting of iron. The focus of research into suitable iron(II) complexes as replacements of ruthenium(II) luminophores has been to incorporate strong σ -donors in form of *N*-heterocyclic carbenes to destabilize dark non-emissive excited MC states in favour of the possibly luminescent excited MLCT states.

In this work, the preparation of three ligands incorporating strong σ -donors in the form of methylimidazolylidenes as well as pyridines as π -acceptors is reported. It was not possible to isolate the formed homoleptic complex of 2,6-bis((3-methyl-2,3-dihydro-1*H*-imidazol-1-ylidene)methyl)pyridine (pbmi). The formation of the homoleptic complex $[\text{Fe}(\text{pbmi})_2]^{2+}$ could be observed *via* ESI⁺-mass spectrometry. DFT calculations reveal that the excited ⁵MC state should be much higher in energy than the ³MC excited state, and therefore shouldn't play a role in the photophysics of $[\text{Fe}(\text{pbmi})_2]^{2+}$. The calculations also indicate that there seems to be no energy barrier between the ³MLCT and ³MC states, which would result in a barrierless deactivation and therefore low lifetime of the excited charge transfer state.

In contrast to complex $[\text{Fe}(\text{pbmi})_2]^{2+}$, the synthesis of the ligands 2,2'-((3-methyl-2,3-dihydro-1*H*-imidazol-1-ylidene)methylene)dipyridine (dpmi) and 2-(bis(3-methyl-2,3-dihydro-1*H*-imidazol-1-yl)methyl)pyridine (pdmi) and their homoleptic complexes $[\text{Fe}(\text{dpmi})_2]^{2+}$ and $[\text{Fe}(\text{pdmi})_2]^{2+}$ was successful. For the complex $[\text{Fe}(\text{dpmi})_2]^{2+}$ only the *cis*-isomer is obtained upon synthesis as revealed by the number of ¹H and ¹³C NMR resonances. This is expected due to the destabilizing *trans* influence of the carbenes in a conceivable *trans* coordination. The electronic absorption spectrum of $[\text{Fe}(\text{dpmi})_2]^{2+}$ in acetonitrile shows two absorption bands at 415 nm ($\epsilon = 17310 \text{ L mol}^{-1} \text{ cm}^{-1}$) and 500 nm ($\epsilon = 19390 \text{ L mol}^{-1} \text{ cm}^{-1}$) which were assigned to MLCT transitions using TD-DFT calculations. Excitation into either of these absorption bands does not give rise to any observable emission neither at room temperature nor at 77 K in frozen solution. To probe the lifetime of the excited states, ultra-fast transient absorption spectroscopy was employed. The analysis of the obtained data gave rise to two lifetimes of $\tau_1 = 1.0 \text{ ps}$ and $\tau_2 = 9.2 \text{ ps}$, of which the component with 9.2 ps was assigned to the ³MLCT state with the help of a simulated TA spectrum obtained via

spectroelectrochemical UV-Vis experiments. Considering the lifetime of 9 ps for the $^3\text{MLCT}$ state and comparison to $[\text{Fe}(\text{bmip})_2]^{2+}$ shows an increase in lifetime of the $^3\text{MLCT}$ state by an order of magnitude, although only two σ -donating carbene moieties were employed in $[\text{Fe}(\text{dpmi})_2]^{2+}$ compared to the four carbene moieties in $[\text{Fe}(\text{bmip})_2]^{2+}$. The difference in the complexes lies in the six-membered-ring chelating nature of the dpmi ligand in contrast to the five-membered-ring chelates in $[\text{Fe}(\text{bmip})_2]^{2+}$. Due to the larger bite angle of dpmi and therefore the better orbital overlap between the ligand and metal orbitals leads to a higher ligand field splitting and therefore an extended $^3\text{MLCT}$ lifetime due to the stronger destabilization of the excited MC states. DFT calculations, furthermore, reveal that for complex $[\text{Fe}(\text{dpmi})_2]^{2+}$ the excited ^5MC state is slightly higher in energy than the excited ^3MC state by approx. 0.06 eV. In addition, the even larger distortion of the ^5MC state, in contrast to the ^3MC state, imposes a large reorganisation barrier between these two excited states, which substantiates the interpretation that the ^5MC state is bypassed and that the complex undergoes ISC from the ^3MC state directly into the ground state.

In contrast to the synthesis of $[\text{Fe}(\text{dpmi})_2]^{2+}$, the synthesis of $[\text{Fe}(\text{pdmi})_2]^{2+}$ in THF at $-70\text{ }^\circ\text{C}$ revealed the presence of both the *cis*- and the *trans*-isomer, which could not be separated by conventional column chromatography. The separation could be carried out using a HPLC revealing a ratio of *trans* and *cis* isomers of 4:1 for the synthesis at low temperatures and yielding pure *trans*- $[\text{Fe}(\text{pdmi})_2]^{2+}$ after HPLC. Due to the low amount of *cis*-isomer obtained at $-70\text{ }^\circ\text{C}$, a high temperature synthesis was carried out in DMF at $20\text{ }^\circ\text{C}$, which pushed the ratio of *trans* and *cis* isomers to 1:2. HPLC separation yielded the pure *cis*- $[\text{Fe}(\text{pdmi})_2]^{2+}$. Both isomers could be characterized by NMR and IR/Raman spectroscopy as well as single crystal X-ray diffraction, which confirmed the proposed symmetries and the diamagnetic nature of the low-spin iron(II) complexes. Both complexes show intense absorption bands in the visible spectral region with maxima at 521 nm ($\epsilon = 7430\text{ L mol}^{-1}\text{ cm}^{-1}$) and 471 nm ($\epsilon = 8680\text{ L mol}^{-1}\text{ cm}^{-1}$) for *trans*- $[\text{Fe}(\text{pdmi})_2]^{2+}$ and *cis*- $[\text{Fe}(\text{pdmi})_2]^{2+}$ in acetonitrile at room temperature, respectively. According to TD-DFT calculations and charge-transfer number analyses, these absorption bands were assigned to MLCT transitions, whereby the sharper absorption band of the *trans*-isomer is assigned to a single transition, while the broader absorption band of the *cis*-isomer is composed of four $\text{Fe}\rightarrow\text{py}_2$ transitions. Neither *trans*- $[\text{Fe}(\text{pdmi})_2]^{2+}$ nor *cis*- $[\text{Fe}(\text{pdmi})_2]^{2+}$ show emission at room-temperature or at 77 K in frozen solution or solid state upon excitation into the MLCT absorption band. To gain insight into the excited state lifetime of the $^3\text{MLCT}$ state, ultra-fast TA spectroscopy was carried out, revealing lifetimes of the excited $^3\text{MLCT}$ state of $\tau_{293\text{ K}}(\textit{trans}) = 8.0/14.5\text{ ps}$ and $\tau_{293\text{ K}}(\textit{cis}) = 8.6/15.2\text{ ps}$ in MeOH/EtOH (2:3 v/v) and MeCN, respectively. Compared to $[\text{Fe}(\text{dpmi})_2]^{2+}$ the increase in σ -

donating NHC-moieties does not lead to a strong increase of the lifetime of the $^3\text{MLCT}$ state, as envisioned. Variable-temperature TA spectroscopy performed in MeOH/EtOH (2:3 v/v) on both *trans*-[Fe(pdmi) $_2$] $^{2+}$ and *cis*-[Fe(pdmi) $_2$] $^{2+}$ revealed a temperature-dependence of the lifetime of the $^3\text{MLCT}$ state for the *cis*-isomer, whereby the lifetime was increased to $\tau_{130\text{K}}(\textit{cis}) = 177$ ps. The obtained Arrhenius data was discussed in the picture of semi-classical Marcus theory, whereby an electronic coupling constant H_{AB} for the IC-barrier could be obtained between the excited $^3\text{MLCT}$ and ^3MC states of $H_{\text{AB}} = 81 \pm 6$ cm $^{-1}$. This relatively small value stems from the tilting of the pyridine ring and the decrease of the N-Fe-C(*trans*) angle, during the $^3\text{MLCT}/^3\text{MC}$ IC process. This motion leads to an overlap between the pyridine π^* and the iron $3d_{z^2}$ orbitals, enabling vibronic coupling along this mode. This motion is hindered in rigid matrices leading to an even higher lifetime of $\tau_{77\text{K}}(\textit{cis}) = 1.67$ ns, however no luminescence was detected either in frozen solution or in the solid state at 77K. This is likely due to the energetically lowest $^1\text{MLCT}$ states exhibiting only small transition dipole moments and a similar orbital composition to the lowest excited $^3\text{MLCT}$ state, preventing large spin-orbit coupling.

In summary, the combination of six-membered-ring chelating ligands with σ -donors and π -acceptors resulted in the increased lifetime of the excited $^3\text{MLCT}$ state. The increased number of σ -donors did not lead to a substantial increase of said lifetime, but gives rise to a temperature dependence in the lifetime of one of the obtained isomers. This complex showed the need of rigidifying the ligands to hinder detrimental motions and so mitigating the electronic coupling between the excited triplet states. Furthermore, since the increased number of σ -donors did not seem to push the energy of all ^3MC states significantly, a new strategy could be to modify the π -acceptor, either by modifying the pyridine with electron withdrawing groups, or substituting the pyridine ring by stronger π -acceptors such as pyrazine.

5 References

- [1] Stefan Bringezu, Anu Ramaswami, Heinz Schandl, Meghan O'Brien, Rylie Pelton, Jean Acquatella, Elias T. Ayuk, Anthony Shun Fung Chiu, Robert Flanegin, Jacob Fry, Stefan Giljum, Seiji Hashimoto, Stefanie Hellweg, Karin Hosking, Yuanchao Hu, Manfred Lenzen, Mirko Lieber, Stephan Lutter, Alessio Miatto, Ajay Singh Nagpure, Michael Obersteiner, Laurant van Oers, Stephan Pfister, Peter-Paul Pichler, Armistead Russell, Lucilla Spini, Hiroki Tanikawa, Ester van der Voet, Helga Weisz, James West, Anders Wijkman, Bing Zhu and Romain Zivy, *Assessing global resource use: A systems approach to resource efficiency and pollution reduction*, **2017**.
- [2] D. Zhang, C. Rong, T. Ahmad, H. Xie, H. Zhu, X. Li, T. Wu, *Eng. Rep.*, **2022**, e12584.
- [3] R. M. Izatt, S. R. Izatt, R. L. Bruening, N. E. Izatt, B. A. Moyer, *Chem. Soc. Rev.*, **2014**, *43*, 2451–2475.
- [4] Intergovernmental Panel on Climate Change, *Climate Change 2022 – Impacts, Adaptation and Vulnerability*, Cambridge University Press, **2022**.
- [5] United Nations, Sustainable development goals, **2015**.
- [6] P. K. Nayak, S. Mahesh, H. J. Snaith, D. Cahen, *Nat. Rev. Mater.*, **2019**, *4*, 269–285.
- [7] R. Naumann, M. Goez, *Chem. Eur. J.*, **2018**, *24*, 17557–17567.
- [8] S. D. Tilley, M. Cornuz, K. Sivula, M. Grätzel, *Angew. Chem. Int. Ed.*, **2010**, *49*, 6405–6408.
- [9] J. Twilton, C. Le, P. Zhang, M. H. Shaw, R. W. Evans, D. W. C. MacMillan, *Nat. Rev. Chem.*, **2017**, *1*.
- [10] R. D. Costa, E. Orti, H. J. Bolink, F. Monti, G. Accorsi, N. Armaroli, *Angew. Chem. Int. Ed.*, **2012**, *51*, 8178–8211.
- [11] C. E. Housecroft, E. C. Constable, *Chem. Sci.*, **2022**, *13*, 1225–1262.
- [12] F. H. Burstall, *J. Chem. Soc.*, **1936**, 173.
- [13] A. Juris, V. Balzani, F. Barigelletti, S. Campagna, P. Belser, A. von Zelewsky, *Coord. Chem. Rev.*, **1988**, *84*, 85–277.
- [14] D. M. Arias-Rotondo, J. K. McCusker in *Visible Light Photocatalysis in Organic Chemistry* (Hrsg.: C. Stephenson, T. Yoon, D. W. C. MacMillan), Wiley, **2018**, 1–24.
- [15] J. K. McCusker, *Acc. Chem. Res.*, **2003**, *36*, 876–887.
- [16] N. E. S. Tay, D. Lehnerr, T. Rovis, *Chem. Rev.*, **2022**, *122*, 2487–2649.
- [17] J. Oh, W. Ghann, H. Kang, F. Nesbitt, S. Providence, J. Uddin, *Inorganica Chim. Acta*, **2018**, *482*, 943–950.

- [18] M. Grätzel, *J. Photochem. Photob. C Reviews*, **2003**, *4*, 145–153.
- [19] M. K. Nazeeruddin, F. de Angelis, S. Fantacci, A. Selloni, G. Viscardi, P. Liska, S. Ito, B. Takeru, M. Grätzel, *J. Am. Chem. Soc.*, **2005**, *127*, 16835–16847.
- [20] L.-X. Xue, T.-T. Meng, W. Yang, K.-Z. Wang, *J. Photochem. Photob. B*, **2015**, *152*, 95–105.
- [21] F. Heinemann, J. Karges, G. Gasser, *Acc. Chem. Res.*, **2017**, *50*, 2727–2736.
- [22] H. Huang, S. Banerjee, P. J. Sadler, *ChemBiochem*, **2018**, *19*, 1574–1589.
- [23] K. K.-W. Lo, *Acc. Chem. Res.*, **2015**, *48*, 2985–2995.
- [24] D. M. Roundhill, *Photochemistry and Photophysics of Metal Complexes*, Springer US, Boston, MA, **1994**.
- [25] J. A. Gareth Williams, S. DEVELAY, D. L. Rochester, L. MURPHY, *Coordin. Chem. Rev.*, **2008**, *252*, 2596–2611.
- [26] P.-T. Chou, Y. Chi, *Eur. J. Inorg. Chem.*, **2006**, *2006*, 3319–3332.
- [27] H. Xiang, J. Cheng, X. Ma, X. Zhou, J. J. Chruma, *Chem. Soc. Rev.*, **2013**, *42*, 6128–6185.
- [28] W. R. Kitzmann, M.-S. Bertrams, P. Boden, A. C. Fischer, R. Klauer, J. Sutter, R. Naumann, C. Förster, G. Niedner-Schatteburg, N. H. Bings, J. Hunger, C. Kerzig, K. Heinze, *J. Am. Chem. Soc.*, **2023**, *145*, 16597–16609.
- [29] C. Förster, K. Heinze, *Chem. Soc. Rev.*, **2020**, *49*, 1057–1070.
- [30] C. Förster, K. Heinze, *Chem. Phys. Rev.*, **2022**, *3*.
- [31] B. M. Hockin, C. Li, N. Robertson, E. Zysman-Colman, *Catal. Sci. Technol.*, **2019**, *9*, 889–915.
- [32] N. Sinha, O. S. Wenger, *J. Am. Chem. Soc.*, **2023**, *145*, 4903–4920.
- [33] C. Wegeberg, O. S. Wenger, *JACS Au*, **2021**, *1*, 1860–1876.
- [34] O. S. Wenger, *J. Am. Chem. Soc.*, **2018**, *140*, 13522–13533.
- [35] M. Dorn, N. R. East, C. Förster, W. R. Kitzmann, J. Moll, F. Reichenauer, T. Reuter, L. Stein, K. Heinze in *Comprehensive Inorganic Chemistry III*, Elsevier, **2023**, 707–788.
- [36] E. M. Kober, B. P. Sullivan, T. J. Meyer, *Inorg. Chem.*, **1984**, *23*, 2098–2104.
- [37] C. M. Marian, *Comput. Mol. Sci.*, **2012**, *2*, 187–203.
- [38] T. M. Dunn, *Trans. Faraday Soc.*, **1961**, *57*, 1441.
- [39] A. Cannizzo, F. van Mourik, W. Gawelda, G. Zgrablic, C. Bressler, M. Chergui, *Angew. Chem. Int. Ed.*, **2006**, *45*, 3174–3176.
- [40] J. N. Demas, D. G. Taylor, *Inorg. Chem.*, **1979**, *18*, 3177–3179.
- [41] S. Campagna, F. Puntoriero, F. Nastasi, G. Bergamini, V. Balzani, *Top. Curr. Chem.*, **2007**, *280*, 117–214.
- [42] D. M. Arias-Rotondo, J. K. McCusker, *Chem. Soc. Rev.*, **2016**, *45*, 5803–5820.

- [43] R. M. O'Donnell, P. G. Johansson, M. Abrahamsson, G. J. Meyer, *Inorg. Chem.*, **2013**, *52*, 6839–6848.
- [44] K. Suzuki, A. Kobayashi, S. Kaneko, K. Takehira, T. Yoshihara, H. Ishida, Y. Shiina, S. Oishi, S. Tobita, *Phys. Chem. Chem. Phys.*, **2009**, *11*, 9850–9860.
- [45] J. R. Lakowicz, *Principles of Fluorescence Spectroscopy*, Springer US, Boston, MA, **2006**.
- [46] V. Balzani, S. Campagna, *Top. Curr. Chem.*, **2007**, *280*.
- [47] D. Hernández-Castillo, R. E. P. Nau, M.-A. Schmid, S. Tschierlei, S. Rau, L. González, *Angewandte Chemie (International ed. in English)*, **2023**, *62*, e202308803.
- [48] S. J. Strickler, R. A. Berg, *J. Chem. Phys.*, **1962**, *37*, 814–822.
- [49] G. S. Ming Tong, K. T. Chan, X. Chang, C.-M. Che, *Chem. Sci.*, **2015**, *6*, 3026–3037.
- [50] G. Baryshnikov, B. Minaev, H. Ågren, *Chem. Rev.*, **2017**, *117*, 6500–6537.
- [51] B. Minaev, G. Baryshnikov, H. Agren, *Phys. Chem. Chem. Phys.*, **2014**, *16*, 1719–1758.
- [52] T. J. Penfold, E. Gindensperger, C. Daniel, C. M. Marian, *Chem. Rev.*, **2018**, *118*, 6975–7025.
- [53] J. T. Malme, R. A. Clendening, R. Ash, T. Curry, T. Ren, J. Vura-Weis, *J. Am. Chem. Soc.*, **2023**, *145*, 6029–6034.
- [54] R. Englman, J. Jortner, *Mol. Phys.*, **1970**, *18*, 145–164.
- [55] B. S. Brunschwig, N. Sutin, *Comments Inorganic Chem.*, **1987**, *6*, 209–235.
- [56] V. M. Miskowski, H. B. Gray, R. B. Wilson, E. I. Solomon, *Inorg. Chem.*, **1979**, *18*, 1410–1412.
- [57] R. B. Wilson, E. I. Solomon, *J. Am. Chem. Soc.*, **1980**, *102*, 4085–4095.
- [58] K. Nisbett, Y.-J. Tu, C. Turro, J. J. Kodanko, H. B. Schlegel, *Inorg. Chem.*, **2018**, *57*, 231–240.
- [59] P. S. Wagenknecht, P. C. Ford, *Coordin. Chem. Rev.*, **2011**, *255*, 591–616.
- [60] P. D. Fleischauer, P. Fleischauer, *Chem. Rev.*, **1970**, *70*, 199–230.
- [61] J. van Houten, R. J. Watts, *J. Am. Chem. Soc.*, **1976**, *98*, 4853–4858.
- [62] J. V. Caspar, T. J. Meyer, *J. Am. Chem. Soc.*, **1983**, *105*, 5583–5590.
- [63] A. Soupart, F. Alary, J.-L. Heully, P. I. P. Elliott, I. M. Dixon, *Inorg. Chem.*, **2018**, *57*, 3192–3196.
- [64] B. Durham, J. L. Walsh, C. L. Carter, T. J. Meyer, *Inorg. Chem.*, **1980**, *19*, 860–865.
- [65] L. Feng, Y. Wang, *Inorg. Chem.*, **2018**, *57*, 8994–9001.
- [66] A. Breivogel, C. Förster, K. Heinze, *Inorg. Chem.*, **2010**, *49*, 7052–7056.
- [67] A. Breivogel, C. Kreitner, K. Heinze, *Eur. J. Inorg. Chem.*, **2014**, *2014*, 5468–5490.
- [68] A. Breivogel, M. Meister, C. Forster, F. Laquai, K. Heinze, *Chemistry (Weinheim an der Bergstrasse, Germany)*, **2013**, *19*, 13745–13760.
- [69] L. Gong, S. P. Mulcahy, D. Devarajan, K. Harms, G. Frenking, E. Meggers, *Inorg. Chem.*, **2010**, *49*, 7692–7699.

- [70] A. Reynal, E. Palomares, *Eur. J. Inorg. Chem.*, **2011**, 2011, 4509–4526.
- [71] C. Fu, M. Wenzel, E. Treutlein, K. Harms, E. Meggers, *Inorg. Chem.*, **2012**, 51, 10004–10011.
- [72] E. Meggers, *Chem. Eur. J.*, **2010**, 16, 752–758.
- [73] E. Meggers, *Eur. J. Inorg. Chem.*, **2011**, 2011, 2911–2926.
- [74] O. S. Wenger, *Chem. Eur. J.*, **2019**, 25, 6043–6052.
- [75] Z. Liu, Z. Bian, C. Huang in *Topics in Organometallic Chemistry* (Hrsg.: H. Bozec, V. Guerschais), Springer Berlin Heidelberg, Berlin, Heidelberg, **2010**, 113–142.
- [76] T.-Y. Li, J. Wu, Z.-G. Wu, Y.-X. Zheng, J.-L. Zuo, Y. Pan, *Coordin. Chem. Rev.*, **2018**, 374, 55–92.
- [77] J. Shum, P. K.-K. Leung, K. K.-W. Lo, *Inorg. Chem.*, **2019**, 58, 2231–2247.
- [78] J. I. Day, K. Teegardin, J. Weaver, J. Chan, *Org. Process Res. Dev.*, **2016**, 20, 1156–1163.
- [79] F. Strieth-Kalthoff, M. J. James, M. Teders, L. Pitzer, F. Glorius, *Chem. Soc. Rev.*, **2018**, 47, 7190–7202.
- [80] D. Liu, Y. Zhao, Z. Wang, K. Xu, J. Zhao, *Dalton Trans.*, **2018**, 47, 8619–8628.
- [81] C. B. Larsen, O. S. Wenger, *Chem. Eur. J.*, **2017**.
- [82] D. R. Lide, *Handbook of Chemistry and Physics on CD-ROM*. CRC Press, Florida, USA, **2002**.
- [83] J. K. McCusker, *Science*, **2019**, 363, 484–488.
- [84] T. Lu, F. Chen, *J. Comput. Chem.*, **2012**, 33, 580–592.
- [85] M. Kaupp, *J. Comput. Chem.*, **2007**, 28, 320–325.
- [86] P. Pyykkö, *Chem. Rev.*, **1988**, 88, 563–594.
- [87] A. Hossain, A. Bhattacharyya, O. Reiser, *Science*, **2019**, 364.
- [88] M. Iwamura, S. Takeuchi, T. Tahara, *Acc. Chem. Res.*, **2015**, 48, 782–791.
- [89] L. Gimeno, B. T. Phelan, E. A. Sprague-Klein, T. Roisnel, E. Blart, C. Gourelaouen, L. X. Chen, Y. Pellegrin, *Inorg. Chem.*, **2022**, 61, 7296–7307.
- [90] M. C. Rosko, E. M. Espinoza, S. Arteta, S. Kromer, J. P. Wheeler, F. N. Castellano, *Inorg. Chem.*, **2023**, 62, 3248–3259.
- [91] R. Hamze, J. L. Peltier, D. Sylvinson, M. Jung, J. Cardenas, R. Haiges, M. Soleilhavoup, R. Jazzar, P. I. Djurovich, G. Bertrand, M. E. Thompson, *Science*, **2019**, 363, 601–606.
- [92] F. A. Cotton, F. Zingales, *J. Am. Chem. Soc.*, **1961**, 83, 351–355.
- [93] D. W. Thompson, A. Ito, T. J. Meyer, *Pure. Appl. Chem.*, **2013**, 85, 1257–1305.
- [94] D. M. Manuta, A. J. Lees, *Inorg. Chem.*, **1986**, 25, 1354–1359.
- [95] L. A. Büldt, X. Guo, A. Prescimone, O. S. Wenger, *Angew. Chem. Int. Ed.*, **2016**, 55, 11247–11250.

- [96] L. A. Büldt, X. Guo, R. Vogel, A. Prescimone, O. S. Wenger, *J. Am. Chem. Soc.*, **2017**, *139*, 985–992.
- [97] E. Kottelat, Z. Fabio, *Inorganics*, **2017**, *5*, 24.
- [98] U. Schatzschneider, *Inorganica Chim. Acta*, **2011**, *374*, 19–23.
- [99] P. Herr, C. Kerzig, C. B. Larsen, D. Häussinger, O. S. Wenger, *Nat. Chem.*, **2021**, *13*, 956–962.
- [100] A. K. Pal, C. Li, G. S. Hanan, E. Zysman-Colman, *Angew. Chem. Int. Ed.*, **2018**, *57*, 8027–8031.
- [101] N. Sinha, B. Pfund, C. Wegeberg, A. Prescimone, O. S. Wenger, *J. Am. Chem. Soc.*, **2022**, *144*, 9859–9873.
- [102] Anderson, D. L., *Theory of the earth*. Blackwell Scientific Publ., **1991**.
- [103] A. Cannizzo, C. J. Milne, C. Consani, W. Gawelda, C. Bressler, F. van Mourik, M. Chergui, *Coordin. Chem. Rev.*, **2010**, *254*, 2677–2686.
- [104] G. Auböck, M. Chergui, *Nat. Chem.*, **2015**, *7*, 629–633.
- [105] W. Zhang, R. Alonso-Mori, U. Bergmann, C. Bressler, M. Chollet, A. Galler, W. Gawelda, R. G. Hadt, R. W. Hartsock, T. Kroll, K. S. Kjaer, K. Kubicek, H. T. Lemke, H. W. Liang, D. A. Meyer, M. M. Nielsen, C. Purser, J. S. Robinson, E. I. Solomon, Z. Sun, D. Sokaras, T. B. van Driel, G. Vanko, T.-C. Weng, D. Zhu, K. J. Gaffney, *Nature*, **2014**, *509*, 345–348.
- [106] J. K. McCusker, K. N. Walda, R. C. Dunn, J. D. Simon, D. Magde, D. N. Hendrickson, *J. Am. Chem. Soc.*, **1993**, *115*, 298–307.
- [107] C. Kreitner, K. Heinze, *Dalton Trans.*, **2016**, *45*, 13631–13647.
- [108] E. C. Constable in *Advances in Inorganic Chemistry*, Elsevier, **1986**, 69–121.
- [109] F. Schramm, V. Meded, H. Fliegl, K. Fink, O. Fuhr, Z. Qu, W. Klopper, S. Finn, T. E. Keyes, M. Ruben, *Inorg. Chem.*, **2009**, *48*, 5677–5684.
- [110] L. L. Jamula, A. M. Brown, D. Guo, J. K. McCusker, *Inorg. Chem.*, **2014**, *53*, 15–17.
- [111] A. Britz, W. Gawelda, T. A. Assefa, L. L. Jamula, J. T. Yarranton, A. Galler, D. Khakhulin, M. Diez, M. Harder, G. Doumy, A. M. March, É. Bajnóczi, Z. Németh, M. Pápai, E. Rozsályi, D. Sárosiné Szemes, H. Cho, S. Mukherjee, C. Liu, T. K. Kim, R. W. Schoenlein, S. H. Southworth, L. Young, E. Jakubikova, N. Huse, G. Vankó, C. Bressler, J. K. McCusker, *Inorg. Chem.*, **2019**, *58*, 9341–9350.
- [112] A. K. C. Mengel, C. Forster, A. Breivogel, K. Mack, J. R. Ochsmann, F. Laquai, V. Ksenofontov, K. Heinze, *Chemistry (Weinheim an der Bergstrasse, Germany)*, **2015**, *21*, 704–714.
- [113] M. Maestri, N. Armaroli, V. Balzani, E. C. Constable, Thompson, Alexander M. W. Cargill, *Inorg. Chem.*, **1995**, *34*, 2759–2767.

- [114] Y. Liu, T. Harlang, S. E. Canton, P. Chabera, K. Suarez-Alcantara, A. Fleckhaus, D. A. Vithanage, E. Goransson, A. Corani, R. Lomoth, V. Sundstrom, K. Wärnmark, *Chem. Commun.*, **2013**, *49*, 6412–6414.
- [115] Y. Liu, P. Persson, V. Sundstrom, K. Wärnmark, *Acc. Chem. Res.*, **2016**, *49*, 1477–1485.
- [116] Y. Liu, K. S. Kjaer, L. A. Fredin, P. Chabera, T. Harlang, S. E. Canton, S. Lidin, J. Zhang, R. Lomoth, K.-E. Bergquist, P. Persson, K. Wärnmark, V. Sundström, *Chem. Eur. J.*, **2015**, *21*, 3628–3639.
- [117] P. Chábera, K. S. Kjaer, O. Prakash, A. Honarfar, Y. Liu, L. A. Fredin, T. C. B. Harlang, S. Lidin, J. Uhlig, V. Sundström, R. Lomoth, P. Persson, K. Wärnmark, *J. Phys. Chem. Lett.*, **2018**, 459–463.
- [118] S. Hohloch, L. Suntrup, B. Sarkar, *Organometallics*, **2013**, *32*, 7376–7385.
- [119] L. A. Fredin, M. Papai, E. Rozsalyi, G. Vanko, K. Warnmark, V. Sundstrom, P. Persson, *J. Phys. Chem. Lett.*, **2014**, *5*, 2066–2071.
- [120] L. Lindh, T. Pascher, S. Persson, Y. Goriya, K. Wärnmark, J. Uhlig, P. Chábera, P. Persson, A. Yartsev, *J. Phys. Chem. A*, **2023**, *127*, 10210–10222.
- [121] P. Zimmer, L. Burkhardt, A. Friedrich, J. Steube, A. Neuba, R. Schepper, P. Müller, U. Flörke, M. Huber, S. Lochbrunner, M. Bauer, *Inorg. Chem.*, **2018**, *57*, 360–373.
- [122] K. S. Kjær, N. Kaul, O. Prakash, P. Chábera, N. W. Rosemann, A. Honarfar, O. Gordivska, L. A. Fredin, K.-E. Bergquist, L. Häggström, T. Ericsson, L. Lindh, A. Yartsev, S. Styring, P. Huang, J. Uhlig, J. Bendix, D. Strand, V. Sundström, P. Persson, R. Lomoth, K. Wärnmark, *Science*, **2019**, *363*, 249–253.
- [123] P. Chábera, Y. Liu, O. Prakash, E. Thyraug, A. E. Nahhas, A. Honarfar, S. Essen, L. A. Fredin, T. C. B. Harlang, K. S. Kjaer, K. Handrup, F. Ericson, H. Tatsuno, K. Morgan, J. Schnadt, L. Haggstrom, T. Ericsson, A. Sobkowiak, S. Lidin, P. Huang, S. Styring, J. Uhlig, J. Bendix, R. Lomoth, V. Sundstrom, P. Persson, K. Warnmark, *Nature*, **2017**, *543*, 695–699.
- [124] L. Liu, T. Duchanois, T. Etienne, A. Monari, M. Beley, X. Assfeld, S. Haacke, P. C. Gros, *Phys. Chem. Chem. Phys.*, **2016**, *18*, 12550–12556.
- [125] W. Leis, M. A. Argüello Cordero, S. Lochbrunner, H. Schubert, A. Berkefeld, *J. Am. Chem. Soc.*, **2022**, *144*, 1169–1173.
- [126] O. Prakash, P. Chábera, N. Kaul, V. F. Hlynsson, N. W. Rosemann, I. B. Losada, Y. T. Hoang Hai, P. Huang, J. Bendix, T. Ericsson, L. Häggström, A. K. Gupta, D. Strand, A. Yartsev, R. Lomoth, P. Persson, K. Wärnmark, *Inorg. Chem.*, **2024**, *63*, 4461–4473.
- [127] R. A. Marcus, *Angew. Chem. Int. Ed.*, **1993**, *32*, 1111–1121.
- [128] A. M. Brown, C. E. McCusker, J. K. McCusker, *Dalton Trans.*, **2014**, *43*, 17635–17646.

- [129] R. A. Marcus, *J. Chem. Phys.*, **1956**, *24*, 966–978.
- [130] B. S. Brunschwig, N. Sutin, *Coordin. Chem. Rev.*, **1999**, *187*, 233–254.
- [131] M. C. Carey, S. L. Adelman, J. K. McCusker, *Chem. Sci.*, **2019**, *10*, 134–144.
- [132] M. Darari, A. Francés-Monerris, B. Marekha, A. Doudouh, E. Wenger, A. Monari, S. Haacke, P. C. Gros, *Molecules*, **2020**, *25*, 5991.
- [133] P. Dierks, A. Pöpcke, O. S. Bokareva, B. Altenburger, T. Reuter, K. Heinze, O. Kühn, S. Lochbrunner, M. Bauer, *Inorg. Chem.*, **2020**, *59*, 14746–14761.
- [134] G. R. Fulmer, A. J. M. Miller, N. H. Sherden, H. E. Gottlieb, A. Nudelman, B. M. Stoltz, J. E. Bercaw, K. I. Goldberg, *Organometallics*, **2010**, *29*, 2176–2179.
- [135] F. Neese, *Comput. Mol. Sci.*, **2012**, *2*, 73–78.
- [136] A. D. Becke, *J. Chem. Phys.*, **1993**, *98*, 5648–5652.
- [137] C. Lee, W. Yang, R. G. Parr, *Phys. Rev. B*, **1988**, *37*, 785–789.
- [138] B. Miehlich, A. Savin, H. Stoll, H. Preuss, *Chem. Phys. Lett.*, **1989**, *157*, 200–206.
- [139] F. Neese, F. Wennmohs, A. Hansen, U. Becker, *Chem. Phys.*, **2009**, *356*, 98–109.
- [140] R. Izsák, F. Neese, *J. Chem. Phys.*, **2011**, *135*, 144105-1–11.
- [141] D. A. Pantazis, X.-Y. Chen, C. R. Landis, F. Neese, *J. Chem. Theory Comput.*, **2008**, *4*, 908–919.
- [142] V. Barone, M. Cossi, *J. Phys. Chem. A*, **1998**, *102*, 1995–2001.
- [143] S. Miertuš, E. Scrocco, J. Tomasi, *Chem. Phys.*, **1981**, *55*, 117–129.
- [144] F. Weigend, R. Ahlrichs, *Phys. Chem. Chem. Phys.*, **2005**, *7*, 3297–3305.
- [145] F. Weigend, *Phys. Chem. Chem. Phys.*, **2006**, *8*, 1057–1065.
- [146] S. Grimme, J. Antony, S. Ehrlich, H. Krieg, *J. Chem. Phys.*, **2010**, *132*, 154104.
- [147] S. Grimme, S. Ehrlich, L. Goerigk, *J. Comput. Chem.*, **2011**, *32*, 1456–1465.
- [148] S. Grimme, F. Neese, *J. Chem. Phys.*, **2007**, *127*, 1–18.
- [149] T. Petrenko, S. Kossmann, F. Neese, *J. Chem. Phys.*, **2011**, *134*, 1–14.
- [150] F. Xue, J. Fang, S. L. Delker, H. Li, P. Martasek, L. J. Roman, T. L. Poulos, R. B. Silverman, *J. Med. Chem.*, **2011**, *54*, 2039–2048.
- [151] A. R. Naziruddin, C.-L. Kuo, W.-J. Lin, W.-H. Lo, C.-S. Lee, B.-J. Sun, A. H. H. Chang, W.-S. Hwang, *Organometallics*, **2014**, *33*, 2575–2582.
- [152] G. J. Barbante, P. S. Francis, C. F. Hogan, P. R. Kheradmand, D. J. D. Wilson, P. J. Barnard, *Inorg. Chem.*, **2013**, *52*, 7448–7459.
- [153] I. J. Lin, C. S. Vasam, *Coordin. Chem. Rev.*, **2007**, *251*, 642–670.
- [154] D. Serra, P. Cao, J. Cabrera, R. Padilla, F. Rominger, M. Limbach, *Organometallics*, **2011**, *30*, 1885–1895.

[155] D. T. Weiss, P. J. Altmann, S. Haslinger, C. Jandl, A. Pöthig, M. Cokoja, F. E. Kühn, *Dalton Trans.*, **2015**, 44, 18329–18339.

[156] D. T. Weiss, S. Haslinger, C. Jandl, A. Pöthig, M. Cokoja, F. E. Kühn, *Inorg. Chem.*, **2015**, 54, 415–417.

6 Appendix

6.1 Supporting Information for Section 3.1 "Synthesis of $[H_2pbmi]^{2+}$ and synthesis attempts of its homoleptic iron(II) complex"

General Procedure: If not otherwise noted, all reactions were carried out under an inert atmosphere. THF was distilled from potassium. All other reagents were used as received from commercial suppliers (Acros, Sigma-Aldrich, abcr, TCI).

ESI+-mass spectrometry was carried out with a *Micromass Q-TOF Ultima 3*-spectrometer.

UV/Vis absorption spectra were carried out on a *Varian Cary 5000* spectrometer in quartz glass cuvettes with 1 cm path length.

NMR spectra were recorded on a *Bruker Avance DRX 400* spectrometer at 400.31 MHz (1H). All resonances are reported in ppm versus tetramethylsilane and referenced against the solvent signal as internal standard (d_6 -DMSO: 1H δ (ppm) = 2.50, CD_3CN : 1H δ (ppm) = 1.94.^[134]

DFT calculations were carried out using the ORCA program package (version 4.0.2).^[135] All calculations were performed using the B3LYP functional^{[136]–[138]} and employed the RIJCOSX approximation.^{[139],[140]} Relativistic effects were calculated at the "zeroth order regular approximation" (ZORA) level.^[141] To account for solvent effects, a conductor-like screening model (CPCM) modelling acetonitrile was used in all calculations.^{[142],[143]} Geometry optimizations were performed using Ahlrichs' split-valence triple-zeta basis set ZORA-def2/J-TZVP.^{[144],[145]} Atom-pairwise dispersion correction was performed with the Becke-Johnson damping scheme (D3BJ).^{[146],[147]} The presence of energy minima was checked by numerical frequency calculations. The simulation of transitions from the ground-state to excited states was done on the same level of theory described above by time-dependent DFT (TD-DFT) calculations, where the 50 energetically lowest excitations were calculated.^{[148],[149]}

Synthesis of 2,6-Bis(bromomethyl)pyridine (I)^[150]

2,6-Bis(hydroxymethyl)pyridine (2.03 g, 14.6 mmol) was heated in Hydrogen bromide (48 % in water, 20 mL) at 125 °C (oil bath) for 15 h. After cooling to room temperature water (50 mL) was added to the yellow solution and the mixture brought to pH = 8 by addition of an aqueous sodium bicarbonate solution. The resulting solution was extracted with DCM (4x 50 mL), the combined organic phases dried over magnesium sulfate and the solvent removed under reduced pressure. The raw product was purified *via* column chromatography on silica with petrolether/ethyl acetate (9:1). The product was obtained as a colourless solid (1.88 g, 7.10 mmol, 49 %).

R_f = 0.03 (petrolether/ ethylacetate 9:1)

¹H-NMR (400 MHz, CD₃CN); δ(ppm) = 7.77 (t, ³J = 7.74 Hz, 1H, H¹), 7.42 (d, ³J = 7.74 Hz, 2H, H²), 4.57 (s, 4H, H³).

MS (ESI⁺): m/z (%) = 265.91 (100) [M+H]⁺.

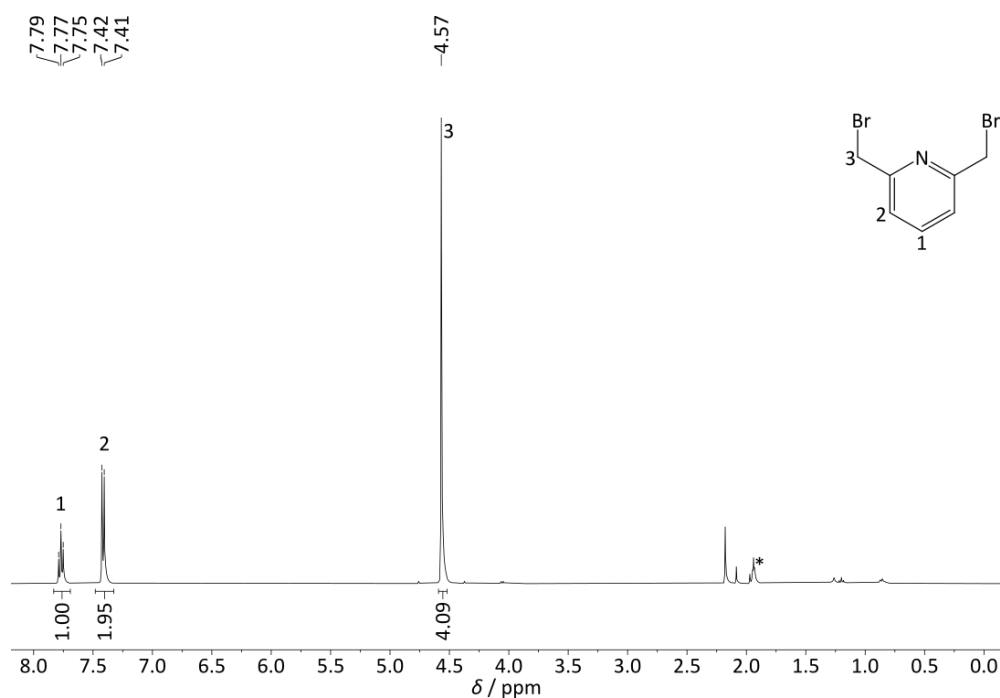


Figure 24: ¹H NMR spectrum of **I** measured in CD₃CN (*).

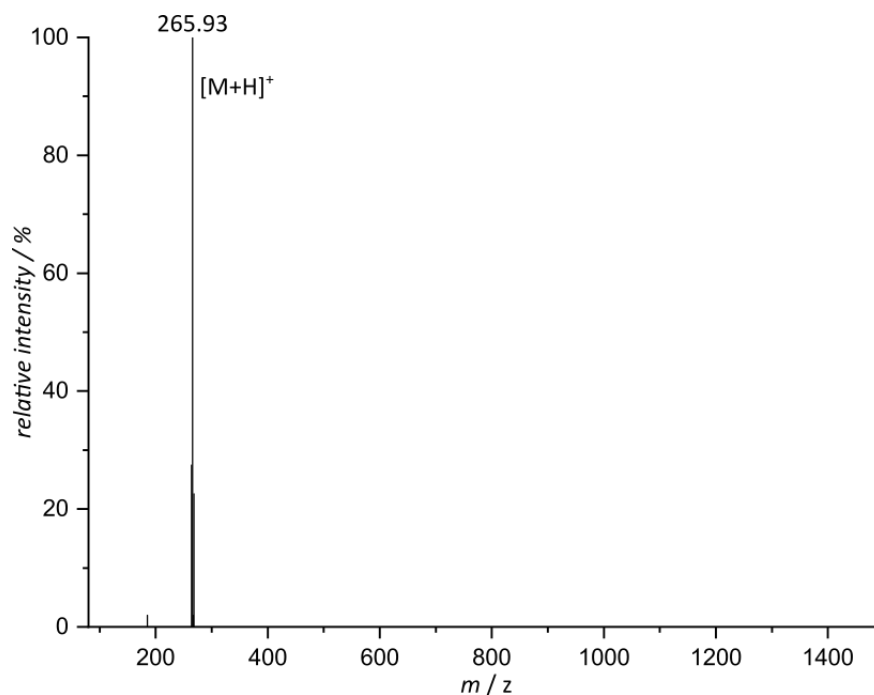


Figure 25: ESI⁺ mass spectrum of **I** measured in CH₃CN.

Synthesis of 2,6-Bis(*N*-methylen-imidazolyl)pyridine (II**)^[151]**

Sodium hydroxide (0.27 g, 6.75 mmol, 2.42 eq.) and Imidazole (0.76 g, 11.2 mmol, 3.99 eq.) were dissolved in THF (30 mL). To this solution was added a solution of 2,6-Bis(bromomethyl)pyridine (0.74 g, 2.79 mmol, 1.00 eq.) in THF (20 mL) and the resulting mixture was stirred at room temperature for 16 h. The solvent was removed under reduced pressure and the residue dissolved in DCM (50 mL). The solution was washed twice with a saturated sodium chloride solution (50 mL), dried over magnesium sulfate. The solvent was removed under reduced pressure to give the product as a colourless solid (0.66 g, 2.76 mmol, 99 %).

¹H-NMR (400 MHz, CD₃CN); δ(ppm) = 7.71 (t, 3J = 7.75 Hz, 1H, H¹), 7.59 (s, 2H, H⁶), 7.06 (m, 4H, H^{4,5}), 6.59 (s, 2H, H²), 5.21 (s, 4H, H³).

MS (ESI⁺): *m/z* (%) = 240.14 (100) [M+H]⁺.

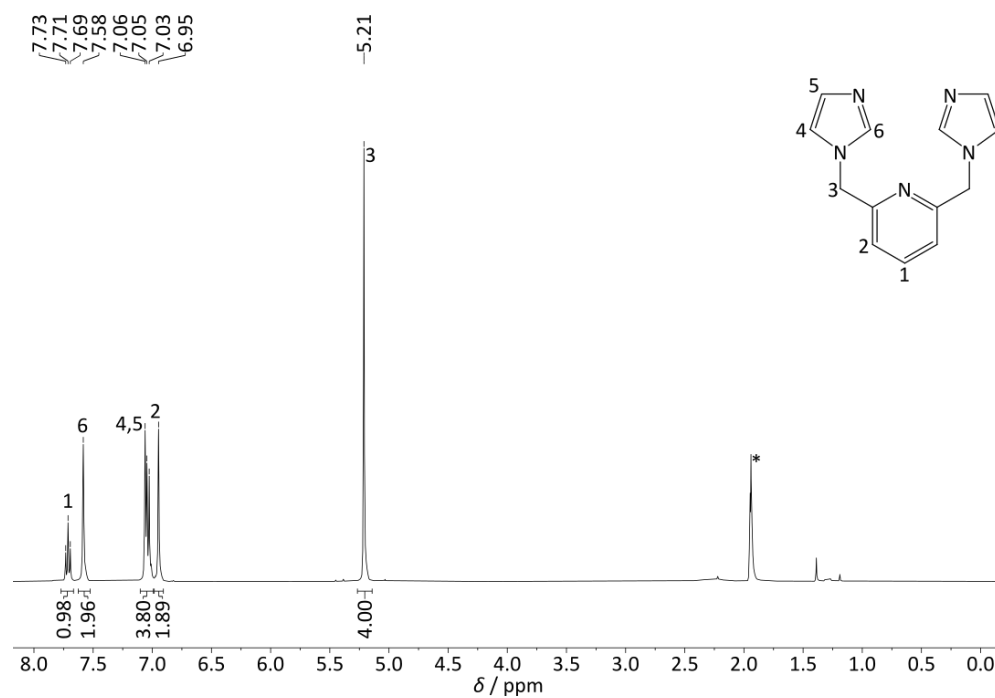


Figure 26: ^1H NMR spectrum of **II** measured in CD_3CN (*).

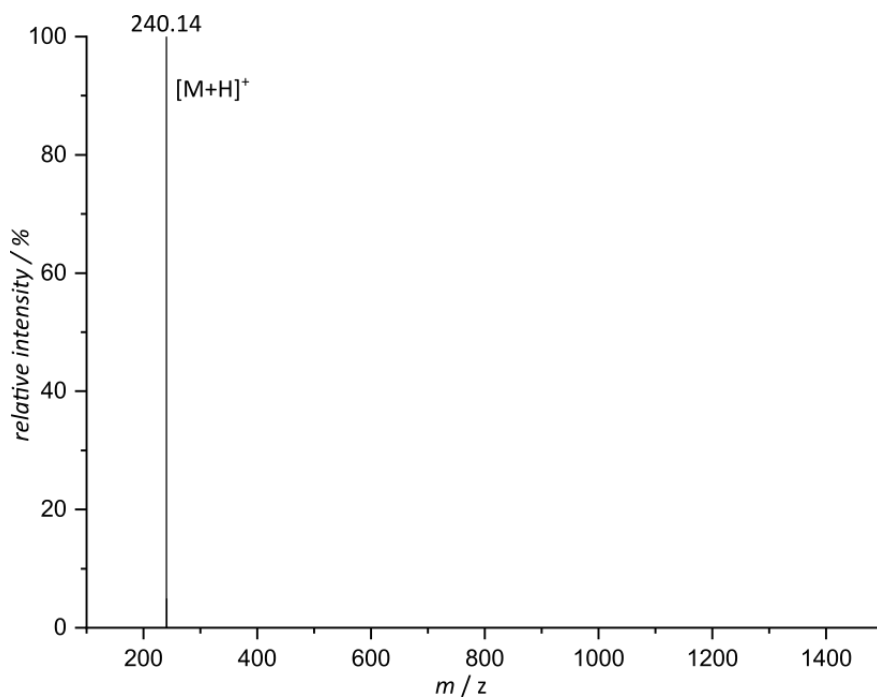


Figure 27: ESI^+ mass spectrum of **II** measured in CH_3CN .

Synthesis of 2,6-Bis(*N*-methylene(*N'*-methylimidazolium)pyridine diiodide [H_2pbmi] $^{\text{I}}_2$)^[152]

In a Schlenk-flask under Ar-atmosphere 2,6-Bis(*N*-methylen-imidazolyl)pyridine (0.80 g, 3.43 mmol, 1.00 eq.) and iodomethane (0.46 mL, 7.39 mmol, 2.20 eq.) were heated in MeCN for 72 h at 95 °C.

After cooling to room temperature the solvent was removed under reduced pressure giving the product as a yellow solid (1.5 g, 2.86 mmol, 86 %).

$^1\text{H-NMR}$ (400 MHz, CD_3CN); $\delta(\text{ppm}) = 9.06$ (s, 2H, H^6) 7.89 (t, $3J = 7.75$ Hz, 1H, H^1), 7.52 (m, 4H, $\text{H}^{4,5}$), 7.43 (s, 2H, H^2), 5.53 (s, 4H, H^3), 3.93 (s, 6H, H^7).

MS (ESI $^+$): m/z (%) = 134.58 (11) $[\text{M}]^{2+}$, 187.11 (11), 254.15 (56) $[\text{M}^{2+}-\text{CH}_3]^+$, 314.02 (50), 396.08 (100) $[\text{M}^{2+}+\text{I}]^+$.

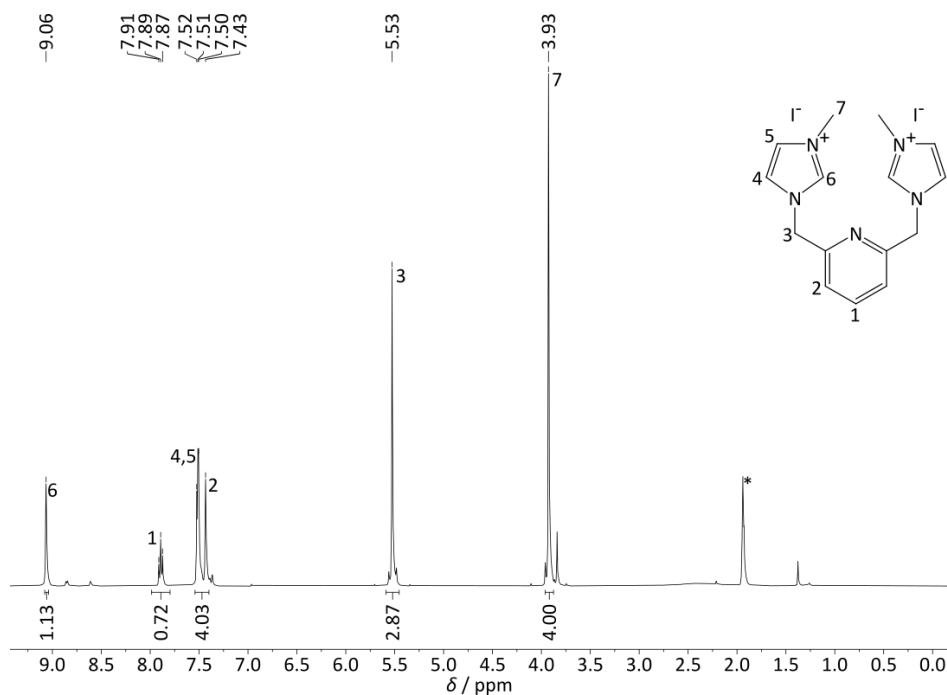


Figure 28: ^1H NMR spectrum of $[\text{H}_2\text{pbmi}]_2$ measured in CD_3CN (*).

Synthesis of 2,6-Bis(*N*-methylene(*N'*-methylimidazolium)pyridine dibromide $[\text{H}_2\text{pbmi}]\text{Br}_2$

In a Schlenk-flask under Ar-atmosphere 2,6-Bis(bromomethyl)pyridine (3.00 g, 11.32 mmol, 1.00 eq.) and 1-Methylimidazole (3.07 g, 2.98 mL, 37.4 mmol, 3.30 eq.) were dissolved in 1,4-Dioxane and heated under reflux for 48 h whereby a beige solid precipitated. After cooling to room temperature the supernatant was decanted and the residue heated in a mixture of DCM/ethanol (1:1, 20 mL) to reflux for 10 min. After cooling to room temperature the solvent mixture was decanted and the solid dried under vacuum to give the product as a beige solid (2.96 g, 6.91 mmol, 61 %).

$^1\text{H-NMR}$ (400 MHz, d_6 -DMSO); $\delta(\text{ppm}) = 9.24$ (s, 2H, H^6) 7.97 (t, $^3J = 7.70$ Hz, 1H, H^1), 7.74 (d, 4H, $\text{H}^{4,5}$), 7.49 (d, 2H, H^2), 5.57 (s, 4H, H^3), 3.92 (s, 6H, H^7).

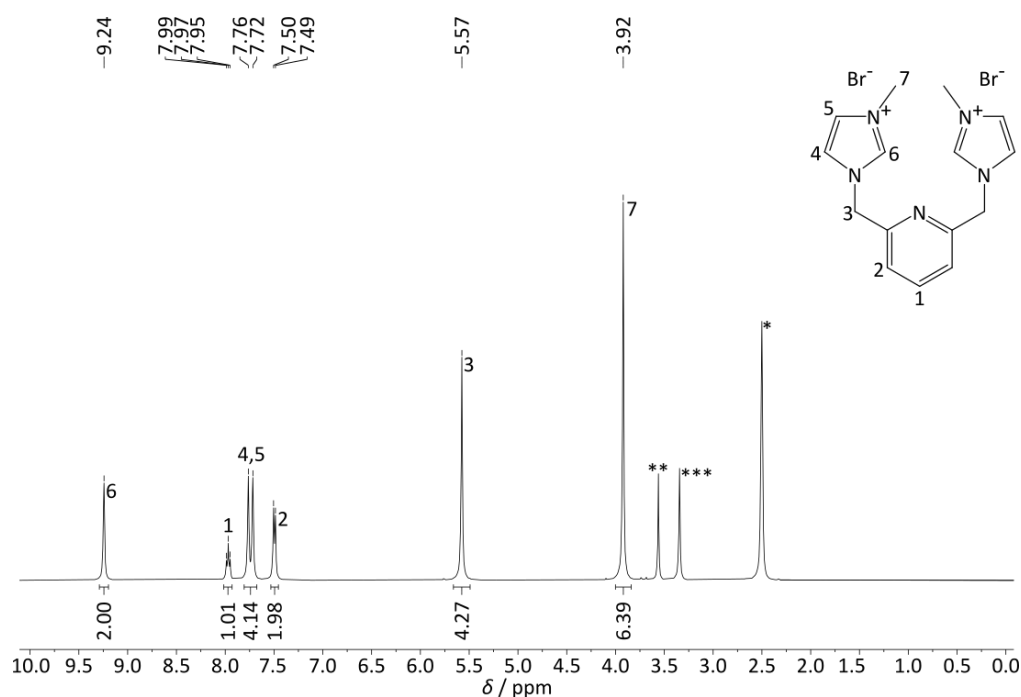


Figure 29: ^1H NMR spectrum of $[\text{H}_2\text{pbmi}]\text{Br}_2$ measured in d_6 -DMSO (*), residues of water (**), and 1,4-dioxane (***) are denoted.

Synthesis of $[\text{Fe}(\text{pbmi})_2]^{2+}$ using FeBr_2

In a Schlenk-flask under Ar-atmosphere $[\text{H}_2\text{pbmi}]\text{I}_2$ (490 mg, 0.93 mmol, 2.00 eq.) was suspended in THF (10 mL) and cooled to $-70\text{ }^\circ\text{C}$ (dry-ice/ethanol bath). To this suspension a solution of KHMDS (370 mg, 1.85 mmol, 4.00 eq.) in THF (5 mL) was added whereby a clear, yellow solution was obtained. After 30 min of stirring at $-70\text{ }^\circ\text{C}$ a solution of iron(II)bromide (100 mg, 0.46 mmol, 1.00 eq.) in THF (15 mL) was added. After stirring overnight a purple solution was obtained. After removal of the solvent under reduced pressure, the formation of product couldn't be verified *via* NMR spectroscopy or Mass spectrometry.

Synthesis of $[\text{Fe}(\text{pbmi})_2]^{2+}$ using $\text{Fe}(\text{OTf})_2$

In a Schlenk-flask under Ar-atmosphere $[\text{H}_2\text{pbmi}]\text{I}_2$ (122 mg, 0.45 mmol, 2.00 eq.) was suspended together with iron(II)triflate (98 mg, 0.23 mmol, 1 eq.) in THF (10 mL) and cooled to $-70\text{ }^\circ\text{C}$ (dry-ice/ethanol bath). To this suspension a solution of KHMDS (187 mg, 0.94 mmol, 4.00 eq.) in THF (5 mL) was added over 10 min. After stirring overnight and warming to room temperature a purple solution was obtained. After removal of the solvent the formation of the complex could be verified *via* ESI⁺-mass spectrometry, but no purification method for the complex could be found.

MS (ESI⁺): m/z (%) = 134.58 (72) [H₂pbmi]²⁺, 254.14 (68) [H₂pbmi²⁺ - CH₃]⁺, 295.12 (40) [Fe(pbmi)₂]²⁺, 396.07 (33) [H₂pbmi²⁺ + I⁻]⁺, 418.12 (100) [H₂pbmi²⁺ + OTf⁻]⁺, 739.18 (13) [Fe(pbmi)₂]²⁺ + OTf⁻]⁺.

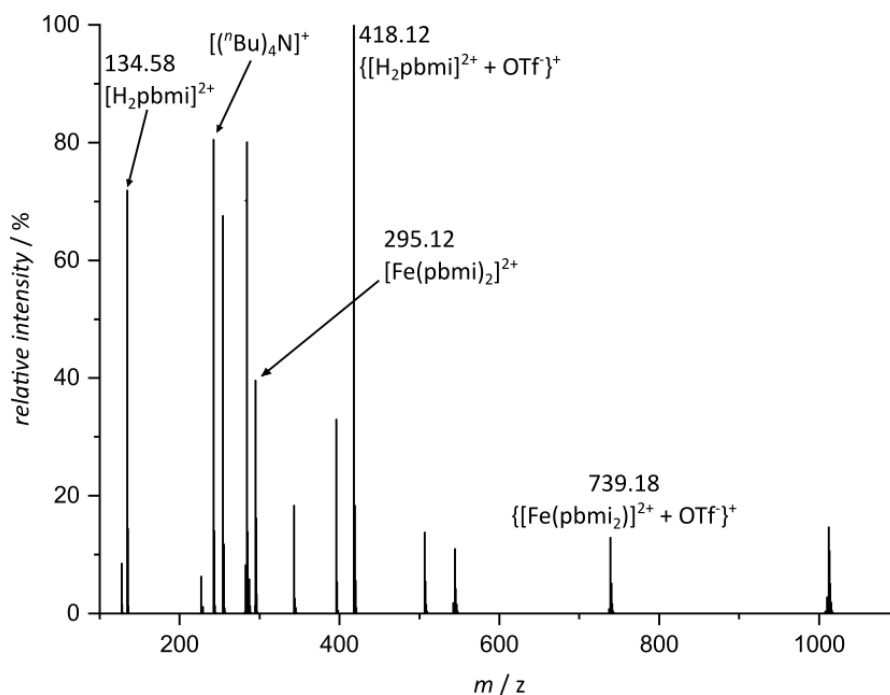


Figure 30: ESI⁺ mass spectrum of the raw product of [Fe(pbmi)₂]²⁺ obtained *via* Fe(OTf)₂ measured in CH₃CN.

Synthesis of [Fe(pbmi)₂]²⁺ *via* transmetalation using Ag₂O^{[153]–[156]}

To a solution of [H₂pbmi]Br₂ (250 mg, 0.58 mmol, 2.00 eq.) in acetonitrile (15 mL) was added Ag₂O (270 mg, 1.17 mmol, 4.00 eq.) and the resulting mixture was stirred under exclusion of light for 6 h. Then iron(II)bromide (63 mg, 0.29 mmol, 1.00 eq.) was added and the mixture stirred overnight. After the removal of the solvent under reduced pressure a brown, insoluble solid was obtained. The formation of the complex could not be verified by NMR-spectroscopy or ESI⁺-mass spectrometry.

Cartesian Coordinates of optimised geometries for [Fe(pbmi)₂]²⁺

¹GS

6	2.141805000	-2.008818000	-0.010239000
6	2.489729000	-3.350520000	0.072674000
6	1.537333000	-4.288067000	0.428182000
6	0.252806000	-3.840357000	0.680759000
6	-0.042841000	-2.489109000	0.563241000

Appendix

7	0.885430000	-1.565423000	0.223725000
1	3.507401000	-3.645538000	-0.139675000
1	-0.530043000	-4.526876000	0.970510000
7	-1.565382000	-0.962341000	1.742856000
6	-2.323470000	-0.977575000	2.902235000
6	-2.134567000	0.226937000	3.481128000
7	-1.259846000	0.934358000	2.668399000
6	-0.894721000	0.204311000	1.573327000
1	-2.908397000	-1.828067000	3.202307000
1	-2.532191000	0.643179000	4.388855000
6	0.850665000	3.440184000	0.145572000
6	0.556673000	4.796363000	0.094138000
6	-0.738112000	5.210766000	-0.160551000
6	-1.703942000	4.237317000	-0.340871000
6	-1.354928000	2.895850000	-0.262195000
7	-0.088085000	2.483764000	-0.027439000
1	1.349564000	5.512921000	0.255970000
1	-2.731992000	4.504797000	-0.539869000
7	2.171593000	0.313845000	2.626424000
6	3.095106000	1.109216000	3.290287000
6	3.255453000	2.227553000	2.551936000
7	2.429535000	2.074323000	1.450544000
6	1.748033000	0.902482000	1.469195000
1	3.543530000	0.805484000	4.218840000

1	3.860621000	3.102546000	2.706860000
6	3.231605000	-1.032568000	-0.358382000
6	-1.464185000	-2.059675000	0.802009000
1	1.790583000	-5.336619000	0.506638000
1	-0.989513000	6.261515000	-0.212642000
26	0.396764000	0.459429000	0.081889000
6	-2.455954000	1.881314000	-0.415590000
6	2.282579000	3.045588000	0.385152000
6	-2.231300000	-0.455142000	-3.122366000
6	-2.906014000	0.515159000	-2.471490000
7	-1.062598000	-0.681034000	-2.409729000
6	-0.980604000	0.125457000	-1.312338000
7	-2.128363000	0.847384000	-1.375618000
1	-3.847340000	0.991021000	-2.678481000
6	-0.041862000	-1.601610000	-2.891427000
1	0.702631000	-1.069253000	-3.482575000
1	0.447012000	-2.089685000	-2.060372000
1	-0.520648000	-2.354099000	-3.513181000
1	-2.470927000	-1.004589000	-4.014656000
1	-2.686552000	1.425778000	0.547189000
1	-3.353078000	2.384989000	-0.763137000
7	1.767962000	1.291264000	-2.580209000
6	1.718308000	0.609144000	-1.399123000
6	2.913927000	0.984411000	-3.299545000

Appendix

6	3.601427000	0.080371000	-2.572299000
7	2.857032000	-0.127137000	-1.423752000
1	4.527780000	-0.430678000	-2.762715000
1	3.126050000	1.431906000	-4.253591000
6	0.799443000	2.257364000	-3.074660000
1	0.824559000	2.245176000	-4.161510000
1	-0.193940000	1.989175000	-2.738118000
1	1.042507000	3.260662000	-2.723962000
1	4.106276000	-1.586348000	-0.686375000
1	3.519867000	-0.458908000	0.522670000
1	-1.927111000	-1.767627000	-0.140181000
1	-2.027161000	-2.896877000	1.202784000
1	2.716303000	2.642216000	-0.529319000
1	2.851464000	3.928729000	0.659871000
6	-0.865073000	2.302235000	2.984011000
1	-1.049022000	2.474645000	4.041455000
1	0.188559000	2.447848000	2.775267000
1	-1.449954000	3.017857000	2.409159000
6	1.785491000	-0.995089000	3.138849000
1	2.344084000	-1.786635000	2.643066000
1	2.011993000	-1.024219000	4.201864000
1	0.723919000	-1.157936000	2.995848000

³MC

6	2.205480000	-2.309396000	0.025993000
6	2.578584000	-3.639840000	0.178735000
6	1.613039000	-4.565902000	0.545854000
6	0.306734000	-4.137348000	0.742763000
6	0.011547000	-2.792461000	0.561103000
7	0.947736000	-1.903639000	0.212972000
1	3.604848000	-3.938581000	0.016263000
1	-0.471054000	-4.829432000	1.034924000
7	-1.498410000	-1.189322000	1.687812000
6	-2.182777000	-1.303874000	2.886192000
6	-2.029437000	-0.124517000	3.524063000
7	-1.247647000	0.672520000	2.704919000
6	-0.903327000	0.029659000	1.554090000
1	-2.710437000	-2.197861000	3.165416000
1	-2.405284000	0.222654000	4.469655000
6	0.726535000	3.779814000	0.141722000
6	0.434140000	5.137098000	0.073260000
6	-0.873115000	5.525076000	-0.187162000
6	-1.847122000	4.550070000	-0.355167000
6	-1.475942000	3.214592000	-0.259121000
7	-0.213728000	2.846733000	-0.021943000
1	1.215643000	5.870235000	0.219085000
1	-2.874401000	4.816715000	-0.562055000

Appendix

7	2.224301000	0.533451000	2.592615000
6	3.017395000	1.430568000	3.287217000
6	3.050050000	2.564980000	2.557758000
7	2.290739000	2.321006000	1.424793000
6	1.762109000	1.067238000	1.428880000
1	3.474623000	1.180290000	4.227266000
1	3.530319000	3.509733000	2.737072000
6	3.235645000	-1.258018000	-0.303772000
6	-1.396599000	-2.276363000	0.722152000
1	1.875864000	-5.606932000	0.679233000
1	-1.131666000	6.573565000	-0.256533000
26	0.392794000	0.446638000	0.067779000
6	-2.495305000	2.111498000	-0.388199000
6	2.139851000	3.296924000	0.351221000
6	-2.273188000	-0.078789000	-3.222677000
6	-2.880061000	0.922855000	-2.551130000
7	-1.177537000	-0.456939000	-2.467316000
6	-1.072919000	0.278974000	-1.328269000
7	-2.143539000	1.117439000	-1.395339000
1	-3.760389000	1.497141000	-2.777161000
6	-0.240747000	-1.476511000	-2.917778000
1	0.495804000	-1.044349000	-3.595117000
1	0.267326000	-1.904183000	-2.063843000
1	-0.791943000	-2.256711000	-3.438086000

1	-2.520825000	-0.558296000	-4.152291000
1	-2.606543000	1.606581000	0.570211000
1	-3.458312000	2.531364000	-0.662858000
7	1.885045000	1.117455000	-2.576492000
6	1.789530000	0.479029000	-1.379023000
6	2.973217000	0.676115000	-3.310232000
6	3.583840000	-0.268146000	-2.565018000
7	2.855890000	-0.369652000	-1.391787000
1	4.460745000	-0.861663000	-2.750928000
1	3.211839000	1.077575000	-4.278390000
6	0.954147000	2.105782000	-3.096478000
1	0.372935000	1.679421000	-3.914142000
1	0.287190000	2.412676000	-2.302684000
1	1.507703000	2.969604000	-3.460900000
1	4.168035000	-1.739465000	-0.583020000
1	3.427462000	-0.652002000	0.581358000
1	-1.765743000	-1.922949000	-0.239189000
1	-2.048041000	-3.077101000	1.059058000
1	2.498393000	2.844872000	-0.573140000
1	2.785241000	4.138740000	0.584525000
6	-0.834490000	2.008436000	3.111495000
1	-1.704721000	2.566919000	3.452147000
1	-0.109357000	1.947118000	3.923108000
1	-0.388752000	2.514031000	2.268062000

Appendix

6	2.004199000	-0.825387000	3.067260000
1	2.697657000	-1.517101000	2.592694000
1	2.175000000	-0.846593000	4.140869000
1	0.987875000	-1.135443000	2.853150000

⁵MC

6	2.213726000	-2.307768000	-0.003676000
6	2.561980000	-3.652593000	-0.009204000
6	1.586033000	-4.601454000	0.256394000
6	0.295914000	-4.172529000	0.529212000
6	0.020350000	-2.810125000	0.512653000
7	0.961042000	-1.894489000	0.241416000
1	3.581548000	-3.944602000	-0.218739000
1	-0.491488000	-4.877561000	0.757826000
7	-1.458900000	-1.335326000	1.843420000
6	-1.970053000	-1.581365000	3.105881000
6	-1.851705000	-0.421534000	3.792178000
7	-1.267793000	0.488196000	2.928717000
6	-1.007021000	-0.063307000	1.720128000
1	-2.375462000	-2.535066000	3.392719000
1	-2.137676000	-0.160927000	4.795674000
6	0.771287000	3.759480000	0.090291000
6	0.499248000	5.115102000	-0.048685000
6	-0.797651000	5.516969000	-0.330166000

6	-1.784059000	4.549394000	-0.450691000
6	-1.438815000	3.212656000	-0.296437000
7	-0.180966000	2.824563000	-0.036689000
1	1.295837000	5.837657000	0.063694000
1	-2.807845000	4.820657000	-0.667686000
7	2.167744000	0.773802000	2.841585000
6	2.851247000	1.756458000	3.535556000
6	2.934555000	2.823958000	2.709566000
7	2.306411000	2.449972000	1.533777000
6	1.818110000	1.187996000	1.602198000
1	3.216425000	1.609178000	4.536213000
1	3.382214000	3.792164000	2.846288000
6	3.262593000	-1.252868000	-0.245837000
6	-1.382927000	-2.319372000	0.772255000
1	1.830082000	-5.655572000	0.257407000
1	-1.037416000	6.565150000	-0.450704000
26	0.381729000	0.463899000	0.080969000
6	-2.493431000	2.140191000	-0.399327000
6	2.182905000	3.295742000	0.353411000
6	-2.392803000	0.117908000	-3.372072000
6	-2.970239000	1.097224000	-2.639603000
7	-1.316758000	-0.344387000	-2.634620000
6	-1.196485000	0.314803000	-1.459027000
7	-2.229669000	1.191639000	-1.474447000

Appendix

1	-3.830759000	1.712706000	-2.832536000
6	-0.424661000	-1.397211000	-3.094736000
1	0.221777000	-1.027691000	-3.890228000
1	0.185801000	-1.722982000	-2.260147000
1	-1.012179000	-2.234202000	-3.468116000
1	-2.653510000	-0.292918000	-4.330872000
1	-2.543708000	1.585710000	0.537233000
1	-3.462568000	2.594584000	-0.582158000
7	2.050773000	0.967987000	-2.725261000
6	1.946017000	0.442861000	-1.482592000
6	3.119743000	0.428609000	-3.421269000
6	3.708367000	-0.461555000	-2.591002000
7	2.981224000	-0.428997000	-1.414454000
1	4.569043000	-1.092079000	-2.725386000
1	3.368534000	0.730497000	-4.422796000
6	1.161445000	1.976530000	-3.279166000
1	0.568723000	1.553540000	-4.089885000
1	0.500371000	2.322199000	-2.492984000
1	1.746642000	2.812088000	-3.659752000
1	4.230187000	-1.723511000	-0.392381000
1	3.326955000	-0.598697000	0.623344000
1	-1.777973000	-1.860994000	-0.133898000
1	-2.022601000	-3.156114000	1.037056000
1	2.543053000	2.729502000	-0.505265000

1	2.832078000	4.155638000	0.488749000
6	-0.971330000	1.864352000	3.298035000
1	-1.873230000	2.346491000	3.671269000
1	-0.204874000	1.893181000	4.072129000
1	-0.613246000	2.387564000	2.418984000
6	1.877538000	-0.541483000	3.394508000
1	1.405655000	-1.141192000	2.625426000
1	2.802485000	-1.017097000	3.716402000
1	1.206089000	-0.452823000	4.247438000

6.2 Supporting Information for Section 3.2 "Higher MLCT lifetime of carbene iron(II) complexes by chelate ring expansion"

Higher MLCT Lifetime of Carbene Iron(II) Complexes by Chelate Ring Expansion

Thomas Reuter, Ayla Kruse, Roland Schoch, Stefan Lochbrunner, Matthias Bauer and Katja Heinze

Supplementary Information

General

All reactions and measurements were performed under argon atmosphere unless otherwise noted. An analytic- and a synthesis glovebox (UniLab/MBraun – Ar 4.8, O₂ < 1 ppm, H₂O < 0.1 ppm) were used to store and weigh sensitive compounds for synthesis as well as to prepare any measurement sample that required absence of oxygen and water. Dichloromethane, acetonitrile and CD₃CN were dried and distilled from calcium hydride and stored over molecular sieve (3 Å). THF was dried from potassium and distilled prior to use. The reagents were used as received from commercial suppliers (ABCR, Acros Organics, Alfa Aesar, Fischer Scientific, Fluka and Sigma-Aldrich). Deuterated solvents were purchased from euriso-top and Deutero GmbH.

¹H and ¹³C{¹H} NMR spectra were recorded on a Bruker Avance DRX 400 spectrometer at 400.31 MHz(¹H), 100.05 MHz (¹³C{¹H}). Chemical shifts (δ) are reported to the shift scale calibrated with the residual non-deuterated NMR solvent; CH₂Cl₂ (5.32 ppm for ¹H NMR) and CD₃CN (1.94 ppm for ¹H NMR and 1.32 and 118.26 ppm for ¹³C{¹H} NMR).¹

Electrospray ionization mass spectra were recorded on an Agilent 6545 QTOF-MS spectrometer.

The elemental analysis was performed by the microanalytical laboratory of the department of chemistry of the University of Mainz on a vario EL cube from Elementar.

IR spectra were recorded on a Bruker Alpha II FTIR spectrometer with an ATR unit containing a diamond crystal.

UV/Vis/NIR spectra were recorded on a Varian Cary 5000 spectrometer and a Jasco V-770 spectrometer using 1.0 cm cells (Hellma, Suprasil).

Electrochemical experiments of [Fe(dpml)₂][PF₆]₂ were carried out on a BioLogic SP-200 voltammetric analyzer using a platinum working electrode, a platinum wire as counter electrode and a 0.01 M Ag/AgNO₃ in CH₃CN reference electrode. The measurements were carried out at a scan rate of 100 mV s⁻¹ for cyclic voltammetry experiments using 0.1 M [ⁿBu₄][PF₆] as supporting electrolyte and 0.001 M of the sample in acetonitrile. Potentials are referenced relative to the ferrocene/ferrocenium couple.

Spectroelectrochemical measurements of [Fe(dpml)₂][PF₆]₂ were performed on a BioLogic SP-50 voltammetric analyser using a Specac omni-cell liquid transmission cell² with CaF₂ windows equipped with a Pt gauze working electrode and an Ag wire as pseudo-reference electrode, melt-sealed in a self-made polyethylene spacer (approximate 0.5 mm path length) containing 0.1 M [ⁿBu₄][PF₆] in acetonitrile.

X-ray absorption spectroscopic measurements of [Fe(dpml)₂][PF₆]₂ were carried out at PETRA III beamline P65 at Deutsches Elektronensynchrotron (DESY) in Hamburg, Germany. The measurements at the iron K-edge (7112 eV) were performed using a Si(111) double-crystal monochromator in continuous scans (180 s per scan) and a maximum synchrotron beam current of 100 mA. Spectra were

S1

recorded in transmission mode in solid form as pellets diluted in boron nitride. The preparation of the sample was carried out under inert atmosphere in a glove box. For energy calibration, an iron foil was measured simultaneously with the sample.

EXAFS data analysis

In the first step of data analysis, the background of the spectrum was removed by subtracting a Victoreen-type polynomial.³ E_0 was defined as the first inflection point in the edge – which was determined using the first maximum in the first derivative. Afterwards a piecewise polynomial was used to determine the smooth part of the spectrum and was adjusted in a way that the low- R components of the resulting Fourier transform were minimal. The background-subtracted spectrum was divided by its smoothed part and the photon energy was converted to photoelectron wave number k . For evaluation of the EXAFS spectra the resulting functions were weighted with k^3 and calculated with EXCURVE98, which works based on the EXAFS function and according to a formulation in terms of radial distribution functions.^{4,5}

$$\chi(k) = \sum_j S_0^2(k) F_j(k) \int P_j(r_j) \frac{e^{-2r_j/\lambda}}{kr_j^2} \sin[2kr_j + \delta_j(k)] dr_j$$

The number of independent points N_{ind} was calculated according to information theory to determine the degree of overdeterminacy.⁵

$$N_{ind} = \frac{2\Delta k \Delta R}{\pi}$$

Here, Δk describes the range in k -space used for data analysis and ΔR corresponds to the distance range in the Fourier filtering process. For the analysis a Δk -range of 9 and a ΔR -range of 5 was used, which yielded a number of independent points of 28. The quality of a fit was determined using two methods. The reduced χ_{red}^2 considers the degree of overdeterminacy of the system and the number of fitted parameters p . It therefore allows a direct comparison of different models:⁶

$$\chi_{red}^2 = \frac{(N_{ind}/N)}{N_{ind} - p} \sum_i \left(\frac{k_i^n}{\sum_j k_j^n |\chi_j^{exp}(k_j)|} \right)^2 (\chi^{exp}(k_i) - \chi^{theo}(k_i))^2$$

The R -factor, which represents the percental disagreement between experiment and adjusted function and takes into account both systematic and random errors according to the equation:⁶

$$R = \sum_i \frac{k_i^n}{\sum_j k_j^n |\chi_j^{exp}(k_j)|} |\chi^{exp}(k_i) - \chi^{theo}(k_i)| \cdot 100\%$$

The accuracy of the determined distances is 1%, of the Debye-Waller-like factor 10%⁷ and of the coordination numbers depending of the distance 5 – 15%. Initial values for coordination numbers and distances were adopted from Rietveld-analysis and afterwards iterated free in every fit as well as the Debye-Waller-like factor and the amplitude reducing factor.

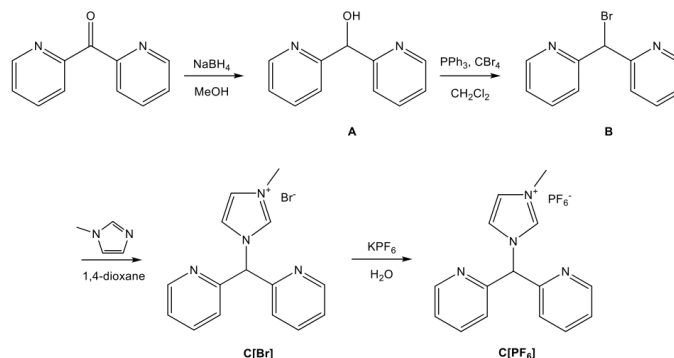
Transient absorption spectra of **[Fe(dpmi)₂][PF₆]₂** were recorded applying a pump-probe setup with an excitation wavelength set to 490 nm.⁸ The setup is pumped by a Ti:Sapphire laser system (Spectra-Physics, Spitfire Pro) which provides ultrashort laser pulses centred at 775 nm with a repetition rate of 1 kHz. A non-collinear optical parametric amplifier (NOPA) tuned to a centre wavelength of 490 nm delivered the excitation pulses whose dispersion was controlled by prism compressor. For probing, a white light continuum generated with a CaF₂ crystal was used. Both beams, with polarizations arranged

S2

in magic angle, were focused onto the sample leading to pump and probe spots with diameters of 390 μm and 120 μm , respectively. Transient absorption spectra were recorded by dispersing the probe beam after the sample with a prism and detecting its spectral intensity distribution with a CCD array. The metal complex was dissolved in acetonitrile under argon atmosphere and the obtained sample was filled into a 1 mm fused silica cuvette. The concentration was 2.8×10^{-4} M resulting in an optical density of 0.43 at 490 nm.

Density functional theory calculations of 1^{2+} were executed with Orca 4.1.1^{9,10} using the Elwetritsch or MOGON high performance computing facilities. The B3LYP¹¹⁻¹³ formulation of DFT and Def2-tzvp^{14,15} as basis set which uses polarization functions for non-hydrogen atoms were employed. For solvent modelling, CPCM^{16,17} in CH_3CN was applied. The “zeroth order regular approximation” (ZORA)¹⁴ was used for relativistic corrections. The RIJCOSX^{18,19} approximation was used along with the auxiliary basis set Def2/J^{14,15} to accelerate the calculations. Atom-pairwise dispersion correction was performed with the Becke-Johnson damping scheme (D3BJ).^{20,21} The character of the states was assigned by dividing the molecule into fragments and calculating charge transfer numbers, as implemented in the TheoDore software package.²²⁻²⁴ For an initial charge transfer number analysis, the complex was divided into three fragments (iron centre and the two tripodal ligands), while for a more detailed analysis the ligands were further partitioned into two parts themselves (pyridine and carbene fragment).

Synthesis



Di(pyridine-2-yl)methanol (A): 1 g (5.43 mmol, 1 eq.) di(pyridine-2-yl)methanone were stirred in methanol (20 mL) at 0 °C. 205.37 mg (5.43 mmol, 1 eq.) NaBH₄ were slowly added. The resulting solution was stirred for 1 h at 0 °C and 12 h at room temperature. The solvent was evaporated under reduced pressure and the resulting residue dissolved in 2 M hydrochloric acid and stirred for 10 min. The pH of the solution was adjusted to 8 using NH₄OH_(aq). The aqueous solution was extracted with dichloromethane. After drying the organic phase with MgSO₄, the solvent was removed under reduced pressure giving the product as a pale brown oil (991 mg, 5.32 mmol, 98 %). ¹H NMR (400 MHz, CD₂Cl₂): δ = 8.53 (d, 2H), 7.66 (td, 2H), 7.51 (d, 2H), 7.20 (m, 2H), 5.84 (d, 1H), 5.72 (d, 1H) ppm.

2,2'-(Bromomethylene)dipyridine (B): 2.01 g (10.8 mmol, 1 eq.) di(pyridine-2-yl)methanol and 7.16 g (21.59 mmol, 1.99 eq.) CBr₄ were dissolved in dichloromethane (20 mL) and cooled to 0 °C. 3.94 g (11.88 mmol, 1.1 eq.) of PPh₃ were added in small portions. The mixture was stirred for 1.5 h. After removal of the solvent under reduced pressure, the residue was purified by column chromatography on silica with ethyl acetate as eluent, giving the product as a colourless solid (1.75 g, 7.03 mmol, 65 %). ¹H NMR (400 MHz, CD₃CN): δ = 8.52 (d, 2H), 7.81 – 7.74 (m, 4H), 7.27 (t, 2H), 6.33 (s, 1H) ppm.

1-(Di(pyridin-2-yl)methyl)-3-methyl-1H-imidazol-3-ium hexafluorophosphate (C[PF₆]) (analogous to ref. 25): 528.83 mg (2.12 mmol, 1 eq.) 2,2'-(bromomethylene)dipyridine and 0.37 mL (4.67 mmol, 2.2 eq.) methylimidazole were refluxed in 1,4-dioxane (30 mL) for 48 h. The resulting precipitate was collected and dried under reduced pressure giving 561.75 mg (1.70 mmol, 80 %) 1-(di(pyridin-2-yl)methyl)-3-methyl-1H-imidazol-3-ium bromide. The hexafluorophosphate salt of the pro-ligand was obtained by dissolving the bromide salt in water (20 mL) and adding an aqueous solution of KPF₆ (3 eq.) whereby 1-(di(pyridin-2-yl)methyl)-3-methyl-1H-imidazol-3-ium hexafluorophosphate precipitated (639.99 mg, 1.62 mmol, 95 %). ¹H NMR (400 MHz, CD₃CN): δ = 8.88 (s, 1H), 8.58 (d, 2H), 7.84 (td, 2H), 7.61 (t, 1H), 7.43 – 7.37 (m, 5H), 6.95 (2, 1H), 3.86 (s, 3H) ppm.

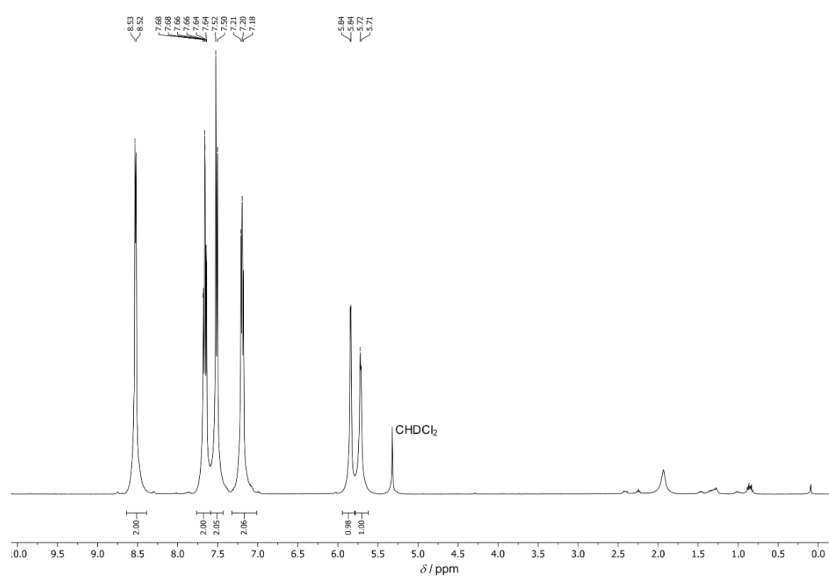
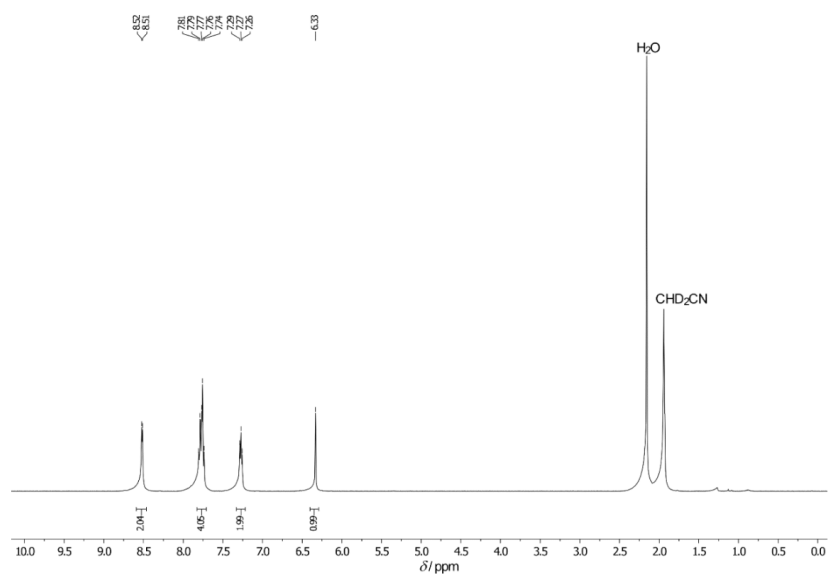
[Fe(dpmi)]₂[PF₆]₂: 396.28 mg (1 mmol, 2 eq.) 1-(di(pyridin-2-yl)methyl)-3-methyl-1H-imidazol-3-ium hexafluorophosphate were suspended in dry THF (25 mL) and cooled to –70 °C in an ethanol/dry ice bath. Addition of a solution of 112.21 mg (1 mmol, 2 eq.) KO^tBu in dry THF (10 mL) yielded a clear orange solution. After 10 min stirring at –70 °C, a solution of 107.83 mg (0.5 mmol, 1 eq.) FeBr₂ in dry THF (20 mL) was added. The resulting mixture was slowly warmed to room temperature and left stirring overnight. An orange precipitate formed. The solvent was removed under reduced pressure. The residue was dissolved in acetonitrile (5 mL), filtered and the product precipitated with diethyl ether giving [Fe(dpmi)]₂[PF₆]₂ as an orange powder (352.1 mg, 0.42 mmol, 83 %). ¹H NMR (400 MHz, CD₃CN): δ = 8.12 (d, 2H), 8.03 (t, 2H), 7.90 (m, 4H), 7.80 (t, 2H), 7.38 (m, 4H), 7.25 (d, 2H), 7.21 (d, 2H), 7.15 (t,

S4

2H), 6.87 (t, 2H), 2.44 (s, 6H) ppm. $^{13}\text{C}\{^1\text{H}\}$ NMR (400 MHz, CD_3CN): 199.12, 160.71, 159.69, 159.05, 157.92, 139.27, 138.56, 126.36, 126.15, 125.31, 125.14, 125.06, 123.58, 66.36, 35.50 ppm. IR (ATR): $\tilde{\nu}$ = 1607 (w), 1566 (w), 1475 (m), 1445 (m), 1420 (m), 1401 (m), 1354 (w), 1332 (w), 1313 (w), 1266 (w), 1244 (w), 1214 (w), 1196 (m), 1170 (w), 1075 (w), 877 (m), 835 (s, PF_6), 771 (m), 756 (m), 738 (m), 723 (m), 694 (m), 657 (m), 557 (s, PF_6), 522 (m), 492 (w), 467 (w), 423 (m) cm^{-1} . ESI⁺-MS (m/z): 278.09 [$\mathbf{1}$]²⁺, 701.14. [$\mathbf{1}^{2+} + \text{PF}_6^-$]⁺. UV/Vis (CH_3CN): λ ($\epsilon/\text{L mol}^{-1} \text{cm}^{-1}$) = 255 (39700), 415 nm (17310), 500 nm (19390). Elemental analysis for $\text{C}_{30}\text{H}_{28}\text{F}_{12}\text{FeN}_8\text{P}_2$: calcd. C 42.57 %, H 3.33 %, N 13.24 %; found C 42.57 %, H 3.19 %, N 12.96 %.

Oxidation to iron(III). The iron(III) complex was obtained in situ by dissolving [$\text{Fe}(\text{dpmi})_2$][PF_6]₂ (15 mg, 17.72 μmol) in CH_3CN (5 mL) or $^n\text{PrCN}$ (5 mL) and adding [NO][PF_6] (3.1 mg, 17.72 μmol) as a solid. The colour of the solution changed from orange to blue. Gas evolution was not observed. This solution was appropriately diluted with the respective solvent and used for absorption and emission experiments. Low temperature emission spectroscopy (77 K) was performed in $^n\text{PrCN}$. UV/Vis (CH_3CN): λ ($\epsilon/\text{L mol}^{-1} \text{cm}^{-1}$) = 338 (5500), 525 nm (3080), 609 nm (3460).

Spectroscopic data

Fig. S1 – ¹H NMR spectrum of **A** in CD₂Cl₂.Fig. S2 – ¹H NMR spectrum of **B** in CD₃CN.

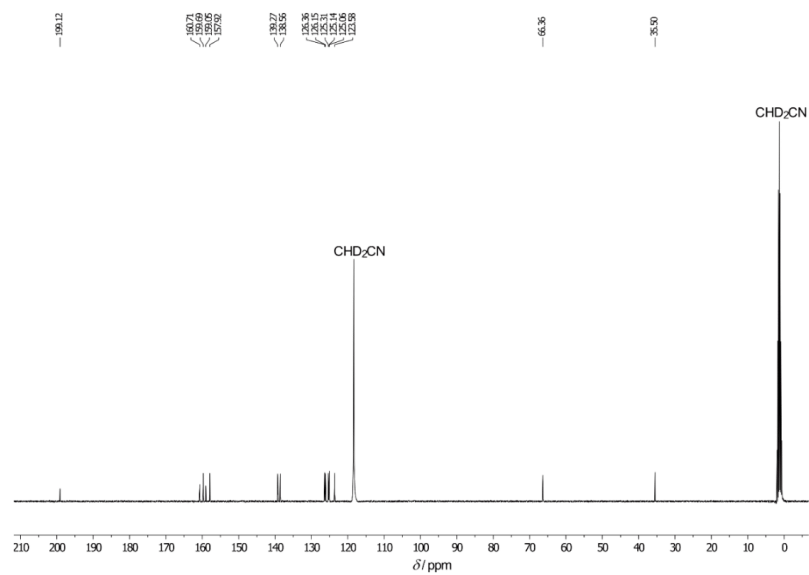


Fig. S5 – $^{13}\text{C}\{^1\text{H}\}$ NMR spectrum of $1[\text{PF}_6]_2$ in CD_3CN .

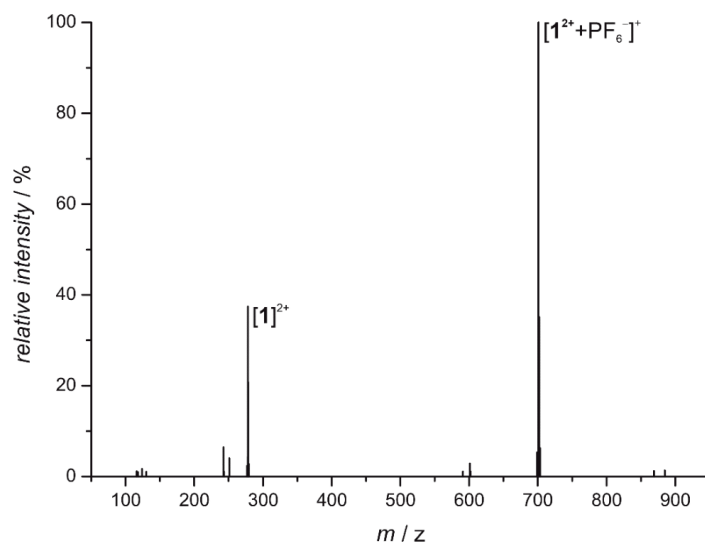


Fig. S6 – ESI+ mass spectrum of $1[\text{PF}_6]_2$ in CH_3CN .

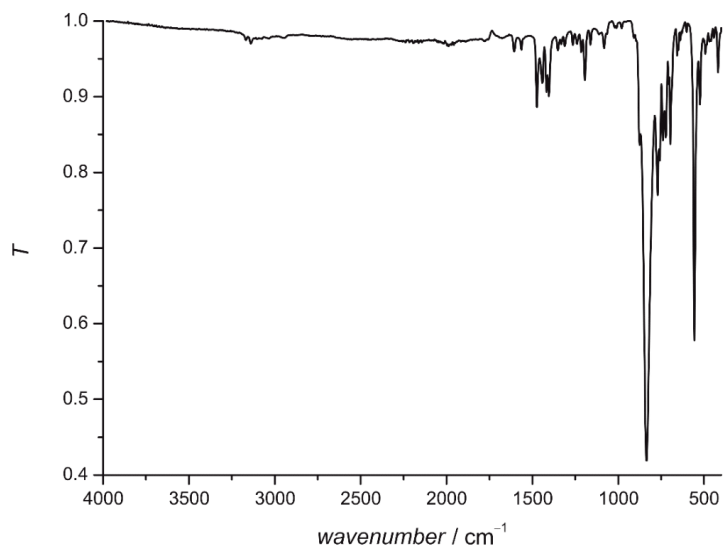


Fig. S7 – ATR IR-spectrum of **1**[PF₆]₂.

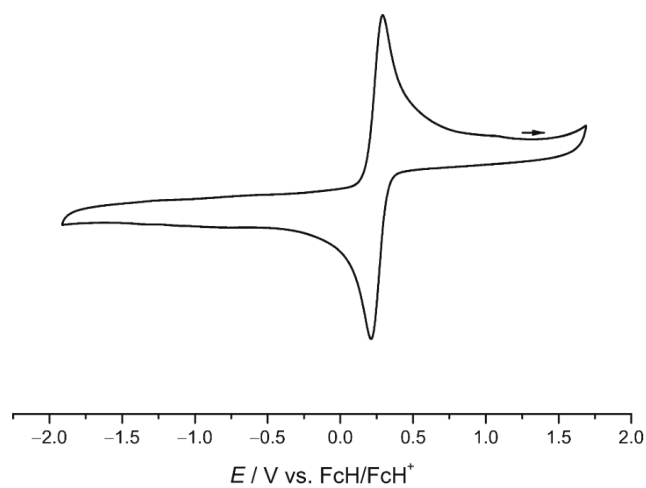


Fig. S8 – Cyclic voltammogram of **1**[PF₆]₂ in dry, deaerated CH₃CN with [tBu₄N][PF₆] as supporting electrolyte.

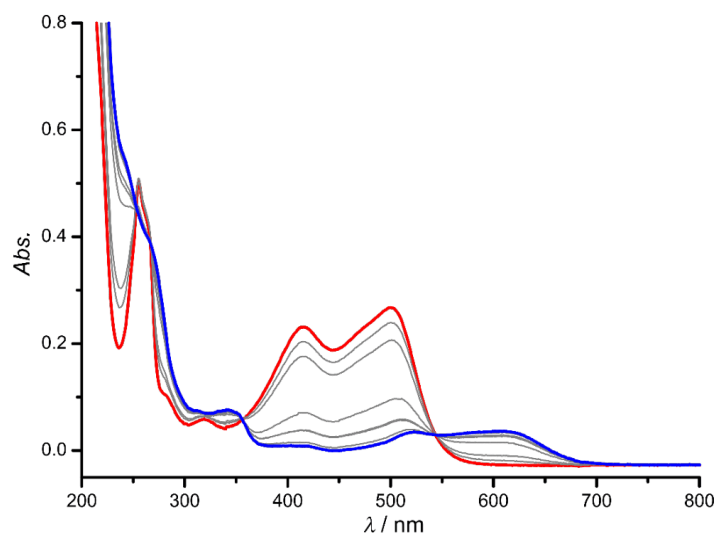


Fig. S9 – Spectroelectrochemical oxidation of $1[\text{PF}_6]_2$ in CH_3CN with $[\text{tBu}_4\text{N}][\text{PF}_6]$ as supporting electrolyte (red \rightarrow blue).

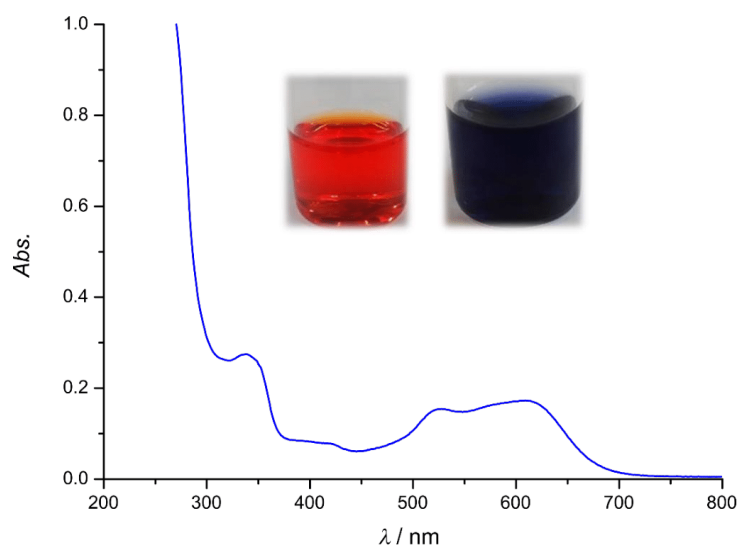


Fig. S10 – UV/Vis spectrum after chemical oxidation of $1[\text{PF}_6]_2$ with $[\text{NO}][\text{PF}_6]$ in CH_3CN and photographs of solutions before and after oxidation.

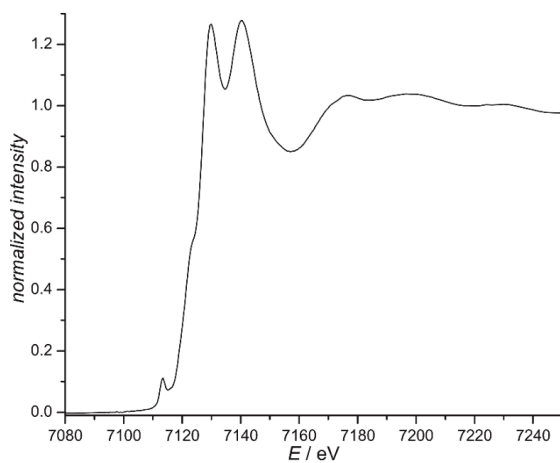


Fig. S11 – XANES spectrum of $1[\text{PF}_6]_2$, $E_0 = 7121.5$ eV.

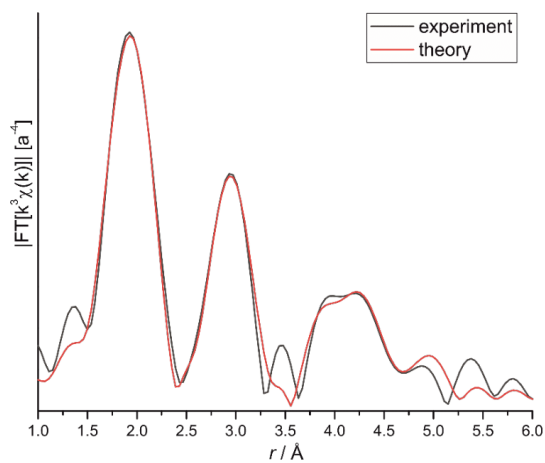


Fig. S12 – Experimental (black) and theoretical (red) EXAFS fit of $1[\text{PF}_6]_2$ after Fourier transformation.

Table S1 – Neighbour atoms, coordination numbers and distances of EXAFS analysis for **1[PF₆]₂**.

Abs-Bs ^[a]	N(Bs) ^[b]	R(Abs-Bs) [Å] ^[c]	σ [Å ⁻¹] ^[d]	R [%] ^[e] χ^2_{red} ^[f] E_f ^[g] Afac ^[h]
N/C	6.0	1.990	0.084	26.28
N	3.8	2.792	0.039	23.9932E-6
C	5.0	2.927	0.032	5.246
C	8.2	3.853	0.112	0.888
C	5.7	4.378	0.067	
C	3.0	4.852	0.032	

[a] Abs: X-ray absorbing atom, Bs: backscattering atom; [b] Number of backscattering atoms; [c] Distance of absorbing atom to backscattering atom; [d] Debye-Waller like factor; [e] Fit index; [f] Reduced χ^2 ; [g] Fermi energy, which accounts for the shift between theory and experiment; [h] Amplitude reducing factor.

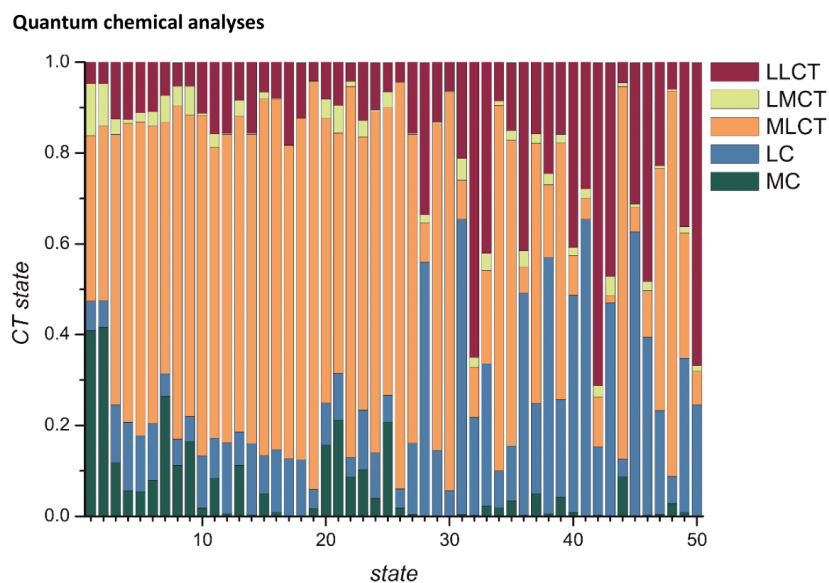


Fig. S13 – Charge transfer number analysis for 1^{2+} from TD-DFT calculation.

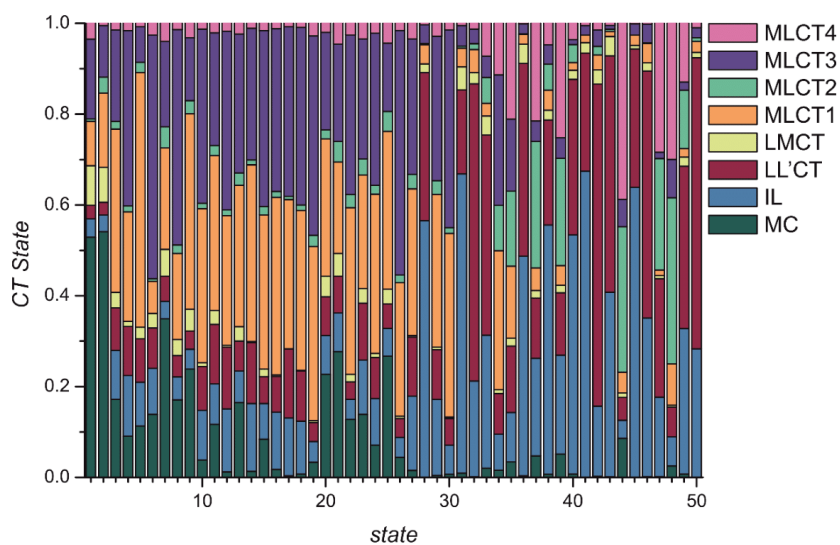
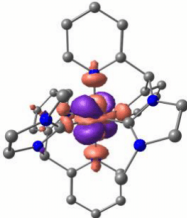
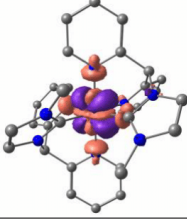
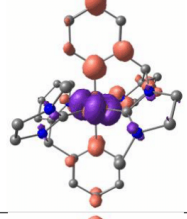
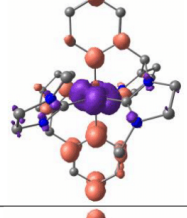
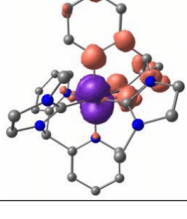


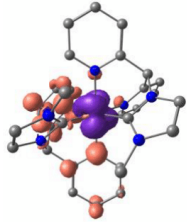
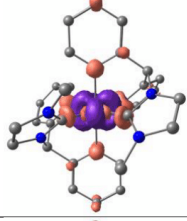
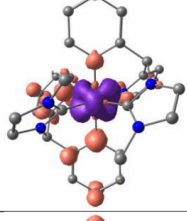
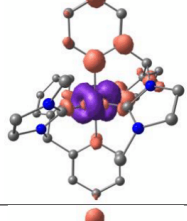
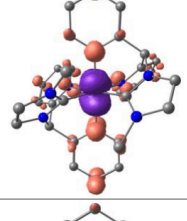
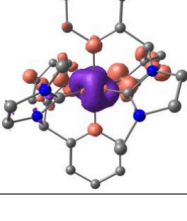
Fig. S14 – Detailed charge transfer number analysis of 1^{2+} ; MLCT1: charge transfer from iron to the pyridine moieties of ligand 1, MLCT2: charge transfer from iron to the NHC of ligand 1, MLCT3: charge transfer from iron to the pyridine moieties of ligand 2, MLCT4: charge transfer from iron to the NHC of ligand 2. LMCT: charge transfer from pyridine and carbene moieties to iron, LL'CT: charge transfer from the ligand fragments of ligand 1 to the fragments of ligand 2 or vice versa.

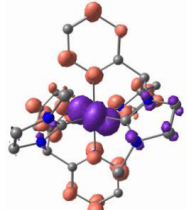
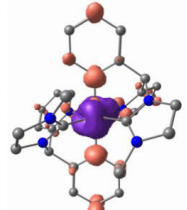
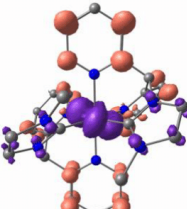
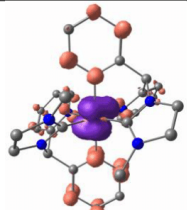
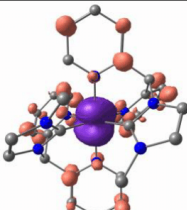
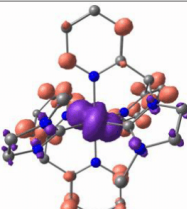
S13

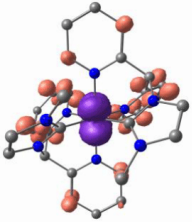
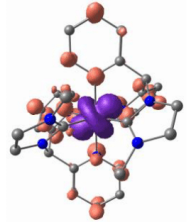
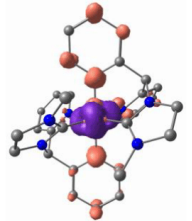
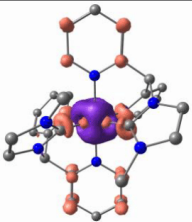
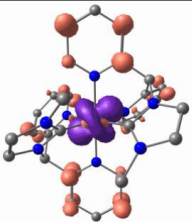
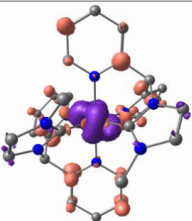
Table S2 – TD-DFT calculated transitions of 1^{2+} with detailed charge transfer number analysis of the transitions; MC = metal centred, LC = ligand centred, LL'CT = ligand-to-ligand charge transfer, LMCT = ligand-to-metal charge transfer, MLCT1 = metal-to-ligand charge transfer from iron to the pyridines of ligand 1, MLCT2 = metal-to-ligand charge transfer from iron to the NHC of ligand 1, MLCT3 = metal-to-ligand charge transfer from iron to the pyridines of ligand 2, MLCT4 = metal-to-ligand charge transfer from iron to the NHC of ligand 2.

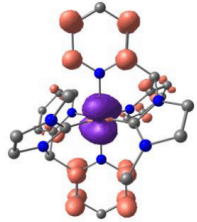
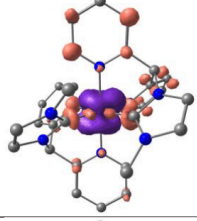
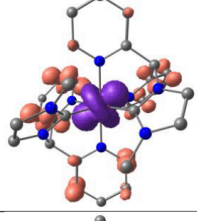
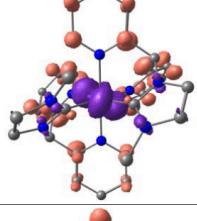
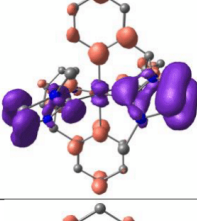
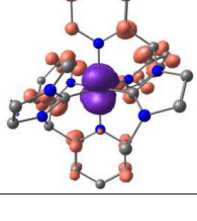
difference density (isosurface value 0.003)	transition number	composition
	1	MC $d_{Fe}-d_{Fe}$ (52.90 %) LC p_L-p_L (4.06 %) LL'CT $p_{L1}-p_{L2}$ (2.93 %) LMCT p_L-d_{Fe} (8.74 %) MLCT1 $d_{Fe}-p_{L1-pyr}$ (9.77 %) MLCT2 $d_{Fe}-p_{L1-carb}$ (0.54 %) MLCT3 $d_{Fe}-p_{L2-pyr}$ (17.57 %) MLCT4 $d_{Fe}-p_{L2-carb}$ (3.49 %)
	2	MC $d_{Fe}-d_{Fe}$ (54.15 %) LC p_L-p_L (3.63 %) LL'CT $p_{L1}-p_{L2}$ (2.81 %) LMCT p_L-d_{Fe} (7.67 %) MLCT1 $d_{Fe}-p_{L1-pyr}$ (16.37 %) MLCT2 $d_{Fe}-p_{L1-carb}$ (3.49 %) MLCT3 $d_{Fe}-p_{L2-pyr}$ (11.35 %) MLCT4 $d_{Fe}-p_{L2-carb}$ (0.53 %)
	3	MC $d_{Fe}-d_{Fe}$ (17.18 %) LC p_L-p_L (10.79 %) LL'CT $p_{L1}-p_{L2}$ (9.36 %) LMCT p_L-d_{Fe} (3.37 %) MLCT1 $d_{Fe}-p_{L1-pyr}$ (36.00 %) MLCT2 $d_{Fe}-p_{L1-carb}$ (1.69 %) MLCT3 $d_{Fe}-p_{L2-pyr}$ (20.14 %) MLCT4 $d_{Fe}-p_{L2-carb}$ (1.48 %)
	4	MC $d_{Fe}-d_{Fe}$ (9.04 %) LC p_L-p_L (13.38 %) LL'CT $p_{L1}-p_{L2}$ (10.84 %) LMCT p_L-d_{Fe} (1.11 %) MLCT1 $d_{Fe}-p_{L1-pyr}$ (24.10 %) MLCT2 $d_{Fe}-p_{L1-carb}$ (1.32 %) MLCT3 $d_{Fe}-p_{L2-pyr}$ (38.54 %) MLCT4 $d_{Fe}-p_{L2-carb}$ (1.67 %)
	5	MC $d_{Fe}-d_{Fe}$ (11.28 %) LC p_L-p_L (9.69 %) LL'CT $p_{L1}-p_{L2}$ (9.61 %) LMCT p_L-d_{Fe} (2.48 %) MLCT1 $d_{Fe}-p_{L1-pyr}$ (56.07 %) MLCT2 $d_{Fe}-p_{L1-carb}$ (2.25 %) MLCT3 $d_{Fe}-p_{L2-pyr}$ (7.89 %) MLCT4 $d_{Fe}-p_{L2-carb}$ (0.73 %)

S14

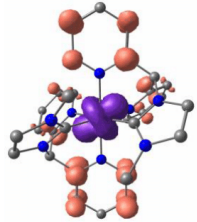
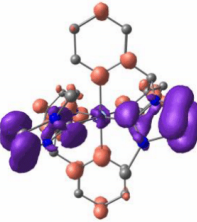
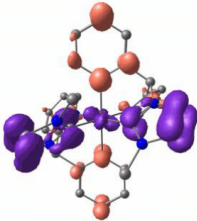
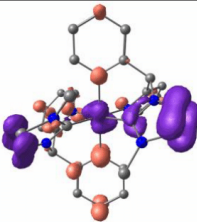
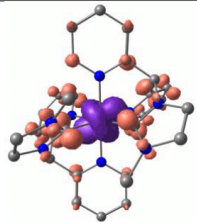
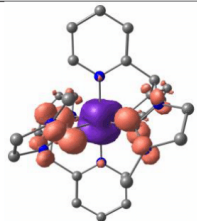
	6	MC d _{Fe} -d _{Fe} (13.86 %) LC p _L -p _L (10.18 %) LL'CT p _{L1} -p _{L2} (8.84 %) LMCT p _L -d _{Fe} (3.21 %) MLCT1 d _{Fe} -p _{L1} -pyr (7.11 %) MLCT2 d _{Fe} -p _{L1} -carb (0.56 %) MLCT3 d _{Fe} -p _{L2} -pyr (53.60 %) MLCT4 d _{Fe} -p _{L2} -carb (2.64 %)
	7	MC d _{Fe} -d _{Fe} (34.95 %) LC p _L -p _L (3.87 %) LL'CT p _{L1} -p _{L2} (5.45 %) LMCT p _L -d _{Fe} (5.93 %) MLCT1 d _{Fe} -p _{L1} -pyr (22.34 %) MLCT2 d _{Fe} -p _{L1} -carb (4.62 %) MLCT3 d _{Fe} -p _{L2} -pyr (18.83 %) MLCT4 d _{Fe} -p _{L2} -carb (4.01 %)
	8	MC d _{Fe} -d _{Fe} (17.10 %) LC p _L -p _L (5.03 %) LL'CT p _{L1} -p _{L2} (4.70 %) LMCT p _L -d _{Fe} (3.57 %) MLCT1 d _{Fe} -p _{L1} -pyr (18.93 %) MLCT2 d _{Fe} -p _{L1} -carb (1.90 %) MLCT3 d _{Fe} -p _{L2} -pyr (47.41 %) MLCT4 d _{Fe} -p _{L2} -carb (1.38 %)
	9	MC d _{Fe} -d _{Fe} (23.87 %) LC p _L -p _L (4.34 %) LL'CT p _{L1} -p _{L2} (4.06 %) LMCT p _L -d _{Fe} (4.76 %) MLCT1 d _{Fe} -p _{L1} -pyr (43.00 %) MLCT2 d _{Fe} -p _{L1} -carb (2.94 %) MLCT3 d _{Fe} -p _{L2} -pyr (13.82 %) MLCT4 d _{Fe} -p _{L2} -carb (3.21 %)
	10	MC d _{Fe} -d _{Fe} (3.89 %) LC p _L -p _L (10.92 %) LL'CT p _{L1} -p _{L2} (9.57 %) LMCT p _L -d _{Fe} (0.82 %) MLCT1 d _{Fe} -p _{L1} -pyr (33.97 %) MLCT2 d _{Fe} -p _{L1} -carb (1.23 %) MLCT3 d _{Fe} -p _{L2} -pyr (38.33 %) MLCT4 d _{Fe} -p _{L2} -carb (1.28 %)
	11	MC d _{Fe} -d _{Fe} (11.68 %) LC p _L -p _L (8.90 %) LL'CT p _{L1} -p _{L2} (13.14 %) LMCT p _L -d _{Fe} (3.05 %) MLCT1 d _{Fe} -p _{L1} -pyr (34.12 %) MLCT2 d _{Fe} -p _{L1} -carb (2.19 %) MLCT3 d _{Fe} -p _{L2} -pyr (24.85 %) MLCT4 d _{Fe} -p _{L2} -carb (2.08 %)

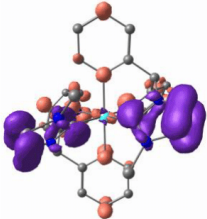
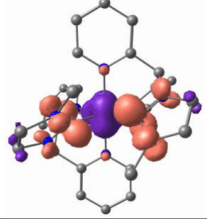
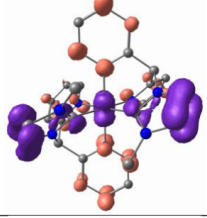
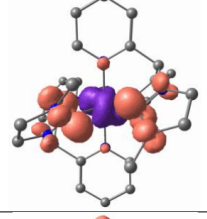
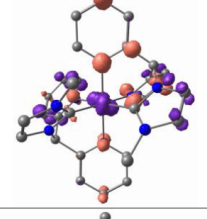
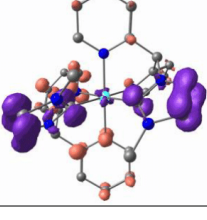
	12	MC $d_{Fe}-d_{Fe}$ (1.26 %) LC p_L-p_L (13.81 %) LL'CT $p_{L1}-p_{L2}$ (13.62 %) LMCT p_L-d_{Fe} (0.39 %) MLCT1 $d_{Fe}-p_{L1-pyr}$ (28.56 %) MLCT2 $d_{Fe}-p_{L1-carb}$ (1.28 %) MLCT3 $d_{Fe}-p_{L2-pyr}$ (39.34 %) MLCT4 $d_{Fe}-p_{L2-carb}$ (1.75 %)
	13	MC $d_{Fe}-d_{Fe}$ (16.49 %) LC p_L-p_L (6.98 %) LL'CT $p_{L1}-p_{L2}$ (6.55 %) LMCT p_L-d_{Fe} (3.15 %) MLCT1 $d_{Fe}-p_{L1-pyr}$ (31.17 %) MLCT2 $d_{Fe}-p_{L1-carb}$ (2.72 %) MLCT3 $d_{Fe}-p_{L2-pyr}$ (30.56 %) MLCT4 $d_{Fe}-p_{L2-carb}$ (2.39 %)
	14	MC $d_{Fe}-d_{Fe}$ (1.34 %) LC p_L-p_L (14.92 %) LL'CT $p_{L1}-p_{L2}$ (13.39 %) LMCT p_L-d_{Fe} (0.28 %) MLCT1 $d_{Fe}-p_{L1-pyr}$ (38.90 %) MLCT2 $d_{Fe}-p_{L1-carb}$ (1.10 %) MLCT3 $d_{Fe}-p_{L2-pyr}$ (28.97 %) MLCT4 $d_{Fe}-p_{L2-carb}$ (1.11 %)
	15	MC $d_{Fe}-d_{Fe}$ (8.45 %) LC p_L-p_L (7.83 %) LL'CT $p_{L1}-p_{L2}$ (5.92 %) LMCT p_L-d_{Fe} (1.66 %) MLCT1 $d_{Fe}-p_{L1-pyr}$ (33.97 %) MLCT2 $d_{Fe}-p_{L1-carb}$ (1.82 %) MLCT3 $d_{Fe}-p_{L2-pyr}$ (38.69 %) MLCT4 $d_{Fe}-p_{L2-carb}$ (1.66 %)
	16	MC $d_{Fe}-d_{Fe}$ (1.74 %) LC p_L-p_L (12.66 %) LL'CT $p_{L1}-p_{L2}$ (7.82 %) LMCT p_L-d_{Fe} (0.37 %) MLCT1 $d_{Fe}-p_{L1-pyr}$ (39.07 %) MLCT2 $d_{Fe}-p_{L1-carb}$ (1.27 %) MLCT3 $d_{Fe}-p_{L2-pyr}$ (35.83 %) MLCT4 $d_{Fe}-p_{L2-carb}$ (1.24 %)
	17	MC $d_{Fe}-d_{Fe}$ (0.38 %) LC p_L-p_L (12.72 %) LL'CT $p_{L1}-p_{L2}$ (15.14 %) LMCT p_L-d_{Fe} (0.10 %) MLCT1 $d_{Fe}-p_{L1-pyr}$ (32.81 %) MLCT2 $d_{Fe}-p_{L1-carb}$ (0.77 %) MLCT3 $d_{Fe}-p_{L2-pyr}$ (37.33 %) MLCT4 $d_{Fe}-p_{L2-carb}$ (0.75 %)

	18	MC $d_{Fe}-d_{Fe}$ (0.78 %) LC p_L-p_L (11.61 %) LL'CT $p_{L1}-p_{L2}$ (11.04 %) LMCT p_L-d_{Fe} (0.16 %) MLCT1 $d_{Fe}-p_{L1-pyr}$ (35.23 %) MLCT2 $d_{Fe}-p_{L1-carb}$ (1.14 %) MLCT3 $d_{Fe}-p_{L2-pyr}$ (39.10 %) MLCT4 $d_{Fe}-p_{L2-carb}$ (0.95 %)
	19	MC $d_{Fe}-d_{Fe}$ (3.33 %) LC p_L-p_L (4.55 %) LL'CT $p_{L1}-p_{L2}$ (4.16 %) LMCT p_L-d_{Fe} (0.45 %) MLCT1 $d_{Fe}-p_{L1-pyr}$ (38.36 %) MLCT2 $d_{Fe}-p_{L1-carb}$ (2.46 %) MLCT3 $d_{Fe}-p_{L2-pyr}$ (43.90 %) MLCT4 $d_{Fe}-p_{L2-carb}$ (2.80 %)
	20	MC $d_{Fe}-d_{Fe}$ (22.69 %) LC p_L-p_L (8.55 %) LL'CT $p_{L1}-p_{L2}$ (8.56 %) LMCT p_L-d_{Fe} (4.52 %) MLCT1 $d_{Fe}-p_{L1-pyr}$ (30.24 %) MLCT2 $d_{Fe}-p_{L1-carb}$ (2.00 %) MLCT3 $d_{Fe}-p_{L2-pyr}$ (21.45 %) MLCT4 $d_{Fe}-p_{L2-carb}$ (1.99 %)
	21	MC $d_{Fe}-d_{Fe}$ (27.71 %) LC p_L-p_L (8.54 %) LL'CT $p_{L1}-p_{L2}$ (8.05 %) LMCT p_L-d_{Fe} (5.03 %) MLCT1 $d_{Fe}-p_{L1-pyr}$ (20.13 %) MLCT2 $d_{Fe}-p_{L1-carb}$ (4.49 %) MLCT3 $d_{Fe}-p_{L2-pyr}$ (21.50 %) MLCT4 $d_{Fe}-p_{L2-carb}$ (4.56 %)
	22	MC $d_{Fe}-d_{Fe}$ (12.74 %) LC p_L-p_L (4.47 %) LL'CT $p_{L1}-p_{L2}$ (3.85 %) LMCT p_L-d_{Fe} (1.67 %) MLCT1 $d_{Fe}-p_{L1-pyr}$ (36.68 %) MLCT2 $d_{Fe}-p_{L1-carb}$ (2.90 %) MLCT3 $d_{Fe}-p_{L2-pyr}$ (35.11 %) MLCT4 $d_{Fe}-p_{L2-carb}$ (2.58 %)
	23	MC $d_{Fe}-d_{Fe}$ (13.86 %) LC p_L-p_L (12.00 %) LL'CT $p_{L1}-p_{L2}$ (12.55 %) LMCT p_L-d_{Fe} (3.17 %) MLCT1 $d_{Fe}-p_{L1-pyr}$ (25.03 %) MLCT2 $d_{Fe}-p_{L1-carb}$ (3.58 %) MLCT3 $d_{Fe}-p_{L2-pyr}$ (26.38 %) MLCT4 $d_{Fe}-p_{L2-carb}$ (3.44 %)

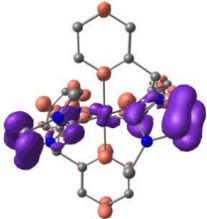
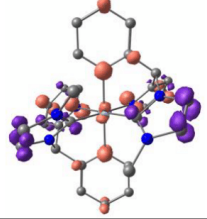
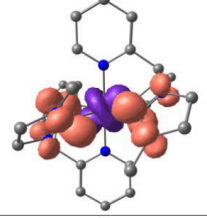
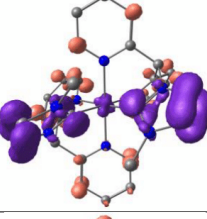
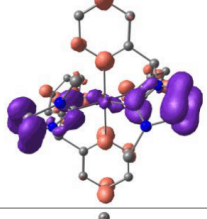
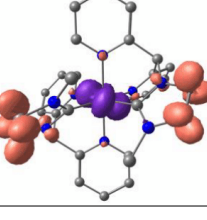
	24	MC $d_{Fe}-d_{Fe}$ (7.12 %) LC p_L-p_L (10.27 %) LL'CT $p_{L1}-p_{L2}$ (9.02 %) LMCT p_L-d_{Fe} (0.93 %) MLCT1 $d_{Fe}-p_{L1-pyr}$ (35.01 %) MLCT2 $d_{Fe}-p_{L1-carb}$ (1.97 %) MLCT3 $d_{Fe}-p_{L2-pyr}$ (33.50 %) MLCT4 $d_{Fe}-p_{L2-carb}$ (2.19 %)
	25	MC $d_{Fe}-d_{Fe}$ (26.70 %) LC p_L-p_L (6.13 %) LL'CT $p_{L1}-p_{L2}$ (5.36 %) LMCT p_L-d_{Fe} (3.33 %) MLCT1 $d_{Fe}-p_{L1-pyr}$ (34.66 %) MLCT2 $d_{Fe}-p_{L1-carb}$ (4.41 %) MLCT3 $d_{Fe}-p_{L2-pyr}$ (15.01 %) MLCT4 $d_{Fe}-p_{L2-carb}$ (4.41 %)
	26	MC $d_{Fe}-d_{Fe}$ (4.45 %) LC p_L-p_L (4.40 %) LL'CT $p_{L1}-p_{L2}$ (4.15 %) LMCT p_L-d_{Fe} (0.54 %) MLCT1 $d_{Fe}-p_{L1-pyr}$ (29.36 %) MLCT2 $d_{Fe}-p_{L1-carb}$ (1.72 %) MLCT3 $d_{Fe}-p_{L2-pyr}$ (53.82 %) MLCT4 $d_{Fe}-p_{L2-carb}$ (1.58 %)
	27	MC $d_{Fe}-d_{Fe}$ (1.53 %) LC p_L-p_L (16.39 %) LL'CT $p_{L1}-p_{L2}$ (12.99 %) LMCT p_L-d_{Fe} (0.35 %) MLCT1 $d_{Fe}-p_{L1-pyr}$ (32.28 %) MLCT2 $d_{Fe}-p_{L1-carb}$ (3.25 %) MLCT3 $d_{Fe}-p_{L2-pyr}$ (29.75 %) MLCT4 $d_{Fe}-p_{L2-carb}$ (3.47 %)
	28	MC $d_{Fe}-d_{Fe}$ (0.08 %) LC p_L-p_L (56.44 %) LL'CT $p_{L1}-p_{L2}$ (32.59 %) LMCT p_L-d_{Fe} (1.95 %) MLCT1 $d_{Fe}-p_{L1-pyr}$ (4.20 %) MLCT2 $d_{Fe}-p_{L1-carb}$ (0.23 %) MLCT3 $d_{Fe}-p_{L2-pyr}$ (4.17 %) MLCT4 $d_{Fe}-p_{L2-carb}$ (0.34 %)
	29	MC $d_{Fe}-d_{Fe}$ (0.46 %) LC p_L-p_L (16.70 %) LL'CT $p_{L1}-p_{L2}$ (10.95 %) LMCT p_L-d_{Fe} (0.56 %) MLCT1 $d_{Fe}-p_{L1-pyr}$ (33.66 %) MLCT2 $d_{Fe}-p_{L1-carb}$ (3.05 %) MLCT3 $d_{Fe}-p_{L2-pyr}$ (31.75 %) MLCT4 $d_{Fe}-p_{L2-carb}$ (2.87 %)

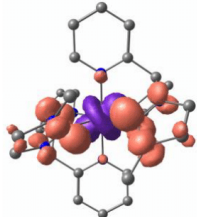
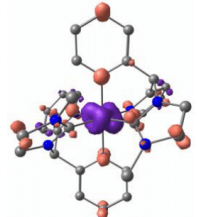
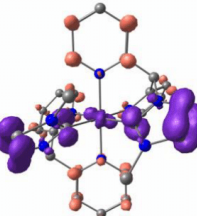
S18

	30	MC $d_{Fe}-d_{Fe}$ (0.72 %) LC p_L-p_L (6.43 %) LL'CT $p_{L1}-p_{L2}$ (5.83 %) LMCT p_L-d_{Fe} (0.29 %) MLCT1 $d_{Fe}-p_{L1-pyr}$ (40.44 %) MLCT2 $d_{Fe}-p_{L1-carb}$ (1.28 %) MLCT3 $d_{Fe}-p_{L2-pyr}$ (43.55 %) MLCT4 $d_{Fe}-p_{L2-carb}$ (1.47 %)
	31	MC $d_{Fe}-d_{Fe}$ (0.96 %) LC p_L-p_L (65.87 %) LL'CT $p_{L1}-p_{L2}$ (18.50 %) LMCT p_L-d_{Fe} (5.10 %) MLCT1 $d_{Fe}-p_{L1-pyr}$ (4.08 %) MLCT2 $d_{Fe}-p_{L1-carb}$ (0.45 %) MLCT3 $d_{Fe}-p_{L2-pyr}$ (4.55 %) MLCT4 $d_{Fe}-p_{L2-carb}$ (0.51 %)
	32	MC $d_{Fe}-d_{Fe}$ (0.14 %) LC p_L-p_L (21.12 %) LL'CT $p_{L1}-p_{L2}$ (65.38 %) LMCT p_L-d_{Fe} (2.48 %) MLCT1 $d_{Fe}-p_{L1-pyr}$ (5.06 %) MLCT2 $d_{Fe}-p_{L1-carb}$ (1.32 %) MLCT3 $d_{Fe}-p_{L2-pyr}$ (3.23 %) MLCT4 $d_{Fe}-p_{L2-carb}$ (1.27 %)
	33	MC $d_{Fe}-d_{Fe}$ (2.04 %) LC p_L-p_L (29.24 %) LL'CT $p_{L1}-p_{L2}$ (44.16 %) LMCT p_L-d_{Fe} (4.15 %) MLCT1 $d_{Fe}-p_{L1-pyr}$ (2.76 %) MLCT2 $d_{Fe}-p_{L1-carb}$ (5.68 %) MLCT3 $d_{Fe}-p_{L2-pyr}$ (4.71 %) MLCT4 $d_{Fe}-p_{L2-carb}$ (7.25 %)
	34	MC $d_{Fe}-d_{Fe}$ (1.57 %) LC p_L-p_L (7.98 %) LL'CT $p_{L1}-p_{L2}$ (8.93 %) LMCT p_L-d_{Fe} (0.82 %) MLCT1 $d_{Fe}-p_{L1-pyr}$ (30.63 %) MLCT2 $d_{Fe}-p_{L1-carb}$ (10.00 %) MLCT3 $d_{Fe}-p_{L2-pyr}$ (28.73 %) MLCT4 $d_{Fe}-p_{L2-carb}$ (11.34 %)
	35	MC $d_{Fe}-d_{Fe}$ (3.39 %) LC p_L-p_L (10.91 %) LL'CT $p_{L1}-p_{L2}$ (14.62 %) LMCT p_L-d_{Fe} (1.74 %) MLCT1 $d_{Fe}-p_{L1-pyr}$ (15.87 %) MLCT2 $d_{Fe}-p_{L1-carb}$ (16.48 %) MLCT3 $d_{Fe}-p_{L2-pyr}$ (15.86 %) MLCT4 $d_{Fe}-p_{L2-carb}$ (21.13 %)

	36	MC $d_{Fe}-d_{Fe}$ (0.38 %) LC p_L-p_L (48.37 %) LL'CT $p_{L1}-p_{L2}$ (42.45 %) LMCT p_L-d_{Fe} (4.23 %) MLCT1 $d_{Fe}-p_{L1-pyr}$ (2.13 %) MLCT2 $d_{Fe}-p_{L1-carb}$ (0.11 %) MLCT3 $d_{Fe}-p_{L2-pyr}$ (2.20 %) MLCT4 $d_{Fe}-p_{L2-carb}$ (0.14 %)
	37	MC $d_{Fe}-d_{Fe}$ (4.74 %) LC p_L-p_L (21.49 %) LL'CT $p_{L1}-p_{L2}$ (13.29 %) LMCT p_L-d_{Fe} (1.61 %) MLCT1 $d_{Fe}-p_{L1-pyr}$ (4.97 %) MLCT2 $d_{Fe}-p_{L1-carb}$ (27.89 %) MLCT3 $d_{Fe}-p_{L2-pyr}$ (4.47 %) MLCT4 $d_{Fe}-p_{L2-carb}$ (21.55 %)
	38	MC $d_{Fe}-d_{Fe}$ (0.68 %) LC p_L-p_L (54.93 %) LL'CT $p_{L1}-p_{L2}$ (23.08 %) LMCT p_L-d_{Fe} (2.16 %) MLCT1 $d_{Fe}-p_{L1-pyr}$ (4.42 %) MLCT2 $d_{Fe}-p_{L1-carb}$ (5.70 %) MLCT3 $d_{Fe}-p_{L2-pyr}$ (4.32 %) MLCT4 $d_{Fe}-p_{L2-carb}$ (4.71 %)
	39	MC $d_{Fe}-d_{Fe}$ (5.15 %) LC p_L-p_L (21.74 %) LL'CT $p_{L1}-p_{L2}$ (13.80 %) LMCT p_L-d_{Fe} (1.62 %) MLCT1 $d_{Fe}-p_{L1-pyr}$ (4.30 %) MLCT2 $d_{Fe}-p_{L1-carb}$ (23.64 %) MLCT3 $d_{Fe}-p_{L2-pyr}$ (4.54 %) MLCT4 $d_{Fe}-p_{L2-carb}$ (25.20 %)
	40	MC $d_{Fe}-d_{Fe}$ (0.76 %) LC p_L-p_L (52.67 %) LL'CT $p_{L1}-p_{L2}$ (34.21 %) LMCT p_L-d_{Fe} (2.00 %) MLCT1 $d_{Fe}-p_{L1-pyr}$ (1.71 %) MLCT2 $d_{Fe}-p_{L1-carb}$ (3.98 %) MLCT3 $d_{Fe}-p_{L2-pyr}$ (1.06 %) MLCT4 $d_{Fe}-p_{L2-carb}$ (3.60 %)
	41	MC $d_{Fe}-d_{Fe}$ (0.03 %) LC p_L-p_L (67.39 %) LL'CT $p_{L1}-p_{L2}$ (26.03 %) LMCT p_L-d_{Fe} (2.29 %) MLCT1 $d_{Fe}-p_{L1-pyr}$ (1.64 %) MLCT2 $d_{Fe}-p_{L1-carb}$ (0.05 %) MLCT3 $d_{Fe}-p_{L2-pyr}$ (2.06 %) MLCT4 $d_{Fe}-p_{L2-carb}$ (0.51 %)

S20

	42	MC $d_{Fe}-d_{Fe}$ (0.23 %) LC p_L-p_L (15.46 %) LL'CT $p_{L1}-p_{L2}$ (70.89 %) LMCT p_L-d_{Fe} (3.19 %) MLCT1 $d_{Fe}-p_{L1-pyr}$ (3.28 %) MLCT2 $d_{Fe}-p_{L1-carb}$ (1.83 %) MLCT3 $d_{Fe}-p_{L2-pyr}$ (3.64 %) MLCT4 $d_{Fe}-p_{L2-carb}$ (1.48 %)
	43	MC $d_{Fe}-d_{Fe}$ (0.11 %) LC p_L-p_L (40.65 %) LL'CT $p_{L1}-p_{L2}$ (52.06 %) LMCT p_L-d_{Fe} (4.23 %) MLCT1 $d_{Fe}-p_{L1-pyr}$ (1.11 %) MLCT2 $d_{Fe}-p_{L1-carb}$ (0.53 %) MLCT3 $d_{Fe}-p_{L2-pyr}$ (0.85 %) MLCT4 $d_{Fe}-p_{L2-carb}$ (0.46 %)
	44	MC $d_{Fe}-d_{Fe}$ (8.61 %) LC p_L-p_L (4.00 %) LL'CT $p_{L1}-p_{L2}$ (5.02 %) LMCT p_L-d_{Fe} (1.00 %) MLCT1 $d_{Fe}-p_{L1-pyr}$ (4.56 %) MLCT2 $d_{Fe}-p_{L1-carb}$ (31.97 %) MLCT3 $d_{Fe}-p_{L2-pyr}$ (6.04 %) MLCT4 $d_{Fe}-p_{L2-carb}$ (38.80 %)
	45	MC $d_{Fe}-d_{Fe}$ (0.02 %) LC p_L-p_L (63.87 %) LL'CT $p_{L1}-p_{L2}$ (30.45 %) LMCT p_L-d_{Fe} (0.83 %) MLCT1 $d_{Fe}-p_{L1-pyr}$ (2.20 %) MLCT2 $d_{Fe}-p_{L1-carb}$ (0.08 %) MLCT3 $d_{Fe}-p_{L2-pyr}$ (2.44 %) MLCT4 $d_{Fe}-p_{L2-carb}$ (0.11 %)
	46	MC $d_{Fe}-d_{Fe}$ (0.18 %) LC p_L-p_L (34.95 %) LL'CT $p_{L1}-p_{L2}$ (54.35 %) LMCT p_L-d_{Fe} (1.81 %) MLCT1 $d_{Fe}-p_{L1-pyr}$ (4.28 %) MLCT2 $d_{Fe}-p_{L1-carb}$ (0.13 %) MLCT3 $d_{Fe}-p_{L2-pyr}$ (4.14 %) MLCT4 $d_{Fe}-p_{L2-carb}$ (0.18 %)
	47	MC $d_{Fe}-d_{Fe}$ (0.17 %) LC p_L-p_L (17.53 %) LL'CT $p_{L1}-p_{L2}$ (26.05 %) LMCT p_L-d_{Fe} (0.73 %) MLCT1 $d_{Fe}-p_{L1-pyr}$ (1.18 %) MLCT2 $d_{Fe}-p_{L1-carb}$ (24.56 %) MLCT3 $d_{Fe}-p_{L2-pyr}$ (1.40 %) MLCT4 $d_{Fe}-p_{L2-carb}$ (28.39 %)

	48	MC $d_{Fe}-d_{Fe}$ (2.52 %) LC p_L-p_L (6.42 %) LL'CT $p_{L1}-p_{L2}$ (6.54 %) LMCT p_L-d_{Fe} (0.42 %) MLCT1 $d_{Fe}-p_{L1-pyr}$ (9.07 %) MLCT2 $d_{Fe}-p_{L1-carb}$ (36.62 %) MLCT3 $d_{Fe}-p_{L2-pyr}$ (8.44 %) MLCT4 $d_{Fe}-p_{L2-carb}$ (29.98 %)
	49	MC $d_{Fe}-d_{Fe}$ (0.77 %) LC p_L-p_L (32.02 %) LL'CT $p_{L1}-p_{L2}$ (35.74 %) LMCT p_L-d_{Fe} (1.98 %) MLCT1 $d_{Fe}-p_{L1-pyr}$ (1.84 %) MLCT2 $d_{Fe}-p_{L1-carb}$ (12.89 %) MLCT3 $d_{Fe}-p_{L2-pyr}$ (1.81 %) MLCT4 $d_{Fe}-p_{L2-carb}$ (12.94 %)
	50	MC $d_{Fe}-d_{Fe}$ (0.05 %) LC p_L-p_L (28.26 %) LL'CT $p_{L1}-p_{L2}$ (64.11 %) LMCT p_L-d_{Fe} (1.21 %) MLCT1 $d_{Fe}-p_{L1-pyr}$ (2.38 %) MLCT2 $d_{Fe}-p_{L1-carb}$ (0.86 %) MLCT3 $d_{Fe}-p_{L2-pyr}$ (2.13 %) MLCT4 $d_{Fe}-p_{L2-carb}$ (1.01 %)

Cartesian coordinates of optimised geometries for 1²⁺¹GS

26	1.791047000	1.634849000	7.351698000
7	2.852863000	-0.074475000	7.240048000
6	3.467245000	2.602920000	7.384318000
7	1.923161000	1.463772000	9.388851000
6	2.164165000	1.083429000	12.133442000
1	2.258529000	0.924281000	13.199243000
6	4.242478000	0.912739000	8.965198000
6	5.328202000	3.882505000	7.234060000
6	5.605913000	2.887985000	8.107069000
7	4.020158000	3.694427000	6.803881000
6	3.099884000	1.113439000	9.934871000
6	0.950591000	1.458226000	11.573963000
1	0.069169000	1.606294000	12.181550000
6	0.873987000	1.642436000	10.203910000
1	-0.054447000	1.932341000	9.735659000
6	3.258881000	0.913237000	11.295602000
1	4.224741000	0.625937000	11.687331000
1	5.154556000	0.703079000	9.514930000
6	3.922638000	-0.240105000	8.039075000
6	4.679826000	-1.400535000	8.034510000
1	5.533299000	-1.487084000	8.692312000
6	4.324811000	-2.433996000	7.178648000
1	4.898854000	-3.350264000	7.157944000
6	3.223865000	-2.263290000	6.349785000
1	2.906355000	-3.036273000	5.664364000
6	2.519809000	-1.074013000	6.407255000
1	1.659502000	-0.906237000	5.777824000
7	4.454215000	2.123454000	8.180446000
7	0.701829000	3.318551000	7.523808000
7	0.035670000	0.588033000	7.400217000
6	1.569211000	1.753922000	5.430593000
6	-0.762253000	2.303271000	5.882236000
6	-1.351364000	-1.173586000	8.233498000
1	-1.431328000	-2.067749000	8.834537000
6	-2.273950000	0.489621000	6.788242000
1	-3.094909000	0.922830000	6.233720000
6	-2.448220000	-0.649575000	7.563756000
1	-3.417905000	-1.123248000	7.633975000
6	-0.133775000	-0.523804000	8.131142000
1	0.735223000	-0.893467000	8.653612000
7	0.334238000	2.049234000	4.955099000
6	1.550573000	1.763454000	3.167666000
7	2.315003000	1.583171000	4.313729000
6	0.294229000	2.059373000	3.571338000
1	-1.647761000	2.540606000	5.301526000
6	-0.405098000	3.470511000	6.775148000
6	-1.171202000	4.624755000	6.806952000
1	-2.050888000	4.701701000	6.183441000
6	-0.782341000	5.669515000	7.633847000

S23

1	-1.356163000	6.585567000	7.667650000
6	0.357288000	5.512357000	8.411861000
1	0.703587000	6.294989000	9.071881000
6	1.065436000	4.326748000	8.332969000
1	1.957367000	4.171377000	8.920180000
6	-1.019033000	1.070568000	6.721260000
1	-0.600797000	2.274672000	3.016417000
1	1.970108000	1.666346000	2.182280000
6	3.738028000	1.280933000	4.279213000
1	4.103571000	1.192006000	5.294852000
1	3.908764000	0.344698000	3.750378000
1	4.272913000	2.081387000	3.770307000
6	3.365194000	4.588362000	5.861036000
1	3.972103000	4.677593000	4.961689000
1	2.395373000	4.181354000	5.603057000
1	3.236810000	5.572663000	6.310003000
1	6.492775000	2.657449000	8.669089000
1	5.930890000	4.700671000	6.882562000

³MLCT

26	1.758494000	1.579271000	7.381116000
7	2.759472000	-0.030170000	7.247907000
6	3.377435000	2.573524000	7.358939000
7	1.895462000	1.438636000	9.270947000
6	2.065892000	0.976637000	12.021913000
1	2.132943000	0.789952000	13.084861000
6	4.222980000	0.912679000	8.909010000
6	5.160312000	3.933189000	7.172377000
6	5.508646000	2.936862000	8.025537000
7	3.856716000	3.697148000	6.775940000
6	3.063472000	1.084363000	9.854548000
6	0.864184000	1.349608000	11.435743000
1	-0.037133000	1.469138000	12.019704000
6	0.817129000	1.572404000	10.073290000
1	-0.103286000	1.864823000	9.596141000
6	3.185440000	0.842375000	11.207913000
1	4.145678000	0.557895000	11.614495000
1	5.139580000	0.711563000	9.452177000
6	3.887110000	-0.215051000	7.967113000
6	4.675305000	-1.346523000	7.858316000
1	5.569238000	-1.431335000	8.459493000
6	4.299269000	-2.346773000	6.973125000
1	4.900864000	-3.238045000	6.860515000
6	3.137352000	-2.169647000	6.232629000
1	2.792684000	-2.918027000	5.533500000
6	2.405039000	-1.010040000	6.388949000
1	1.497748000	-0.850963000	5.830876000
7	4.398612000	2.129730000	8.119558000
7	0.724616000	3.165895000	7.535127000
7	0.152755000	0.563803000	7.360448000
6	1.640639000	1.717498000	5.489819000

S24

6	-0.702387000	2.230390000	5.824358000
6	-1.312035000	-0.949536000	8.541548000
1	-1.401565000	-1.769277000	9.241097000
6	-2.243380000	0.636406000	7.002494000
1	-3.072379000	1.096839000	6.480359000
6	-2.448977000	-0.388805000	7.924572000
1	-3.441539000	-0.753013000	8.147112000
6	-0.069046000	-0.464590000	8.246725000
1	0.806879000	-0.890123000	8.709386000
7	0.434192000	1.957670000	4.938996000
6	1.763339000	1.659276000	3.239784000
7	2.463890000	1.532427000	4.429755000
6	0.474838000	1.926101000	3.561924000
1	-1.572007000	2.464041000	5.220043000
6	-0.327719000	3.391384000	6.702533000
6	-1.016118000	4.593815000	6.675439000
1	-1.837948000	4.714212000	5.982572000
6	-0.635362000	5.618227000	7.524159000
1	-1.142337000	6.572599000	7.501624000
6	0.421790000	5.382611000	8.410292000
1	0.752804000	6.137898000	9.108798000
6	1.063867000	4.167892000	8.385848000
1	1.890806000	3.974206000	9.050355000
6	-0.964236000	1.069514000	6.727590000
1	-0.393355000	2.092850000	2.950571000
1	2.244636000	1.548749000	2.284672000
6	3.902276000	1.293491000	4.458023000
1	4.216010000	1.045918000	5.463601000
1	4.141101000	0.465328000	3.795044000
1	4.430795000	2.184969000	4.123066000
6	3.122476000	4.617180000	5.913154000
1	3.801221000	5.009778000	5.160939000
1	2.308645000	4.093310000	5.427445000
1	2.721519000	5.437616000	6.505579000
1	6.421048000	2.735908000	8.556884000
1	5.717126000	4.780263000	6.814181000

³MC

26	1.767853000	1.630782000	7.386372000
7	2.966404000	-0.386515000	7.304323000
6	3.496822000	2.561828000	7.465891000
7	1.971113000	1.397752000	9.414839000
6	2.192470000	0.823864000	12.125345000
1	2.280503000	0.588330000	13.177293000
6	4.290633000	0.777525000	8.972410000
6	5.391681000	3.781558000	7.307758000
6	5.660104000	2.738692000	8.126587000
7	4.067549000	3.655548000	6.914634000
6	3.129861000	0.947612000	9.926959000
6	1.005811000	1.317398000	11.601968000
1	0.139348000	1.487618000	12.225040000

6	0.936129000	1.587971000	10.246928000
1	0.028130000	1.964446000	9.800361000
6	3.271876000	0.643523000	11.271325000
1	4.219439000	0.275497000	11.639471000
1	5.194244000	0.613960000	9.551657000
6	4.083417000	-0.403874000	8.035793000
6	5.015374000	-1.427340000	7.942950000
1	5.910632000	-1.408471000	8.549096000
6	4.771866000	-2.465577000	7.050636000
1	5.481033000	-3.276780000	6.951370000
6	3.611371000	-2.443983000	6.287958000
1	3.383787000	-3.231818000	5.583527000
6	2.735170000	-1.379646000	6.444963000
1	1.820377000	-1.314083000	5.869030000
7	4.487155000	2.009277000	8.208144000
7	0.396116000	3.532945000	7.635187000
7	-0.031731000	0.628755000	7.405255000
6	1.491540000	1.784859000	5.451776000
6	-0.851884000	2.371754000	5.902158000
6	-1.456572000	-1.049855000	8.337118000
1	-1.547610000	-1.938927000	8.944009000
6	-2.375886000	0.662573000	6.947453000
1	-3.206371000	1.140057000	6.446077000
6	-2.563825000	-0.458624000	7.744239000
1	-3.553434000	-0.870740000	7.888137000
6	-0.213633000	-0.472284000	8.149574000
1	0.669338000	-0.887791000	8.611071000
7	0.257397000	2.099558000	4.989747000
6	1.459864000	1.788527000	3.193109000
7	2.228397000	1.605497000	4.333447000
6	0.210833000	2.104566000	3.606233000
1	-1.734691000	2.540743000	5.293088000
6	-0.568021000	3.625639000	6.715326000
6	-1.251333000	4.807609000	6.472302000
1	-2.023492000	4.847403000	5.716081000
6	-0.908692000	5.935537000	7.208266000
1	-1.413171000	6.875405000	7.028239000
6	0.094039000	5.839226000	8.164776000
1	0.393884000	6.693156000	8.755729000
6	0.720024000	4.614053000	8.346200000
1	1.513251000	4.491195000	9.073931000
6	-1.095890000	1.169444000	6.786686000
1	-0.683859000	2.333644000	3.056254000
1	1.869378000	1.678099000	2.204911000
6	3.641426000	1.257742000	4.304266000
1	4.025868000	1.282831000	5.316903000
1	3.776525000	0.258207000	3.893368000
1	4.182299000	1.975325000	3.690228000
6	3.397393000	4.610223000	6.044933000
1	3.972557000	4.734747000	5.129374000
1	2.410285000	4.232346000	5.804739000
1	3.304861000	5.570877000	6.549710000

Appendix

1	6.556875000	2.451730000	8.645242000
1	6.011282000	4.594797000	6.974781000

⁵MC

26	1.898810000	1.699650000	7.216122000
7	3.032784000	-0.232064000	7.318343000
6	3.801741000	2.624429000	7.463095000
7	1.991634000	1.450627000	9.496730000
6	2.222286000	1.140802000	12.240219000
1	2.317093000	1.017233000	13.310733000
6	4.324063000	0.837557000	9.099706000
6	5.730812000	3.792920000	7.580493000
6	5.841587000	2.754834000	8.442369000
7	4.479737000	3.689757000	6.994259000
6	3.157175000	1.077951000	10.040322000
6	1.018177000	1.537010000	11.675744000
1	0.146154000	1.732024000	12.283702000
6	0.948413000	1.679398000	10.298638000
1	0.028880000	1.981401000	9.815923000
6	3.310952000	0.909462000	11.408574000
1	4.266890000	0.606103000	11.812445000
1	5.196870000	0.600221000	9.700268000
6	4.068411000	-0.330238000	8.162359000
6	4.888907000	-1.447801000	8.190761000
1	5.716139000	-1.495488000	8.885164000
6	4.631717000	-2.491623000	7.309895000
1	5.260123000	-3.372143000	7.309390000
6	3.562976000	-2.383968000	6.431532000
1	3.328108000	-3.171036000	5.729138000
6	2.787910000	-1.234967000	6.471211000
1	1.941740000	-1.103979000	5.809173000
7	4.652317000	2.053069000	8.347840000
7	0.542153000	3.471153000	7.441577000
7	-0.116521000	0.588665000	7.368112000
6	1.398615000	1.798026000	5.146636000
6	-0.919419000	2.326633000	5.849430000
6	-1.501432000	-1.184694000	8.169157000
1	-1.591439000	-2.078088000	8.770709000
6	-2.404454000	0.474018000	6.701194000
1	-3.220047000	0.897424000	6.131349000
6	-2.581375000	-0.674586000	7.462571000
1	-3.545700000	-1.163515000	7.497338000
6	-0.287076000	-0.519777000	8.093288000
1	0.579372000	-0.878799000	8.632382000
7	0.115048000	2.095144000	4.837182000
6	1.109744000	1.833501000	2.907749000
7	2.000468000	1.645701000	3.951960000
6	-0.089728000	2.116692000	3.468471000
1	-1.834064000	2.551793000	5.309855000
6	-0.588155000	3.521948000	6.725409000
6	-1.445867000	4.610481000	6.783468000

S27

1	-2.353295000	4.618132000	6.195802000
6	-1.114725000	5.682138000	7.603783000
1	-1.766693000	6.543159000	7.665672000
6	0.063587000	5.631968000	8.335278000
1	0.362000000	6.444999000	8.981783000
6	0.863227000	4.505215000	8.223163000
1	1.790048000	4.415957000	8.774712000
6	-1.154500000	1.074674000	6.675988000
1	-1.047054000	2.329257000	3.027252000
1	1.403641000	1.752870000	1.876385000
6	3.407530000	1.311183000	3.783785000
1	3.879817000	1.315612000	4.761658000
1	3.506554000	0.323162000	3.335935000
1	3.889018000	2.048528000	3.143602000
6	3.961847000	4.614289000	5.995533000
1	4.635119000	4.650141000	5.140400000
1	2.986057000	4.261239000	5.675026000
1	3.866781000	5.611582000	6.423011000
1	6.641413000	2.458465000	9.097129000
1	6.420593000	4.580514000	7.334675000

- 1 G. R. Fulmer, A. J. M. Miller, N. H. Sherden, H. E. Gottlieb, A. Nudelman, B. M. Stoltz, J. E. Bercaw and K. I. Goldberg, *Organometallics*, 2010, **29**, 2176.
- 2 M. Krejčík, M. Daněk and F. Hartl, *J. Electroanal. Chem.*, 1991, **317**, 179.
- 3 a) T. S. Ertel, H. Bertagnolli, S. Hückmann, U. Kolb and D. Peter, *Appl. Spectrosc.*, 1992, **46**, 690; b) M. Newville, *J. Synchrotron. Rad.*, 2001, **8**, 322; c) M. Newville, P. Liviņš, Y. Yacoby, J. J. Rehr and E. A. Stern, *Phys. Rev. B*, 1993, **47**, 14126; d) B. Ravel and M. Newville, *J. Synchrotron. Rad.*, 2005, **12**, 537.
- 4 N. Binsted and S. S. Hasnain, *J. Synchrotron. Rad.*, 1996, **3**, 185.
- 5 N. Binsted and F. Mosselmans, EXCURV98 Manual, Daresbury, UK.
- 6 M. Bauer and H. Bertagnolli, *J. Phys. Chem. B*, 2007, **111**, 13756.
- 7 D. C. Koningsberger, B. L. Mojat, G. E. van Dorssen and D. E. Ramaker, *Top. Catal.*, 2000, **10**, 143.
- 8 A. Pöpcke, A. Friedrich and S. Lochbrunner, *J. Phys.: Condens. Matter*, 2020, **32**, 153001.
- 9 F. Neese, *WIREs Comput. Mol. Sci.*, 2012, **2**, 73–78.
- 10 F. Neese, *WIREs Comput. Mol. Sci.*, 2018, **8**, e1327.
- 11 A. D. Becke, *J. Chem. Phys.*, 1993, **98**, 5648–5652.
- 12 C. Lee, W. Yang and R. G. Parr, *Phys. Rev. B*, 1988, **37**, 785–789.
- 13 B. Miehlisch, A. Savin, H. Stoll and H. Preuss, *Chem. Phys. Lett.*, 1989, **157**, 200–206.
- 14 D. A. Pantazis, X.-Y. Chen, C. R. Landis and F. Neese, *J. Chem. Theory Comput.*, 2008, **4**, 908–919.
- 15 F. Weigend and R. Ahlrichs, *Phys. Chem. Chem. Phys.*, 2005, **7**, 3297–3305.
- 16 S. Miertuš, E. Scrocco and J. Tomasi, *Chem. Phys.*, 1981, **55**, 117–129.
- 17 V. Barone and M. Cossi, *J. Phys. Chem. A*, 1998, **102**, 1995–2001.
- 18 F. Neese, F. Wennmohs, A. Hansen and U. Becker, *Chem. Phys.*, 2009, **356**, 98–109.
- 19 R. Izsák and F. Neese, *J. Chem. Phys.*, 2011, **135**, 144105.
- 20 S. Grimme, J. Antony, S. Ehrlich and H. Krieg, *J. Chem. Phys.*, 2010, **132**, 154104.
- 21 S. Grimme, S. Ehrlich and L. Goerigk, *J. Comput. Chem.*, 2011, **32**, 1456–1465.
- 22 S. Mai, F. Plasser, J. Dorn, M. Fumanal, C. Daniel and L. González, *Coord. Chem. Rev.*, 2018, **361**, 74–97.
- 23 F. Plasser, Theodore 2.0, <http://theodore-qc.sourceforge.net>.
- 24 F. Plasser, *J. Chem. Phys.*, 2020, **152**, 084108.
- 25 V. Tran, K. E. Allen, M. Garcia Chavez, C. Aaron, J. J. Dumais, J. T. York and E. C. Brown, *Polyhedron*, 2018, **147**, 131–141.

6.3 Supporting Information for Section 3.2 "A Tetracarbene Iron(II) Complex with a Long-lived Triplet Metal-to-Ligand Charge Transfer State due to a Triplet-Triplet Barrier"



Supporting Information

A Tetracarbene Iron(II) Complex with a Long-lived Triplet Metal-to-Ligand Charge Transfer State due to a Triplet-Triplet Barrier

*T. Reuter, D. Zorn, R. Naumann, J. Klett, C. Förster, K. Heinze**

Supporting Information

1. Methods	S2
2. DFT calculations	S5
3. Syntheses	S27
4. Spectroscopic and analytical data	S31
5. References	S55

Methods

All reactions and measurements were performed under argon atmosphere unless otherwise noted. Gloveboxes (UniLab/MBraun – Ar 4.8, O₂ < 0.1 ppm, H₂O < 0.1 ppm) were used to store and weigh oxygen and/or water sensitive compounds. Acetonitrile and CD₃CN were dried and distilled from calcium hydride and stored over molecular sieve (4 Å). THF was dried from potassium and distilled prior to use. Dry chloroform was received from Acros Organics and used as obtained. All other reagents were used as received from commercial suppliers (ABCR, Acros Organics, Alfa Aesar, Fischer Scientific, Fluka and Sigma-Aldrich). Deuterated solvents were purchased from euriso-top and Deutero GmbH.

The HPLC setup consists of a *Jasco* LC-NetII/ADC control unit, two *Jasco* PU-2087 Plus pumps, and a *Jasco* CO-4060 column oven. Absorption and CD detection is performed using a *Jasco* UV-2075 Plus and a *Jasco* CD-4095 detector, respectively. Fractions are collected using an *Advantec* CHF122SC fraction collector. Eluents are degassed by a *Gastorr* AG-42 degassing unit and mixed using a high-pressure mixing unit. Analytical runs were performed with a *ChiralPAK IC* (5 μm, 4.6×250 mm) column and semi-preparative runs with a *ChiralPAK IC* (5 μm, 10×250 mm) column.

NMR spectra were recorded on a *Bruker Avance DRX 400* as well as on a *Bruker Avance III HD 400* spectrometer at 400.31 MHz (¹H), 100.05 MHz (¹³C{¹H}), 377.63 MHz (¹⁹F), and 162.04 MHz (³¹P) at 25 °C. Chemical shifts (δ) are reported to the shift scale calibrated with the residual non-deuterated NMR solvent; CD₂Cl₂ (5.32 ppm for ¹H NMR) and CD₃CN (1.94 ppm for ¹H NMR and 1.32 and 118.26 ppm for ¹³C NMR) or H₃PO₄ (85%) (δ = 0.00 ppm) or CFC₃ (δ = 0.00 ppm) as external standards for ³¹P and ¹⁹F NMR, respectively.

Electrospray ionization mass spectra were recorded on an *Agilent 6545 QTOF-HRAM* mass spectrometer.

IR spectra were recorded on a *Bruker Alpha FTIR* spectrometer with an ATR unit containing a diamond crystal. The intensities are qualitatively indicated with weak (w), medium (m) and strong (s).

Raman spectra were measured on a *Nicolet 5700 FT-IR* spectrometer combined with a *NXR 9650 FT-Raman* Module equipped with a 1064 nm laser (laser power 20–1500 mW; resolution 2 cm⁻¹; number of scans 1024–4098), a Microstage microscope, and a *NXR Genie Ge-detector* using single crystals or crystalline powders in glass capillaries (under inert gas). The intensities are qualitatively indicated with weak (w), medium (m) and strong (s).

The **elemental analyses** were performed by the microanalytical laboratory of the Department of Chemistry of the Johannes Gutenberg University Mainz, Germany, on a *vario EL cube* from *Elementar* and by the Mikroanalytisches Labor Kolbe, c/o Fraunhofer Institut UMSICHT, Oberhausen, Germany for [H₂pdmi][PF₆]₂ and [Fe(pdmi)₂][PF₆]₂, respectively.

UV/Vis/NIR absorption spectra were recorded on a *Jasco V-770* or an *Agilent Cary 5000* spectrometer using 1.0 cm cells (*Hellma*, Suprasil).

Electrochemical experiments were carried out on a *BioLogic SP-200* voltammetric analyzer using a platinum working electrode, a platinum wire as counter electrode and a 0.01 M Ag/AgNO₃ in CH₃CN reference electrode. All potentials were referenced vs. the ferrocenium/ferrocene couple. The cyclic voltammetry experiments were carried out at a scan rate of 100 mV s⁻¹ using 0.1 M [ⁿBu₄N][PF₆] as supporting electrolyte and 0.001 M of the sample in CH₃CN.

Spectroelectrochemical measurements were carried out on a *BioLogic SP-50* voltammetric analyzer using a *Specac omni-cell* liquid transmission cell with CaF₂ windows equipped with a Pt-gauze working electrode and an Ag wire as pseudo-reference electrode, melt-sealed in a self-made polyethylene

spacer (approximate 0.5 mm path length) in CH₃CN containing 0.1 M [ⁿBu₄N][PF₆]. Absorption spectra were measured on a *Jasco V-770* spectrometer.

Variable temperature steady-state emission spectra were recorded with a *FLS1000* spectrometer from *Edinburgh Instruments* equipped with the cooled, red and NIR sensitive photomultiplier detectors *PMT-980* and *N-G09 PMT-1700*. A xenon arc lamp *Xe2* from *Edinburgh Instruments* or a cw-laser *RLTMDL-450-1W-3* from *Roithner Lasertechnik* (450 nm, *P* = 1089 mW) were employed for excitation. The measurements were carried out in a liquid nitrogen cooled cryostat *Optistat DN* from *Oxford Instruments*.

fs-Transient absorption experiments were conducted using a *Helios* pump-probe setup from *Ultrafast Systems* paired with a regeneratively amplified 1030 nm laser (*Pharos, Light Conversion, 1030 nm, < 190 fs, 2 mJ*). The effective laser repetition rate of 1 kHz was set via an internal pulse picker. A small portion of the 1030 nm fundamental was directed to the optical delay line and was subsequently used to generate broadband probe light by focusing the beam onto a sapphire for measurements in the Vis/NIR range (450 nm – 900 nm). In the UV/Vis spectral range (330 nm – 500 nm) the second harmonic was focused onto a second sapphire instead of the fundamental. The pump pulse was generated with an optical parametric amplifier (*Apollo Y, Ultrafast Systems*). The sample solutions were measured in a 1 mm quartz cuvette. Measurements at temperatures below 193 K were carried out in a self-made PEEK sample holder with two quartz windows and an optical pathlength of 2 mm. Low temperature and variable temperature measurements were conducted under nitrogen atmosphere in an *Optistat DN* cryostat from *Oxford Instruments*. To generate spectra that cover the whole spectral region from 350 nm to 900 nm, the UV/Vis and Vis/NIR part of the transient absorption spectra were recorded separately under identical conditions and were combined using the overlap of both datasets in the visible region (475 nm – 525 nm). For the *cis* isomer both datasets were combined as obtained from the measurement without an adjustment to match the absolute signal height as the scattered light of the pump pulse around 470 nm prevents accurate measurements in the overlapping region. Preprocessing of the data, including chirp and baseline correction, were performed using the *Surface Explorer 4.3.0* software from *Ultrafast Systems*. The open source *Python* based data analysis tool *KiMoPack 7.4.9* was employed for global analysis of the TA data.^[1]

Density Functional Theory (DFT) calculations were carried out using the *ORCA* program package^[2] (version 5.0.1). Tight convergence criteria were chosen for all calculations (keywords *tightscf* and *tightopt*). All calculations were performed using the B3LYP functional^[3-5] using Ahlrichs' polarized valence triple-zeta basis set (def2-TZVPP)^[6,7] employing the RIJCOSX approximation (keyword *RIJCOSX*).^[10,11] To account for solvent effects, a conductor-like screening model (keyword *CPCM*) modeling acetonitrile was used in all calculations.^[8,9] Relativistic effects were calculated at the zeroth order regular approximation (keyword *ZORA*) level^[6] using relativistically adjusted basis sets. Geometry optimizations were performed Atom-pairwise dispersion correction was performed with the Becke-Johnson damping scheme (keyword *D3BJ*).^[12,13] Explicit counter ions and/or solvent molecules were not taken into account. The charge transfer number analyses of the fifty time-dependent DFT (TDDFT)-calculated transitions (keyword *nroots 50*) were done using *TheoDORE 2.2*.^[14,15] For charge transfer number analyses the complex cation was divided into three fragments: a) the iron centre and the two tripodal ligands and b) the iron center, the pyridines and the carbenes.

X-Ray Crystal structure analyses of *trans*-[Fe(pdmi)₂][PF₆]₂ and *cis*-[Fe(pdmi)₂][PF₆]₂. Intensity data for crystal structure determination were collected with a *STOE IPDS-2T* diffractometer from STOE & CIE GmbH with an Oxford cooling using Mo-K α radiation ($\lambda = 0.71073$ Å). The diffraction frames were integrated using the *STOE X-Area*^[16] software package and were corrected for absorption with *MULABS*^[17] of the *PLATON* software package^[18] or with STOE LANA^[19,20] of the STOE X-Area software package.^[20] The structures were solved with *SHELXT*^[21] and refined by the full-matrix method based on F^2 using *SHELXL*^[22] of the *SHELX*^[23] software package and the *ShelXle*^[24] graphical interface. All non-hydrogen atoms were refined anisotropically, while the positions of all hydrogen atoms were generated with appropriate geometric constraints and allowed to ride on their respective parent atoms with fixed isotropic thermal parameters. Crystallographic data for the structures reported in this paper have been deposited with the Cambridge Crystallographic Data Centre as supplementary publication no. CCDC-2339759 and 2339760 for *trans*-[Fe(pdmi)₂][PF₆]₂ and *cis*-[Fe(pdmi)₂][PF₆]₂, respectively.

Crystallographic Data of *trans*-[Fe(pdmi)₂][PF₆]₂. C₂₈H₃₀F₁₂FeN₁₀P₂ (852.41); monoclinic; $I2/a$; $a = 16.744(3)$ Å, $b = 10.758(2)$ Å, $c = 18.668(4)$ Å, $\alpha = 90^\circ$, $\beta = 94.91(3)^\circ$, $\gamma = 90^\circ$; $V = 3350.3(12)$ Å³; $Z = 4$; density (calculated) 1.690 g cm⁻³, $T = 120(2)$ K, $\mu = 0.652$ mm⁻¹, $F(000) = 1728$; crystal size 0.250 x 0.197 x 0.150 mm³; $\theta = 3.069$ to 28.119 deg.; $-22 \leq h \leq 22$, $-12 \leq k \leq 14$, $-21 \leq l \leq 24$; rfln collected = 10442; rfln unique = 4042 [$R(\text{int}) = 0.0398$]; completeness to $\theta = 25.242$ deg. = 99.5 %; semi empirical absorption correction from equivalents; max. and min. transmission 1.06581 and 0.92442; data 4042; restraints 0, parameters 243; goodness-of-fit on $F^2 = 1.111$, final indices [$I > 2\sigma(I)$] $R_1 = 0.0518$, $wR_2 = 0.1272$; R indices (all data) $R_1 = 0.0659$, $wR_2 = 0.1371$; largest diff. peak and hole 0.943 and -0.549 e Å⁻³.

Crystallographic Data of *cis*-[Fe(pdmi)₂][PF₆]₂. C₂₈H₃₀F₁₂FeN₁₀P₂ (852.41)x3CH₃CN; triclinic; $P\bar{1}$; $a = 11.352(2)$ Å, $b = 13.735(2)$ Å, $c = 14.138(2)$ Å, $\alpha = 79.268(13)^\circ$, $\beta = 67.057(12)^\circ$, $\gamma = 70.131(13)^\circ$; $V = 1905.5(6)$ Å³; $Z = 2$; density (calculated) 1.593 g cm⁻³, $T = 120(2)$ K, $\mu = 0.581$ mm⁻¹, $F(000) = 930$; $\theta = 2.039$ to 21.554 deg.; $-10 \leq h \leq 5$, $-14 \leq k \leq 13$, $-13 \leq l \leq 13$; rfln collected = 3943; rfln unique = 2555 [$R(\text{int}) = 0.1653$]; completeness to $\theta = 21.554$ deg. = 57.9 %; semi empirical absorption correction from equivalents; max. and min. transmission 1.0000 and 0.0163; data 2555; restraints 1323, parameters 600; goodness-of-fit on $F^2 = 1.352$, final indices [$I > 2\sigma(I)$] $R_1 = 0.1585$, $wR_2 = 0.3506$; R indices (all data) $R_1 = 0.2619$, $wR_2 = 0.4157$; largest diff. peak and hole 1.255 and -0.974 e Å⁻³.

2. DFT calculations

Table S1. Bond lengths [Å] and angles [deg] of *trans*-[Fe(pdmi)₂]²⁺ from SC-XRD measurements and DFT calculations (for atom numbering see Figure S1).

	SC-XRD	DFT (¹ GS)	DFT (³ MC)	DFT (⁵ MC)
Fe-N1	1.999(2)	2.032	2.445	2.314
Fe-C1	1.965(3)	1.972	2.003	2.219
Fe-C2	1.966(3)	1.977	2.002	2.205
Fe-N2	1.999(2)	2.032	2.446	2.315
Fe-C3	1.965(3)	1.972	2.004	2.218
Fe-C4	1.966(3)	1.977	2.002	2.207
N1-Fe-C1	87.02(10)	87.10	83.47	81.75
N1-Fe-C2	87.38(10)	87.23	83.75	82.12
C1-Fe-C2	86.63(10)	86.81	84.49	82.86
N2-Fe-C3	87.02(10)	87.11	83.44	81.64
N2-Fe-C4	87.38(10)	87.23	83.80	82.24
C3-Fe-C4	86.63(10)	86.61	84.49	82.89
N1-Fe-N2	180.0	179.99	179.97	179.89
C1-Fe-C3	180.0	180.00	179.96	179.74
C2-Fe-C4	180.0	179.99	179.98	179.70

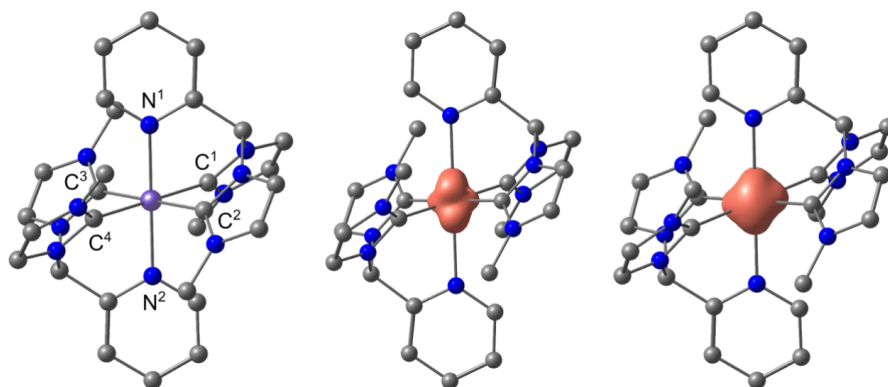
**Fig. S1.** Optimized geometries of *trans*-[Fe(pdmi)₂]²⁺ (¹GS, ³MC, ⁵MC) including atom numbering (¹GS) and spin densities (³MC, ⁵MC, 0.03 a.u.).

Table S2. Bond lengths [Å] and angles [deg] of *cis*-[Fe(pdmi)₂]²⁺ from DFT calculations (for atom numbering see Figure S2).

	DFT (¹ GS)	DFT (³ MC)	DFT (⁵ MC)
Fe-N1	2.058	2.175	2.415
Fe-C1	1.939	2.128	2.162
Fe-C2	1.977	1.975	2.202
Fe-N2	2.060	2.518	2.419
Fe-C3	1.980	1.976	2.185
Fe-C4	1.936	2.027	2.162
N1-Fe-C1	87.10	85.69	81.38
N1-Fe-C2	86.82	84.56	79.80
C1-Fe-C2	87.30	85.89	84.75
N2-Fe-C3	86.52	80.97	80.08
N2-Fe-C4	87.21	83.19	80.80
C3-Fe-C4	87.53	84.92	84.33
N1-Fe-N2	178.02	166.60	167.98
C1-Fe-C3	177.52	171.56	165.99
C2-Fe-C4	177.76	168.99	167.93

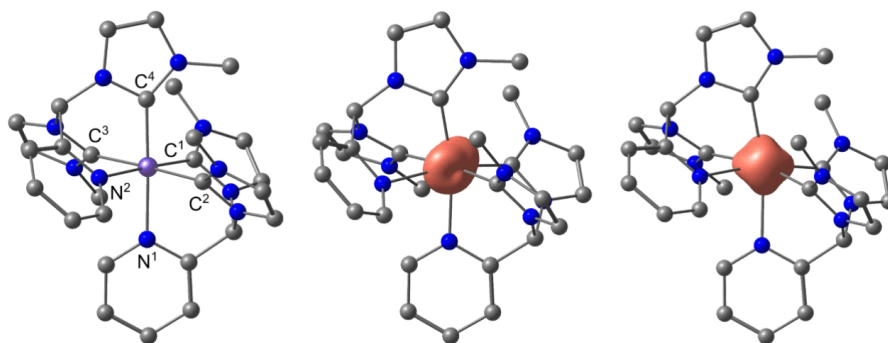


Fig. S2. Optimized geometries of *cis*-[Fe(pdmi)₂]²⁺ (¹GS, ³MC, ⁵MC) including atom numbering (¹GS) and spin densities (³MC, ⁵MC, 0.03 a.u.).

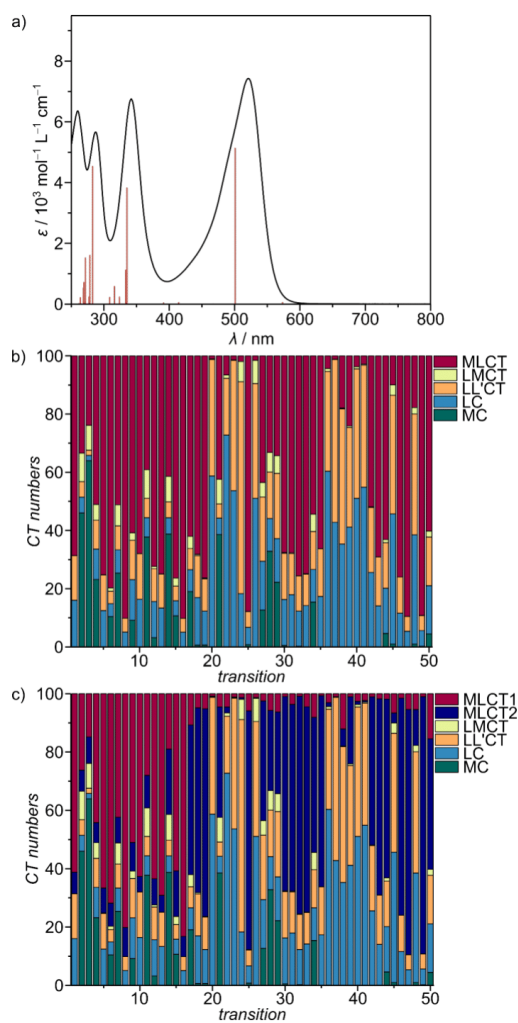


Fig. S3. a) Absorption spectrum of $\text{trans-}[\text{Fe}(\text{pdmi})_2]^{2+}$ in CH_3CN at 293 K. DFT calculated singlet transitions shown as sticks are bathochromically shifted by 3600 cm^{-1} . Charge transfer number analyses for $\text{trans-}[\text{Fe}(\text{pdmi})_2]^{2+}$ from TDDFT calculations b) with iron, ligand1, ligand2 as fragments and c) with iron, pyridines, carbenes as fragments.

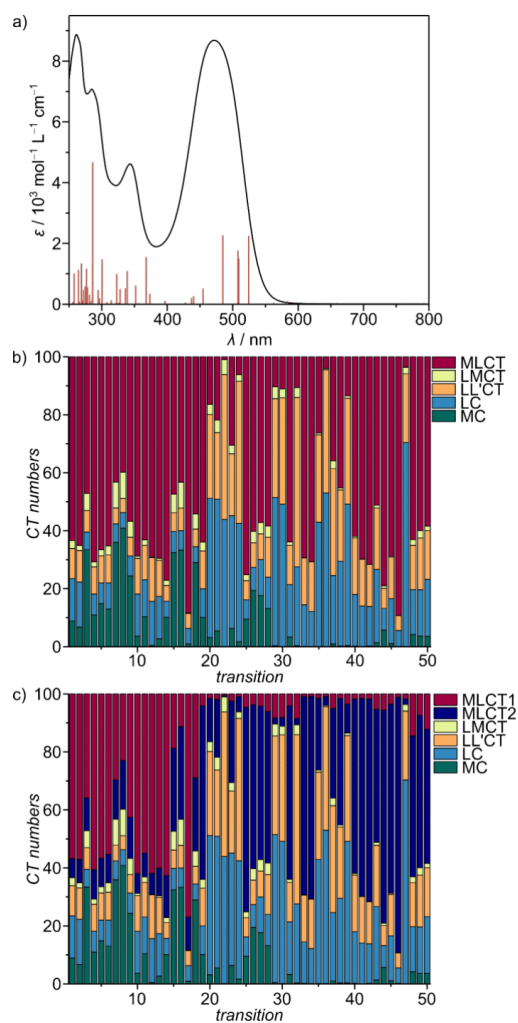
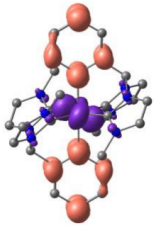
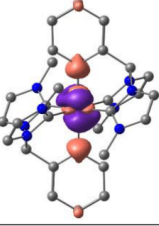
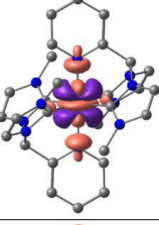
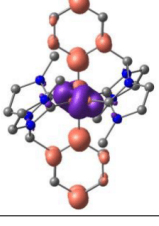
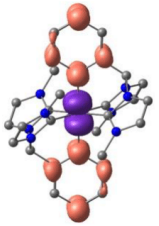
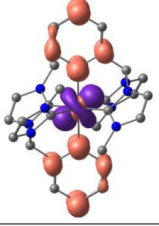
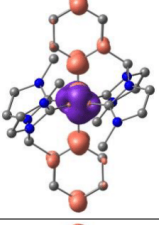
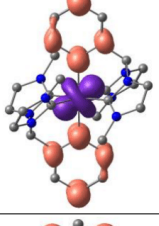
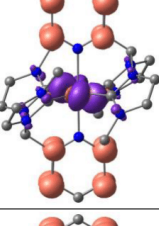
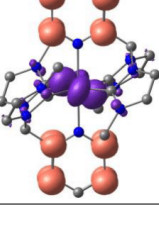


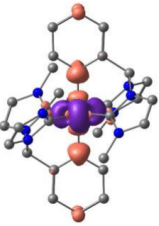
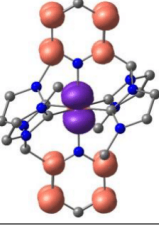
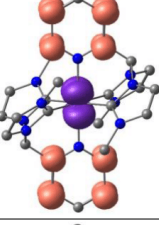
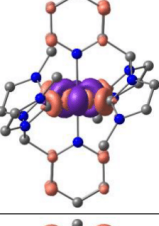
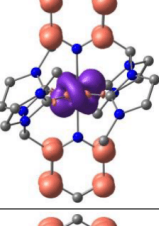
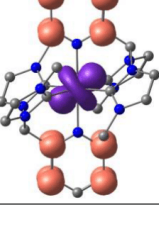
Fig. S4. a) Absorption spectrum of $cis-[Fe(pdmi)_2]^{2+}$ in CH_3CN at 293 K. DFT calculated singlet transitions shown as sticks are bathochromically shifted by 3600 cm^{-1} . Charge transfer number analyses for $cis-[Fe(pdmi)_2]^{2+}$ from TDDFT calculations a) with iron, ligand1, ligand2 as fragments and b) with iron, pyridines, carbenes as fragments.

Table S3. TDDFT calculated transitions of ***trans*-[Fe(pdmi)₂]²⁺** with charge transfer number analysis of the transitions; MC = metal centred, LC = ligand centred, LL'CT = ligand-to-ligand charge transfer, LMCT = ligand-to-metal charge transfer, MLCT1 = metal-to-ligand charge transfer from iron to the pyridines, MLCT2 = metal-to-ligand charge transfer from iron to the carbenes. Hydrogen atoms omitted.

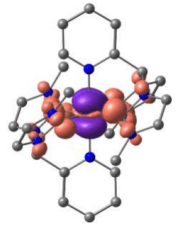
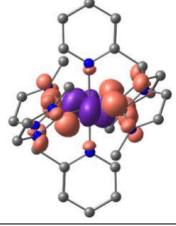
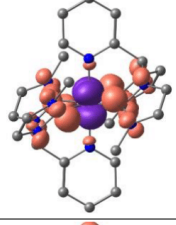
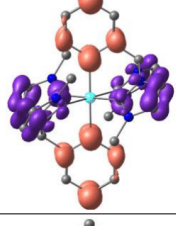
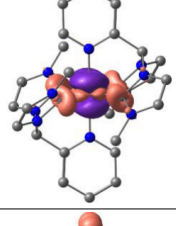
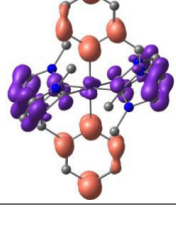
TDDFT difference density (isosurface value 0.003)	wavelength λ / nm	oscillator strength f	number	character
	475.2	1.52E-03	1	MLCT1 d _{Fe} -p _{py} (61.22 %) MLCT2 d _{Fe} -p _{NHC} (7.36 %) LMCT p _L -d _{Fe} (0.03 %) LL'CT p _{L1} -p _{L2} (15.36 %) LC p _L -p _L (15.97 %) MC d _{Fe} -d _{Fe} (0.07 %)
	470.4	8.00E-09	2	MLCT1 d _{Fe} -p _{py} (26.25 %) MLCT2 d _{Fe} -p _{NHC} (7.16 %) LMCT p _L -d _{Fe} (9.84 %) LL'CT p _{L1} -p _{L2} (5.31 %) LC p _L -p _L (5.45 %) MC d _{Fe} -d _{Fe} (46.00 %)
	462.2	1.10E-08	3	MLCT1 d _{Fe} -p _{py} (14.82 %) MLCT2 d _{Fe} -p _{NHC} (9.08 %) LMCT p _L -d _{Fe} (8.53 %) LL'CT p _{L1} -p _{L2} (1.78 %) LC p _L -p _L (1.82 %) MC d _{Fe} -d _{Fe} (63.97 %)
	455.3	1.50E-08	4	MLCT1 d _{Fe} -p _{py} (44.24 %) MLCT2 d _{Fe} -p _{NHC} (6.83 %) LMCT p _L -d _{Fe} (5.38 %) LL'CT p _{L1} -p _{L2} (9.97 %) LC p _L -p _L (10.42 %) MC d _{Fe} -d _{Fe} (23.17 %)

	424.3	1.62E-01	5	MLCT1 d _{Fe} -p _{py} (66.62 %) MLCT2 d _{Fe} -p _{NHC} (8.57 %) LMCT p _L -d _{Fe} (0.13 %) LL'CT p _{L1} -p _{L2} (12.24 %) LC p _L -p _L (12.37 %) MC d _{Fe} -d _{Fe} (0.07 %)
	402.1	2.00E-09	6	MLCT1 d _{Fe} -p _{py} (71.84 %) MLCT2 d _{Fe} -p _{NHC} (7.85 %) LMCT p _L -d _{Fe} (1.18 %) LL'CT p _{L1} -p _{L2} (4.25 %) LC p _L -p _L (4.44 %) MC d _{Fe} -d _{Fe} (10.44 %)
	400.6	4.10E-08	7	MLCT1 d _{Fe} -p _{py} (42.37 %) MLCT2 d _{Fe} -p _{NHC} (8.75 %) LMCT p _L -d _{Fe} (7.31 %) LL'CT p _{L1} -p _{L2} (8.21 %) LC p _L -p _L (7.98 %) MC d _{Fe} -d _{Fe} (25.38 %)
	399.6	9.48E-05	8	MLCT1 d _{Fe} -p _{py} (80.14 %) MLCT2 d _{Fe} -p _{NHC} (9.99 %) LMCT p _L -d _{Fe} (0.01 %) LL'CT p _{L1} -p _{L2} (4.77 %) LC p _L -p _L (5.00 %) MC d _{Fe} -d _{Fe} (0.09 %)
	373.2	1.00E-08	9	MLCT1 d _{Fe} -p _{py} (51.05 %) MLCT2 d _{Fe} -p _{NHC} (9.75 %) LMCT p _L -d _{Fe} (2.56 %) LL'CT p _{L1} -p _{L2} (13.50 %) LC p _L -p _L (14.01 %) MC d _{Fe} -d _{Fe} (9.12 %)
	360.7	1.50E-03	10	MLCT1 d _{Fe} -p _{py} (62.71 %) MLCT2 d _{Fe} -p _{NHC} (5.23 %) LMCT p _L -d _{Fe} (0.01 %) LL'CT p _{L1} -p _{L2} (15.69 %) LC p _L -p _L (16.36 %) MC d _{Fe} -d _{Fe} (0.01 %)

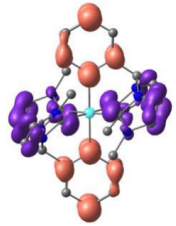
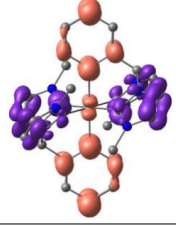
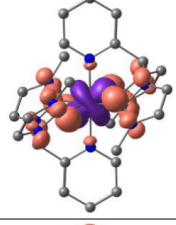
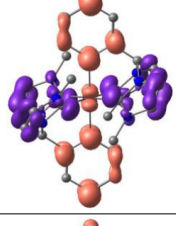
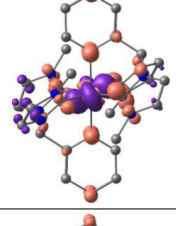
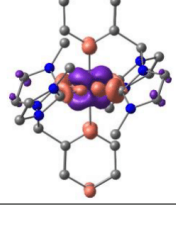
S10

	354.4	4.80E-08	11	MLCT1 $d_{Fe}-p_{py}$ (28.00 %) MLCT2 $d_{Fe}-p_{NHC}$ (11.15 %) LMCT p_L-d_{Fe} (9.79 %) LL'CT $p_{L1}-p_{L2}$ (6.66 %) LC p_L-p_L (6.65 %) MC $d_{Fe}-d_{Fe}$ (37.76 %)
	353.7	5.60E-08	12	MLCT1 $d_{Fe}-p_{py}$ (63.45 %) MLCT2 $d_{Fe}-p_{NHC}$ (8.91 %) LMCT p_L-d_{Fe} (0.78 %) LL'CT $p_{L1}-p_{L2}$ (11.25 %) LC p_L-p_L (12.41 %) MC $d_{Fe}-d_{Fe}$ (3.20 %)
	343.1	1.14E-03	13	MLCT1 $d_{Fe}-p_{py}$ (69.13 %) MLCT2 $d_{Fe}-p_{NHC}$ (5.76 %) LMCT p_L-d_{Fe} (0.05 %) LL'CT $p_{L1}-p_{L2}$ (11.72 %) LC p_L-p_L (13.34 %) MC $d_{Fe}-d_{Fe}$ (0.01 %)
	329.2	3.00E-09	14	MLCT1 $d_{Fe}-p_{py}$ (19.00 %) MLCT2 $d_{Fe}-p_{NHC}$ (22.38 %) LMCT p_L-d_{Fe} (8.83 %) LL'CT $p_{L1}-p_{L2}$ (5.41 %) LC p_L-p_L (5.65 %) MC $d_{Fe}-d_{Fe}$ (38.73 %)
	317.5	2.60E-08	15	MLCT1 $d_{Fe}-p_{py}$ (60.79 %) MLCT2 $d_{Fe}-p_{NHC}$ (15.58 %) LMCT p_L-d_{Fe} (2.79 %) LL'CT $p_{L1}-p_{L2}$ (5.00 %) LC p_L-p_L (5.18 %) MC $d_{Fe}-d_{Fe}$ (10.67 %)
	313.2	5.70E-05	16	MLCT1 $d_{Fe}-p_{py}$ (83.23 %) MLCT2 $d_{Fe}-p_{NHC}$ (6.94 %) LMCT p_L-d_{Fe} (0.00 %) LL'CT $p_{L1}-p_{L2}$ (4.80 %) LC p_L-p_L (5.02 %) MC $d_{Fe}-d_{Fe}$ (0.01 %)

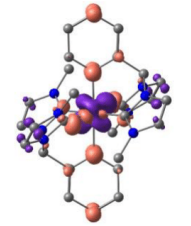
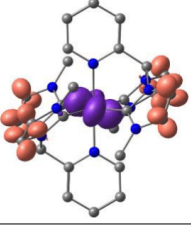
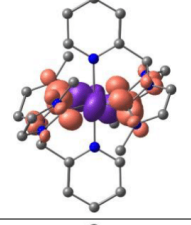
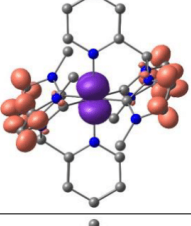
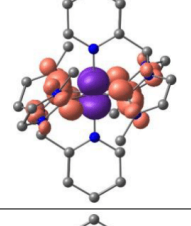
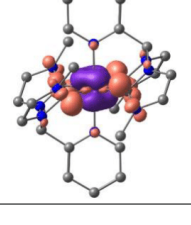
S11

	301.7	2.55E-06	17	MLCT1 $d_{Fe}-p_{py}$ (10.70 %) MLCT2 $d_{Fe}-p_{NHC}$ (51.33 %) LMCT p_L-d_{Fe} (4.13 %) LL'CT $p_{L1}-p_{L2}$ (7.29 %) LC p_L-p_L (7.50 %) MC $d_{Fe}-d_{Fe}$ (19.04 %)
	299.1	1.21E-01	18	MLCT1 $d_{Fe}-p_{py}$ (4.84 %) MLCT2 $d_{Fe}-p_{NHC}$ (63.36 %) LMCT p_L-d_{Fe} (0.44 %) LL'CT $p_{L1}-p_{L2}$ (14.41 %) LC p_L-p_L (16.35 %) MC $d_{Fe}-d_{Fe}$ (0.61 %)
	297.7	3.52E-02	19	MLCT1 $d_{Fe}-p_{py}$ (5.19 %) MLCT2 $d_{Fe}-p_{NHC}$ (71.15 %) LMCT p_L-d_{Fe} (0.23 %) LL'CT $p_{L1}-p_{L2}$ (11.16 %) LC p_L-p_L (11.66 %) MC $d_{Fe}-d_{Fe}$ (0.62 %)
	295.8	3.50E-07	20	MLCT1 $d_{Fe}-p_{py}$ (0.86 %) MLCT2 $d_{Fe}-p_{NHC}$ (0.20 %) LMCT p_L-d_{Fe} (0.19 %) LL'CT $p_{L1}-p_{L2}$ (40.06 %) LC p_L-p_L (58.64 %) MC $d_{Fe}-d_{Fe}$ (0.06 %)
	292.4	3.88E-07	21	MLCT1 $d_{Fe}-p_{py}$ (4.50 %) MLCT2 $d_{Fe}-p_{NHC}$ (37.88 %) LMCT p_L-d_{Fe} (8.47 %) LL'CT $p_{L1}-p_{L2}$ (4.92 %) LC p_L-p_L (5.66 %) MC $d_{Fe}-d_{Fe}$ (38.57 %)
	290	7.27E-03	22	MLCT1 $d_{Fe}-p_{py}$ (4.51 %) MLCT2 $d_{Fe}-p_{NHC}$ (2.04 %) LMCT p_L-d_{Fe} (1.16 %) LL'CT $p_{L1}-p_{L2}$ (19.56 %) LC p_L-p_L (72.70 %) MC $d_{Fe}-d_{Fe}$ (0.03 %)

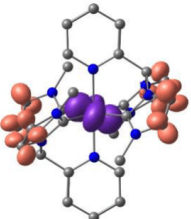
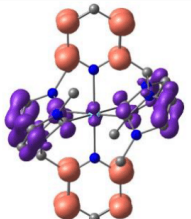
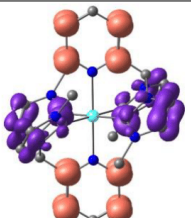
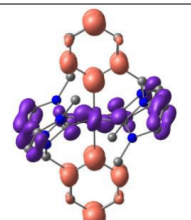
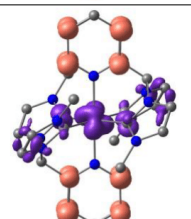
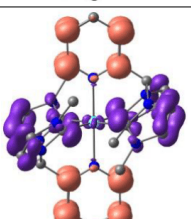
S12

	286.7	1.40E-08	23	MLCT1 $d_{Fe}-p_{py}$ (1.14 %) MLCT2 $d_{Fe}-p_{NHC}$ (0.27 %) LMCT p_L-d_{Fe} (0.12 %) LL'CT $p_{L1}-p_{L2}$ (44.81 %) LC p_L-p_L (53.55 %) MC $d_{Fe}-d_{Fe}$ (0.11 %)
	283.9	1.81E-02	24	MLCT1 $d_{Fe}-p_{py}$ (1.35 %) MLCT2 $d_{Fe}-p_{NHC}$ (0.58 %) LMCT p_L-d_{Fe} (6.96 %) LL'CT $p_{L1}-p_{L2}$ (72.83 %) LC p_L-p_L (18.18 %) MC $d_{Fe}-d_{Fe}$ (0.11 %)
	277.9	6.90E-03	25	MLCT1 $d_{Fe}-p_{py}$ (5.87 %) MLCT2 $d_{Fe}-p_{NHC}$ (81.88 %) LMCT p_L-d_{Fe} (0.11 %) LL'CT $p_{L1}-p_{L2}$ (5.43 %) LC p_L-p_L (5.97 %) MC $d_{Fe}-d_{Fe}$ (0.73 %)
	276	4.92E-05	26	MLCT1 $d_{Fe}-p_{py}$ (1.32 %) MLCT2 $d_{Fe}-p_{NHC}$ (0.24 %) LMCT p_L-d_{Fe} (7.95 %) LL'CT $p_{L1}-p_{L2}$ (39.42 %) LC p_L-p_L (50.96 %) MC $d_{Fe}-d_{Fe}$ (0.12 %)
	274.6	6.52E-05	27	MLCT1 $d_{Fe}-p_{py}$ (2.48 %) MLCT2 $d_{Fe}-p_{NHC}$ (41.05 %) LMCT p_L-d_{Fe} (4.93 %) LL'CT $p_{L1}-p_{L2}$ (22.13 %) LC p_L-p_L (16.74 %) MC $d_{Fe}-d_{Fe}$ (12.67 %)
	268.7	2.12E-07	28	MLCT1 $d_{Fe}-p_{py}$ (5.77 %) MLCT2 $d_{Fe}-p_{NHC}$ (27.42 %) LMCT p_L-d_{Fe} (6.71 %) LL'CT $p_{L1}-p_{L2}$ (15.99 %) LC p_L-p_L (11.27 %) MC $d_{Fe}-d_{Fe}$ (32.84 %)

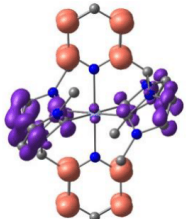
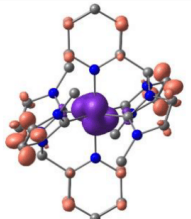
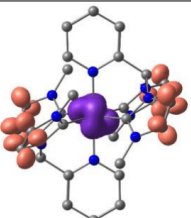
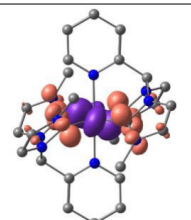
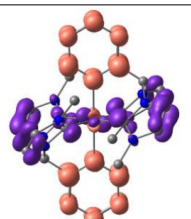
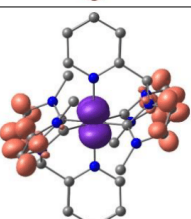
S13

	267.7	2.32E-07	29	MLCT1 $d_{Fe}-p_{py}$ (6.28 %) MLCT2 $d_{Fe}-p_{NHC}$ (27.99 %) LMCT p_L-d_{Fe} (6.16 %) LL'CT $p_{L1}-p_{L2}$ (22.35 %) LC p_L-p_L (15.02 %) MC $d_{Fe}-d_{Fe}$ (22.21 %)
	258.6	3.34E-06	30	MLCT1 $d_{Fe}-p_{py}$ (0.95 %) MLCT2 $d_{Fe}-p_{NHC}$ (66.65 %) LMCT p_L-d_{Fe} (0.21 %) LL'CT $p_{L1}-p_{L2}$ (15.89 %) LC p_L-p_L (15.76 %) MC $d_{Fe}-d_{Fe}$ (0.53 %)
	256.7	1.43E-01	31	MLCT1 $d_{Fe}-p_{py}$ (3.68 %) MLCT2 $d_{Fe}-p_{NHC}$ (63.95 %) LMCT p_L-d_{Fe} (0.29 %) LL'CT $p_{L1}-p_{L2}$ (14.12 %) LC p_L-p_L (17.87 %) MC $d_{Fe}-d_{Fe}$ (0.08 %)
	253.7	6.80E-08	32	MLCT1 $d_{Fe}-p_{py}$ (0.91 %) MLCT2 $d_{Fe}-p_{NHC}$ (74.62 %) LMCT p_L-d_{Fe} (0.09 %) LL'CT $p_{L1}-p_{L2}$ (12.12 %) LC p_L-p_L (12.00 %) MC $d_{Fe}-d_{Fe}$ (0.27 %)
	253.3	5.05E-02	33	MLCT1 $d_{Fe}-p_{py}$ (4.48 %) MLCT2 $d_{Fe}-p_{NHC}$ (70.37 %) LMCT p_L-d_{Fe} (0.17 %) LL'CT $p_{L1}-p_{L2}$ (10.82 %) LC p_L-p_L (14.08 %) MC $d_{Fe}-d_{Fe}$ (0.08 %)
	252.2	7.56E-06	34	MLCT1 $d_{Fe}-p_{py}$ (8.13 %) MLCT2 $d_{Fe}-p_{NHC}$ (46.25 %) LMCT p_L-d_{Fe} (5.97 %) LL'CT $p_{L1}-p_{L2}$ (13.07 %) LC p_L-p_L (11.19 %) MC $d_{Fe}-d_{Fe}$ (15.40 %)

S14

	252.2	7.35E-03	35	MLCT1 d _{Fe} -p _{py} (0.68 %) MLCT2 d _{Fe} -p _{NHC} (65.52 %) LMCT p _L -d _{Fe} (0.04 %) LL'CT p _{L1} -p _{L2} (16.41 %) LC p _L -p _L (17.34 %) MC d _{Fe} -d _{Fe} (0.00 %)
	250.7	4.97E-05	36	MLCT1 d _{Fe} -p _{py} (3.03 %) MLCT2 d _{Fe} -p _{NHC} (1.35 %) LMCT p _L -d _{Fe} (0.94 %) LL'CT p _{L1} -p _{L2} (34.33 %) LC p _L -p _L (60.25 %) MC d _{Fe} -d _{Fe} (0.11 %)
	249	2.67E-06	37	MLCT1 d _{Fe} -p _{py} (1.01 %) MLCT2 d _{Fe} -p _{NHC} (0.15 %) LMCT p _L -d _{Fe} (0.10 %) LL'CT p _{L1} -p _{L2} (55.93 %) LC p _L -p _L (42.78 %) MC d _{Fe} -d _{Fe} (0.04 %)
	247.8	5.84E-04	38	MLCT1 d _{Fe} -p _{py} (12.06 %) MLCT2 d _{Fe} -p _{NHC} (5.91 %) LMCT p _L -d _{Fe} (0.23 %) LL'CT p _{L1} -p _{L2} (46.47 %) LC p _L -p _L (35.31 %) MC d _{Fe} -d _{Fe} (0.02 %)
	247.5	4.80E-02	39	MLCT1 d _{Fe} -p _{py} (1.05 %) MLCT2 d _{Fe} -p _{NHC} (23.02 %) LMCT p _L -d _{Fe} (0.51 %) LL'CT p _{L1} -p _{L2} (34.24 %) LC p _L -p _L (41.18 %) MC d _{Fe} -d _{Fe} (0.01 %)
	246.9	2.22E-03	40	MLCT1 d _{Fe} -p _{py} (2.63 %) MLCT2 d _{Fe} -p _{NHC} (1.08 %) LMCT p _L -d _{Fe} (0.78 %) LL'CT p _{L1} -p _{L2} (44.47 %) LC p _L -p _L (51.03 %) MC d _{Fe} -d _{Fe} (0.02 %)

S15

	245.8	5.86E-04	41	MLCT1 $d_{Fe}-p_{py}$ (2.32 %) MLCT2 $d_{Fe}-p_{NHC}$ (0.51 %) LMCT p_L-d_{Fe} (0.40 %) LL'CT $p_{L1}-p_{L2}$ (41.86 %) LC p_L-p_L (54.91 %) MC $d_{Fe}-d_{Fe}$ (0.00 %)
	245.7	2.25E-02	42	MLCT1 $d_{Fe}-p_{py}$ (1.08 %) MLCT2 $d_{Fe}-p_{NHC}$ (50.75 %) LMCT p_L-d_{Fe} (0.21 %) LL'CT $p_{L1}-p_{L2}$ (22.41 %) LC p_L-p_L (25.56 %) MC $d_{Fe}-d_{Fe}$ (0.00 %)
	245	1.65E-02	43	MLCT1 $d_{Fe}-p_{py}$ (1.75 %) MLCT2 $d_{Fe}-p_{NHC}$ (67.27 %) LMCT p_L-d_{Fe} (0.06 %) LL'CT $p_{L1}-p_{L2}$ (16.87 %) LC p_L-p_L (14.05 %) MC $d_{Fe}-d_{Fe}$ (0.00 %)
	242.6	1.22E-05	44	MLCT1 $d_{Fe}-p_{py}$ (1.83 %) MLCT2 $d_{Fe}-p_{NHC}$ (61.27 %) LMCT p_L-d_{Fe} (1.13 %) LL'CT $p_{L1}-p_{L2}$ (15.60 %) LC p_L-p_L (15.55 %) MC $d_{Fe}-d_{Fe}$ (4.62 %)
	242.4	2.80E-08	45	MLCT1 $d_{Fe}-p_{py}$ (6.58 %) MLCT2 $d_{Fe}-p_{NHC}$ (3.41 %) LMCT p_L-d_{Fe} (3.57 %) LL'CT $p_{L1}-p_{L2}$ (40.77 %) LC p_L-p_L (44.69 %) MC $d_{Fe}-d_{Fe}$ (0.98 %)
	241.1	6.50E-03	46	MLCT1 $d_{Fe}-p_{py}$ (1.52 %) MLCT2 $d_{Fe}-p_{NHC}$ (74.43 %) LMCT p_L-d_{Fe} (0.02 %) LL'CT $p_{L1}-p_{L2}$ (12.44 %) LC p_L-p_L (11.59 %) MC $d_{Fe}-d_{Fe}$ (0.00 %)

S16

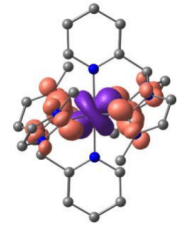
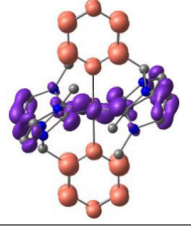
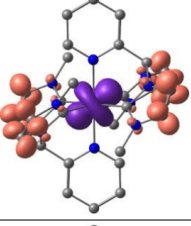
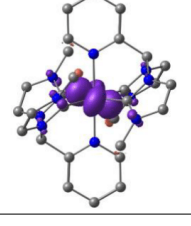
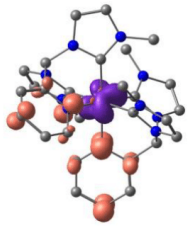
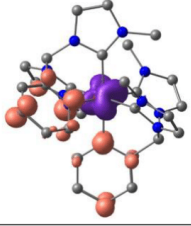
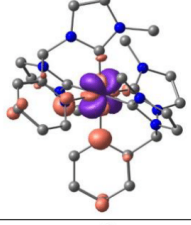
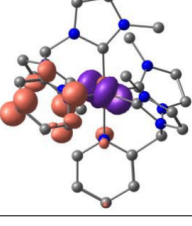
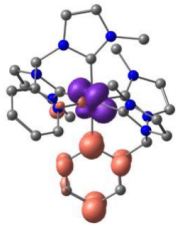
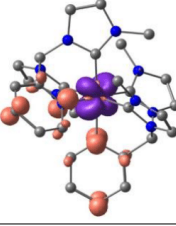
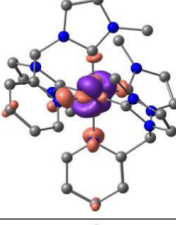
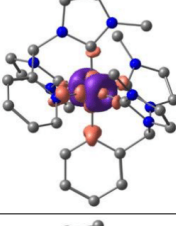
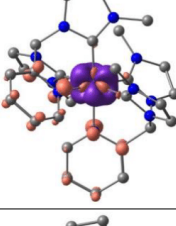
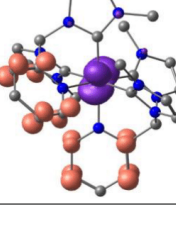
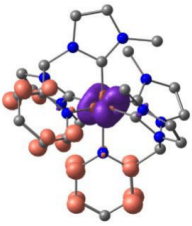
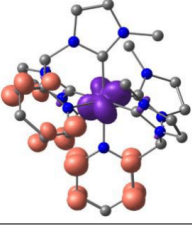
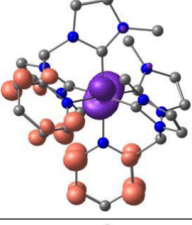
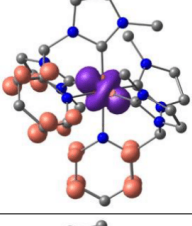
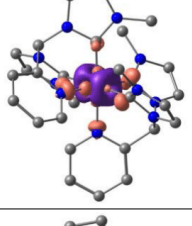
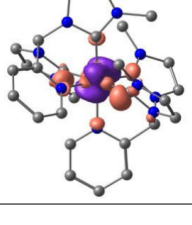
	239.3	5.04E-04	47	MLCT1 $d_{Fe}-p_{py}$ (5.38 %) MLCT2 $d_{Fe}-p_{NHC}$ (84.14 %) LMCT p_L-d_{Fe} (0.02 %) LL'CT $p_{L1}-p_{L2}$ (5.08 %) LC p_L-p_L (5.31 %) MC $d_{Fe}-d_{Fe}$ (0.07 %)
	238.5	1.50E-08	48	MLCT1 $d_{Fe}-p_{py}$ (5.42 %) MLCT2 $d_{Fe}-p_{NHC}$ (12.32 %) LMCT p_L-d_{Fe} (2.19 %) LL'CT $p_{L1}-p_{L2}$ (41.56 %) LC p_L-p_L (37.53 %) MC $d_{Fe}-d_{Fe}$ (0.98 %)
	236	1.00E-09	49	MLCT1 $d_{Fe}-p_{py}$ (1.03 %) MLCT2 $d_{Fe}-p_{NHC}$ (88.17 %) LMCT p_L-d_{Fe} (0.04 %) LL'CT $p_{L1}-p_{L2}$ (5.16 %) LC p_L-p_L (5.37 %) MC $d_{Fe}-d_{Fe}$ (0.22 %)
	235	5.20E-08	50	MLCT1 $d_{Fe}-p_{py}$ (15.43 %) MLCT2 $d_{Fe}-p_{NHC}$ (44.79 %) LMCT p_L-d_{Fe} (2.07 %) LL'CT $p_{L1}-p_{L2}$ (16.65 %) LC p_L-p_L (16.62 %) MC $d_{Fe}-d_{Fe}$ (4.44 %)

Table S4. TDDFT calculated transitions of *cis*-[Fe(pdmi)₂]²⁺ with charge transfer number analysis of the transitions; MC = metal centred, LC = ligand centred, LL'CT = ligand-to-ligand charge transfer, LMCT = ligand-to-metal charge transfer, MLCT1 = metal-to-ligand charge transfer from iron to the pyridines, MLCT2 = metal-to-ligand charge transfer from iron to the carbenes. Hydrogen atoms omitted.

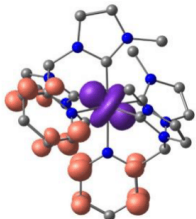
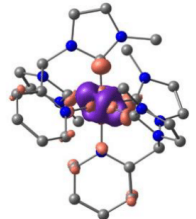
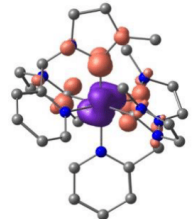
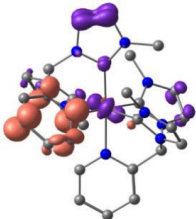
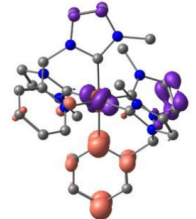
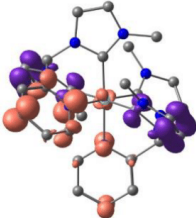
TDDFT difference density (isosurface value 0.005)	Wavelength λ / nm	oscillator strength f	number	character
	482.6	1.85E-03	1	MLCT1 d _{Fe} -p _{py} (56.84 %) MLCT2 d _{Fe} -p _{NHC} (6.53 %) LMCT p _L -d _{Fe} (2.75 %) LL'CT p _{L1} -p _{L2} (10.42 %) LC p _L -p _L (14.59 %) MC d _{Fe} -d _{Fe} (8.88 %)
	467.8	5.84E-04	2	MLCT1 d _{Fe} -p _{py} (57.03 %) MLCT2 d _{Fe} -p _{NHC} (8.07 %) LMCT p _L -d _{Fe} (1.76 %) LL'CT p _{L1} -p _{L2} (10.83 %) LC p _L -p _L (15.55 %) MC d _{Fe} -d _{Fe} (6.77 %)
	441.1	4.70E-02	3	MLCT1 d _{Fe} -p _{py} (35.88 %) MLCT2 d _{Fe} -p _{NHC} (11.25 %) LMCT p _L -d _{Fe} (5.87 %) LL'CT p _{L1} -p _{L2} (7.46 %) LC p _L -p _L (6.12 %) MC d _{Fe} -d _{Fe} (33.41 %)
	430.4	3.13E-02	4	MLCT1 d _{Fe} -p _{py} (60.67 %) MLCT2 d _{Fe} -p _{NHC} (10.02 %) LMCT p _L -d _{Fe} (1.81 %) LL'CT p _{L1} -p _{L2} (9.34 %) LC p _L -p _L (7.18 %) MC d _{Fe} -d _{Fe} (10.98 %)

	429.4	3.70E-02	5	MLCT1 $d_{Fe}-p_{py}$ (56.65 %) MLCT2 $d_{Fe}-p_{NHC}$ (9.88 %) LMCT p_L-d_{Fe} (2.14 %) LL'CT $p_{L1}-p_{L2}$ (9.35 %) LC p_L-p_L (7.13 %) MC $d_{Fe}-d_{Fe}$ (14.86 %)
	412.8	4.73E-02	6	MLCT1 $d_{Fe}-p_{py}$ (55.29 %) MLCT2 $d_{Fe}-p_{NHC}$ (9.91 %) LMCT p_L-d_{Fe} (3.19 %) LL'CT $p_{L1}-p_{L2}$ (9.63 %) LC p_L-p_L (8.99 %) MC $d_{Fe}-d_{Fe}$ (13.00 %)
	390.8	1.05E-02	7	MLCT1 $d_{Fe}-p_{py}$ (29.59 %) MLCT2 $d_{Fe}-p_{NHC}$ (13.62 %) LMCT p_L-d_{Fe} (8.91 %) LL'CT $p_{L1}-p_{L2}$ (5.49 %) LC p_L-p_L (6.45 %) MC $d_{Fe}-d_{Fe}$ (35.95 %)
	380.1	5.28E-03	8	MLCT1 $d_{Fe}-p_{py}$ (22.97 %) MLCT2 $d_{Fe}-p_{NHC}$ (16.83 %) LMCT p_L-d_{Fe} (9.08 %) LL'CT $p_{L1}-p_{L2}$ (4.86 %) LC p_L-p_L (5.38 %) MC $d_{Fe}-d_{Fe}$ (40.88 %)
	377.7	3.98E-03	9	MLCT1 $d_{Fe}-p_{py}$ (42.49 %) MLCT2 $d_{Fe}-p_{NHC}$ (14.24 %) LMCT p_L-d_{Fe} (5.51 %) LL'CT $p_{L1}-p_{L2}$ (6.46 %) LC p_L-p_L (6.91 %) MC $d_{Fe}-d_{Fe}$ (24.39 %)
	370.7	6.09E-04	10	MLCT1 $d_{Fe}-p_{py}$ (61.93 %) MLCT2 $d_{Fe}-p_{NHC}$ (6.82 %) LMCT p_L-d_{Fe} (0.76 %) LL'CT $p_{L1}-p_{L2}$ (12.34 %) LC p_L-p_L (14.51 %) MC $d_{Fe}-d_{Fe}$ (3.64 %)

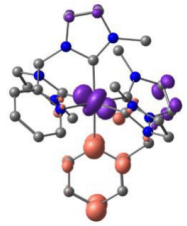
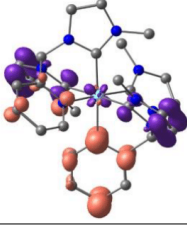
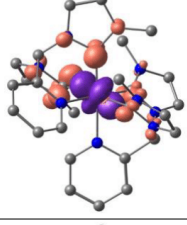
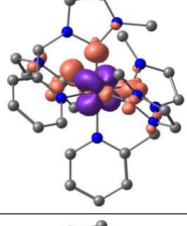
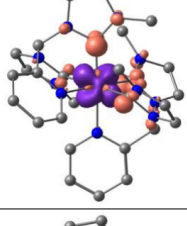
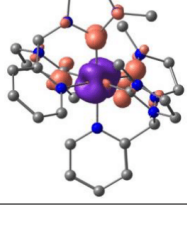
S19

	370.2	4.62E-04	11	MLCT1 $d_{Fe}-p_{py}$ (54.93 %) MLCT2 $d_{Fe}-p_{NHC}$ (8.19 %) LMCT p_L-d_{Fe} (1.92 %) LL'CT $p_{L1}-p_{L2}$ (11.90 %) LC p_L-p_L (12.73 %) MC $d_{Fe}-d_{Fe}$ (10.34 %)
	353.5	4.80E-05	12	MLCT1 $d_{Fe}-p_{py}$ (61.88 %) MLCT2 $d_{Fe}-p_{NHC}$ (7.22 %) LMCT p_L-d_{Fe} (0.12 %) LL'CT $p_{L1}-p_{L2}$ (15.18 %) LC p_L-p_L (15.15 %) MC $d_{Fe}-d_{Fe}$ (0.45 %)
	347	1.97E-03	13	MLCT1 $d_{Fe}-p_{py}$ (60.08 %) MLCT2 $d_{Fe}-p_{NHC}$ (9.49 %) LMCT p_L-d_{Fe} (0.62 %) LL'CT $p_{L1}-p_{L2}$ (12.47 %) LC p_L-p_L (14.62 %) MC $d_{Fe}-d_{Fe}$ (2.72 %)
	329.3	6.89E-03	14	MLCT1 $d_{Fe}-p_{py}$ (62.61 %) MLCT2 $d_{Fe}-p_{NHC}$ (14.50 %) LMCT p_L-d_{Fe} (1.75 %) LL'CT $p_{L1}-p_{L2}$ (5.46 %) LC p_L-p_L (5.57 %) MC $d_{Fe}-d_{Fe}$ (10.11 %)
	324.7	3.22E-02	15	MLCT1 $d_{Fe}-p_{py}$ (18.72 %) MLCT2 $d_{Fe}-p_{NHC}$ (28.66 %) LMCT p_L-d_{Fe} (6.47 %) LL'CT $p_{L1}-p_{L2}$ (6.39 %) LC p_L-p_L (7.30 %) MC $d_{Fe}-d_{Fe}$ (32.47 %)
	315.6	4.15E-04	16	MLCT1 $d_{Fe}-p_{py}$ (11.22 %) MLCT2 $d_{Fe}-p_{NHC}$ (32.01 %) LMCT p_L-d_{Fe} (8.96 %) LL'CT $p_{L1}-p_{L2}$ (7.82 %) LC p_L-p_L (6.66 %) MC $d_{Fe}-d_{Fe}$ (33.33 %)

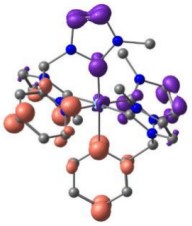
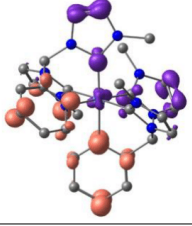
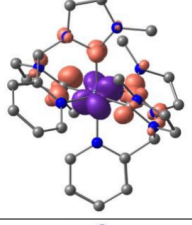
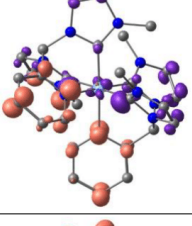
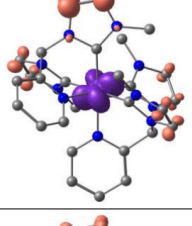
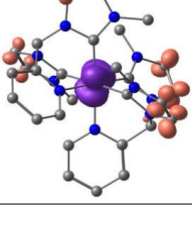
S20

	312.3	1.31E-04	17	MLCT1 $d_{Fe}-p_{py}$ (76.94 %) MLCT2 $d_{Fe}-p_{NHC}$ (11.41 %) LMCT p_L-d_{Fe} (0.18 %) LL'CT $p_{L1}-p_{L2}$ (5.17 %) LC p_L-p_L (5.36 %) MC $d_{Fe}-d_{Fe}$ (0.94 %)
	312.2	1.25E-02	18	MLCT1 $d_{Fe}-p_{py}$ (28.92 %) MLCT2 $d_{Fe}-p_{NHC}$ (25.26 %) LMCT p_L-d_{Fe} (5.28 %) LL'CT $p_{L1}-p_{L2}$ (6.05 %) LC p_L-p_L (5.50 %) MC $d_{Fe}-d_{Fe}$ (28.99 %)
	302.1	2.27E-02	19	MLCT1 $d_{Fe}-p_{py}$ (4.13 %) MLCT2 $d_{Fe}-p_{NHC}$ (59.80 %) LMCT p_L-d_{Fe} (3.03 %) LL'CT $p_{L1}-p_{L2}$ (13.04 %) LC p_L-p_L (9.89 %) MC $d_{Fe}-d_{Fe}$ (10.11 %)
	299.8	1.07E-02	20	MLCT1 $d_{Fe}-p_{py}$ (1.53 %) MLCT2 $d_{Fe}-p_{NHC}$ (14.87 %) LMCT p_L-d_{Fe} (3.47 %) LL'CT $p_{L1}-p_{L2}$ (28.98 %) LC p_L-p_L (48.02 %) MC $d_{Fe}-d_{Fe}$ (3.14 %)
	293.3	1.00E-02	21	MLCT1 $d_{Fe}-p_{py}$ (1.87 %) MLCT2 $d_{Fe}-p_{NHC}$ (19.97 %) LMCT p_L-d_{Fe} (4.36 %) LL'CT $p_{L1}-p_{L2}$ (22.93 %) LC p_L-p_L (45.41 %) MC $d_{Fe}-d_{Fe}$ (5.47 %)
	291.6	7.50E-04	22	MLCT1 $d_{Fe}-p_{py}$ (0.50 %) MLCT2 $d_{Fe}-p_{NHC}$ (0.49 %) LMCT p_L-d_{Fe} (5.18 %) LL'CT $p_{L1}-p_{L2}$ (49.93 %) LC p_L-p_L (43.80 %) MC $d_{Fe}-d_{Fe}$ (0.11 %)

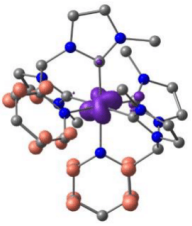
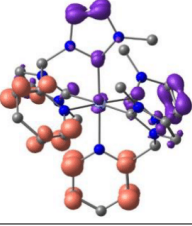
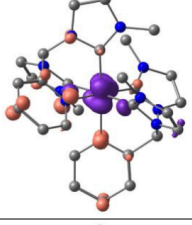
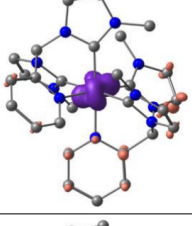
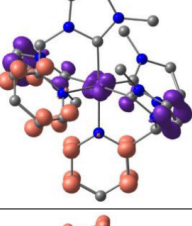
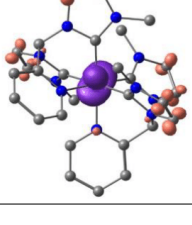
S21

	289.1	2.06E-02	23	MLCT1 $d_{Fe}-p_{py}$ (2.45 %) MLCT2 $d_{Fe}-p_{NHC}$ (28.06 %) LMCT p_L-d_{Fe} (2.96 %) LL'CT $p_{L1}-p_{L2}$ (21.37 %) LC p_L-p_L (38.80 %) MC $d_{Fe}-d_{Fe}$ (6.37 %)
	288.5	9.69E-04	24	MLCT1 $d_{Fe}-p_{py}$ (0.95 %) MLCT2 $d_{Fe}-p_{NHC}$ (5.21 %) LMCT p_L-d_{Fe} (2.30 %) LL'CT $p_{L1}-p_{L2}$ (49.05 %) LC p_L-p_L (40.80 %) MC $d_{Fe}-d_{Fe}$ (1.68 %)
	282.4	2.34E-03	25	MLCT1 $d_{Fe}-p_{py}$ (4.62 %) MLCT2 $d_{Fe}-p_{NHC}$ (70.52 %) LMCT p_L-d_{Fe} (2.06 %) LL'CT $p_{L1}-p_{L2}$ (6.61 %) LC p_L-p_L (6.68 %) MC $d_{Fe}-d_{Fe}$ (9.51 %)
	277	1.01E-03	26	MLCT1 $d_{Fe}-p_{py}$ (3.73 %) MLCT2 $d_{Fe}-p_{NHC}$ (56.50 %) LMCT p_L-d_{Fe} (3.96 %) LL'CT $p_{L1}-p_{L2}$ (8.51 %) LC p_L-p_L (7.87 %) MC $d_{Fe}-d_{Fe}$ (19.43 %)
	271	3.07E-02	27	MLCT1 $d_{Fe}-p_{py}$ (4.20 %) MLCT2 $d_{Fe}-p_{NHC}$ (52.96 %) LMCT p_L-d_{Fe} (3.92 %) LL'CT $p_{L1}-p_{L2}$ (8.90 %) LC p_L-p_L (12.40 %) MC $d_{Fe}-d_{Fe}$ (17.63 %)
	267.9	3.69E-03	28	MLCT1 $d_{Fe}-p_{py}$ (6.08 %) MLCT2 $d_{Fe}-p_{NHC}$ (52.27 %) LMCT p_L-d_{Fe} (3.92 %) LL'CT $p_{L1}-p_{L2}$ (13.77 %) LC p_L-p_L (10.78 %) MC $d_{Fe}-d_{Fe}$ (13.19 %)

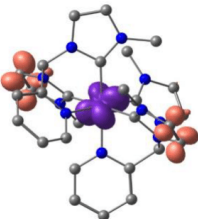
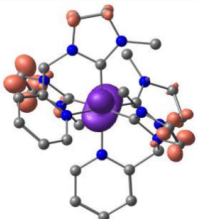
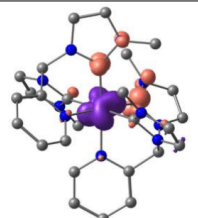
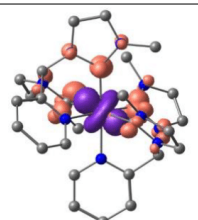
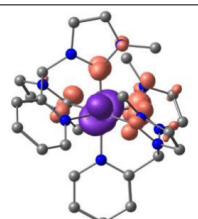
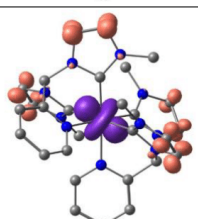
S22

	266.3	3.84E-05	29	MLCT1 $d_{Fe}-p_{py}$ (8.27 %) MLCT2 $d_{Fe}-p_{NHC}$ (2.07 %) LMCT p_L-d_{Fe} (4.12 %) LL'CT $p_{L1}-p_{L2}$ (34.07 %) LC p_L-p_L (51.04 %) MC $d_{Fe}-d_{Fe}$ (0.43 %)
	266.2	9.47E-03	30	MLCT1 $d_{Fe}-p_{py}$ (8.07 %) MLCT2 $d_{Fe}-p_{NHC}$ (3.00 %) LMCT p_L-d_{Fe} (3.04 %) LL'CT $p_{L1}-p_{L2}$ (36.70 %) LC p_L-p_L (49.07 %) MC $d_{Fe}-d_{Fe}$ (0.12 %)
	259.4	2.81E-02	31	MLCT1 $d_{Fe}-p_{py}$ (4.14 %) MLCT2 $d_{Fe}-p_{NHC}$ (59.79 %) LMCT p_L-d_{Fe} (1.08 %) LL'CT $p_{L1}-p_{L2}$ (13.61 %) LC p_L-p_L (18.09 %) MC $d_{Fe}-d_{Fe}$ (3.30 %)
	259.1	2.81E-02	32	MLCT1 $d_{Fe}-p_{py}$ (8.47 %) MLCT2 $d_{Fe}-p_{NHC}$ (2.12 %) LMCT p_L-d_{Fe} (3.42 %) LL'CT $p_{L1}-p_{L2}$ (58.40 %) LC p_L-p_L (27.27 %) MC $d_{Fe}-d_{Fe}$ (0.31 %)
	258.8	2.43E-03	33	MLCT1 $d_{Fe}-p_{py}$ (0.92 %) MLCT2 $d_{Fe}-p_{NHC}$ (68.36 %) LMCT p_L-d_{Fe} (0.10 %) LL'CT $p_{L1}-p_{L2}$ (16.14 %) LC p_L-p_L (14.33 %) MC $d_{Fe}-d_{Fe}$ (0.14 %)
	256	1.73E-03	34	MLCT1 $d_{Fe}-p_{py}$ (0.89 %) MLCT2 $d_{Fe}-p_{NHC}$ (69.78 %) LMCT p_L-d_{Fe} (0.06 %) LL'CT $p_{L1}-p_{L2}$ (17.10 %) LC p_L-p_L (12.07 %) MC $d_{Fe}-d_{Fe}$ (0.11 %)

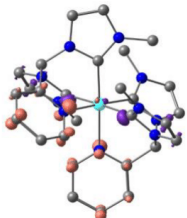
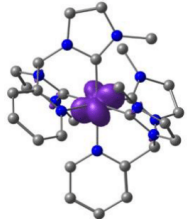
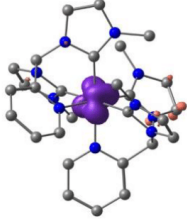
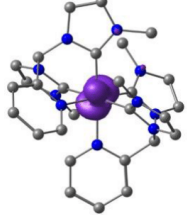
S23

	255.2	6.28E-03	35	MLCT1 $d_{Fe}-p_{py}$ (1.44 %) MLCT2 $d_{Fe}-p_{NHC}$ (24.83 %) LMCT p_L-d_{Fe} (0.69 %) LL'CT $p_{L1}-p_{L2}$ (30.09 %) LC p_L-p_L (42.85 %) MC $d_{Fe}-d_{Fe}$ (0.11 %)
	252.9	1.11E-02	36	MLCT1 $d_{Fe}-p_{py}$ (0.87 %) MLCT2 $d_{Fe}-p_{NHC}$ (3.17 %) LMCT p_L-d_{Fe} (0.44 %) LL'CT $p_{L1}-p_{L2}$ (42.53 %) LC p_L-p_L (52.90 %) MC $d_{Fe}-d_{Fe}$ (0.11 %)
	251.7	2.42E-02	37	MLCT1 $d_{Fe}-p_{py}$ (5.04 %) MLCT2 $d_{Fe}-p_{NHC}$ (30.85 %) LMCT p_L-d_{Fe} (2.69 %) LL'CT $p_{L1}-p_{L2}$ (36.83 %) LC p_L-p_L (23.59 %) MC $d_{Fe}-d_{Fe}$ (1.00 %)
	251.7	1.02E-02	38	MLCT1 $d_{Fe}-p_{py}$ (1.57 %) MLCT2 $d_{Fe}-p_{NHC}$ (43.59 %) LMCT p_L-d_{Fe} (0.75 %) LL'CT $p_{L1}-p_{L2}$ (24.59 %) LC p_L-p_L (29.22 %) MC $d_{Fe}-d_{Fe}$ (0.29 %)
	250.9	9.15E-03	39	MLCT1 $d_{Fe}-p_{py}$ (3.47 %) MLCT2 $d_{Fe}-p_{NHC}$ (10.03 %) LMCT p_L-d_{Fe} (0.84 %) LL'CT $p_{L1}-p_{L2}$ (36.49 %) LC p_L-p_L (48.83 %) MC $d_{Fe}-d_{Fe}$ (0.35 %)
	250.2	1.20E-02	40	MLCT1 $d_{Fe}-p_{py}$ (1.78 %) MLCT2 $d_{Fe}-p_{NHC}$ (60.13 %) LMCT p_L-d_{Fe} (0.56 %) LL'CT $p_{L1}-p_{L2}$ (19.52 %) LC p_L-p_L (17.80 %) MC $d_{Fe}-d_{Fe}$ (0.21 %)

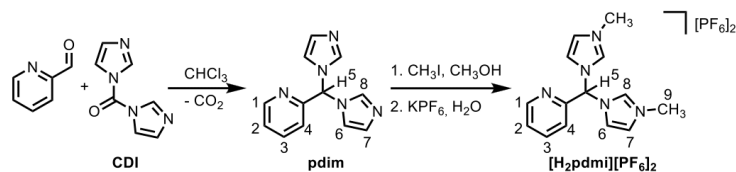
S24

	247.6	9.58E-03	41	MLCT1 $d_{Fe}-p_{py}$ (1.54 %) MLCT2 $d_{Fe}-p_{NHC}$ (68.24 %) LMCT p_L-d_{Fe} (0.08 %) LL'CT $p_{L1}-p_{L2}$ (16.08 %) LC p_L-p_L (13.99 %) MC $d_{Fe}-d_{Fe}$ (0.07 %)
	246.4	2.02E-03	42	MLCT1 $d_{Fe}-p_{py}$ (1.70 %) MLCT2 $d_{Fe}-p_{NHC}$ (69.90 %) LMCT p_L-d_{Fe} (0.05 %) LL'CT $p_{L1}-p_{L2}$ (14.48 %) LC p_L-p_L (13.68 %) MC $d_{Fe}-d_{Fe}$ (0.19 %)
	245	2.79E-02	43	MLCT1 $d_{Fe}-p_{py}$ (5.24 %) MLCT2 $d_{Fe}-p_{NHC}$ (45.96 %) LMCT p_L-d_{Fe} (1.01 %) LL'CT $p_{L1}-p_{L2}$ (21.12 %) LC p_L-p_L (25.31 %) MC $d_{Fe}-d_{Fe}$ (1.37 %)
	242.6	1.49E-03	44	MLCT1 $d_{Fe}-p_{py}$ (5.58 %) MLCT2 $d_{Fe}-p_{NHC}$ (73.44 %) LMCT p_L-d_{Fe} (0.84 %) LL'CT $p_{L1}-p_{L2}$ (6.93 %) LC p_L-p_L (7.51 %) MC $d_{Fe}-d_{Fe}$ (5.71 %)
	241.4	2.34E-02	45	MLCT1 $d_{Fe}-p_{py}$ (3.53 %) MLCT2 $d_{Fe}-p_{NHC}$ (65.20 %) LMCT p_L-d_{Fe} (0.39 %) LL'CT $p_{L1}-p_{L2}$ (14.31 %) LC p_L-p_L (15.51 %) MC $d_{Fe}-d_{Fe}$ (1.07 %)
	237.6	7.82E-05	46	MLCT1 $d_{Fe}-p_{py}$ (1.14 %) MLCT2 $d_{Fe}-p_{NHC}$ (88.14 %) LMCT p_L-d_{Fe} (0.03 %) LL'CT $p_{L1}-p_{L2}$ (5.16 %) LC p_L-p_L (5.38 %) MC $d_{Fe}-d_{Fe}$ (0.15 %)

S25

	235.9	2.10E-02	47	MLCT1 $d_{Fe}-p_{py}$ (1.70 %) MLCT2 $d_{Fe}-p_{NHC}$ (1.91 %) LMCT p_L-d_{Fe} (2.31 %) LL'CT $p_{L1}-p_{L2}$ (23.70 %) LC p_L-p_L (70.32 %) MC $d_{Fe}-d_{Fe}$ (0.05 %)
	235.8	4.59E-04	48	MLCT1 $d_{Fe}-p_{py}$ (14.48 %) MLCT2 $d_{Fe}-p_{NHC}$ (48.59 %) LMCT p_L-d_{Fe} (1.99 %) LL'CT $p_{L1}-p_{L2}$ (15.22 %) LC p_L-p_L (15.53 %) MC $d_{Fe}-d_{Fe}$ (4.19 %)
	234.4	1.20E-03	49	MLCT1 $d_{Fe}-p_{py}$ (7.42 %) MLCT2 $d_{Fe}-p_{NHC}$ (52.54 %) LMCT p_L-d_{Fe} (2.55 %) LL'CT $p_{L1}-p_{L2}$ (17.84 %) LC p_L-p_L (16.03 %) MC $d_{Fe}-d_{Fe}$ (3.63 %)
	233	1.49E-04	50	MLCT1 $d_{Fe}-p_{py}$ (12.18 %) MLCT2 $d_{Fe}-p_{NHC}$ (46.21 %) LMCT p_L-d_{Fe} (1.57 %) LL'CT $p_{L1}-p_{L2}$ (16.82 %) LC p_L-p_L (19.67 %) MC $d_{Fe}-d_{Fe}$ (3.56 %)

3. Syntheses



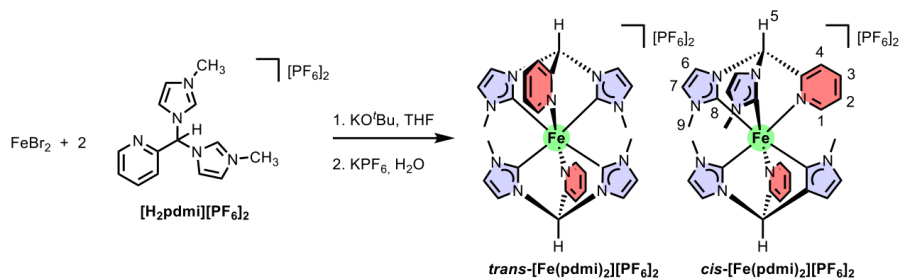
(2-Pyridyl)di(imidazolyl)methane (pdim): A mixture of 1,1-carbonyldiimidazole **CDI** (4.40 g, 27.14 mmol, 1.00 eq) and pyridine-2-carbaldehyde (2.58 mL, 27.14 mmol, 1.00 eq) was stirred in chloroform (30 mL) under reflux for 16 h. After cooling the resulting brown mixture to room temperature, the solvent was removed under reduced pressure. Column chromatography on silica (CH₂Cl₂/MeOH 9:1) afforded the **pdim** as a brown oil (3.66 g, 16.28 mmol, 60 %). *R*_f = 0.52.

¹H NMR (CD₂Cl₂): δ = 8.69 (d, 1H, ³J_{HH} = 4.8 Hz, H¹), 7.82 (pt, 1H, ³J_{HH} = 7.8 Hz, H³), 7.60 (s, 2H, H⁸), 7.41 (m, 1H, H²), 7.41 (s, 1H, H⁵), 7.21 (d, 1H, H⁴, ³J_{HH} = 7.9 Hz), 7.06 (m, 4H, H^{6,7}) ppm.

(2-Pyridyl)di(3-methylimidazolium-1-yl)methane-bis(hexafluorophosphate) [H₂pdmi][PF₆]₂: A mixture of **pdim** (3.66 g, 16.28 mmol, 1.00 eq) and methyl iodide (22 mL, 0.35 mol, 21.71 eq) was refluxed in methanol (30 mL) over night. After cooling the resulting mixture to room temperature, the solvent was removed under reduced pressure. The residue was dissolved in water (20 mL) and the product precipitated with a saturated solution of KPF₆ (8.35 g) in water (100 mL). After filtration and drying under reduced pressure, **[H₂pdmi][PF₆]₂** was obtained as a yellow solid (6.11 g, 11.20 mmol, 69 %).

Elemental analysis for C₁₄H₁₇F₁₂N₅P₂: calcd. C 30.84 %, H 3.14 %, N 12.84 %; found C 30.86 %, H 3.04 %, N 12.81 %.

¹H NMR (CD₃CN): δ = 8.82 (s, 2H, H⁸), 8.77 (d, 1H, ³J_{HH} = 4.6 Hz, H¹), 8.03 (t, 1H, ³J_{HH} = 7.8 Hz, H³), 7.82 (s, 1H, H⁵), 7.75 (d, 1H, ³J_{HH} = 7.8 Hz, H²), 7.69 (m, 2H, H⁷), 7.63 (m, 1H, H⁴), 7.45 (m, 2H, H⁶), 3.85 (s, 6H, H⁹) ppm.



Low-temperature synthesis (-70°C) of *trans* enriched $[\text{Fe}(\text{pdmi})_2][\text{PF}_6]_2$. A mixture of the pro-ligand $[\text{H}_2\text{pdmi}][\text{PF}_6]_2$ (505.68 mg, 0.93 mmol, 2.00 eq) and FeBr_2 (100 mg, 0.46 mmol, 1.00 eq) in THF (10 mL) was cooled to -70°C in an EtOH/dry ice bath. A solution of potassium *tert*-butoxide (208.13 mg, 1.85 mmol, 4.00 eq) in THF (5 mL) was added over 5 minutes to this suspension forming a dark reddish solution. The mixture was slowly warmed to room temperature and stirred overnight. The solvent was removed under reduced pressure and the reddish solid residue purified by column chromatography on silica (acetone/ $\text{H}_2\text{O}/\text{KNO}_3(\text{aq})$ 10:2:2). The first orange coloured fraction was collected ($R_f = 0.63$). After removal of acetone under reduced pressure, the resulting aqueous solution was treated with a saturated solution of KPF_6 (2.51 g) in water (30 mL) precipitating $[\text{Fe}(\text{pdmi})_2][\text{PF}_6]_2$. After filtration and drying under reduced pressure, the complex $[\text{Fe}(\text{pdmi})_2][\text{PF}_6]_2$ was obtained as an orange solid (30 mg, 0.04 mmol, 7.7 %) as mixture of *trans* and *cis* isomers (4:1 ratio according to HPLC analysis). Elemental analysis for $\text{C}_{28}\text{H}_{30}\text{F}_{12}\text{FeN}_{10}\text{P}_2$: calcd. C 39.45 %, H 3.55 %, N 16.43 %; found C 39.29 %, H 3.59 %, N 16.27 %. ESI⁺ MS (CH_3CN): $m/z(\%) = 281.10$ (96.5) $[\text{Fe}(\text{pdmi})_2]^{2+}$, 707.16 (100.0) $[\text{Fe}(\text{pdmi})_2+\text{PF}_6]^+$.

High-temperature synthesis ($+20^\circ\text{C}$) of *cis* enriched $[\text{Fe}(\text{pdmi})_2][\text{PF}_6]_2$. To a solution of $[\text{H}_2\text{pdmi}][\text{PF}_6]_2$ (505.68 mg, 0.93 mmol, 2.00 eq) and FeBr_2 (100 mg, 0.46 mmol, 1.00 eq) in dry DMF (10 mL) was added a solution of potassium *tert*-butoxide (208.13 mg, 1.85 mmol, 4.00 eq) in dry DMF (5 mL) at room temperature. A dark reddish solution formed which was stirred overnight at 20°C . The solvent was removed under reduced pressure and the solid reddish residue purified by column chromatography on silica (acetone/ $\text{H}_2\text{O}/\text{KNO}_3(\text{aq})$ 10:2:2). The first orange coloured fraction was collected ($R_f = 0.63$). After removal of acetone under reduced pressure, the resulting aqueous solution was treated with a saturated solution of KPF_6 (2.51 g) in water (30 mL) precipitating $[\text{Fe}(\text{pdmi})_2][\text{PF}_6]_2$. After filtration and drying under vacuum the complex $[\text{Fe}(\text{pdmi})_2][\text{PF}_6]_2$ was obtained as an orange solid (28 mg, 0.03 mmol, 7.1 %) as mixture of *trans* and *cis* isomers (1:2 ratio according to HPLC analysis).

Separation via HPLC (*ChiralPAK IC*; 5 μM , 10 \times 250 mm; $\text{CH}_2\text{Cl}_2/\text{CH}_3\text{OH}$ (9:1), 0.1% formic acid, 50 mM [$^n\text{Bu}_4\text{N}$]Cl) yielded the pure *trans* and *cis* isomers from low and high temperature syntheses, respectively.

The obtained mixture was dried under reduced pressure at 25°C . To remove the [$^n\text{Bu}_4\text{N}$]Cl, the residue was washed with acetonitrile (5 mL). For the anion exchange to $[\text{PF}_6]^-$, the $[\text{Fe}(\text{pdmi})_2][\text{Cl}]_2$ salt was dissolved in water (2 mL) and treated with a saturated solution of KPF_6 in water (5 mL). The $[\text{Fe}(\text{pdmi})_2][\text{PF}_6]_2$ salt was obtained by diffusion of diethylether into a CH_3CN solution. These purified samples were used for the following analyses and the TA spectroscopic studies.

trans-[Fe(pdmi)₂][PF₆]₂:

¹H NMR (CD₃CN): δ = 7.84 (d, 4H, ³J_{HH} = 1.8 Hz, H⁷), 7.82 (s, 2H, H⁵), 7.70-7.63 (m, 4H, H^{1,2}), 7.33 (d, 2H, ³J_{HH} = 5.6 Hz, H⁴), 7.14 (d, 4H, ³J_{HH} = 1.6 Hz, H⁶), 6.72 (m, 2H, H³), 2.46 (s, 12H, H⁸) ppm.

¹³C{¹H} NMR (CD₃CN): δ = 205.40 (C⁹), 160.73 (C⁴), 160.23 (C⁵), 137.50 (C¹), 125.03 (C⁶), 124.34 (C^{2,3}), 122.09 (C⁷), 72.05 (C¹⁰), 35.56 (C⁸) ppm.

³¹P NMR (CD₃CN): δ = -144.46 (sept, ¹J_{PF} = 706.5 Hz).

¹⁹F NMR (CD₃CN): δ = 73.94 (d, ¹J_{PF} = 706.5 Hz).

UV/Vis/NIR (CH₃CN): λ (ϵ) = 521 (7430), 342 (6750), 287 (5660), 260 nm (6360 M⁻¹ cm⁻¹).

IR (ATR): $\tilde{\nu}$ = 3165 (w), 3136 (w), 2959 (w), 1669 (w), 1607 (w), 1561 (w), 1473 (m), 1440 (m), 1395 (m), 1215 (m), 1189 (w), 1080 (w), 1048 (w), 832 (s, PF₆), 778 (m), 719 (s), 556 (s, PF₆), 521 (w), 457 (m), 430 (w) cm⁻¹.

Raman: $\tilde{\nu}$ = 3162 (w), 3127 (w), 3102 (w), 2961 (w), 1604 (s), 1562 (m), 1473 (m), 1441 (w), 1419 (m), 1403 (m), 1357 (m), 1309 (w), 1262 (m), 1215 (m), 1189 (w), 1160 (w), 1110 (m), 1064 (w), 1019 (s), 876 (m), 741 (w), 677 (w), 656 (w), 633 (s), 606 (w), 350 (w), 314 (w), 277 (w), 228 (w) cm⁻¹.

CV (CH₃CN/[ⁿBu₄N][PF₆]): E_{1/2} = 0.04 V (rev.), 1.56 (qrev.) versus FcH/FcH⁺.

cis-[Fe(pdmi)₂][PF₆]₂:

¹H NMR (CD₃CN): δ = 7.94-7.91 (m, 3H), 7.89-7.87 (m, 3H), 7.78 (d, ³J_{HH} = 1.9 Hz, 2H), 7.72 (d, ³J_{HH} = 2.0 Hz, 2H), 7.42 (d, ³J_{HH} = 5.4 Hz, 2H), 7.03-6.99 (m, 4H), 6.96 (d, ³J_{HH} = 2.0 Hz, 2H), 2.39 (s, 6H), 2.32 (s, 6H) ppm.

¹³C{¹H} NMR (CD₃CN): δ = 203.72 (C¹⁴), 203.13 (C¹³), 158.17 (C¹²), 158.07 (C⁴), 137.86 (C¹), 125.29 (C³), 124.36 (C⁹), 124.09 (C⁶), 123.76 (C²), 121.76 (C⁷), 121.46 (C¹⁰), 71.85 (C⁵), 34.82 (C⁸), 34.55 (C¹¹) ppm.

UV/Vis/NIR (CH₃CN): λ (ϵ) = 471 (8680), 343 (4615), 285 (7075), 261 nm (8875 M⁻¹ cm⁻¹).

IR (ATR): $\tilde{\nu}$ = 3359 (w), 3170 (w), 3141 (w), 2959 (w), 2921 (w), 2853 (w), 1659 (w), 1633 (w), 1606 (w), 1472 (w), 1443 (w), 1394 (m), 1343 (w), 1308 (w), 1263 (w), 1245 (w), 1214 (w), 1088 (m), 1081 (w), 1047 (w), 1008 (w), 832 (s, PF₆), 761 (m), 714 (s), 674 (m), 633 (w), 602 (w), 556 (s, PF₆), 518 (w), 459 (w), 418 (w), 400 (w) cm⁻¹.

Raman: $\tilde{\nu}$ = 3149 (w), 3126 (w), 3059 (m), 3029 (w), 2938 (w), 1603 (s), 1559 (m), 1472 (m), 1431 (w), 1410 (w), 1355 (w), 1335 (w), 1036 (w), 1262 (m), 1213 (m), 1102 (m), 1063 (w), 1013 (s), 873 (m), 680 (w), 658 (m), 633 (s), 608 (w), 460 (w), 418 (w), 377 (m), 360 (w), 310 (w), 275 (w), 226 (w), 196 (m) cm⁻¹.

CV (CH₃CN/[ⁿBu₄N][PF₆]): E_{1/2} = 0.04 V (rev.) versus FcH/FcH⁺.

Oxidation of *trans*-[Fe(pdmi)₂][PF₆]₂ to *trans*-[Fe(pdmi)₂]³⁺ for spectroscopic analysis. The iron(III) complex was obtained *in situ* by dissolving *trans*-[Fe(pdmi)₂][PF₆]₂ (15 mg, 17.60 μmol) in CH₃CN (5 mL) and adding [NO][PF₆] (3.1 mg, 17.72 μmol) as a solid. The colour of the solution changed from orange to purple. Gas evolution (NO) was not observed due to the small scale. This solution was diluted with CH₃CN and used for absorption experiments.

UV/Vis/NIR (CH₃CN): λ (ϵ) = 572 (2370), 517 (2200), 366 nm (2620 M⁻¹ cm⁻¹).

Oxidation of *cis*-[Fe(pdmi)₂][PF₆]₂ to *cis*-[Fe(pdmi)₂]³⁺ for spectroscopic analysis. The iron(III) complex was obtained *in situ* by dissolving *cis*-[Fe(pdmi)₂][PF₆]₂ (15 mg, 17.60 μmol) in CH₃CN (5 mL) and adding [NO][PF₆] (3.1 mg, 17.72 μmol) as a solid. The colour of the solution changed from orange to purple. Gas evolution (NO) was not observed due to the small scale. This solution was diluted with CH₃CN and used for absorption experiments.

UV/Vis/NIR (CH₃CN): λ (ϵ) = 620 (1870, sh), 582 (2740), 529 (3330), 490 (2990), 343 nm (3480 M⁻¹ cm⁻¹).

4. Spectroscopic and analytical data

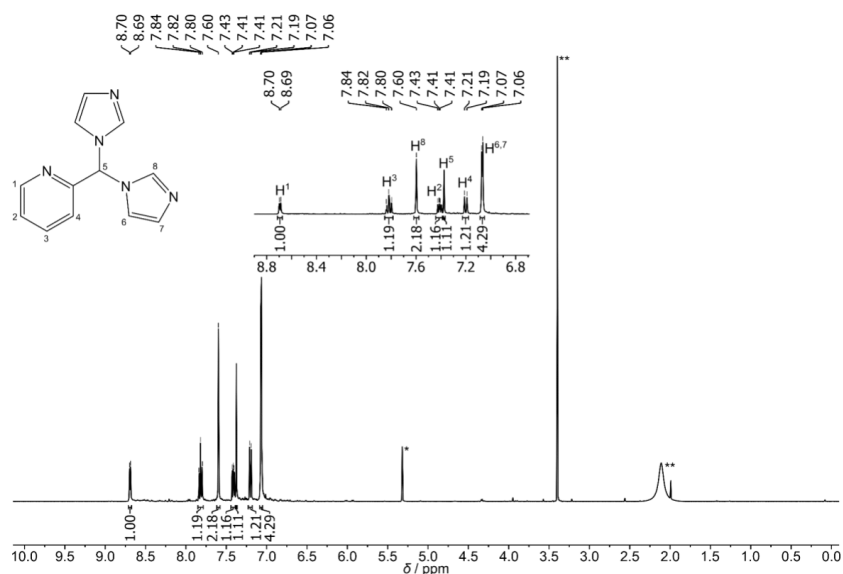


Fig. S5. ¹H NMR spectrum of (2-pyridyl)di(imidazolyl)methane (**pdim**) in CD₂Cl₂. * CHCl₃. ** Water.

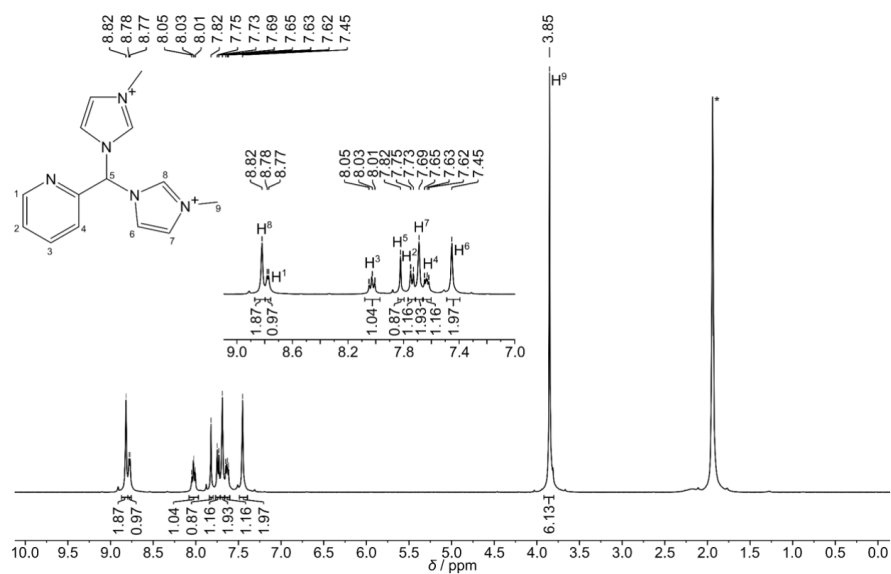


Fig. S6. ¹H NMR spectrum of (2-pyridyl)di(3-methylimidazolium-1-yl)methane-bis(hexafluorophosphate) [**H₂pdmi**][PF₆]₂ in CD₃CN. * CHD₂CN.

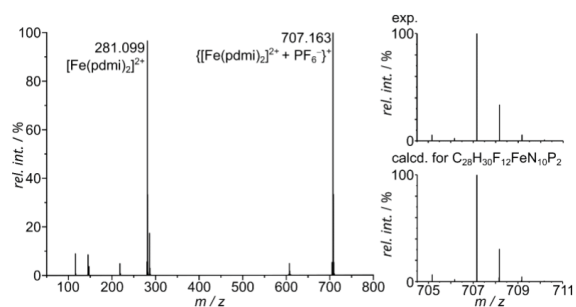


Fig. S7. ESI⁺ mass spectrum of $[\text{Fe}(\text{pdmi})_2][\text{PF}_6]_2$ in CH_3CN (low temperature synthesis). The insets show the experimental and calculated isotopic patterns of the $\{[\text{Fe}(\text{pdmi})_2][\text{PF}_6]\}^+$ cation.

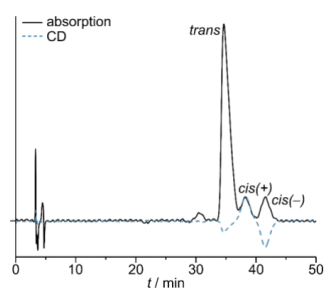


Fig. S8. HPLC (chiral column, $\text{CH}_2\text{Cl}_2/\text{CH}_3\text{OH}$ (9:1), 0.1% formic acid, 50 mM $[\text{tBu}_4\text{N}]\text{Cl}$) trace of the products *trans/cis*- $[\text{Fe}(\text{pdmi})_2][\text{PF}_6]_2$ of the low-temperature synthesis. The *cis* isomer is even separated into its (+) and (-) enantiomers as seen from the CD detected trace (dashed blue line).

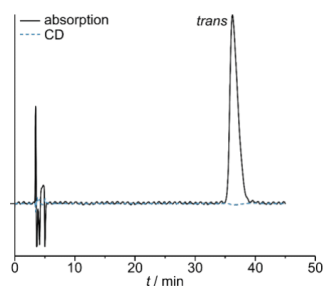


Fig. S9. HPLC (chiral column, $\text{CH}_2\text{Cl}_2/\text{CH}_3\text{OH}$ (9:1), 0.1% formic acid, 50 mM $[\text{tBu}_4\text{N}]\text{Cl}$) trace of *trans*- $[\text{Fe}(\text{pdmi})_2]^{2+}$ after HPLC separation.

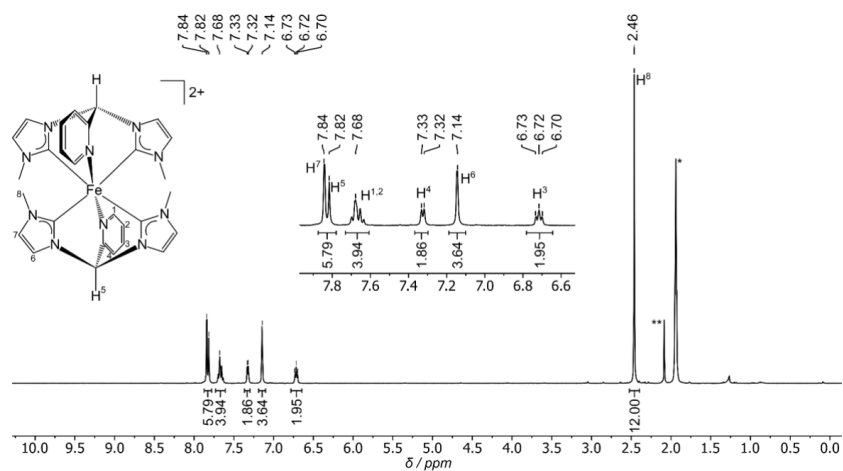


Fig. S10. ^1H NMR spectrum of $\text{trans-[Fe(pdmi)}_2\text{][PF}_6\text{]}_2$ in CD_3CN (low temperature synthesis). * CHD_2CN . ** Water.

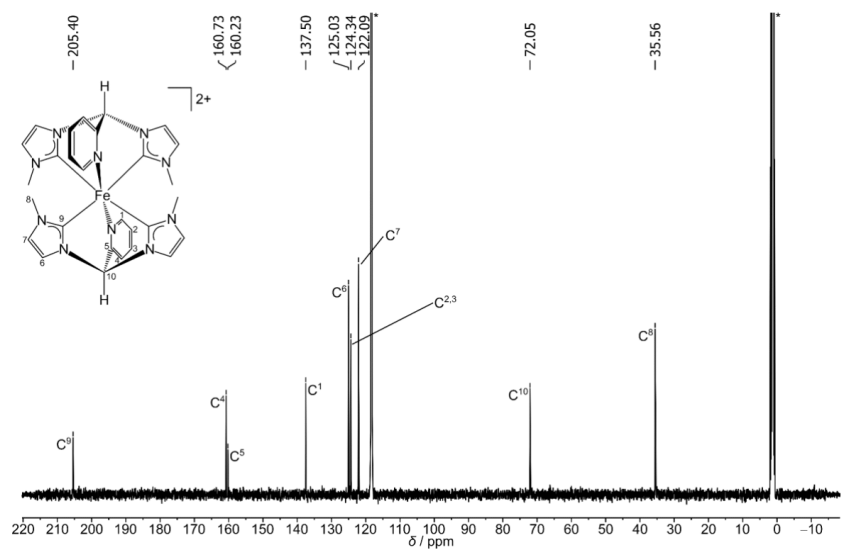


Fig. S11. $^{13}\text{C}\{^1\text{H}\}$ NMR spectrum of $\text{trans-[Fe(pdmi)}_2\text{][PF}_6\text{]}_2$ in CD_3CN (low temperature synthesis). * CD_3CN .

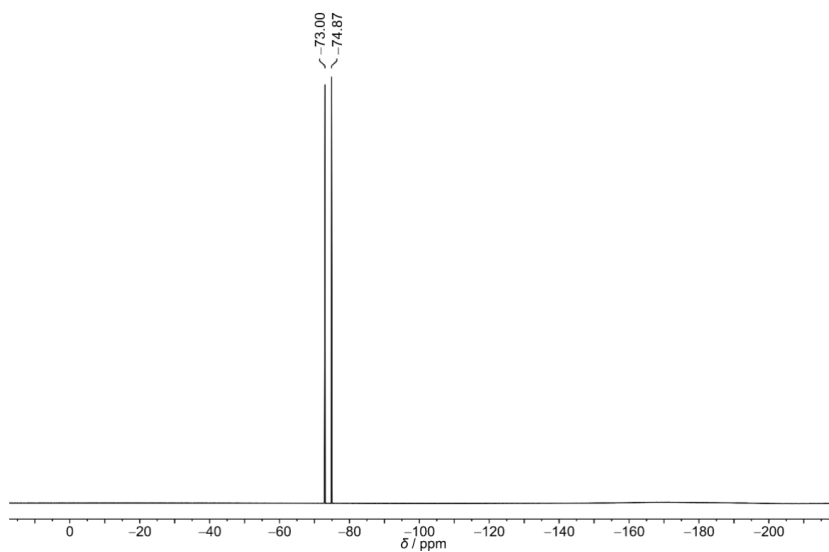


Fig. S12. ^{19}F NMR spectrum of *trans*-[Fe(pdmi) $_2$][PF $_6$] $_2$ in CD $_3$ CN (low temperature synthesis).

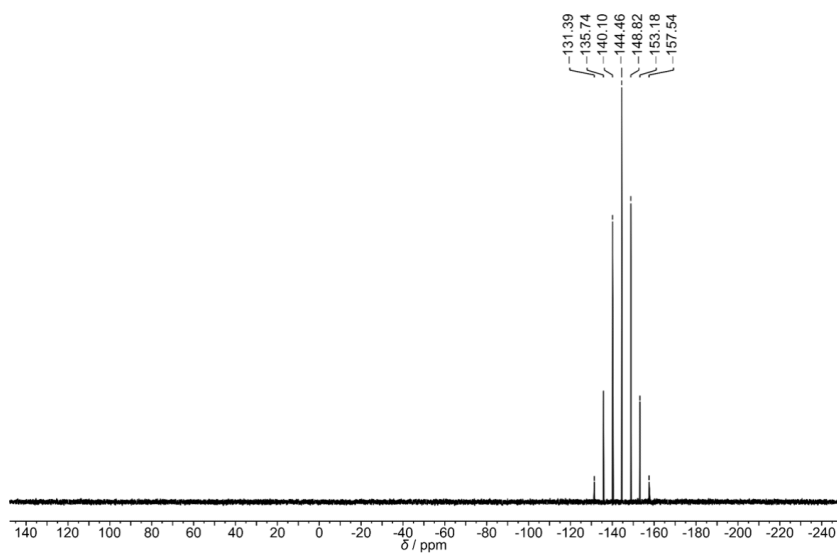


Fig. S13. ^{31}P NMR spectrum of *trans*-[Fe(pdmi) $_2$][PF $_6$] $_2$ in CD $_3$ CN (low temperature synthesis).

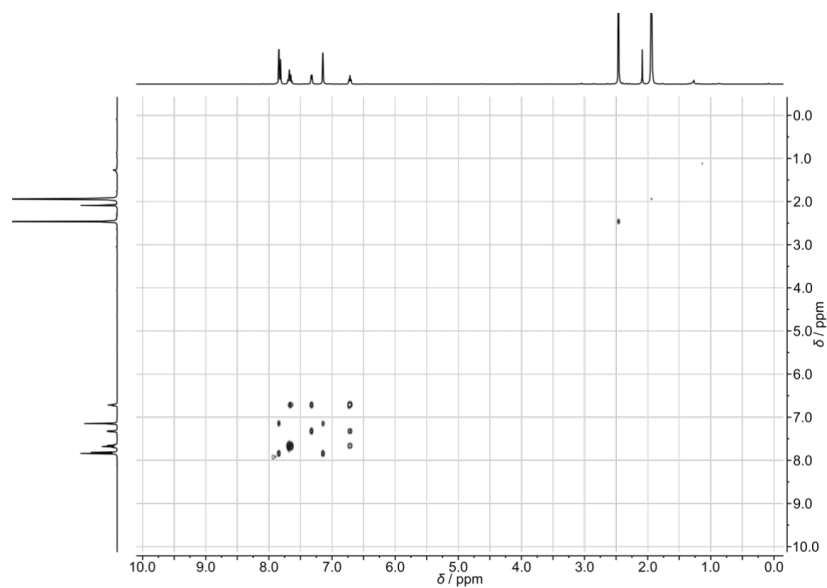


Fig. S14. ^1H , ^1H -COSY of *trans*-[Fe(pdmi) $_2$][PF $_6$] $_2$ in CD $_3$ CN (low temperature synthesis).

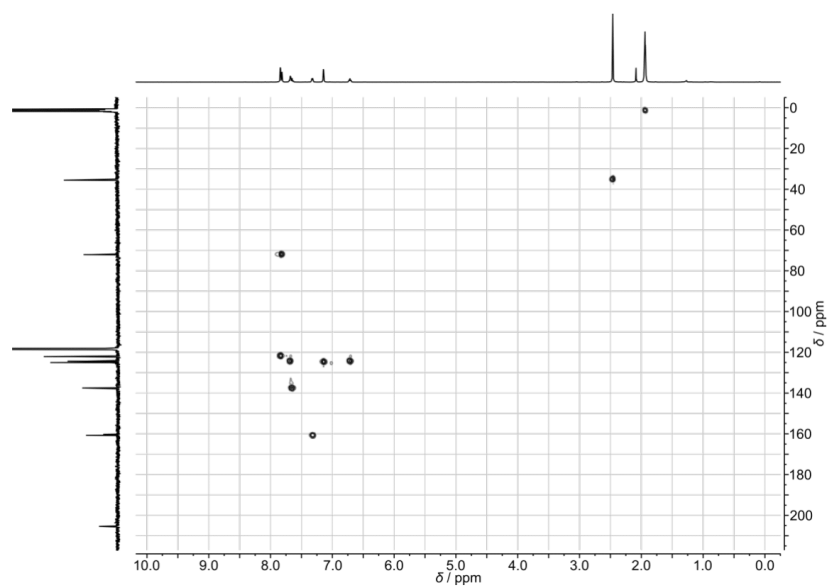


Fig. S15. ^1H , ^{13}C -HSQC of *trans*-[Fe(pdmi) $_2$][PF $_6$] $_2$ in CD $_3$ CN (low temperature synthesis).

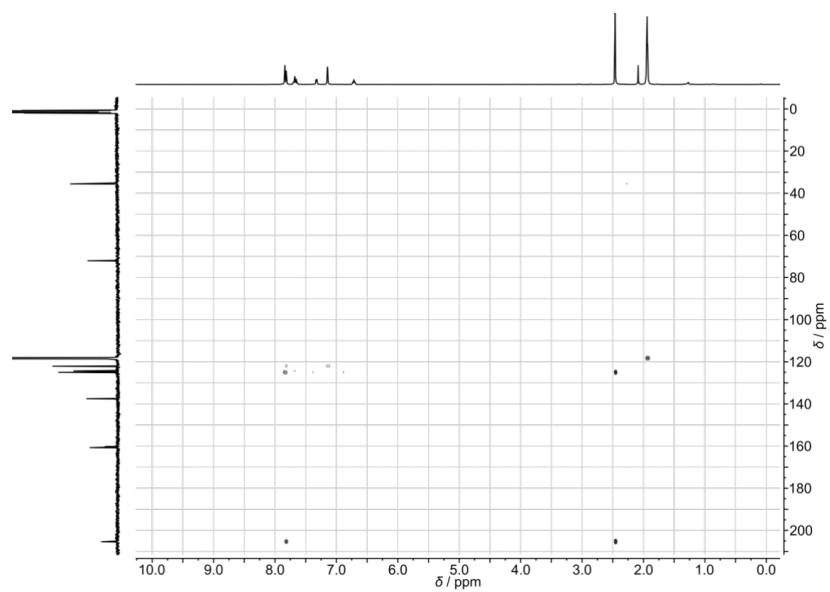


Fig. S16. ^1H , ^{13}C -HMBC of *trans*-[Fe(pdmi) $_2$][PF $_6$] $_2$ in CD $_3$ CN (low temperature synthesis).

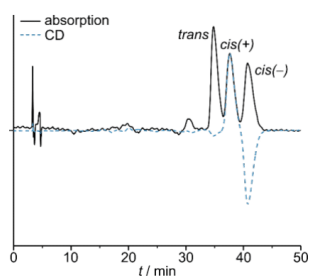


Fig. S17. HPLC (chiral column, $\text{CH}_2\text{Cl}_2/\text{CH}_3\text{OH}$ (9:1), 0.1% formic acid, 50 mM [$n\text{Bu}_4\text{N}$]Cl) trace of the products *trans/cis*- $[\text{Fe}(\text{pdmi})_2][\text{PF}_6]_2$ of the high-temperature synthesis. The *cis* isomer is even separated into its (+) and (-) enantiomers as seen from the CD detected trace (dashed blue line).

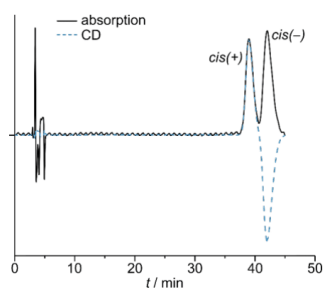


Fig. S18. HPLC (chiral column, $\text{CH}_2\text{Cl}_2/\text{CH}_3\text{OH}$ (9:1), 0.1% formic acid, 50 mM [$n\text{Bu}_4\text{N}$]Cl) trace of *cis*- $[\text{Fe}(\text{pdmi})_2]^{2+}$ after HPLC separation. The *cis* isomer is even separated into its (+) and (-) enantiomers. Due to the tailing of the band of the *trans* isomer into the band of the (+)-enantiomer, the carefully purified *cis* sample is slightly enriched in the (-) enantiomer as seen from the CD detected trace (dashed blue line).

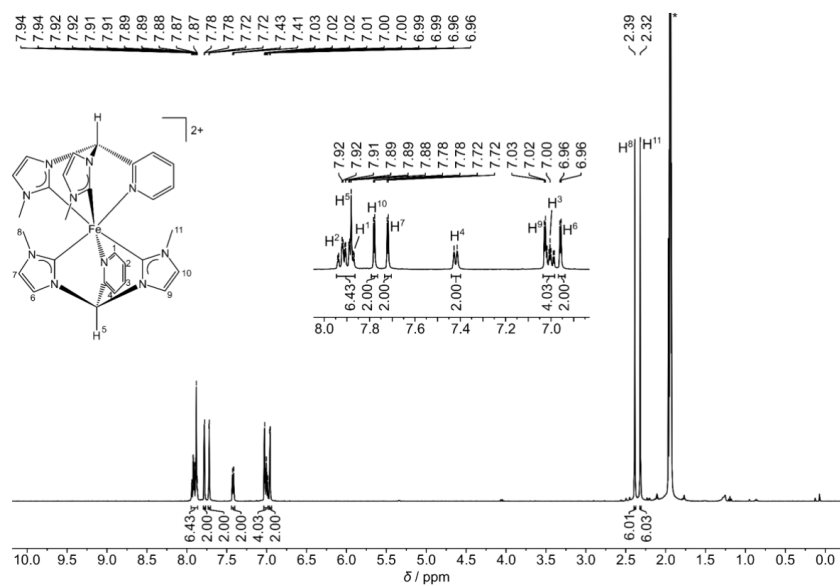


Fig. S19. ¹H NMR spectrum of *cis*-[Fe(pdmi)₂][PF₆]₂ in CD₃CN (after HPLC). * CHD₂CN. ** Water.

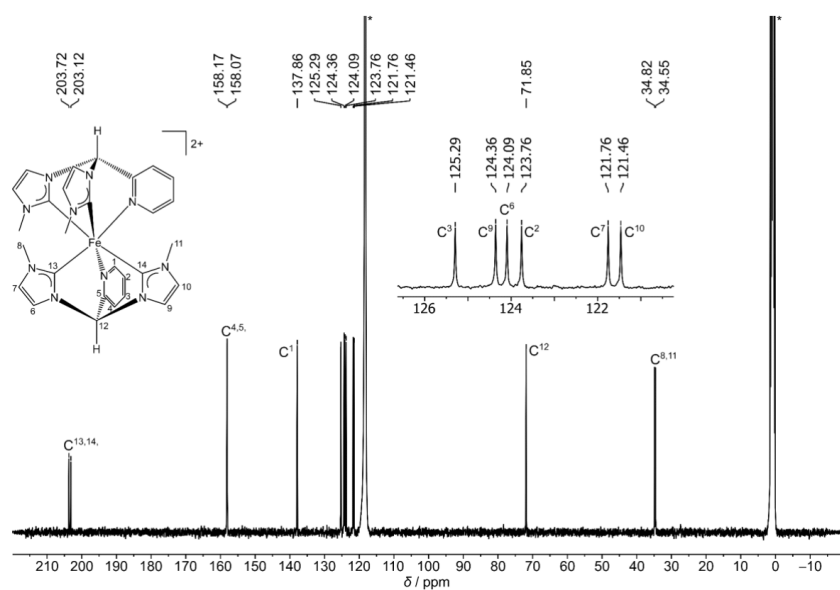


Fig. S20. ¹³C{¹H} NMR spectrum of *cis*-[Fe(pdmi)₂][PF₆]₂ in CD₃CN (after HPLC). * CD₃CN.

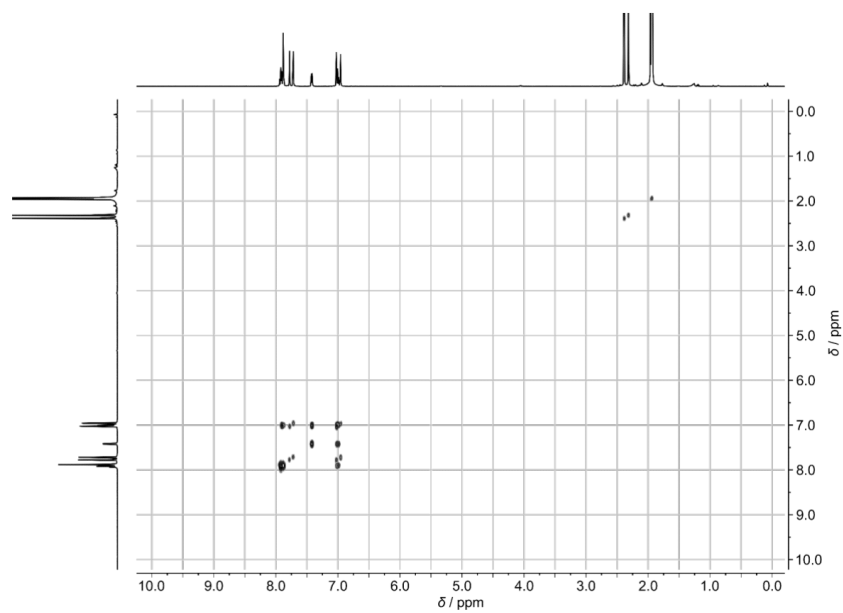


Fig. S21. ^1H , ^1H -COSY of *cis*-[Fe(pdmi) $_2$][PF $_6$] $_2$ in CD $_3$ CN (high temperature synthesis).

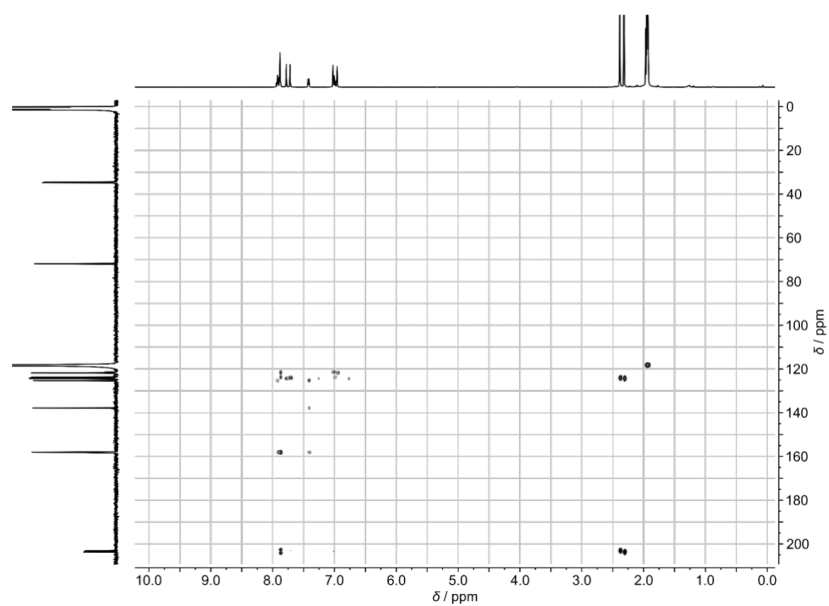


Fig. S22. ^1H , ^{13}C -HMBC of *cis*-[Fe(pdmi) $_2$][PF $_6$] $_2$ in CD $_3$ CN (high temperature synthesis).

S39

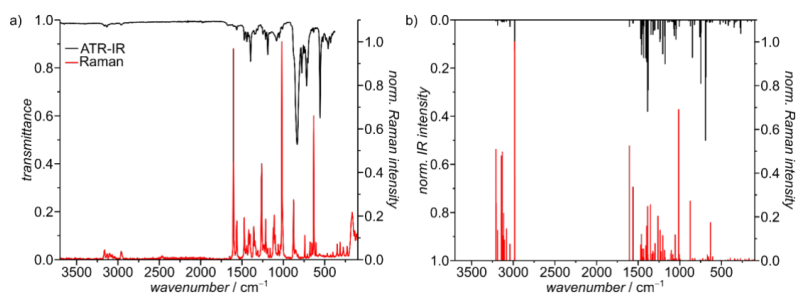


Fig. S23. a) ATR-IR and Raman spectra of $\text{trans-}[\text{Fe}(\text{pdmi})_2][\text{PF}_6]_2$. b) DFT calculated IR and Raman spectra of $\text{trans-}[\text{Fe}(\text{pdmi})_2]^{2+}$ (wavenumbers scaled by 0.975).

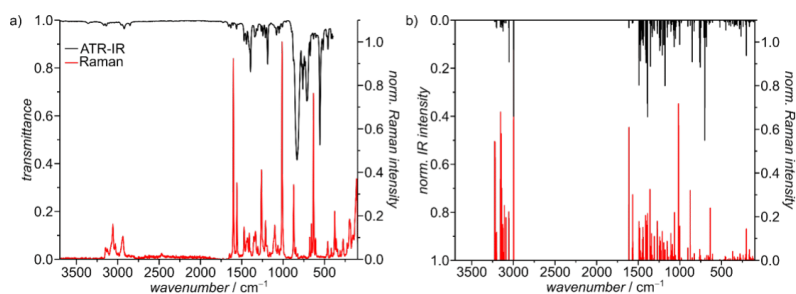


Fig. S24. A) ATR-IR and Raman spectra of $\text{cis-}[\text{Fe}(\text{pdmi})_2][\text{PF}_6]_2$. b) DFT calculated IR and Raman spectra of $\text{cis-}[\text{Fe}(\text{pdmi})_2]^{2+}$ (wavenumbers scaled by 0.979).

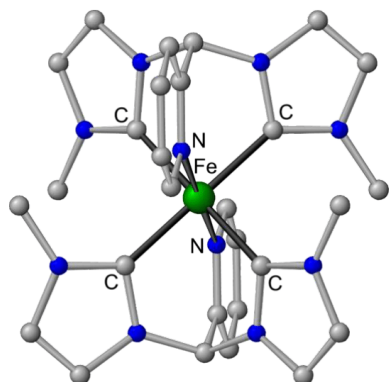


Fig. S25. Molecular structure of the cation of *trans*-[Fe(pdmi)₂][PF₆]₂ determined by SC-XRD. Hydrogen atoms omitted.

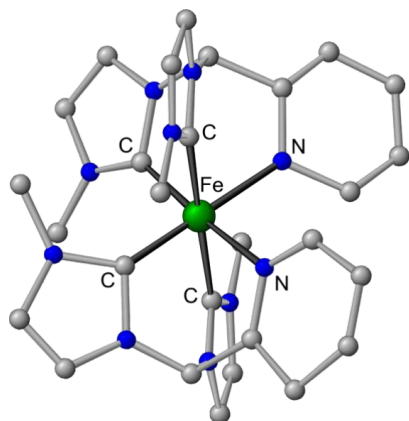


Fig. S26. Molecular structure of the cation of *cis*-[Fe(pdmi)₂][PF₆]₂ determined by SC-XRD. Hydrogen atoms omitted.

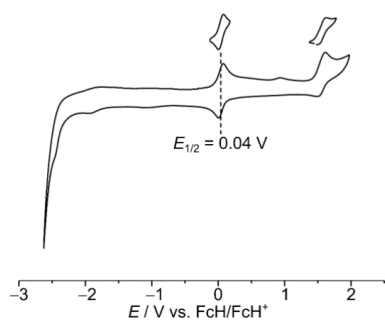


Fig. S27. Cyclic voltammograms of *trans*-[Fe(pdmi)₂][PF₆]₂ in dry, deaerated CH₃CN with [nBu₄N][PF₆] as supporting electrolyte.

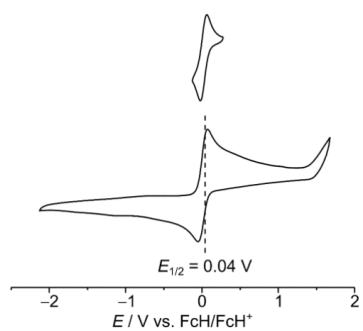


Fig. S28. Cyclic voltammograms of *cis*-[Fe(pdmi)₂][PF₆]₂ in dry, deaerated CH₃CN with [nBu₄N][PF₆] as supporting electrolyte.

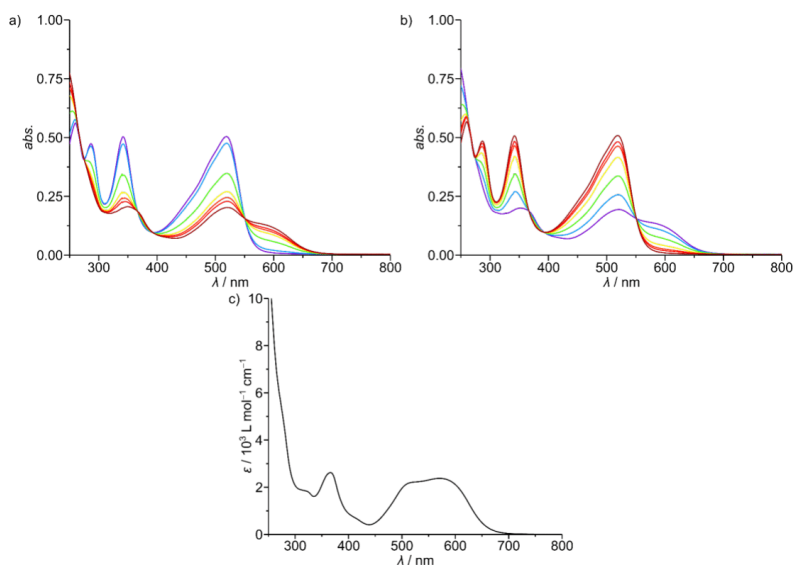


Fig. S29. a) Spectroelectrochemical oxidation (purple → red) of *trans*-[Fe(pdmi)₂][PF₆]₂ in dry, deaerated CH₃CN with [tBu₄N][PF₆] as supporting electrolyte (low temperature synthesis), b) spectroelectrochemical re-reduction (purple → red) and c) UV/Vis/NIR spectrum after chemical oxidation of *trans*-[Fe(pdmi)₂][PF₆]₂ with 1 eq [NO][PF₆] in CH₃CN.

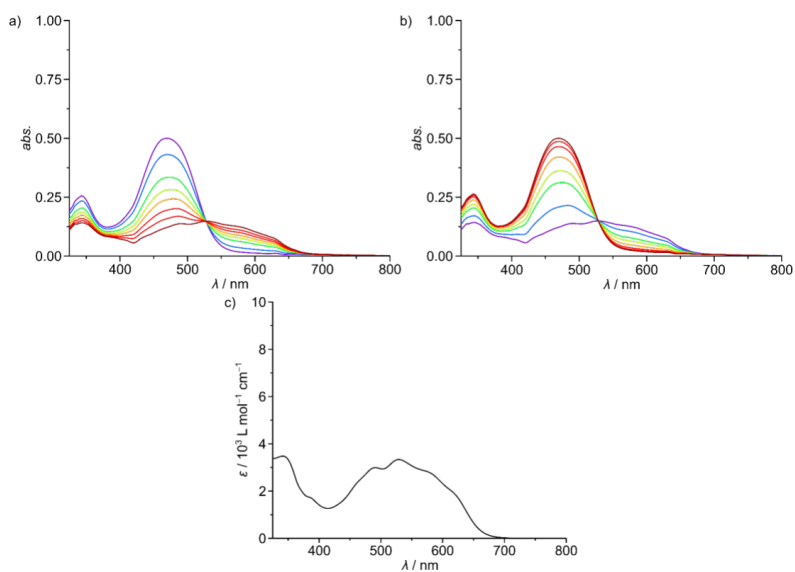


Fig. S30. a) Spectroelectrochemical oxidation (purple → red) of *cis*-[Fe(pdmi)₂][PF₆]₂ in dry, deaerated CH₃CN with [tBu₄N][PF₆] as supporting electrolyte (low temperature synthesis), b) spectroelectrochemical re-reduction (purple → red) and c) UV/Vis/NIR spectrum after chemical oxidation of *trans*-[Fe(pdmi)₂][PF₆]₂ with 1 eq [NO][PF₆] in CH₃CN.

S43

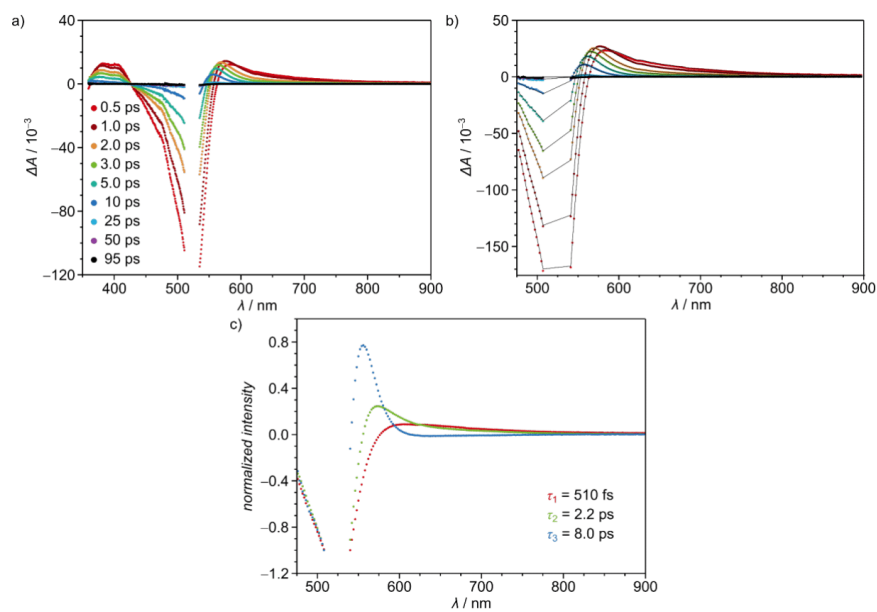
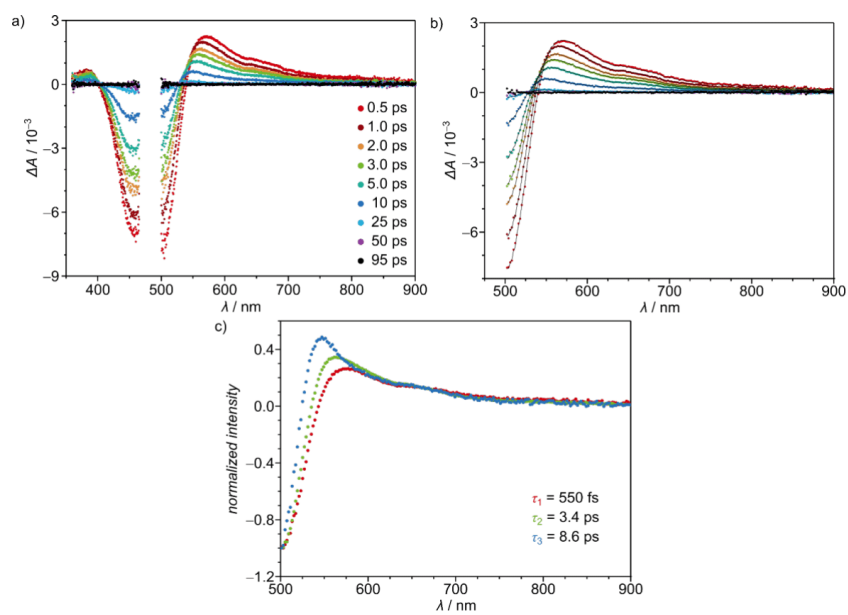


Fig. S31. a) TA spectra of *trans*-[Fe(pdmi)₂][PF₆]₂ in MeOH/EtOH (2:3 v/v) at 293 K ($\lambda_{\text{exc}} = 520 \text{ nm}$), b) rebinned data vs. fit and c) EADS from a global fit.



S44

Fig. S32. TA spectra of *cis*-[Fe(pdmi)₂][PF₆]₂ in MeOH/EtOH (2:3 v/v) at 293 K ($\lambda_{\text{exc}} = 470$ nm), b) rebinned data vs. fit and c) EADS from a global fit.

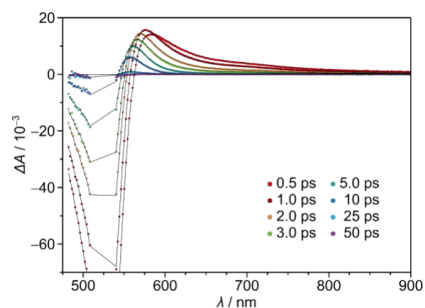


Fig. S33. TA spectra of *trans*-[Fe(pdmi)₂][PF₆]₂ in MeOH/EtOH (2:3 v/v) at 293 K ($\lambda_{\text{exc}} = 520$ nm), rebinned data vs. fit.

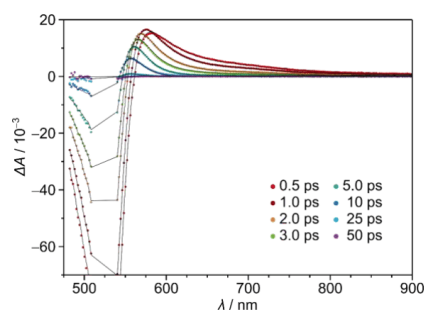


Fig. S34. TA spectra of *trans*-[Fe(pdmi)₂][PF₆]₂ in MeOH/EtOH (2:3 v/v) at 283 K ($\lambda_{\text{exc}} = 520$ nm), rebinned data vs. fit.

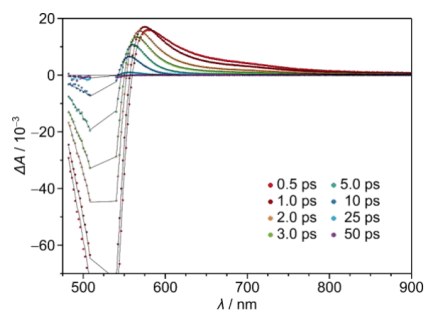


Fig. S35. TA spectra of *trans*-[Fe(pdmi)₂][PF₆]₂ in MeOH/EtOH (2:3 v/v) at 273 K ($\lambda_{\text{exc}} = 520$ nm), rebinned data vs. fit.

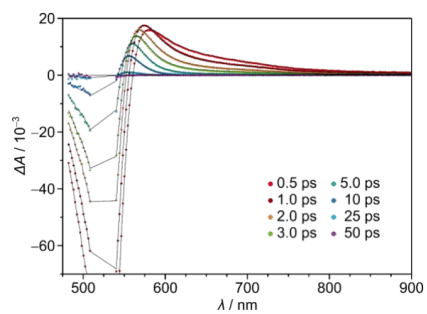


Fig. S36. TA spectra of $trans-[Fe(pdmi)_2][PF_6]_2$ in MeOH/EtOH (2:3 v/v) at 263 K ($\lambda_{exc} = 520$ nm), rebinned data vs. fit.

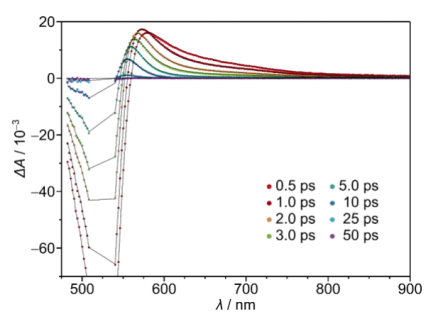


Fig. S37. TA spectra of $trans-[Fe(pdmi)_2][PF_6]_2$ in MeOH/EtOH (2:3 v/v) at 253 K ($\lambda_{exc} = 520$ nm), rebinned data vs. fit.

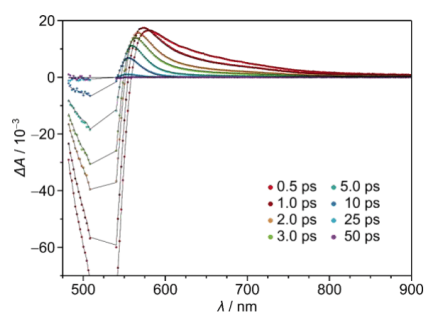


Fig. S38. TA spectra of $trans-[Fe(pdmi)_2][PF_6]_2$ in MeOH/EtOH (2:3 v/v) at 243 K ($\lambda_{exc} = 520$ nm), rebinned data vs. fit.

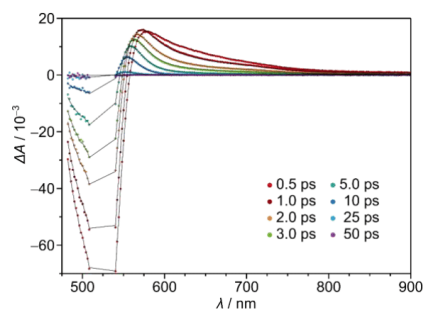


Fig. S39. TA spectra of $trans\text{-[Fe(pdmi)}_2\text{][PF}_6\text{]}_2$ in MeOH/EtOH (2:3 v/v) at 233 K ($\lambda_{\text{exc}} = 520$ nm), rebinned data vs. fit.

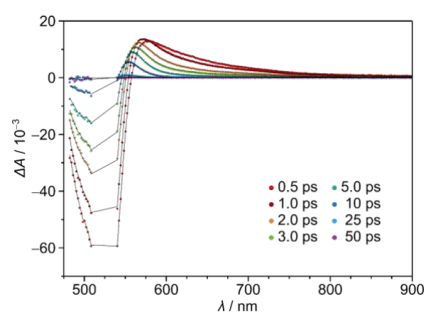


Fig. S40. TA spectra of $trans\text{-[Fe(pdmi)}_2\text{][PF}_6\text{]}_2$ in MeOH/EtOH (2:3 v/v) at 223 K ($\lambda_{\text{exc}} = 520$ nm), rebinned data vs. fit.

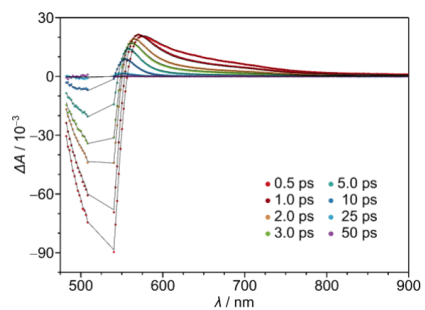


Fig. S41. TA spectra of $trans\text{-[Fe(pdmi)}_2\text{][PF}_6\text{]}_2$ in MeOH/EtOH (2:3 v/v) at 213 K ($\lambda_{\text{exc}} = 520$ nm), rebinned data vs. fit.

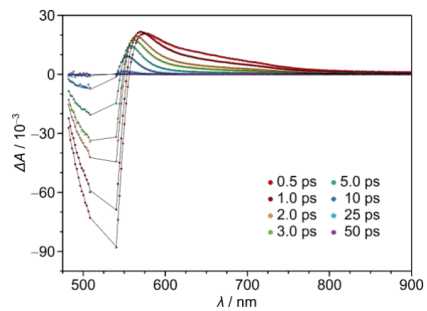


Fig. S42. TA spectra of $trans\text{-[Fe(pdmi)}_2\text{][PF}_6\text{]}_2$ in MeOH/EtOH (2:3 v/v) at 203 K ($\lambda_{\text{exc}} = 520$ nm), rebinned data vs. fit.

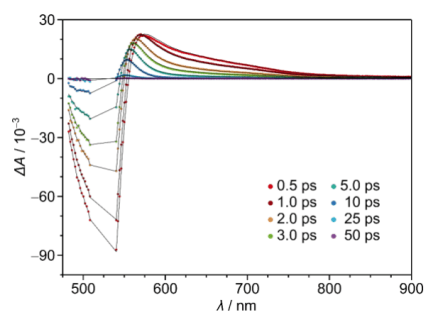


Fig. S43. TA spectra of $trans\text{-[Fe(pdmi)}_2\text{][PF}_6\text{]}_2$ in MeOH/EtOH (2:3 v/v) at 193 K ($\lambda_{\text{exc}} = 520$ nm), rebinned data vs. fit.

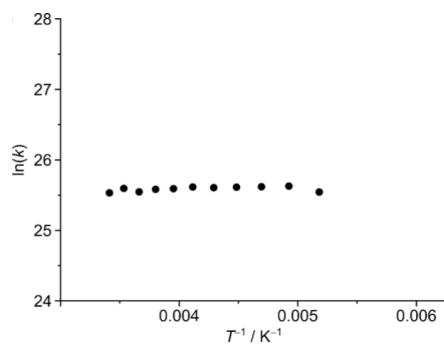


Fig. S44. $\ln(k)$ vs. $1/T$ plot of $trans\text{-[Fe(pdmi)}_2\text{][PF}_6\text{]}_2$ in MeOH/EtOH (2:3 v/v).

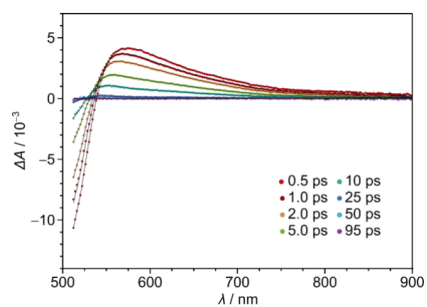


Fig. S45. TA spectra of *cis*-[Fe(pdmi)₂][PF₆]₂ in MeOH/EtOH (2:3 v/v) at 293 K ($\lambda_{\text{exc}} = 470$ nm), rebinned data vs. fit.

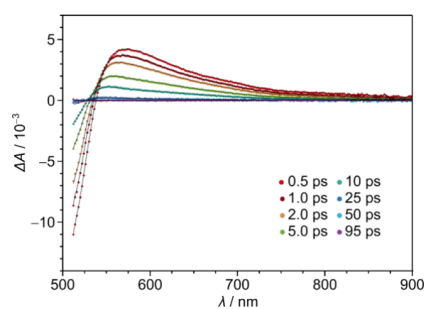


Fig. S46. TA spectra of *cis*-[Fe(pdmi)₂][PF₆]₂ in MeOH/EtOH (2:3 v/v) at 283 K ($\lambda_{\text{exc}} = 470$ nm), rebinned data vs. fit.

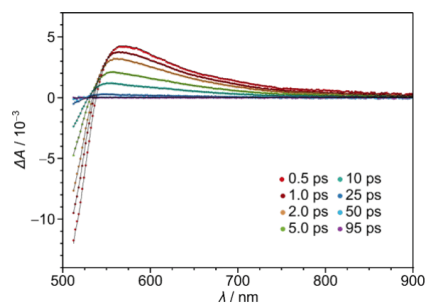


Fig. S47. TA spectra of *cis*-[Fe(pdmi)₂][PF₆]₂ in MeOH/EtOH (2:3 v/v) at 273 K ($\lambda_{\text{exc}} = 470$ nm), rebinned data vs. fit.

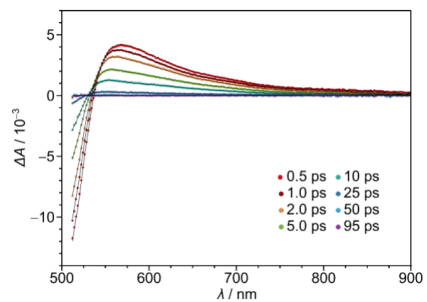


Fig. S48. TA spectra of *cis*-[Fe(pdmi)₂][PF₆]₂ in MeOH/EtOH (2:3 v/v) at 263 K ($\lambda_{\text{exc}} = 470$ nm), rebinned data vs. fit.

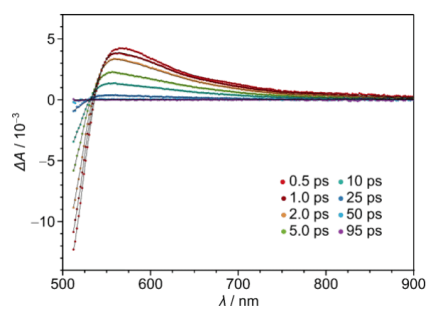


Fig. S49. TA spectra of *cis*-[Fe(pdmi)₂][PF₆]₂ in MeOH/EtOH (2:3 v/v) at 253 K ($\lambda_{\text{exc}} = 470$ nm), rebinned data vs. fit.

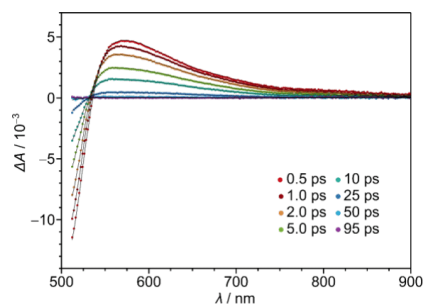


Fig. S50. TA spectra of *cis*-[Fe(pdmi)₂][PF₆]₂ in MeOH/EtOH (2:3 v/v) at 243 K ($\lambda_{\text{exc}} = 470$ nm), rebinned data vs. fit.

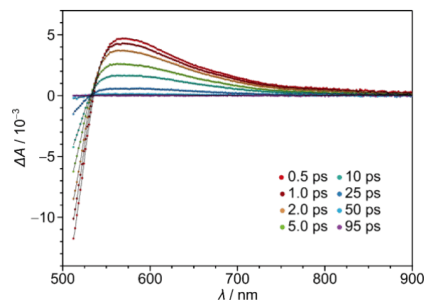


Fig. S51. TA spectra of *cis*-[Fe(pdmi)₂][PF₆]₂ in MeOH/EtOH (2:3 v/v) at 233 K ($\lambda_{\text{exc}} = 470$ nm), rebinned data vs. fit.

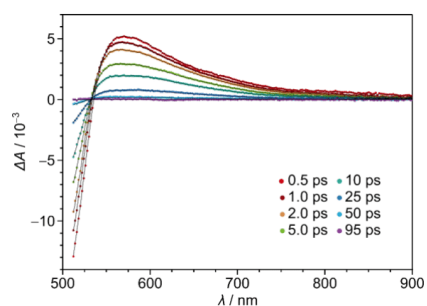


Fig. S52. TA spectra of *cis*-[Fe(pdmi)₂][PF₆]₂ in MeOH/EtOH (2:3 v/v) at 223 K ($\lambda_{\text{exc}} = 470$ nm), rebinned data vs. fit.

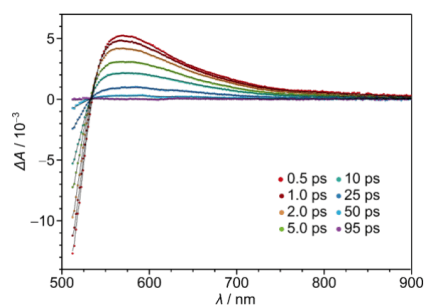


Fig. S53. TA spectra of *cis*-[Fe(pdmi)₂][PF₆]₂ in MeOH/EtOH (2:3 v/v) at 213 K ($\lambda_{\text{exc}} = 470$ nm), rebinned data vs. fit.

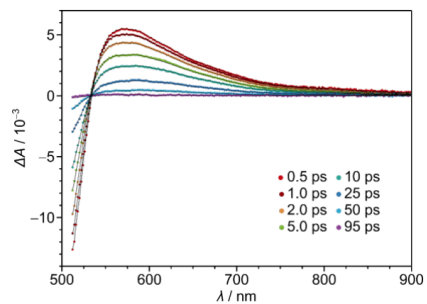


Fig. S54. TA spectra of *cis*-[Fe(pdmi)₂][PF₆]₂ in MeOH/EtOH (2:3 v/v) at 203 K ($\lambda_{\text{exc}} = 470$ nm), rebinned data vs. fit.

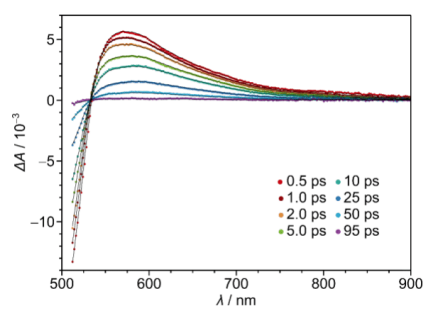


Fig. S55. TA spectra of *cis*-[Fe(pdmi)₂][PF₆]₂ in MeOH/EtOH (2:3 v/v) at 193 K ($\lambda_{\text{exc}} = 470$ nm), rebinned data vs. fit.

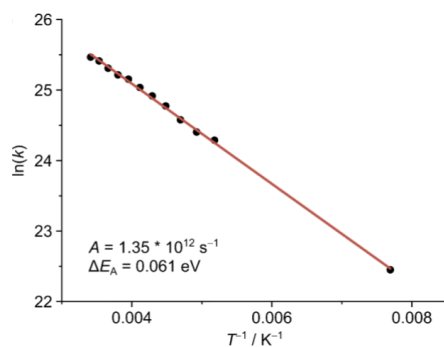


Fig. S56. $\ln(k)$ vs. $1/T$ plot of *cis*-[Fe(pdmi)₂][PF₆]₂ in MeOH/EtOH (2:3 v/v).

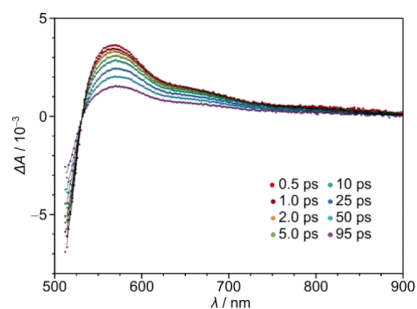


Fig. S57. TA spectra of *cis*-[Fe(pdmi)₂][PF₆]₂ in MeOH/EtOH (2:3 v/v) at 130 K ($\lambda_{exc} = 470$ nm), rebinned data vs. fit.

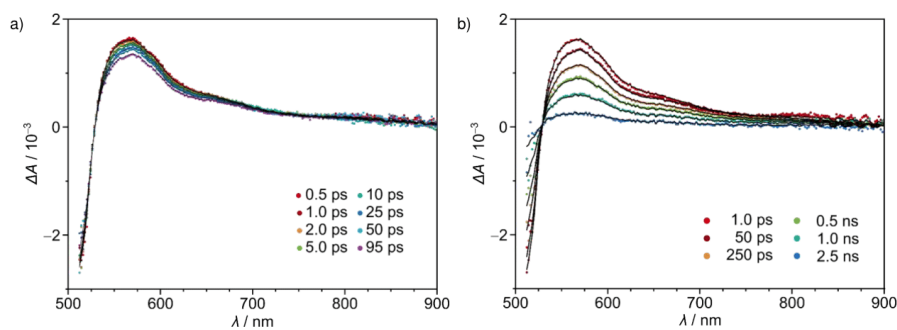


Fig. S58. TA spectra of *cis*-[Fe(pdmi)₂][PF₆]₂ in MeOH/EtOH (2:3 v/v) at 77 K ($\lambda_{exc} = 470$ nm), rebinned data vs. fit on a) short time scales (for better comparison with the spectra a higher temperature) and b) longer time scales.

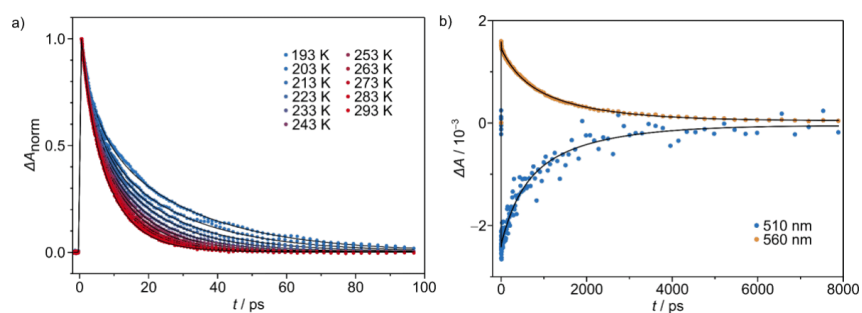


Fig. S59. Decay traces of *cis*-[Fe(pdmi)₂][PF₆]₂ at observed at 560 nm in MeOH/EtOH (2:3 v/v) a) at 193 – 293 K and b) at 77 K observed at 510 and 560 nm.

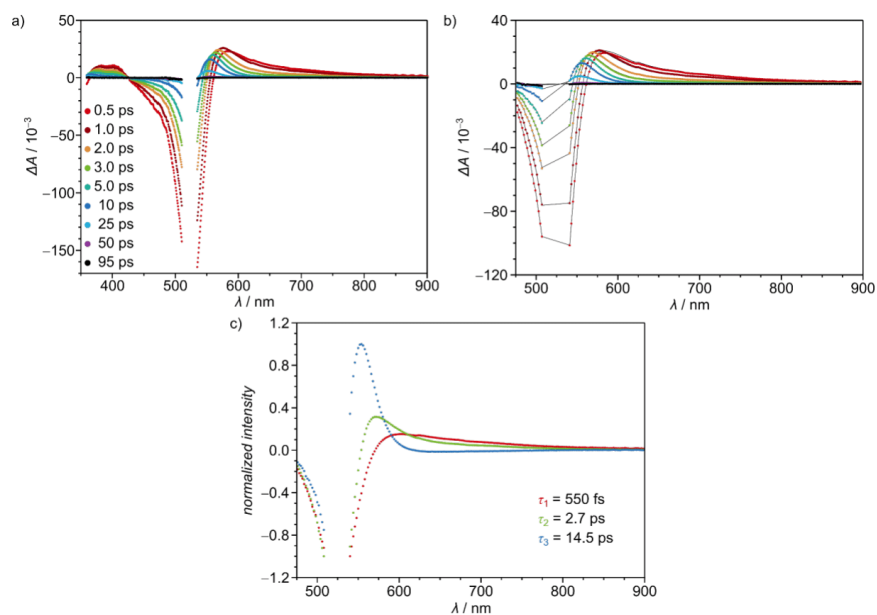


Fig. S60. a) TA spectra of *trans*-[Fe(pdmi)₂][PF₆]₂ in CH₃CN at 293 K (λ_{exc} = 520 nm), b) rebinned data vs. fit and c) EADS from a global fit.

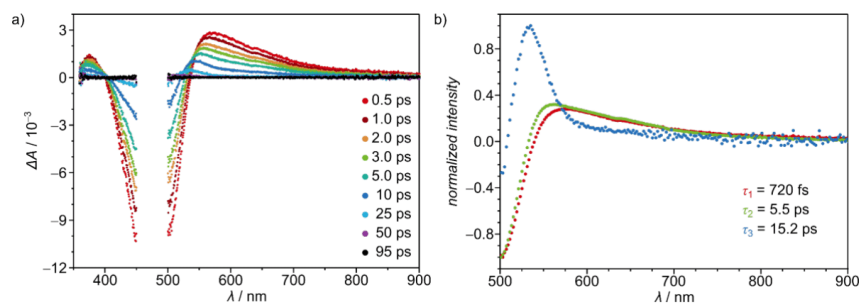


Fig. S61. a) TA spectra of *cis*-[Fe(pdmi)₂][PF₆]₂ in CH₃CN at 293 K (λ_{exc} = 470 nm) and b) EADS from a global fit.

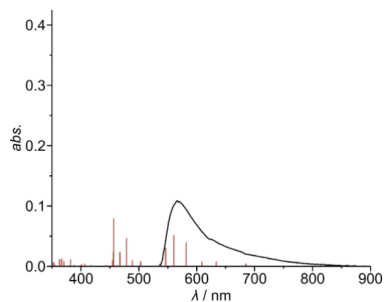


Fig. S62. TA spectrum (0 – 5 ps) minus GS spectrum of *trans*-[Fe(pdmi)₂][PF₆]₂ in MeOH/EtOH (2:3 v/v) at 293 K and DFT calculated triplet transitions of the ³MLCT state of *trans*-[Fe(pdmi)₂]²⁺ shown as sticks (bathochromically shifted by 3600 cm⁻¹).

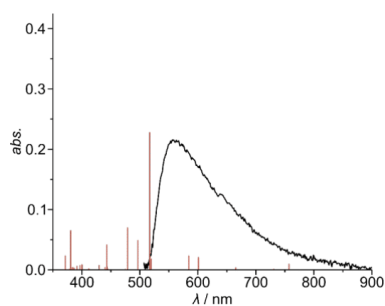


Fig. S63. TA spectrum (0 – 5 ps) minus GS spectrum of *cis*-[Fe(pdmi)₂][PF₆]₂ in MeOH/EtOH (2:3 v/v) at 293 K and DFT calculated triplet transitions of the ³MLCT state of *cis*-[Fe(pdmi)₂]²⁺ shown as sticks (bathochromically shifted by 3600 cm⁻¹).

5. References

- [1] C. Müller, T. Pascher, A. Eriksson, P. Chabera, J. Uhlig, *J. Phys. Chem. A* **2022**, *126*, 4087–4099.
- [2] F. Neese, *WIREs Comput. Mol. Sci.* **2018**, *8*, e1327.
- [3] A. D. Becke, *J. Chem. Phys.* **1993**, *98*, 5648–5652.
- [4] C. Lee, W. Yang, R. G. Parr, *Phys. Rev. B* **1988**, *37*, 785–789.
- [5] B. Miehlich, A. Savin, H. Stoll, H. Preuss, *Chem. Phys. Lett.* **1989**, *157*, 200–206.
- [6] D. A. Pantazis, X.-Y. Chen, C. R. Landis, F. Neese, *J. Chem. Theory Comput.* **2008**, *4*, 908–919.
- [7] F. Weigend, R. Ahlrichs, *Phys. Chem. Chem. Phys.* **2005**, *7*, 3297–3305.
- [8] F. Neese, F. Wennmohs, A. Hansen, U. Becker, *Chem. Phys.* **2009**, *356*, 98–109.
- [9] R. Izsák, F. Neese, *J. Chem. Phys.* **2011**, *135*, 144105.
- [10] S. Miertuš, E. Scrocco, J. Tomasi, *Chem. Phys.* **1981**, *55*, 117–129.
- [11] V. Barone, M. Cossi, *J. Phys. Chem. A* **1998**, *102*, 1995–2001.
- [12] S. Grimme, J. Antony, S. Ehrlich, H. Krieg, *J. Chem. Phys.* **2010**, *132*, 154104.
- [13] S. Grimme, S. Ehrlich, L. Goerigk, *J. Comput. Chem.* **2011**, *32*, 1456–1465.
- [14] S. Mai, F. Plasser, J. Dorn, M. Fumanal, C. Daniel, L. González, *Coord. Chem. Rev.* **2018**, *361*, 74–97.
- [15] F. Plasser, Theodore 2.0, <http://theodore-qc.sourceforge.net>.
- [16] STOE & Cie, X-Area, STOE & Cie GmbH, Darmstadt, Germany.
- [17] R. H. Blessing, *Acta Crystallogr., Sect. A* **1995**, *51*, 33–38.
- [18] A. L. Spek, *Acta Crystallogr., Sect. D* **2009**, *65*, 148–155.
- [19] J. Koziskova, F. Hahn, J. Richter, J. Kožíšek, *Acta Chim. Slovaca* **2016**, *9*, 136–140.
- [20] STOE & Cie, X-Area LANA, STOE & Cie GmbH, Darmstadt, Germany.
- [21] G. M. Sheldrick, *Acta Crystallogr., Sect. A* **2015**, *71*, 3–8.
- [22] G. M. Sheldrick, *Acta Crystallogr., Sect. C* **2015**, *71*, 3–8.
- [23] G. M. Sheldrick, *Acta Crystallogr., Sect. A* **2008**, *64*, 112–122.
- [24] C. B. Hübschle, G. M. Sheldrick, B. Dittrich, *J. Appl. Crystallogr.* **2011**, *44*, 1281–1284.

6.4 Supporting Information for Section 3.2 "Ground- and Excited-State Properties of Iron(II) Complexes Linked to Organic Chromophores"

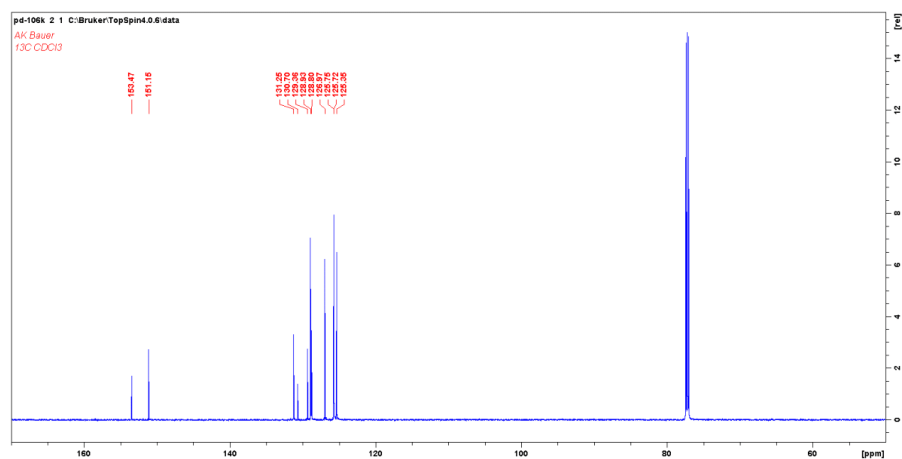
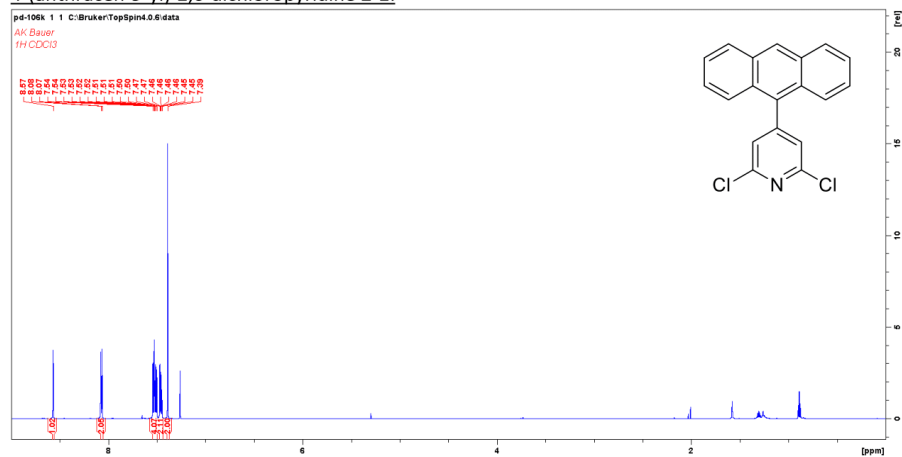
Supporting Information

Table of Content

NMR spectra and MS data.....	2
Computational Chemistry	14
Electrochemistry.....	21
Electrochemical data of [C0]²⁺	21
Electrochemical data of [C1]²⁺	22
Electrochemical data of [C2]²⁺	24
Cyclic voltammetry of [H₂-L0]²⁺ , [H₂-L1]²⁺ and [H₂-L2]²⁺	26
Cyclic voltammetry of anthracene and pyrene	27
Spectroelectrochemical data of [C1]²⁺	28
Spectroelectrochemical data of [C2]²⁺	29
Luminescence Properties	30
Singlet Oxygen Experiments.....	33
References.....	34

NMR spectra and MS data

4-(anthracen-9-yl)-2,6-dichloropyridine 2-1:



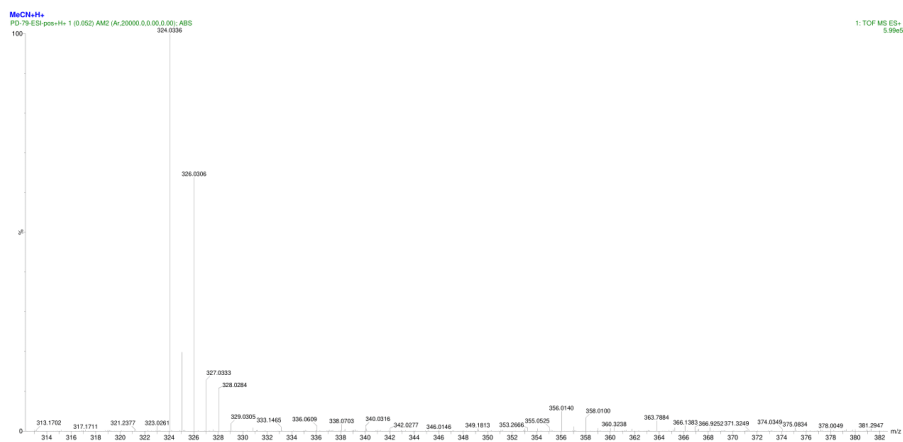


Figure S 3: ESI-MS of 4-(anthracen-9-yl)-2,6-dichloropyridine 2-1 in MeCN.

2,6-dichloro-4-(pyren-1-yl)pyridine 2-2:

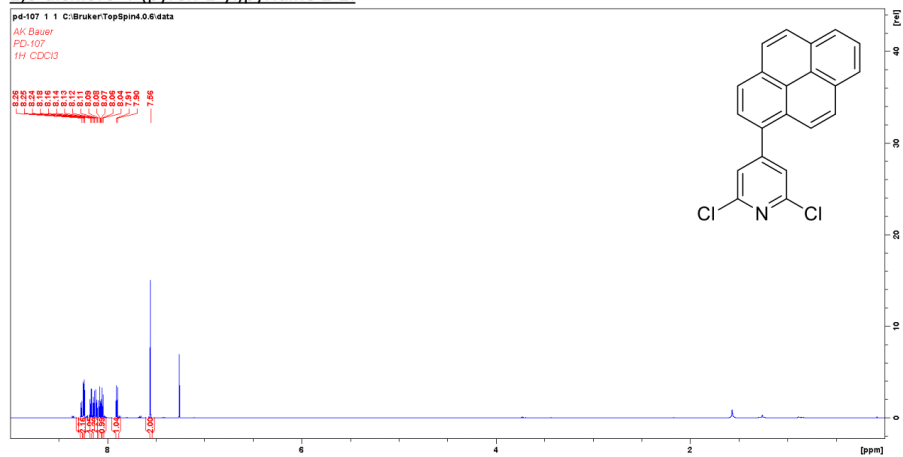


Figure S 4: ¹H-NMR of 2,6-dichloro-4-(pyren-1-yl)pyridine 2-2 in CDCl₃.

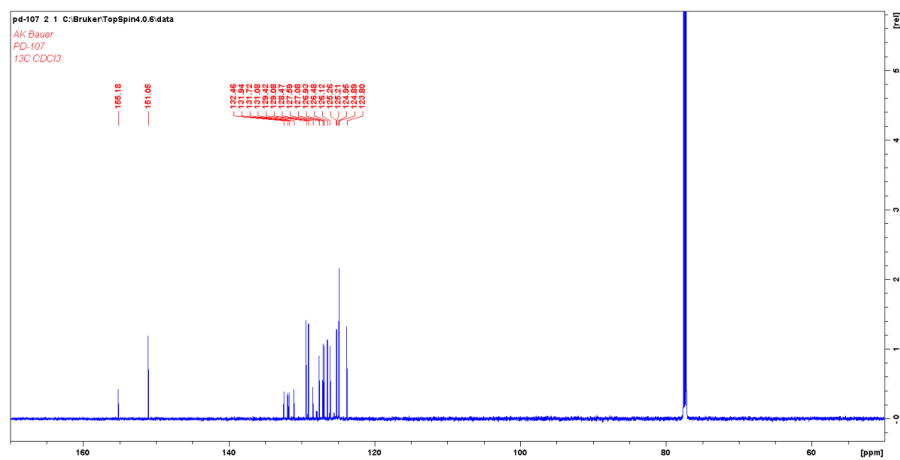


Figure S 5: ^{13}C -NMR of 2,6-dichloro-4-(pyren-1-yl)pyridine 2-2 in CDCl_3 .

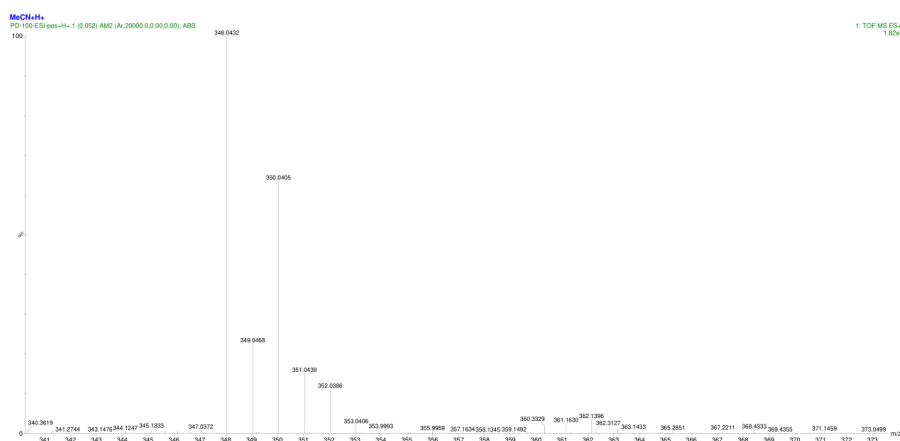


Figure S 6: ESI-MS of 2,6-dichloro-4-(pyren-1-yl)pyridine 2-2 in MeCN.

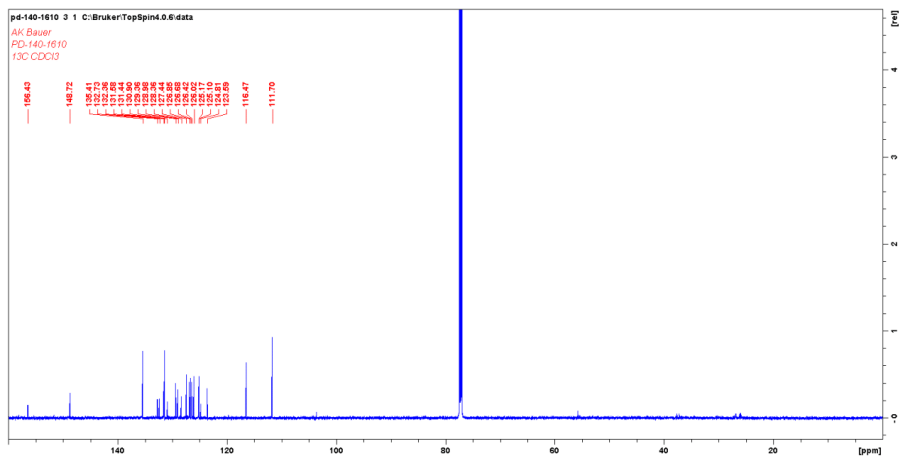


Figure S 11: ^{13}C -NMR of 2,6-di(1H-imidazol-1-yl)-4-(pyren-1-yl)pyridine 3-2 in CDCl_3 .

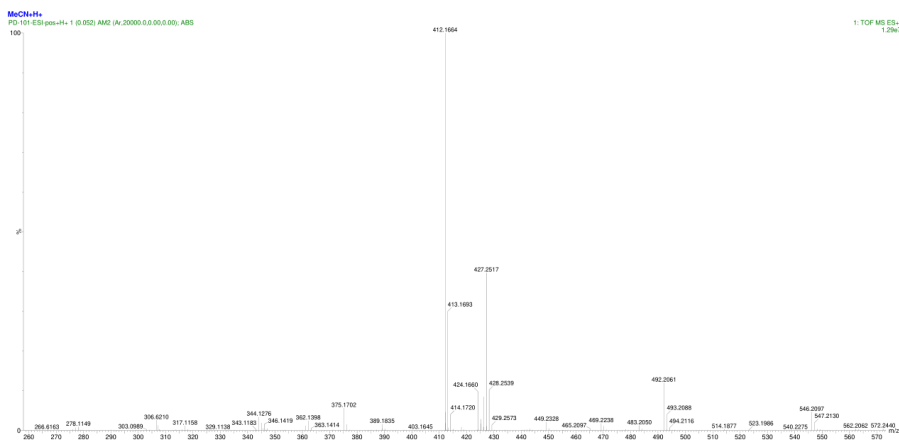
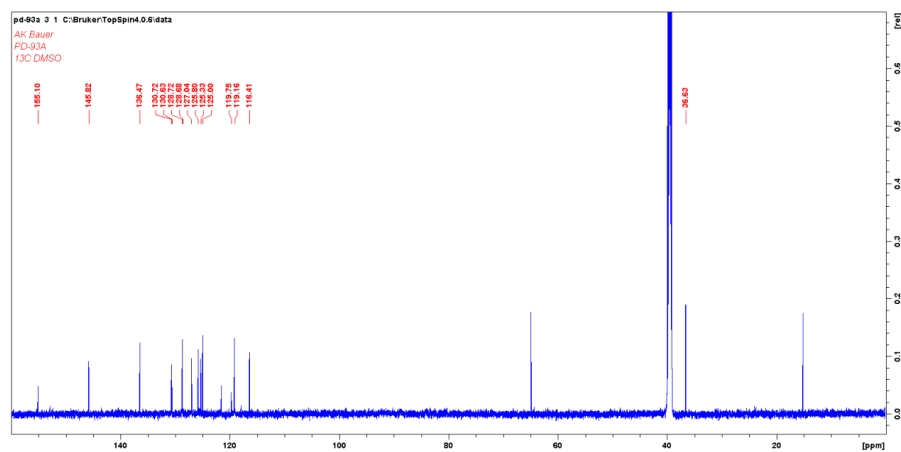
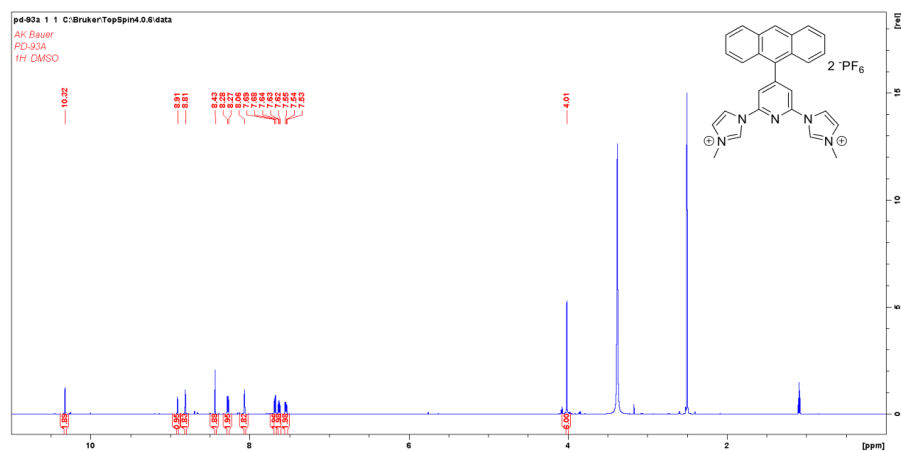


Figure S 12: ESI-MS of 2,6-di(1H-imidazol-1-yl)-4-(pyren-1-yl)pyridine 3-2 in MeCN.

1,1'-(4-(anthracen-9-yl)pyridine-2,6-diyl)bis(3-methyl-1H-imidazol-3-ium) [H₂-L1](PF₆)₂:

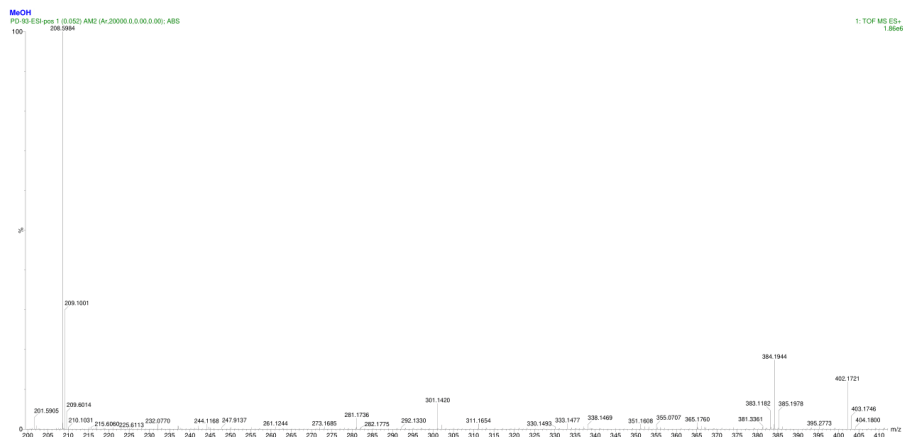


Figure S 15: ESI-MS of 1,1'-(4-(anthracen-9-yl)pyridine-2,6-diyl)bis(3-methyl-1H-imidazol-3-ium) [H₂-L1](PF₆)₂ in MeOH.

1,1'-(4-(pyren-1-yl)pyridine-2,6-diyl)bis(3-methyl-1H-imidazol-3-ium) [H₂-L2](PF₆)₂:

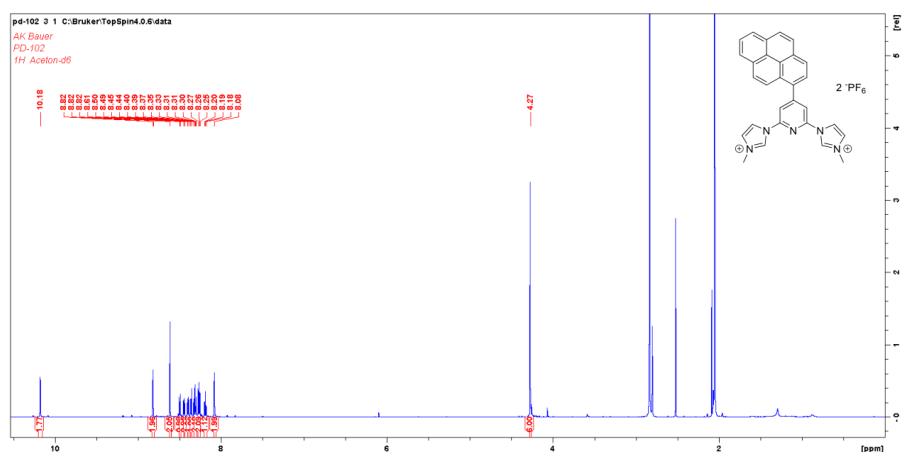
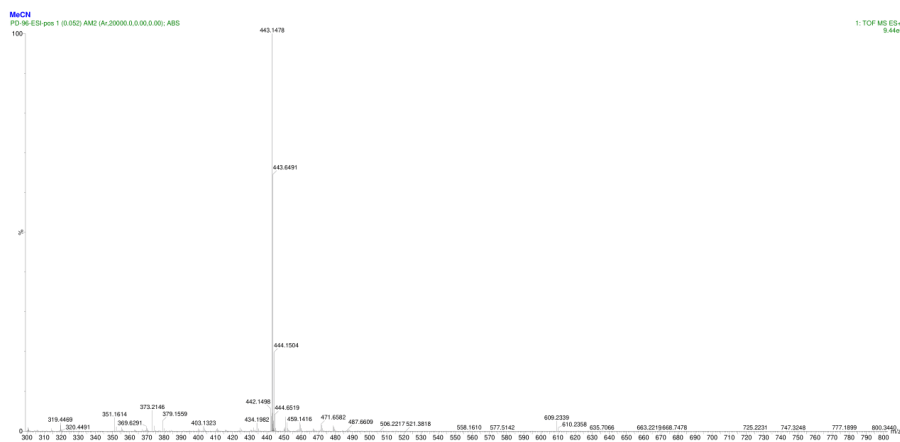
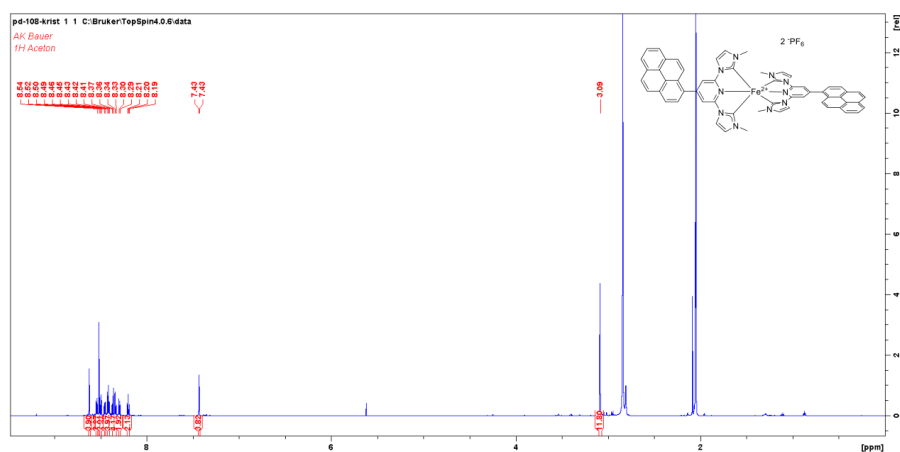


Figure S 16: ¹H-NMR of 1,1'-(4-(pyren-1-yl)pyridine-2,6-diyl)bis(3-methyl-1H-imidazol-3-ium) [H₂-L2](PF₆)₂ in d₆-acetone.

Figure S 21: ESI-MS of $[\text{Fe}(\text{bim-ant})_2](\text{PF}_6)_2$ [C1](PF_6)₂ in MeCN. **$[\text{Fe}(\text{bim-pyr})_2](\text{PF}_6)_2$ [C2](PF_6)₂:**Figure S 22: $^1\text{H-NMR}$ of $[\text{Fe}(\text{bim-pyr})_2](\text{PF}_6)_2$ [C2](PF_6)₂ d_6 -acetone.

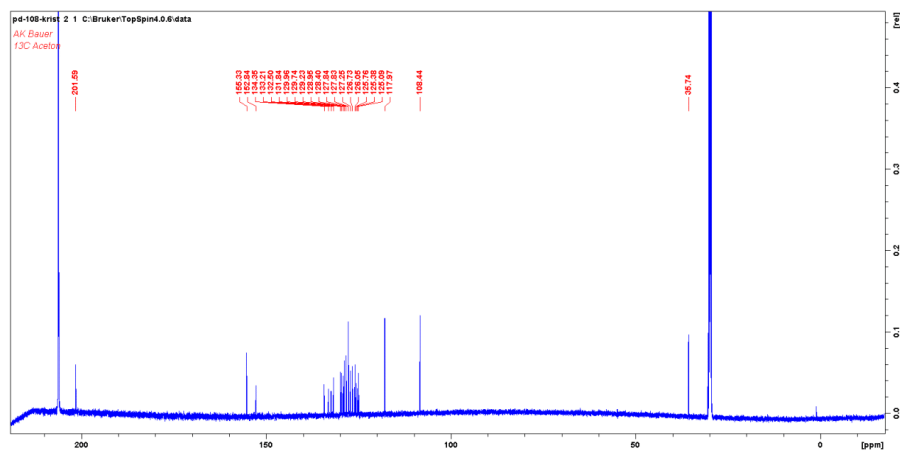


Figure S 23: ^{13}C -NMR of $[\text{Fe}(\text{bim-pyr})_2](\text{PF}_6)_2 [\text{C}2](\text{PF}_6)_2$ in d_6 -acetone.

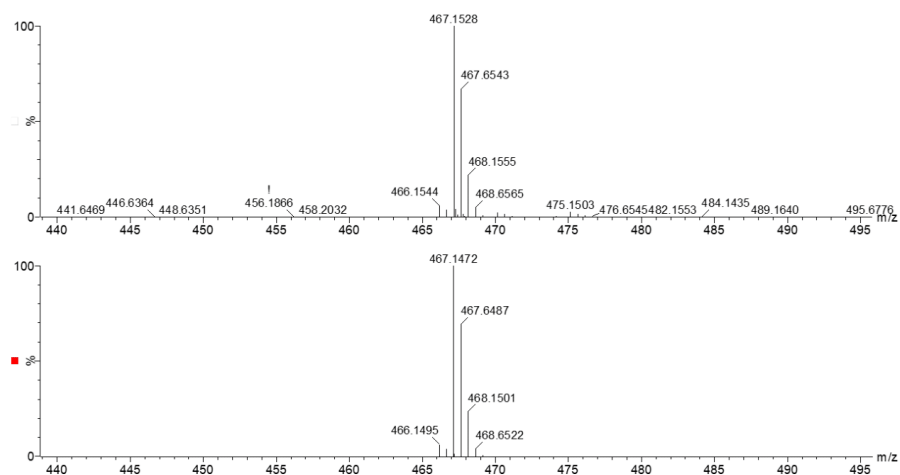


Figure S 24: Observed isotope pattern for $[\text{Fe}(\text{bim-pyr})_2](\text{PF}_6)_2 [\text{C}2](\text{PF}_6)_2$ in MeCN (top) and calculated isotope pattern for $\text{C}_{58}\text{H}_{42}\text{FeN}_{10}^{2+}$ (bottom). Intensities are given in relation to the most intensive signal.

Computational Chemistry

Table S 1: Optimal range-separation parameters for LC-BLYP calculations as obtained using the protocol described in literature.¹

compound	α	ω , Bohr ⁻¹
[C0] ²⁺	0.00	0.15
anthracene	0.50	0.12
pyrene	0.40	0.15

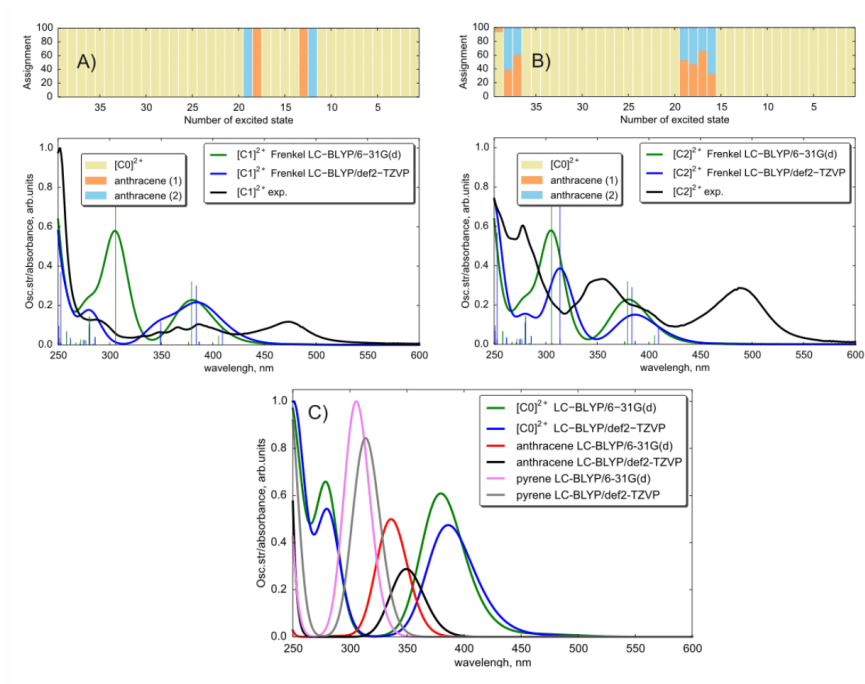


Figure S 25: Absorption spectra of [C1]²⁺ (panel A) and [C2]²⁺ (panel B) modeled with Frenkel exciton approach compared with experiment. The spectra of [C0]²⁺, anthracene, and pyrene computed with LC-BLYP/def2-TZVP and LC-BLYP/6-31G(d) are shown in panel C. The assignment in the upper parts of panels A) and B) corresponds to the larger basis set.

Appendix

Table S 2: Assignment of absorption spectrum of [CO]²⁺.

LC-BLYP/6-31G(d)										LC-BLYP/def2-TZVP									
state number	E, ev	wavelength, nm	osc.str.	% MC	% LC	% MLCT	% LMCT	% LLCT	state number	E, ev	wavelength, nm	osc.str.	% MC	% LC	% MLCT	% LMCT	% LLCT		
1	2,634	470,711	0,003	6,4	20,1	55,1	3,9	14,6	1	2,691	460,74	0,002	5,9	21,3	53,8	3,9	15,2		
2	2,635	470,532	0,003	6,4	20,1	55,1	3,9	14,6	2	2,692	460,569	0,002	5,9	21,3	53,8	3,9	15,2		
3	2,867	432,456	0	7,6	7,1	68,2	2,4	14,6	3	2,848	435,341	0	7,1	7,9	67,2	2,5	15,3		
4	2,924	424,026	0	10,2	7,1	64,8	3,9	14	4	2,911	425,92	0	8,9	7,9	64,7	3,5	14,9		
5	3,057	405,578	0,04	4,7	18,1	65,5	1,6	10,2	5	3,031	409,057	0,072	5,1	18,5	64,7	1,9	9,7		
6	3,074	403,335	0	6,9	18,3	60,3	3,4	11,1	6	3,05	406,509	0	6,3	19,4	59	3,4	11,9		
7	3,272	378,928	0,283	2,7	18,9	63,5	1	14	7	3,205	386,849	0,017	6,8	18,3	64	2,6	8,3		
8	3,292	376,626	0,015	9,6	16,9	62,9	3,4	7,3	8	3,207	386,608	0,017	6,6	18,5	64,1	2,5	8,3		
9	3,295	376,283	0,016	9,3	17,1	63,2	3,2	7,2	9	3,236	383,143	0,253	1,6	20,6	61,4	0,7	15,8		
10	3,393	365,415	0,001	5,6	8,4	69,5	1,8	14,7	10	3,32	373,449	0,001	3,5	9	70,2	1,2	16,1		
11	3,394	365,307	0,001	5,7	8,4	69,4	1,8	14,6	11	3,321	373,337	0,001	3,5	9,1	70,2	1,2	16,1		
12	3,546	349,648	0,003	43,5	5,3	31,3	14,1	5,9	12	3,554	348,861	0,002	45,1	5,2	28,4	15,8	5,5		
13	3,547	349,549	0,003	43,2	5,3	31,6	14	5,9	13	3,554	348,861	0,002	45,1	5,2	28,4	15,8	5,5		
14	3,727	332,668	0	3,3	18,1	61,5	2,4	14,7	14	3,651	339,592	0	3,1	19	60,4	2,2	15,2		
15	3,798	326,449	0	37,3	7,1	23,6	24,4	7,6	15	3,876	319,879	0	35,2	8,1	23,8	24,6	8,4		
16	4,209	294,572	0	36,6	8	27,8	20	7,7	16	4,293	288,808	0	36,5	8,2	26,3	21,2	7,9		
17	4,365	284,044	0,007	1	51,1	15,4	7,9	24,6	17	4,338	285,812	0,043	0,5	59,1	6,4	8,5	25,5		
18	4,365	284,044	0,006	1,1	50,6	16,1	7,8	24,5	18	4,339	285,746	0,043	0,5	59	6,7	8,4	25,4		
19	4,421	280,446	0,148	3,2	31,4	40,7	4,5	20,2	19	4,423	280,319	0,116	0,3	28,4	51,7	1,1	18,5		
20	4,423	280,319	0,144	3,4	30,3	42,1	4,4	19,8	20	4,426	280,129	0,113	0,3	28,2	52	1	18,5		
21	4,519	274,364	0,023	0,3	71	5,8	9,2	13,7	21	4,48	276,753	0,022	0,2	67,6	9,7	8,2	14,3		
22	4,546	272,735	0	3,7	23,3	61,9	2,2	8,9	22	4,495	275,829	0	0,2	22,9	66,1	0,5	10,3		
23	4,56	271,897	0,025	4,1	22,5	62,1	2,2	9,1	23	4,505	275,217	0,025	0,3	27,3	60	1,5	11		
24	4,573	271,124	0	4,6	7,6	70,7	1,6	15,6	24	4,531	273,638	0	0,2	9,1	73,4	0,1	17,1		
25	4,575	271,006	0	4,6	7,6	70,4	1,6	15,7	25	4,532	273,577	0	0,3	9,1	73,2	0,2	17,2		

15

26	4,614	268,715	0	0,8	71,4	7,8	8,3	11,7	26	4,569	271,362	0,009	20,9	11,7	50	7,5	9,9
27	4,638	267,325	0,012	23,3	10,9	48,7	8	9,1	27	4,57	271,302	0,009	20,8	12	49,6	7,6	10
28	4,638	267,325	0,012	23,4	10,8	48,6	8	9,2	28	4,572	271,184	0	0,6	72,2	6,3	8,3	12,6
29	4,703	263,63	0	0,6	20,4	4	9,6	65,4	29	4,672	265,379	0	0,8	22,2	4,4	9	63,7
30	4,737	261,738	0	0,5	19,3	4,2	9,6	66,4	30	4,7	263,798	0	0,5	21,3	4,8	8,9	64,4
31	4,801	258,249	0,069	1,4	67,4	2,6	8,1	20,6	31	4,732	262,014	0,036	1,1	67,4	2,3	7,5	21,7
32	4,801	258,249	0,07	1,4	67,4	2,5	8,2	20,6	32	4,732	262,014	0,036	1,1	67,3	2,3	7,5	21,8
33	4,973	249,317	0,005	19,2	16,7	39,2	10,4	14,4	33	4,907	252,67	0,015	21	19,3	32	11,7	16
34	4,974	249,267	0,005	19,5	16,5	39,3	10,4	14,3	34	4,909	252,567	0,015	21,2	19,3	31,9	11,7	15,9
35	5,009	247,525	0,275	0,4	47	5	9,6	38	35	4,911	252,464	0,345	0,1	49,3	6,7	8,6	35,3
36	5,012	247,377	0,005	4	35,5	19,4	4	37	36	4,925	251,747	0	4,1	41,1	16,9	3,5	34,3
37	5,024	246,786	0,081	5,4	56,6	13,5	7,5	17	37	4,933	251,338	0	9,7	18,1	47,2	7	18
38	5,025	246,737	0,081	5,4	56,6	13,4	7,5	17,1	38	4,943	250,83	0,093	8	49,3	16,7	8,1	17,8
39	5,145	240,982	0	5,2	37,4	30,6	5,9	20,9	39	4,944	250,779	0,094	7,8	49,5	16,5	8	18,1
40	5,187	239,031	0,008	0,2	18,8	4,1	4,8	72,2	40	5,05	245,515	0	6	36,5	31	7,1	19,3

16

Table S 3: Assignment of absorption spectra of [C1]²⁺ and [C2]²⁺ computed with LC-BLYP/6-31G(d).

[C1] ²⁺							[C2] ²⁺										
state number	E, ev	wavelength, nm	osc.str.	% MC	% LC	% MLCT	% LMCT	% LLCT	state number	E, ev	wavelength, nm	osc.str.	% MC	% LC	% MLCT	% LMCT	% LLCT
1	2,604	476,134	0,002	6,3	20,4	54,8	3,8	14,7	1	2,577	481,122	0,002	6	20,7	54,8	3,7	14,8
2	2,609	475,221	0,002	6,3	20,4	54,8	3,9	14,6	2	2,586	479,448	0,002	6,2	20,6	54,7	3,8	14,7
3	2,839	436,721	0,001	7,5	7,2	67,8	2,5	15	3	2,802	442,488	0,006	7,3	7,3	67,4	2,5	15,5
4	2,898	427,83	0	9,9	7,1	64,6	3,8	14,5	4	2,863	433,06	0	9,4	7,2	64,6	3,6	15,1
5	2,973	417,037	0,456	4,7	33,6	52,3	2,4	7	5	2,896	428,126	1,016	5,1	32,1	53,4	2,8	6,7
6	3,027	409,598	0,001	6,3	24,1	55,8	3,5	10,4	6	2,995	413,974	0	6,2	24,6	55,7	3,5	10
7	3,116	397,899	0,465	0	53,3	35,9	0,9	10	7	3,146	394,104	0,677	0	31,4	53,4	0,5	14,7
8	3,173	390,751	0,01	0,4	90,2	5,4	2	1,9	8	3,228	384,093	0,015	7,4	20,6	62	2,9	7,1
9	3,245	382,081	0,015	7,4	19,7	63	2,8	7,2	9	3,234	383,38	0,013	6,3	21,5	62,7	2,5	7,1
10	3,248	381,728	0,013	7,1	19,6	63,5	2,7	7,2	10	3,318	373,674	0,005	0,7	82,8	9,6	3,3	3,6
11	3,285	377,428	0,028	2,3	50,3	38,3	1,3	7,8	11	3,343	370,88	0,001	5,7	8,1	68,6	1,9	15,8
12	3,351	369,995	0	5,7	7,9	69	1,9	15,5	12	3,345	370,658	0	5,6	7,9	68,6	1,8	16,1
13	3,354	369,664	0,001	5,4	8	69,4	1,8	15,4	13	3,426	361,895	0,292	1,7	70,5	20,8	2,8	4,2
14	3,446	359,795	0,011	0,1	90,7	0,9	5,7	2,6	14	3,531	351,133	0,002	45,4	5,2	28,7	15,2	5,5
15	3,463	358,028	0,017	0,1	90,5	1,3	5,5	2,5	15	3,537	350,538	0,003	43,8	5,9	29,6	14,8	5,8
16	3,539	350,34	0,002	44,8	5,4	29,5	14,8	5,6	16	3,653	339,406	0	0,8	76,3	17,3	1,2	4,4
17	3,542	350,043	0,002	45	5,3	29,4	14,8	5,5	17	3,669	337,926	0,036	0,3	96,7	1,8	0,7	0,5
18	3,69	336,003	0	3,2	19,8	60,2	2,4	14,4	18	3,702	334,914	0,001	2,1	46,1	40,2	1,7	9,9
19	3,768	329,048	0,001	0,1	96,8	1,2	1,5	0,4	19	3,8	326,277	0	37,1	7,2	23,3	24,4	7,9
20	3,773	328,612	0,001	0,1	96,4	1,6	1,4	0,5	20	3,971	312,227	0,046	0,1	88,9	5,6	3,3	2,2
21	3,8	326,277	0	37,3	7,1	23,3	24,5	7,8	21	3,972	312,148	0,066	0,1	88,7	5,7	3,3	2,2
22	3,926	315,805	0,012	0,1	81,5	13,4	1	4	22	4,091	303,068	0,049	1,7	25,7	54,9	1,2	16,5
23	3,931	315,404	0,01	0,1	77,6	16,6	0,9	4,8	23	4,113	301,447	0,044	1,8	26,1	54,6	1,2	16,3

17

24	3,955	313,49	0,003	0,2	47,6	40,1	0,4	11,7	24	4,161	297,97	0,011	0,5	85,3	8,8	2,7	2,6
25	3,96	313,094	0,005	0,1	51,4	37,1	0,4	10,9	25	4,162	297,898	0,004	0,5	85,2	8,9	2,7	2,7
26	4,117	301,154	0,003	0,3	26,9	65	0,1	7,7	26	4,207	294,712	0	35,9	8,1	28,3	19,8	7,9
27	4,118	301,081	0	0,3	26,7	65	0,1	7,8	27	4,26	291,045	0,195	1,8	44,3	39,5	2,9	11,5
28	4,203	294,992	0	36	8,1	28,2	19,9	7,9	28	4,262	290,908	0,024	1,8	43	42,1	2,6	10,6
29	4,306	287,936	0,017	0,7	57,4	9,3	8,1	24,5	29	4,283	289,482	0,046	0,8	59	15,7	5,9	18,7
30	4,315	287,335	0,016	0,7	57,1	9,4	8,2	24,6	30	4,287	289,212	0,033	0,7	60,4	13,3	6,4	19,2
31	4,332	286,208	0	0,9	7,7	71,1	0,3	19,9	31	4,325	286,671	0,012	2,7	10,7	66,5	1,1	19
32	4,34	285,68	0	0,7	7,7	70,9	0,3	20,4	32	4,333	286,142	0	3	8,7	68,1	1,2	18,9
33	4,388	282,555	0,086	3,3	28,2	46,5	3,5	18,5	33	4,346	285,286	0,003	0,1	94,6	2	1,5	1,8
34	4,404	281,529	0,104	3,4	27,1	48,2	3,4	18	34	4,346	285,286	0,003	0,1	94,6	1,9	1,5	1,8
35	4,47	277,372	0,033	0,2	73,7	3,3	9,2	13,6	35	4,413	280,954	0,457	0,1	92,2	4	2,1	1,6
36	4,515	274,607	0	3	28,8	55,9	2,8	9,5	36	4,417	280,7	0,012	0,1	93,3	3	2,1	1,5
37	4,531	273,638	0,036	3,8	21,2	63,9	1,9	9,2	37	4,435	279,561	0,011	0,2	75,9	2,9	8,5	12,4
38	4,535	273,396	0	0,1	5,1	1,3	8,9	84,7	38	4,445	278,932	0,043	0,1	94,7	2,6	1,5	1,2
39	4,548	272,615	0	0,1	5,1	1,6	9	84,2	39	4,445	278,932	0,044	0,1	94,9	2,5	1,5	1,1
40	4,558	272,017	0	1,2	65,7	14,3	7,3	11,4	40	4,504	275,278	0	0,3	76,2	4,1	8,2	11,1

18

Appendix

Table S 4: Assignment of absorption spectra of [C1]²⁺ and [C2]²⁺ computed with Frenkel exciton approach.

State number	[C1] ²⁺ based on LC-BLYP/6-31G(d)					[C1] ²⁺ based on LC-BLYP/def2-TZVP					[C2] ²⁺ based on LC-BLYP/6-31G(d)					[C2] ²⁺ based on LC-BLYP/def2-TZVP				
	wavelength, nm	osc.str.	% [CO] ²⁺	% ant1	% ant2	wavelength, nm	osc.str.	% [CO] ²⁺	% ant1	% ant1	wavelength, nm	osc.str.	% [CO] ²⁺	% pyr1	% pyr1	wavelength, nm	osc.str.	% [CO] ²⁺	% pyr1	% pyr1
1	470,73	0,003	1	0	0	460,77	0,0021	1	0	0	470,73	0,0031	1	0	0	460,77	0,0022	1	0	0
2	470,5	0,0027	1	0	0	460,59	0,0019	1	0	0	470,5	0,0028	1	0	0	460,59	0,002	1	0	0
3	432,47	0	1	0	0	435,33	0	1	0	0	432,47	0	1	0	0	435,33	0	1	0	0
4	424,08	0	1	0	0	425,93	0	1	0	0	424,08	0	1	0	0	425,93	0	1	0	0
5	405,61	0,0473	1	0	0	409,25	0,0865	1	0	0	405,58	0,0462	1	0	0	409,18	0,084	1	0	0
6	403,36	0	1	0	0	406,54	0	1	0	0	403,36	0	1	0	0	406,54	0	1	0	0
7	379,6	0,3285	0,99	0,01	0	386,83	0,0163	1	0	0	379,3	0,3212	1	0	0	386,83	0,0176	1	0	0
8	376,59	0,0149	1	0	0	386,64	0,0158	1	0	0	376,59	0,0156	1	0	0	386,63	0,0163	1	0	0
9	376,35	0,0144	1	0	0	383,82	0,3013	0,99	0,01	0	376,34	0,0149	1	0	0	383,47	0,2916	1	0	0
10	365,43	0,0013	1	0	0	373,48	0,0005	1	0	0	365,43	0,0013	1	0	0	373,48	0,0005	1	0	0
11	365,36	0,0012	1	0	0	373,39	0,0006	1	0	0	365,36	0,0013	1	0	0	373,39	0,0006	1	0	0
12	349,64	0,0022	1	0	0	349,58	0,1171	0	0	1	349,64	0,0024	1	0	0	348,91	0,0017	1	0	0
13	349,55	0,0026	1	0	0	349,14	0,0751	0,02	0,98	0	349,55	0,0027	1	0	0	348,86	0,0019	1	0	0
14	336,19	0,134	0	0	1	348,91	0,0015	1	0	0	332,69	0	1	0	0	339,61	0	1	0	0
15	335,87	0,0914	0,01	0,99	0	348,86	0,0019	1	0	0	326,41	0	1	0	0	319,89	0	1	0	0
16	332,69	0	1	0	0	339,61	0	1	0	0	305,75	0,0101	0	0,4	0,6	313,9	0,0276	0	0,33	0,67
17	326,41	0	1	0	0	319,89	0	1	0	0	305,63	0,9157	0	0,6	0,4	313,8	0,8957	0	0,66	0,33
18	294,56	0	1	0	0	297,75	0,0001	0	1	0	300,11	0,0001	0	0,42	0,58	307,08	0	0	0,47	0,53
19	290,43	0	0	0,59	0,41	297,75	0	0	0	1	300,1	0,0013	0	0,58	0,42	307,06	0,004	0	0,53	0,47
20	290,41	0,0013	0	0,41	0,59	288,78	0	1	0	0	294,56	0	1	0	0	288,78	0	1	0	0
21	284,06	0,0058	1	0	0	285,88	0,0336	1	0	0	284,06	0,0071	1	0	0	285,84	0,0428	1	0	0
22	284,03	0,0062	1	0	0	285,77	0,042	1	0	0	284,03	0,0061	1	0	0	285,77	0,0419	1	0	0
23	280,52	0,1124	1	0	0	280,35	0,0906	1	0	0	280,48	0,1439	1	0	0	280,32	0,1137	1	0	0
24	280,42	0,1452	1	0	0	280,2	0,1036	1	0	0	280,34	0,144	1	0	0	280,12	0,1102	1	0	0

19

25	274,37	0,0234	1	0	0	276,73	0,0226	1	0	0	274,38	0,0261	1	0	0	276,74	0,026	1	0	0
26	272,74	0	1	0	0	275,83	0	1	0	0	272,74	0	1	0	0	275,83	0	1	0	0
27	271,89	0,0251	1	0	0	275,25	0,0256	1	0	0	271,89	0,0281	1	0	0	275,25	0,0292	1	0	0
28	271,12	0,0001	1	0	0	273,64	0	1	0	0	271,12	0,0001	1	0	0	273,64	0	1	0	0
29	270,98	0	1	0	0	273,56	0	1	0	0	270,98	0	1	0	0	273,56	0	1	0	0
30	268,73	0	1	0	0	271,34	0,0082	1	0	0	268,73	0	1	0	0	271,34	0,0089	1	0	0
31	267,33	0,0114	1	0	0	271,31	0,0064	1	0	0	267,33	0,0122	1	0	0	271,3	0,0083	1	0	0
32	267,32	0,0095	1	0	0	271,21	0	1	0	0	267,31	0,0117	1	0	0	271,21	0,0001	1	0	0
33	263,61	0	1	0	0	265,4	0	1	0	0	263,61	0	1	0	0	265,4	0	1	0	0
34	261,75	0	1	0	0	263,78	0	1	0	0	261,75	0	1	0	0	263,78	0	1	0	0
35	258,31	0,0435	1	0	0	262,08	0,0201	1	0	0	258,25	0,064	1	0	0	262,04	0,0324	1	0	0
36	258,23	0,0711	1	0	0	262,02	0,0368	1	0	0	258,23	0,0703	1	0	0	262,02	0,0368	1	0	0
37	249,32	0,0036	1	0	0	252,7	0,0097	1	0	0	249,31	0,0049	1	0	0	261,77	0	0	0,61	0,39
38	249,27	0,0045	1	0	0	252,59	0,0136	1	0	0	249,27	0,0051	1	0	0	261,77	0	0	0,39	0,61
39	247,55	0,2896	1	0	0	252,53	0,3689	1	0	0	248,91	0	0	0,96	0,04	252,94	0,569	0,94	0,06	0
40	247,4	0,0024	1	0	0	251,76	0,0001	1	0	0	248,91	0	0	0,04	0,96	252,67	0,0282	1	0	0

20

Electrochemistry

Reversibility of the oxidation of the complexes between 0.3 V and 0.4 V assigned to the oxidation of Fe^{2+} to Fe^{3+} has been tested by the criterion of Nicholson² and the Randles-Sevcik-equation.³

Electrochemical data of $[\text{Co}]^{2+}$

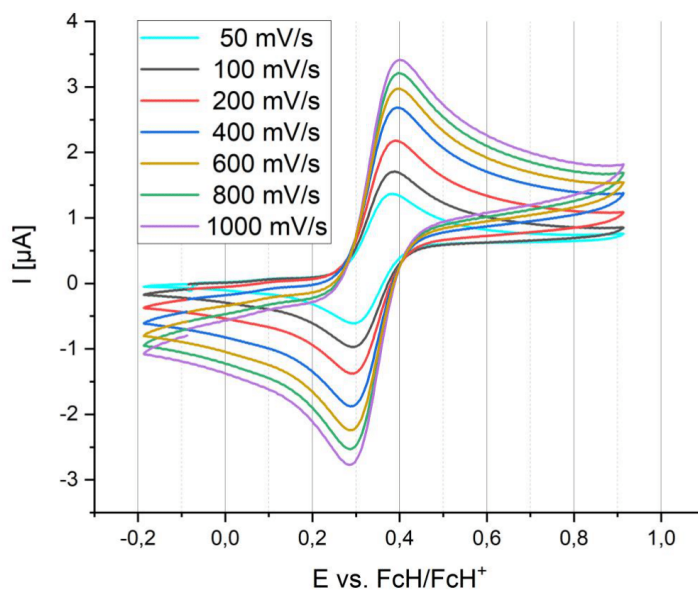


Figure S 26: Cyclic voltammograms of the reversible oxidation of $[\text{Co}]^{2+}$ at $E_{1/2} = 0.34$ V vs. FcH/FcH^+ recorded at different scan rates confirming the diagnostic criterion of Nicholson.

Table S 5: Electrochemical data for the reversible oxidation of $[\text{Co}]^{2+}$ at $E_{1/2} = 0.34$ V vs. Fc/Fc^+ .

scan rate	[mV/s]	50	100	200	400	600	800	1000
E_{cat}	[V]	0.30	0.30	0.29	0.30	0.29	0.29	0.29
E_{an}	[V]	0.38	0.38	0.39	0.39	0.40	0.39	0.39
$E_{1/2}$	[V]	0.34	0.34	0.34	0.34	0.34	0.34	0.34
ΔE	[V]	0.08	0.08	0.10	0.10	0.10	0.10	0.10
I_{an}	[μA]	1.06	1.41	1.82	2.31	2.64	2.89	3.09
$ I_{\text{cat}} $	[μA]	1.01	1.33	1.72	2.22	2.58	2.86	3.08
$ I_{\text{an}}/I_{\text{cat}} $	[-]	1.05	1.05	1.06	1.04	1.02	1.01	1.00

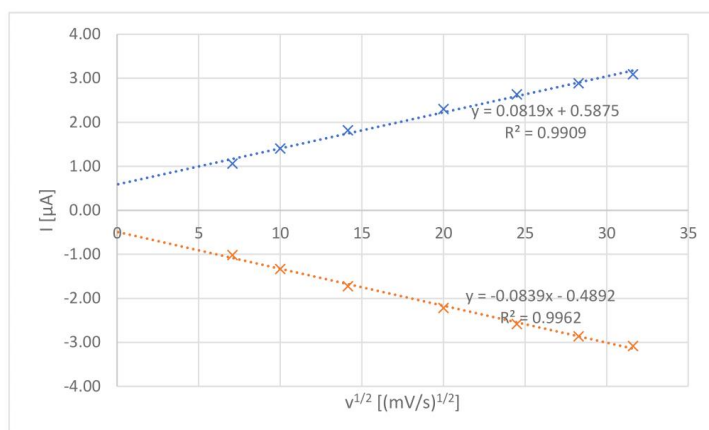


Figure S 27: Linear dependence of forward current peaks I_{on} and I_{cat} versus the square root of the scan rate for the reversible oxidation of $[C0]^{2+}$ at $E_{1/2} = 0.34$ V vs. FcH/FcH⁺.

Electrochemical data of $[C1]^{2+}$

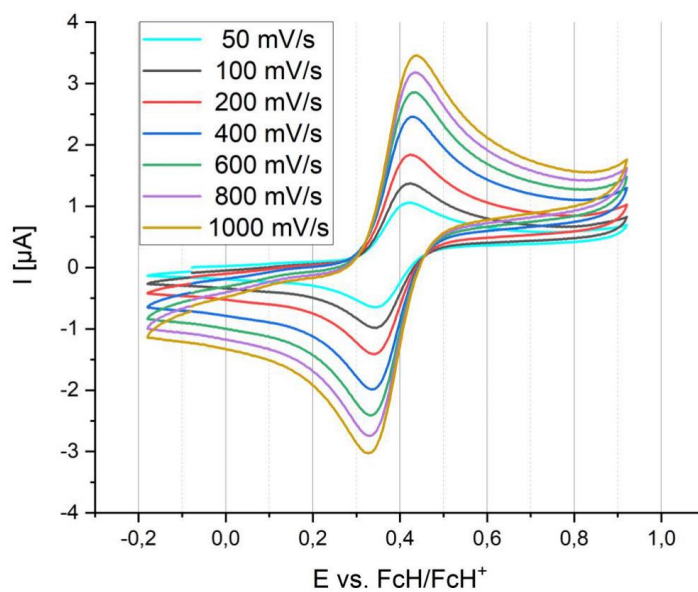
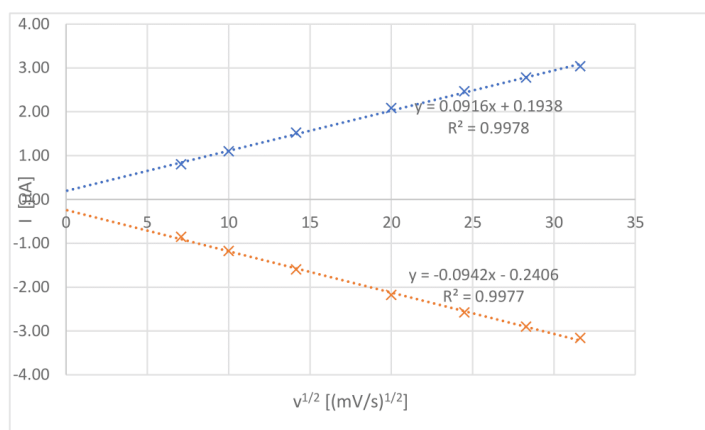


Figure S 28: Cyclic voltammograms of the reversible oxidation of $[C1]^{2+}$ at $E_{1/2} = 0.38$ V vs. FcH/FcH⁺ recorded at different scan rates confirming the diagnostic criterion of Nicholson.

Table S 6: Electrochemical data for the reversible oxidation of $[C1]^{2+}$ at $E_{1/2} = 0.38$ V vs. FcH/FcH⁺.

scan rate	[mV/s]	50	100	200	400	600	800	1000
E_{cat}	[V]	0.35	0.34	0.34	0.34	0.34	0.34	0.33
E_{an}	[V]	0.42	0.42	0.42	0.42	0.43	0.43	0.43
$E_{1/2}$	[V]	0.38	0.38	0.38	0.38	0.38	0.39	0.38
ΔE	[V]	0.07	0.08	0.08	0.09	0.09	0.10	0.10
I_{an}	[μ A]	0.80	1.09	1.52	2.08	2.47	2.78	3.04
$ I_{cat} $	[μ A]	0.86	1.18	1.60	2.18	2.58	2.90	3.16
$ I_{an}/I_{cat} $	[-]	0.93	1.08	1.05	1.05	1.05	1.04	1.04

Figure S 29: Linear dependence of forward current peaks I_{an} and I_{cat} versus the square root of the scan rate for the reversible oxidation of $[C1]^{2+}$ at $E_{1/2} = 0.38$ V vs. FcH/FcH⁺.

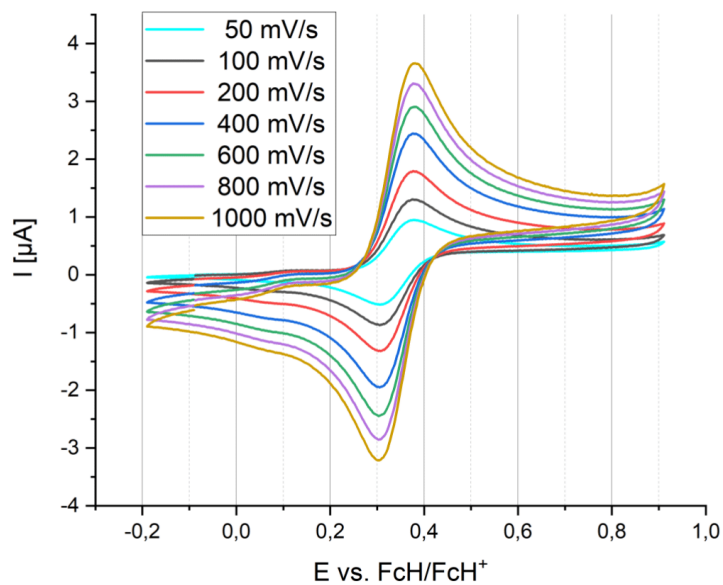
Electrochemical data of $[C2]^{2+}$ 

Figure S 30: Cyclic voltammograms of the reversible oxidation of $[C2]^{2+}$ at $E_{1/2} = 0.34$ V vs. FcH/FcH⁺ recorded at different scan rates confirming the diagnostic criterion of Nicholson.

Table S 7: Electrochemical data for the reversible oxidation of $[C2]^{2+}$ at $E_{1/2} = 0.34$ V vs. FcH/FcH⁺.

scan rate	[mV/s]	50	100	200	400	600	800	1000
E_{cat}	[V]	0.31	0.31	0.31	0.31	0.30	0.31	0.31
E_{an}	[V]	0.37	0.38	0.37	0.37	0.37	0.38	0.38
$E_{1/2}$	[V]	0.34	0.35	0.34	0.34	0.34	0.34	0.34
ΔE	[V]	0.06	0.07	0.07	0.07	0.07	0.07	0.08
I_{an}	[μA]	0.76	1.08	1.53	2.16	2.63	3.04	3.40
$ I_{cat} $	[μA]	0.79	1.11	1.57	2.20	2.67	3.09	3.44
$ I_{an}/I_{cat} $	[-]	0.96	0.97	0.98	0.98	0.99	0.98	0.99

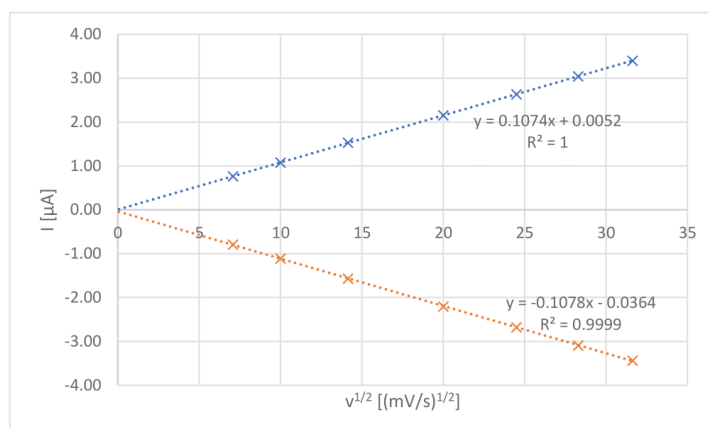


Figure S 31: Linear dependence of forward current peaks I_{an} and I_{cat} versus the square root of the scan rate for the reversible oxidation of $[C2]^{2+}$ at $E_{1/2} = 0.34$ V vs. FcH/FcH⁺.

Cyclic voltammetry of $[\text{H}_2\text{-L0}]^{2+}$, $[\text{H}_2\text{-L1}]^{2+}$ and $[\text{H}_2\text{-L2}]^{2+}$

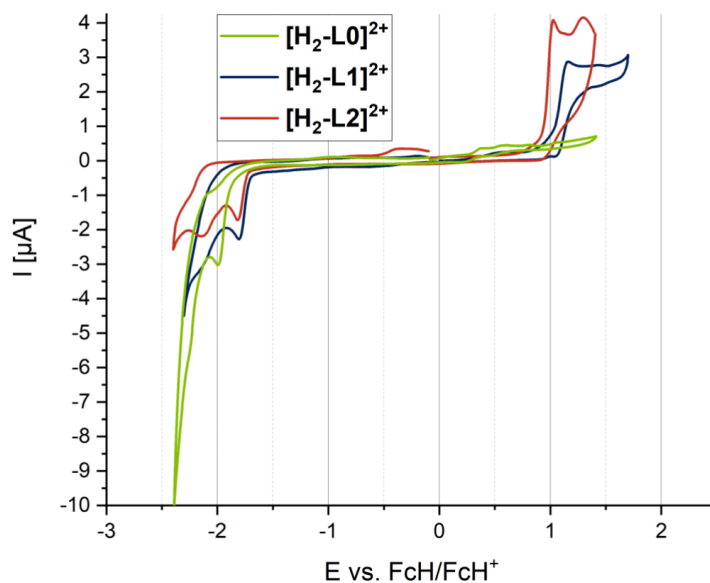


Figure S 32: Cyclic voltammograms of Ligands $[\text{H}_2\text{-L0}]^{2+}$ - $[\text{H}_2\text{-L2}]^{2+}$ vs. FcH/FcH^+ with 100 mV/s scan rate.

Cyclic voltammetry of $[\text{H}_2\text{-L0}]^{2+}$ shows the first irreversible reduction peak at -2.0 V. No oxidation is observed. The first peaks of the irreversible reduction of $[\text{H}_2\text{-L1}]^{2+}$ (-1.8 V) and $[\text{H}_2\text{-L2}]^{2+}$ (-1.8 V) are at more anodic potentials, in line with the interpretation of $[\text{H}_2\text{-L1}]^{2+}$ and $[\text{H}_2\text{-L2}]^{2+}$ as better π -acceptors than $[\text{H}_2\text{-L0}]^{2+}$. Irreversible oxidation occurs at 1.2 V ($[\text{H}_2\text{-L1}]^{2+}$) and 1.0 V ($[\text{H}_2\text{-L2}]^{2+}$) assigned to oxidation of the organic chromophores.

Cyclic voltammetry of anthracene and pyrene

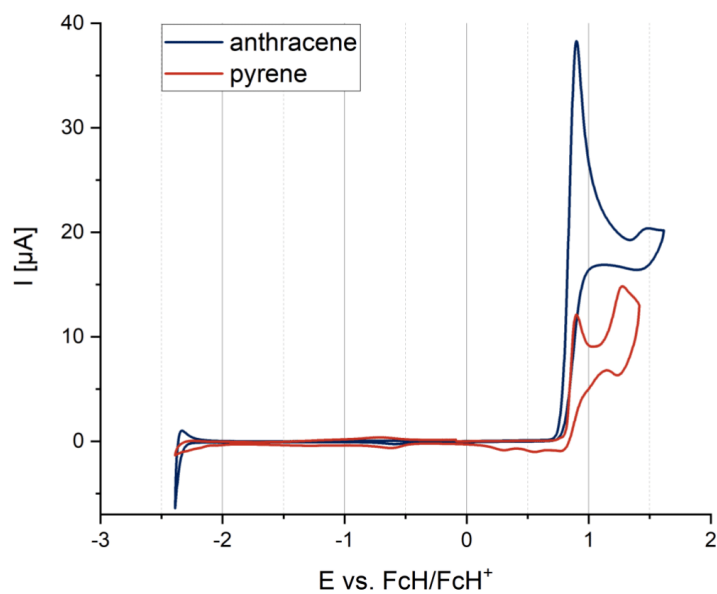


Figure S 33: Cyclic voltammograms of anthracene and pyrene vs. FcH/FcH⁺ with 100 mV/s scan rate.

Irreversible oxidation occurs at 0.9 V for both compounds, anthracene and pyrene, assigned to the oxidation of the organic chromophores, confirming the interpretation of the irreversible oxidation in $[\text{H}_2\text{-L1}]^{2+}$, $[\text{H}_2\text{-L2}]^{2+}$, $[\text{C1}]^{2+}$ and $[\text{C2}]^{2+}$ corresponding to the oxidation of the organic chromophores.

Spectroelectrochemistry

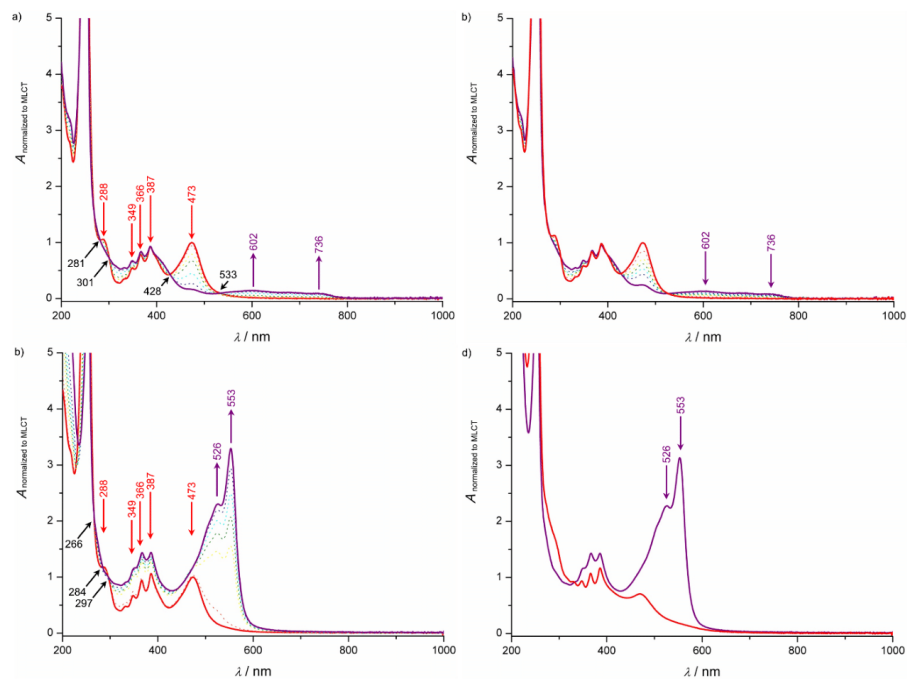
Spectroelectrochemical data of $[C1]^{2+}$ 

Figure S 34: Changes in the UV/Vis/NIR spectra of $[C1]^{2+}$ a) during oxidation (red \rightarrow purple), b) during re-reduction (purple \rightarrow red), c) during reduction (red \rightarrow purple) and d) during re-oxidation (purple \rightarrow red) in $\text{MeCN}/[n\text{-Bu}_4\text{N}][\text{PF}_6]$.

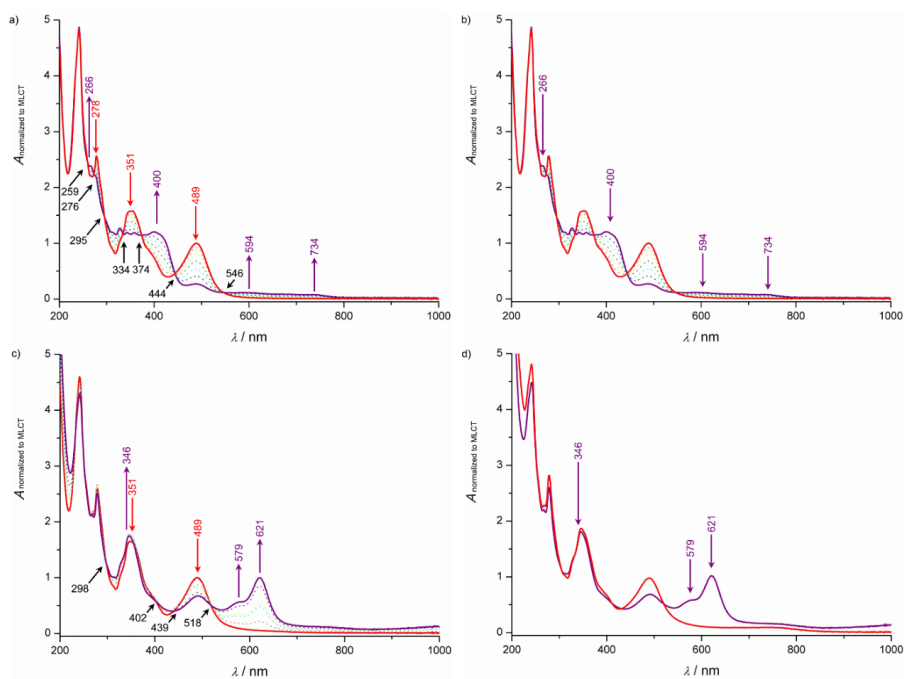
Spectroelectrochemical data of $[C2]^{2+}$ 

Figure S 35: Changes in the UV/Vis/NIR spectra of $[C2]^{2+}$ a) during oxidation (red \rightarrow purple), b) during re-reduction (purple \rightarrow red), c) during reduction (red \rightarrow purple) and d) during re-oxidation (purple \rightarrow red) in MeCN/[*n*-Bu₄N][PF₆].

Ground state absorption spectra A_{gr} and absorption spectra of the oxidized states A_{ox} and reduced states A_{red} were used to approximate the excited-state differential spectra ΔA_{ex}^{sim} using the following equation⁴:

$$\Delta A_{ex}^{sim} = (A_{ox} + A_{red}) \cdot \eta - 2 \cdot A_{gr} \cdot (1 - \eta)$$

Luminescence Properties

Fluorescence quantum yields are determined with sample solutions exhibiting an optical density of less than 0.1 at the excitation wavelengths. As standard coumarin 153 in ethanol is applied for excitation wavelengths greater than 380 nm and quinine bisulfate in 0.05 M H₂SO₄ for shorter excitation wavelengths. For coumarin 153 a quantum yield of 53 % and for quinine bisulfate of 52 % is assumed based on the literature.^{5,6} The area under the emission spectra recorded for different excitation wavelengths is plotted against the absorbance at the respective excitation wavelength. The slope of the resulting curve is used to calculate the quantum yield according to the following equation:

$$\phi_{Sample} = \phi_{Standard} \left(\frac{Gradient_{sample}}{Gradient_{standard}} \right) \left(\frac{\eta_{Sample}^2}{\eta_{Standard}^2} \right)$$

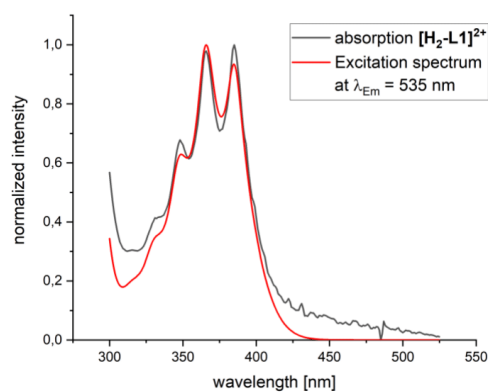


Figure S 36: Absorption (black) and normalized excitation (red) spectrum of [H₂-L1]²⁺. Excitation spectrum showing the intensity of the emission at λ_{em} = 535 nm as function of the excitation wavelength.

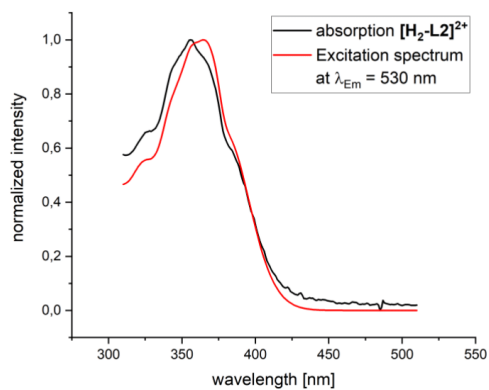


Figure S 37: Absorption (black) and normalized excitation (red) spectrum of $[H_2-L2]^{2+}$. Excitation spectrum showing the intensity of the emission at $\lambda_{em} = 530$ nm as function of the excitation wavelength.

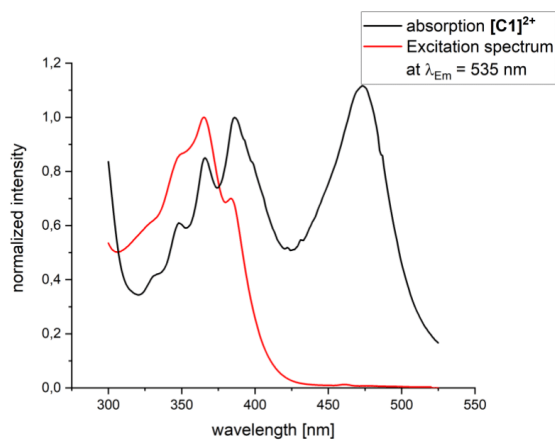


Figure S 38: Absorption (black) and normalized excitation (red) spectrum of $[C1]^{2+}$. Excitation spectrum showing the intensity of the emission at $\lambda_{em} = 535$ nm as function of the excitation wavelength.

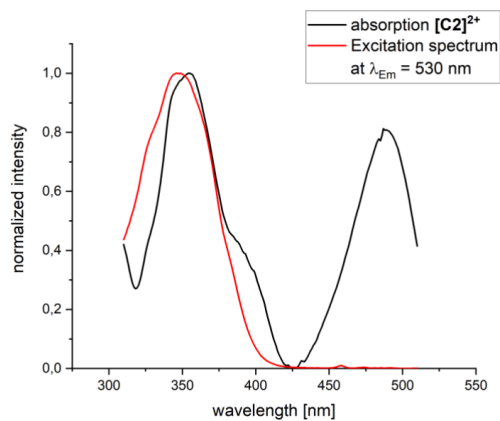


Figure S 39: Absorption (black) and normalized excitation (red) spectrum of $[C2]^{2+}$. Excitation spectrum showing the intensity of the emission at $\lambda_{Em} = 530$ nm as function of the excitation wavelength.

Excitation spectra at $\lambda_{Em} = 535$ nm reproduce only chromophore part of the spectra in $[H_2-L1]^{2+}$, $[H_2-L2]^{2+}$, $[C1]^{2+}$ and $[C2]^{2+}$. For $[C1]^{2+}$ and $[C2]^{2+}$ the MLCT band in the range of 450–500 nm is not reproduced, confirming the assignment of the luminescence to singlet states of the organic chromophores. The MLCT states are not involved in the emission.

Singlet Oxygen Experiments

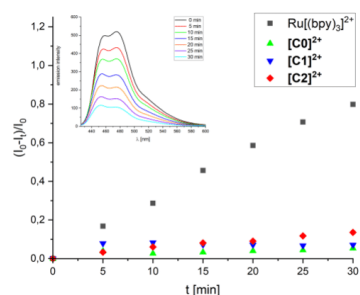


Figure S 40: **DPBF** consumption as function of irradiation time ($\lambda_{ir} = 480$ nm) in air equilibrated MeOH. Inset: time dependent emission spectra of the system with $[Ru(bpy)_3]^{2+}$ as PS, showing the decrease of emission intensity in presence of a long-lived triplet state.

Black squares represent the consumption of **DPBF** after irradiation with $\lambda_{ir} = 480$ nm. $[Ru(bpy)_3]^{2+}$ sensitizes 1O_2 with a quantum yield of 0.86.⁷ In none of the probed iron complexes $[C0]^{2+}$ - $[C2]^{2+}$ reactive 1O_2 was detected after irradiation with $\lambda_{ir} = 480$ nm.

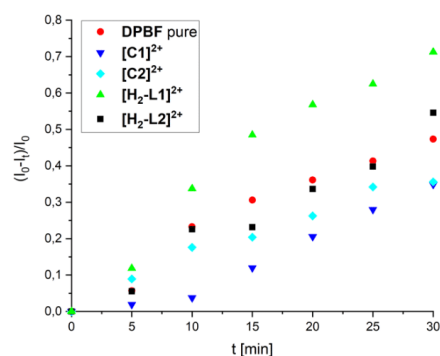


Figure S 41: **DPBF** consumption as function of irradiation time ($\lambda_{ir} = 346$ nm) in air equilibrated MeOH.

DPBF is not photostable after irradiation with $\lambda_{ir} = 346$ nm, therefore the consumption of pure **DPBF** without further photosensitizer is taken as reference. None of the compounds $[H_2-L1]^{2+}$, $[H_2-L2]^{2+}$, $[C1]^{2+}$ and $[C2]^{2+}$ show a significant difference in the slope of **DPBF** consumption in comparison to pure **DPBF**. This leads to the interpretation, that no long-lived triplet state is populated in $[H_2-L1]^{2+}$, $[H_2-L2]^{2+}$, $[C1]^{2+}$ and $[C2]^{2+}$ after excitation with $\lambda_{ir} = 346$ nm.

References

- (1) Möhle, T.; Bokareva, O. S.; Grell, G.; Kühn, O.; Bokarev, S. I. Tuned Range-Separated Density Functional Theory and Dyson Orbital Formalism for Photoelectron Spectra. *Journal of chemical theory and computation* **2018**, *14*, 5870–5880.
- (2) Nicholson, R. S.; Shain, I. Theory of Stationary Electrode Polarography. Single Scan and Cyclic Methods Applied to Reversible, Irreversible, and Kinetic Systems. *Anal. Chem.* **1964**, *36*, 706–723.
- (3) Randles, J. E. B. A cathode ray polarograph. Part II.—The current-voltage curves. *Trans. Faraday Soc.* **1948**, *44*, 327–338.
- (4) Brown, A. M.; McCusker, C. E.; McCusker, J. K. Spectroelectrochemical identification of charge-transfer excited states in transition metal-based polypyridyl complexes. *Dalton transactions (Cambridge, England : 2003)* **2014**, *43*, 17635–17646.
- (5) Meech, S. R.; Phillips, D. Photophysics of some common fluorescence standards. *Journal of Photochemistry* **1983**, *23*, 193–217.
- (6) Würth, C.; Grabolle, M.; Pauli, J.; Spieles, M.; Resch-Genger, U. Relative and absolute determination of fluorescence quantum yields of transparent samples. *Nature protocols* **2013**, *8*, 1535–1550.
- (7) Demas, J. N.; Harris, E. W.; McBride, R. P. Energy transfer from luminescent transition metal complexes to oxygen. *J. Am. Chem. Soc.* **1977**, *99*, 3547–3551.

7 Acknowledgements

[Redacted text block]

[Redacted text block]

[Redacted text block]

[Redacted text block]

[Redacted text block]

[Redacted text block]

[Redacted text block]

[Redacted text block]

8 Curriculum vitae

